

# Measurement and simulation of extreme ultraviolet ablation of solids

James Alexander Lolley

Doctor of Philosophy

University of York

Physics

November 2021



# Abstract

This thesis reports an experimental and modelling investigation of ablation of solid targets by Extreme Ultra-Violet (EUV) laser light at 46.9 nm. The increased photon energy at these wavelengths enables photo-ionization and increases the critical density above solid density; setting EUV ablation apart from optical wavelength ablation. Experimental ablation features on aluminium, gold, and copper targets are created by focussing radiation from a capillary discharge laser emitting at 46.9 nm to produce on-target fluences from  $50 \text{ J cm}^{-2}$  to  $500 \text{ J cm}^{-2}$ . The ablation features have depths in the region of  $0.5 \mu\text{m}$  to  $1.2 \mu\text{m}$  and crater radii between  $2 \mu\text{m}$  and  $3.5 \mu\text{m}$ , measured by post-shot atomic force microscopy. Four models are compared to the metal ablation depths; an optical femtosecond pulse model proposed by Gamaly, a ‘bleaching wave’ model, a hydrostatic transmission model with spatial resolution, and the radiation hydrodynamics code MULTI-IFE. The transmission model is developed in this thesis; it employs a Saha-Boltzmann ionization model and uses classical expressions for photo-ionization and inverse bremsstrahlung absorption. Additional physics including degenerate ionization models and absorption coefficients, Gaunt factors, and ionization potential lowering are tested; only the latter is found to significantly affect ablation depth. The model is also adapted to use an existing ionization tool, FLYCHK, to calculate ablation depths with increased accuracy. Investigations into the ‘bleaching’ of the plasma implied by the bleaching wave model show little evidence to support it.

The ablation depth behaviour of targets was found to depend on the attenuation length of the solid target material to the EUV radiation. For targets with long attenuation lengths such as aluminium, the femtosecond optical ablation model and the hydrostatic transmission model predict ablation depths close to those measured experimentally. For short attenuation length targets such as gold and copper, the one-dimensional hydrodynamic model MULTI-IFE predicts similar ablation depths to those measured experimentally – suggesting lateral transport is not significant. This shows that EUV ablation interactions can be modelled using one-dimensional fluid codes intended for optical laser interactions.

# Contents

|  |           |
|--|-----------|
| <b>Abstract</b>  | <b>3</b>  |
| <b>Contents</b>  | <b>4</b>  |
| <b>List of Tables</b>  | <b>7</b>  |
| <b>List of Figures</b>                                       | <b>8</b>  |
| <b>Acknowledgements</b>                                      | <b>19</b> |
| <b>Declaration of Authorship</b>                             | <b>20</b> |
| <b>1 Introduction</b>  | <b>21</b> |
| 1.1 The premise of the Thesis . . . . .                      | 23        |
| 1.2 Thesis structure . . . . .                               | 24        |
| <b>2 EUV radiation sources and laser-plasma interactions</b> | <b>26</b> |
| 2.1 EUV radiation sources . . . . .                          | 26        |
| 2.1.1 Laser-Produced Plasma sources . . . . .                | 27        |
| 2.1.2 Synchrotrons and Free Electron Lasers . . . . .        | 27        |
| 2.1.3 High Harmonic Generation . . . . .                     | 29        |
| 2.2 Capillary Discharge Lasers . . . . .                     | 30        |
| 2.3 Applications of EUV radiation sources . . . . .          | 33        |
| 2.3.1 Imaging . . . . .                                      | 33        |
| 2.3.2 Nanofabrication . . . . .                              | 34        |
| 2.4 Laser ablation . . . . .                                 | 35        |
| 2.4.1 Properties of Laser-Produced Plasmas . . . . .         | 35        |
| 2.4.2 The mechanics of ablation . . . . .                    | 40        |
| 2.4.3 EUV Ablation . . . . .                                 | 51        |

|          |   |            |
|----------|---|------------|
| <b>3</b> | <b>EUV solid target ablation</b>                                  | <b>53</b>  |
| 3.1      | Experimental dimensions and components . . . . .                  | 53         |
| 3.1.1    | Experimental layout geometry . . . . .                            | 53         |
| 3.1.2    | EUV laser light source . . . . .                                  | 55         |
| 3.1.3    | Optics and focussing . . . . .                                    | 56         |
| 3.1.4    | Detectors and pulse energy measurements . . . . .                 | 61         |
| 3.1.5    | Vacuum system . . . . .   | 63         |
| 3.1.6    | Target dimensions and materials . . . . .                         | 63         |
| 3.2      | Methodology . . . . .   | 64         |
| 3.2.1    | Detector calibration . . . . .                                    | 64         |
| 3.2.2    | Capillary laser alignment . . . . .                               | 65         |
| 3.2.3    | Empirical ablation study . . . . .                                | 66         |
| 3.2.4    | Analysis of targets . . . . .                                     | 67         |
| 3.2.5    | Two-dimensional profile extraction and analysis . . . . .         | 68         |
| 3.2.6    | Lateral transport . . . . .                                       | 78         |
| 3.3      | Simple modelling of target ablation . . . . .                     | 80         |
| 3.3.1    | The Gamaly model . . . . .  | 81         |
| 3.3.2    | The bleaching wave model . . . . .                                | 84         |
| 3.4      | Summary and conclusions . . . . .                                 | 87         |
| <b>4</b> | <b>A study of the assumptions behind the bleaching wave model</b> | <b>90</b>  |
| 4.1      | Transmission calculations . . . . .                               | 91         |
| 4.1.1    | Ion population algorithms . . . . .                               | 92         |
| 4.1.2    | Absorption coefficients . . . . .                                 | 95         |
| 4.1.3    | Energy content . . . . .  | 97         |
| 4.2      | Model corrections . . . . .                                       | 100        |
| 4.2.1    | Ion population model corrections . . . . .                        | 100        |
| 4.2.2    | Absorption coefficient corrections . . . . .                      | 107        |
| 4.3      | Benchmarking against an existing model . . . . .                  | 114        |
| 4.4      | On the opacity of warm dense aluminium . . . . .                  | 117        |
| 4.5      | Summary and conclusions . . . . .                                 | 119        |
| <b>5</b> | <b>Time-resolved constant density models of EUV ablation</b>      | <b>122</b> |
| 5.1      | Novel rate equation model . . . . .                               | 123        |
| 5.2      | Temporal intensity variations . . . . .                           | 125        |

|          |   |            |
|----------|---|------------|
| 5.2.1    | Saha-Boltzmann based ionization model . . . . .           | 127        |
| 5.2.2    | FLYCHK ionization model . . . . .                         | 130        |
| 5.3      | Replacing the bleaching wave model . . . . .              | 134        |
| 5.3.1    | Saha-Boltzmann based ionization model . . . . .           | 136        |
| 5.3.2    | FLYCHK ionization model . . . . .                         | 138        |
| 5.4      | Aluminium Oxide . . . . .                                 | 140        |
| 5.5      | Summary and Conclusions . . . . .                         | 141        |
| <b>6</b> | <b>Hydrodynamic simulations of EUV ablation</b>           | <b>143</b> |
| 6.1      | MULTI-IFE . . . . .                                       | 144        |
| 6.2      | Laser deposition algorithm . . . . .                      | 145        |
| 6.2.1    | Adjustments . . . . .                                     | 147        |
| 6.3      | Electron collision frequency . . . . .                    | 149        |
| 6.3.1    | Classical collision frequency . . . . .                   | 149        |
| 6.3.2    | Electron-phonon collision frequency . . . . .             | 150        |
| 6.4      | Methodology for simulations . . . . .                     | 153        |
| 6.4.1    | The electron-phonon model for gold . . . . .              | 153        |
| 6.4.2    | Controlling MULTI-IFE . . . . .                           | 154        |
| 6.4.3    | Data output from MULTI-IFE . . . . .                      | 156        |
| 6.5      | Simulations of experimental ablation conditions . . . . . | 157        |
| 6.5.1    | Testing the absorption coefficient correction . . . . .   | 157        |
| 6.5.2    | Initial testing of independent variables . . . . .        | 160        |
| 6.5.3    | Comparing to experimental ablation depths . . . . .       | 164        |
| 6.6      | Energy Deposition . . . . .                               | 167        |
| 6.7      | Summary and Conclusions . . . . .                         | 172        |
| <b>7</b> | <b>Conclusions</b>  | <b>174</b> |
| 7.1      | Summary of results . . . . .                              | 174        |
| 7.2      | Conclusions . . . . .                                     | 178        |
| 7.3      | Future work . . . . .                                     | 179        |
| <b>A</b> | <b>Changes to MULTI-IFE source code</b>                   | <b>181</b> |
|          | <b>References</b>   | <b>192</b> |

# List of Tables

|     |   |     |
|-----|---|-----|
| 2.1 | Most important characteristics of the laser system, taken from various characterisation experiments of the prototypes. . . . .  | 33  |
| 3.1 | Attenuation lengths in nm of 46.9 nm radiation for our target materials using the IMD software package [62] and the CXRO database [3]. . . . .  | 63  |
| 3.2 | Relevant material properties for the target metals. . . . .   | 82  |
| 6.1 | Constant $k_s$ values for aluminium and gold as required by the electron-phonon electron-ion collision frequency model, labelled with associated variables in the MULTI-IFE input file. Al values are from [59] and Au values are deduced in the text. $K$ is the absorption coefficient (equation 6.5), $\kappa$ is the thermal heat conductivity (equation 6.21) and $\gamma$ is the electron-ion coupling coefficient (equation 6.22). . . . . | 154 |
| 6.2 | List of relevant switches in the <code>&amp;parameters</code> section of the input file with chosen or default values (in the correct units) and explanatory notes. . .   | 155 |
| 6.3 | List of relevant switches in the <code>&amp;layer</code> section of the input file with chosen or default values (in the correct units) and explanatory notes. . .  | 156 |
| 6.4 | List of relevant switches in the <code>&amp;pulse</code> section of the input file with chosen or default values (in the correct units) and explanatory notes. . .  | 156 |

# List of Figures

|     |   |    |
|-----|---|----|
| 2.1 | Left: only radiation in phase with the undulator frequency will constructively interfere. Right: Electrons in a FEL pass through the undulator and are steadily shifted into bunches by the potential wells [16]. . . . .   | 28 |
| 2.2 | Example Grotrian diagram for neon-like argon showing the possible lasing transitions [20]. The lasing transition exploited by the CDL source is labelled with the photon wavelength. . . . .  | 31 |
| 2.3 | Diagram of an example high voltage 2-gap hydrogen thyratron trigger such as may be found in the capillary discharge laser [21]. . . . .   | 32 |
| 2.4 | Phase diagram for aluminium showing the parameter space covered by Warm Dense Matter (WDM). Contours of constant coupling parameter and the boundary to the right of which degeneracy effects become significant are also shown [42]. The parameter spaces of ICF [43], EUV ablation (predicted), and the solar chromosphere [44] are shown to illustrate WDM's position as an intermediate parameter regime. . . . . | 39 |
| 2.5 | An illustration of a decelerated electron in the reference frame moving with velocity $v_0$ . In Zone 1 the field lines have moved to correspond with the new electron position. In Zone 3 they are still positioned relative to the original electron position. Subsequently, in Zone 2 we have the field lines that must exist in order to connect Zones 1 & 3. . . . .   | 42 |
| 3.1 | A schematic of the experimental setup illustrating the on-axis geometry for the mirror and sample holder. . . . .   | 54 |
| 3.2 | A cartoon illustrating the structure of a multilayer mirror and the partial reflections that occur at the material interfaces. . . . .  | 56 |
| 3.3 | Reflectivity as a function of Sc:Si multilayer mirror bilayer spacing, with a range of thickness ratios between the two materials. . . . .  | 57 |

|      |   |    |
|------|---|----|
| 3.4  | Reflectivity calculations for a Sc:Si multilayer mirror reflecting 46.9 nm light made using the IMD software package [62]. . . . .  | 58 |
| 3.5  | Diagram of the circular lens problem definition [63]. . . . .   | 59 |
| 3.6  | On-target intensity curve as a percentage of peak intensity plotted as a function of on-target radial position for a lens with a focal length of 50 mm focussing an annular beam of constant intensity between on-lens radii of 1.5 mm and 4.5 mm. The red curve is a Gaussian function fitted to the Bessel function curve and is a suitable approximation for the beam shape. . . . . | 61 |
| 3.7  | Diagrams of (a) the normal incidence photodetector and (b) the in-line photodetector [1]. . . . .   | 62 |
| 3.8  | Normal-incidence photodetector voltage plotted as a function of in-line photodetector voltage, shown for a large number of different capillary laser shots. . . . .   | 64 |
| 3.9  | A schematic of the mirror layout required to align the EUV laser using an optical substitute. . . . .   | 65 |
| 3.10 | Example images of (a) an in-focus ablation shot and (b) an out-of-focus ablation shot demonstrating the ‘hamburger’ shape, both on gold targets.  | 67 |
| 3.11 | An AFM image of a Sc:Si multilayer mirror focussed shot on a gold target.   | 69 |
| 3.12 | A linear profile extracted from a Sc:Si mirror shot on a gold target. The shaded area is the range the data is clipped to to ensure accurate fitting.   | 71 |
| 3.13 | The ablation crater area, measured at the target surface, as a function of the natural logarithm of the pulse energy for aluminium. Also shown is a linear fit, or so-called Liu plot, of the data and the physical parameters that can be drawn from it. . . . .   | 73 |
| 3.14 | The ablation crater area, measured at the target surface, as a function of the natural logarithm of the pulse energy for gold. Also shown is a linear fit, or so-called Liu plot, of the data and the physical parameters that can be drawn from it. . . . .  | 73 |
| 3.15 | The ablation crater area, measured at the target surface, as a function of the natural logarithm of the pulse energy for copper. Also shown is a linear fit, or so-called Liu plot, of the data and the physical parameters that can be drawn from it. . . . .  | 74 |

|   |    |
|---|----|
| 3.16 Focal spot size as predicted by Abbe’s criterion and a two-dimensional ray tracing code as a function of radius of curvature of a spherical optic for 46.9 nm radiation. . . . .   | 75 |
| 3.17 (a) A highly asymmetric ablation feature on aluminium compared to (b) a highly symmetric ablation feature on gold. . . . .   | 75 |
| 3.18 The ablation depth as a function of the laser fluence on target for aluminium. . . . .   | 76 |
| 3.19 The ablation depth as a function of the laser fluence on target for gold.  | 76 |
| 3.20 The ablation depth as a function of the laser fluence on target for copper.  | 77 |
| 3.21 (a) An example of high ablation depth variance occurring in copper, compared to (b) a typical ablation depth variation (also copper). The maximum ablation depth is marked for each profile with a dotted horizontal line. . . . . | 78 |
| 3.22 The ablation crater profile with the highest aspect ratio on the gold targets (black). Also shown is the corresponding fitted Gaussian profile (red). . . . .  | 79 |
| 3.23 The ablation crater profile with the highest aspect ratio on the aluminium targets (black). Also shown is the corresponding fitted Gaussian profile (red). . . . .   | 80 |
| 3.24 Ablation depth as a function of fluence incident on an aluminium target as experimentally measured and as calculated using the Gamaly model [10] with the parameters from table 3.2. . . . .                                       | 83 |
| 3.25 Ablation depth as a function of fluence incident on a gold target as experimentally measured and as calculated using the Gamaly model [10] with the parameters from table 3.2. . . . .   | 83 |
| 3.26 Ablation depth as a function of fluence incident on a copper target as experimentally measured and as calculated using the Gamaly model [10] with the parameters from table 3.2. . . . .   | 84 |
| 3.27 Ablation depth as a function of fluence incident on a aluminium target as experimentally measured and as calculated using the Gamaly [10] and bleaching wave [73] models with parameters from table 3.2. . . . .                   | 86 |
| 3.28 Ablation depth as a function of fluence incident on a gold target as experimentally measured and as calculated using the Gamaly [10] and bleaching wave [73] models with parameters from table 3.2. . . . .                        | 86 |

|      |   |     |
|------|---|-----|
| 3.29 | Ablation depth as a function of fluence incident on a copper target as experimentally measured and as calculated using the Gamaly [10] and bleaching wave [73] models with parameters from table 3.2. . . . .   | 87  |
| 4.1  | A flowchart of the computer algorithm used to calculate the ion populations predicted by the Saha-Boltzmann ratio for a given electron temperature $T_e$ . . . . .  | 93  |
| 4.2  | Free electron densities as a function of plasma temperature, as predicted by the Saha-Boltzmann ionization model for an aluminium, gold, and copper plasma at solid density. . . . .  | 94  |
| 4.3  | Absorption coefficient as a function of plasma temperature with Saha-Boltzmann ionization for an aluminium target at solid density. The dotted curves show the contribution to the total of the free-free and bound-free absorption coefficients. . . . .   | 96  |
| 4.4  | Absorption coefficient as a function of plasma temperature with Saha-Boltzmann ionization for a gold target at solid density. The dotted curves show the contribution to the total of the free-free and bound-free absorption coefficients. . . . .   | 96  |
| 4.5  | Absorption coefficient as a function of plasma temperature with Saha-Boltzmann ionization for a copper target at solid density. The dotted curves show the contribution to the total of the free-free and bound-free absorption coefficients. . . . .   | 97  |
| 4.6  | Plasma energy content (expressed as a density) as a function of plasma temperature with Saha-Boltzmann ionization for an aluminium, gold, and copper target at solid density. . . . .   | 98  |
| 4.7  | Transmission through a 10 nm slice as a function of plasma temperature with Saha-Boltzmann ionization for an aluminium, gold, and copper plasma at solid density. Also shown (dashed lines) are the transmissions of a 10 nm slice of unheated solid material for each element calculated using attenuation lengths from table 3.1. . . . . | 99  |
| 4.8  | Electron density as a function of plasma temperature, as predicted by the high- and low-density forms of the Saha-Boltzmann ionization model, for an aluminium, gold, and copper target at solid density. . . . .   | 103 |

4.9 Free electron density as a function of plasma temperature, as predicted by the Saha-Boltzmann ionization model with and without ionization potential lowering (IPL), for an aluminium, gold, and copper target at solid density. . . . . 105

4.10 Total absorption coefficient as a function of plasma temperature, as predicted by the Saha-Boltzmann ionization model with and without ionization potential lowering (IPL), for an aluminium, gold, and copper target at solid density. . . . . 105

4.11 Plasma energy content as a function of plasma temperature, as predicted by the Saha-Boltzmann ionization model with and without ionization potential lowering (IPL), for an aluminium, gold, and copper target at solid density. . . . . 106

4.12 Transmission through a 10 nm slice as a function of plasma temperature, as predicted by the Saha-Boltzmann ionization model with and without ionization potential lowering (IPL), for an aluminium, gold, and copper target at solid density. . . . . 107

4.13 Maxwell-averaged free-free Gaunt factors as a function of the dimensionless parameter  $\gamma^2 = Z_i^2 R_y/k_B T$  for a range of values of  $u$  where  $u = \hbar\omega/k_B T$  [84]. . . . . 108

4.14 Maxwell-averaged free-free Gaunt factor  $\bar{g}_{ff}$  as a function of plasma temperature, for conditions predicted by the Saha-Boltzmann ionization model with and without ionization potential lowering (IPL), for an aluminium, gold, and copper, target at solid density. . . . . 109

4.15 Level-averaged bound-free gaunt factors  $\bar{g}_{bf}$  as a function of  $E/Z^2 R_y$  where  $E$  is the incident electron energy.  $\bar{g}_{bf}$  is shown for a range of principle quantum number  $n$  values. . . . . 110

4.16 Free-free absorption coefficient as a function of plasma temperature, as predicted by absorption coefficients both with (solid lines) and without (dashed lines) our degeneracy correction, for an aluminium, gold, and copper target at solid density. . . . . 112

4.17 Bound-free absorption coefficient as a function of plasma temperature, as predicted by absorption coefficients both with (solid lines) and without (dashed lines) our degeneracy correction, for an aluminium, gold, and copper target at solid density. . . . . 113

|      |  |     |
|------|--|-----|
| 4.18 | Transmission through a 10 nm slice as a function of plasma temperature, as predicted by absorption coefficients both with (solid lines) and without (dashed lines) our degeneracy correction, for an aluminium, gold, and copper target at solid density. . . . .  | 113 |
| 4.19 | Free electron densities as a function of plasma temperature, as predicted by the FLYCHK ionization model (solid lines) and the High-Density Saha-Boltzmann model with Ionization Potential Lowering (HDSB/IPL - dashed lines) for an aluminium, gold, and copper plasma at solid density.  | 115 |
| 4.20 | Total absorption coefficients as a function of plasma temperature, as predicted by the FLYCHK ionization model (solid lines) and the High-Density Saha-Boltzmann model with Ionization Potential Lowering (HDSB/IPL - dashed lines) for an aluminium, gold, and copper plasma at solid density.  | 116 |
| 4.21 | Transmission fractions through 10 nm slices of solid material as a function of plasma temperature, as predicted by the FLYCHK ionization model (solid lines) and the High-Density Saha-Boltzmann model with Ionization Potential Lowering (HDSB/IPL - dashed lines) for an aluminium, gold, and copper plasma at solid density. . . . .  | 117 |
| 4.22 | Total absorption coefficient of an aluminium plasma for 32 nm wavelength radiation as a function of plasma temperature calculated using the High Density Saha-Boltzmann ionization model with ionization potential lowering and classical absorption coefficients both with (blue line) and without (black line) degeneracy corrections. The degeneracy-corrected coefficient predicted by the FLYCHK ionization model is shown in orange. Also shown are absorption coefficient values from the models of Iglesias [53] (red points), Shaffer [96] (green points), and Hollebon [97] (blue points). . . . . | 118 |
| 5.1  | A cartoon of the populating and de-populating processes affecting a single ionization stage $i$ and a plasma with three relevant ionization stages.  | 123 |
| 5.2  | A cartoon of the populating and de-populating processes, including photoionization, affecting a single ionization stage $i$ and a plasma with three relevant ionization stages. . . . .  | 124 |

|      |  |     |
|------|--|-----|
| 5.3  | Electron density as a function of plasma temperature predicted by the Saha-Boltzmann and rate equation ionization models for a range of intensities of 46.9 nm radiation incident on a solid density aluminium target. The Saha-Boltzmann curve is obscured by higher intensity curves. . . .              | 125 |
| 5.4  | A flowchart of the computer algorithm used to calculate the time-resolved energy deposition (and consequent electron density, temperature, absorption coefficients and energy content) in a single target cell. . . . .  | 126 |
| 5.5  | Plasma temperature as a function of time for a range of peak incident intensities $I_0$ irradiating an aluminium target cell modelled using Saha-Boltzmann ionization. The EUV laser pulse has a $\sin^2 t$ temporal shape with a pulse duration of 1.2 ns. . . . .  | 128 |
| 5.6  | Maximum achieved plasma temperature as a function of peak incident fluence for aluminium, gold, and copper target cells at solid density as predicted by the Saha-Boltzmann ionization model. . . . .  | 128 |
| 5.7  | Transmission fraction as a function of time for a 10 nm thick aluminium target cell at solid density for EUV laser pulses with peak intensities as labelled. . . . .   | 129 |
| 5.8  | Transmission fraction as a function of time for a 10 nm thick gold target cell at solid density for EUV laser pulses with peak intensities as labelled.  | 129 |
| 5.9  | Transmission fraction as a function of time for a 10 nm thick copper target cell at solid density for EUV laser pulses with peak intensities as labelled. . . . .  | 130 |
| 5.10 | Plasma temperature as a function of elapsed time for a range of peak incident intensities $I_0$ irradiating an aluminium target cell modelled using FLYCHK ionization. The EUV laser pulse has a $\sin^2 t$ temporal shape with a pulse duration of 1.2 ns. . . . .  | 131 |
| 5.11 | Maximum achieved plasma temperature as a function of peak incident fluence for aluminium, gold, and copper target cells at solid density as predicted by the FLYCHK ionization model (dashed lines) and by the previous calculations using a Saha-Boltzmann based model (HDSB/IPL - dotted lines). . . . . | 131 |
| 5.12 | Transmission fraction as a function of time for a 10 nm thick aluminium target cell at solid density for EUV laser pulses with peak intensities as labelled and ionization calculated using the FLYCHK code. . . . .   | 132 |

|      |  |     |
|------|--|-----|
| 5.13 | Transmission fraction as a function of time for a 10 nm thick gold target cell at solid density for EUV laser pulses with peak intensities as labelled and ionization calculated using the FLYCHK code. . . . .  | 132 |
| 5.14 | Transmission fraction as a function of time for a 10 nm thick copper target cell at solid density for EUV laser pulses with peak intensities as labelled and ionization calculated using the FLYCHK code. . . . .  | 133 |
| 5.15 | A flowchart of the computer algorithm used to calculate the time-resolved energy deposition (and consequent electron density, temperature, absorption coefficients and energy content) in a mesh of target cells. . . . .  | 134 |
| 5.16 | Plasma temperature as a function of cell position at a range of times for an aluminium target at solid density irradiated with a peak intensity of $5 \times 10^{10} \text{ W cm}^{-2}$ of 46.9 nm wavelength radiation delivered in a 1.2 ns pulse. . . . .   | 135 |
| 5.17 | Ablation depths as a function of incident fluence as predicted by the spatially-resolved model with a range of ablation criteria for an aluminium target at solid density. Experimentally measured ablation depths (see Chapter 3) are also shown. . . . .   | 136 |
| 5.18 | Ablation depths as a function of incident fluence as predicted by the spatially-resolved model with a range of ablation criteria for a gold target at solid density. Experimentally measured ablation depths (see Chapter 3) are also shown. . . . .   | 137 |
| 5.19 | Ablation depths as a function of incident fluence as predicted by the spatially-resolved model with a range of ablation criteria for a copper target at solid density. Experimentally measured ablation depths (see Chapter 3) are also shown. . . . .   | 137 |
| 5.20 | Ablation depths as a function of incident fluence as predicted by the spatially-resolved model with ionization calculated using FLYCHK (red curve) and the Saha-Boltzmann model (blue curve) for an aluminium target at solid density. Experimentally measured ablation depths (see Chapter 3) are also shown. . . . . | 138 |

5.21 Ablation depths as a function of incident fluence as predicted by the spatially-resolved model with ionization calculated using FLYCHK (red curve) and the Saha-Boltzmann model (blue curve) for a gold target at solid density. Experimentally measured ablation depths (see Chapter 3) are also shown. . . . . 139

5.22 Ablation depths as a function of incident fluence as predicted by the spatially-resolved model with ionization calculated using FLYCHK (red curve) and the Saha-Boltzmann model (blue curve) for a copper target at solid density. Experimentally measured ablation depths (see Chapter 3) are also shown. . . . . 139

5.23 Ablation depths as a function of incident fluence as predicted by the spatially-resolved model with ionization calculated using FLYCHK (red, purple, & brown curves) and the Saha-Boltzmann model (blue, orange, & green curves) for an aluminium target at solid density. The three curves shown for each model are calculations simulating an aluminium oxide layer at the surface of 0 nm, 2 nm, and 3 nm thickness. Experimentally measured ablation depths (see Chapter 3) are also shown. . . . . 141

6.1 Corrected and un-corrected absorption coefficients as a function of plasma temperature for an aluminium plasma with electron density  $n_e = 1 \times 10^{20} \text{ cm}^{-3}$  and incident radiation at  $1.064 \mu\text{m}$ . . . . . 148

6.2 Corrected and un-corrected absorption coefficients as a function of plasma temperature for an aluminium plasma with electron density  $n_e = 1 \times 10^{20} \text{ cm}^{-3}$  and incident radiation at  $46.9 \text{ nm}$ . . . . . 148

6.3 Electron-ion collision frequency values as a function of temperature as predicted by the electron-phonon and Spitzer (classical) collision frequency models. An interpolation between the electron-phonon and Spitzer model is shown as a solid curve [59]. . . . . 152

6.4 Absorption coefficient as function of cell position for a MULTI-IFE simulation of  $1 \times 10^{11} \text{ W cm}^{-2}$  of radiation incident on an aluminium target at time  $t = 1.2 \text{ ns}$ .  $K$  is the uncorrected absorption coefficient and  $K^*C$  is the corrected form allowing for stimulated emission. The absorption coefficient for both  $1.064 \mu\text{m}$  and  $46.9 \text{ nm}$  wavelengths are shown. . . . . 158

|      |  |     |
|------|--|-----|
| 6.5  | Material density as function of cell position for a MULTI-IFE simulation of $1 \times 10^{11} \text{ W cm}^{-2}$ of radiation incident on an aluminium target at time $t = 1.2 \text{ ns}$ . Curves for both corrected and uncorrected absorption at $1.064 \mu\text{m}$ and $46.9 \text{ nm}$ are shown. . . . .                            | 159 |
| 6.6  | Electron temperature as function of cell position for a MULTI-IFE simulation of $1 \times 10^{11} \text{ W cm}^{-2}$ of radiation incident on an aluminium target at time $t = 1.2 \text{ ns}$ . Curves for both corrected and uncorrected absorption at $1.064 \mu\text{m}$ and $46.9 \text{ nm}$ are shown. . . . .                        | 159 |
| 6.7  | Material density as a function of cell position for a MULTI-IFE simulation of an aluminium target irradiated with a range of intensities in $\text{W cm}^{-2}$ at $46.9 \text{ nm}$ at time $t = 1.2 \text{ ns}$ . The rear boundary of the target is allowed to expand. The thermal conduction includes electron-phonon conduction. . . . . | 161 |
| 6.8  | Material density as a function of cell position for a MULTI-IFE simulation of an aluminium target irradiated with a range of intensities in $\text{W cm}^{-2}$ at $46.9 \text{ nm}$ at time $t = 1.2 \text{ ns}$ . The rear boundary of the target is fixed. The thermal conduction includes electron-phonon conduction. . . . .             | 161 |
| 6.9  | Ablation depths predicted by MULTI-IFE simulations of a range of fluences of $46.9 \text{ nm}$ radiation incident on an aluminium target. Results for simulations with a fixed and unfixed (free) left boundary are shown. . . . .   | 162 |
| 6.10 | Ablation depths predicted by MULTI-IFE simulations of a range of fluences of $46.9 \text{ nm}$ radiation incident on an aluminium target. Results for simulations without a flux limiting factor, and with a flux limiting factor of $0.1$ and $0.01$ are shown. . . . .   | 163 |
| 6.11 | Ablation depths predicted by MULTI-IFE simulations of a range of fluences of $46.9 \text{ nm}$ radiation incident on both aluminium and gold targets. Results for simulations with the maximum and minimum possible values of <b>flaser</b> are shown. . . . .   | 164 |
| 6.12 | Density $\rho$ and ion temperature $T_i$ profiles predicted by MULTI-IFE after $1.2 \text{ ns}$ simulations of an aluminium target with no incident radiation. Also shown is a profile of the melting temperature $T_m$ for each cell. . . . .   | 165 |

6.13 Ablation depths predicted by MULTI-IFE simulations of a range of fluences of 46.9 nm radiation incident on an aluminium target compared to results collected experimentally in Chapter 3. Results for simulations using both the classical and electron-phonon electron-ion collision frequency models are shown. . . . . 166

6.14 Ablation depths predicted by MULTI-IFE simulations of a range of fluences of 46.9 nm radiation incident on a gold target compared to results collected experimentally in Chapter 3. Results for simulations using both the classical and electron-phonon electron-ion collision frequency models are shown. . . . . 167

6.15 Deposited laser energy as a function of spatial position for the Saha Boltzmann (HDSB/IPL) and FLYCHK hydrostatic models and MULTI-IFE hydrodynamic model at time  $t = 0.637$  ns with  $1 \times 10^{12}$  W cm<sup>-2</sup> incident on an aluminium target. The broken green line shows the ablation depth predicted by the MULTI-IFE simulation. . . . . 168

6.16 Deposited laser energy as a function of spatial position for the Saha Boltzmann (HDSB/IPL) and FLYCHK hydrostatic models and MULTI-IFE hydrodynamic model at time  $t = 0.637$  ns with  $1 \times 10^{12}$  W cm<sup>-2</sup> incident on a gold target. The broken green line shows the ablation depth predicted by the MULTI-IFE simulation. . . . . 169

6.17 Total energy deposited per gram of ablated mass as predicted by the Saha-Boltzmann (HDSB/IPL) and FLYCHK hydrostatic models and the MULTI-IFE hydrodynamic model for an aluminium target. . . . . 170

6.18 Total energy deposited per gram of ablated mass as predicted by the Saha-Boltzmann (HDSB/IPL) and FLYCHK hydrostatic models and the MULTI-IFE hydrodynamic model for a gold target. . . . . 171

6.19 Total deposited laser energy as a function of fluence for the High Density Saha-Boltzmann simulations (with IPL), and for the MULTI-IFE simulations of both aluminium and gold targets. . . . . 171

# Acknowledgements

It goes without saying that projects like this don't happen without the help and support of a great number of people. First and foremost I must thank my supervisor Professor Greg Tallents for his guidance, support, and patience over the course of the project. I must also thank Dr Sarah Wilson, who has worked tirelessly on the capillary laser throughout the project and whose excellent company has seen me through many a long day in the lab. I would also like to thank Eduardo Solis Meza for his company and support during lab days and our visit to Colorado State University (and for his excellent cooking during the latter).

The experiments in this thesis wouldn't have happened without Richard and Kari, thank you for being on hand in the Plasma Institute labs and helping us with the laser.

The project would also not have been possible without the collaboration of Professors Jorge Rocca and Carmen Menoni and their team at Colorado State University; Herman, Chad, Lydia, and Chase. You could not ask for more welcoming and generous hosts, or a more helpful and friendly team of people to work with.

To my colleagues on the Fusion CDT Matt K, Matt S, Steve, Joe, Michael, and Stuart; thank you for many happy memories and for making the office such a warm place to be.

Lastly, I would like to say thank you to my family for all their love, support, and advice throughout this process. Thank you to my Aunt Madelaine for putting me up (and putting up with me) for several months of this process, allowing me to stay in York. Most of all, thank you to my wonderful parents, Carolyn and Mark, who have always loved and supported me and encouraged me to achieve my potential. This thesis is dedicated to you, the best parents anyone could ask for.

# Declaration of Authorship

I declare that this thesis is a presentation of original work and I am the sole author. This work has not previously been presented for an award at this, or any other, University. The experimental data collected and presented in Chapter 3 was obtained collaboratively with Sarah Wilson and has been presented with a preliminary interpretation in her thesis, entitled “A Study of Extreme Ultraviolet Capillary Discharge Lasers and the Ablation of Solid Targets” (submitted 2018) [1]. All the further analysis and interpretation of these results presented in this thesis is the work of the author. Publications from the thesis are listed below. All sources are acknowledged as References.

## List of publications

- (I). J A Lolley, G J Tallents, ”The role of photo-ionization in extreme ultraviolet ablation interactions,” Proc. SPIE 11886, International Conference on X-Ray Lasers 2020, 18860T, (2021).
- (II). G J Tallents, S A Wilson, J A Lolley, E Solis Meza, E Wagenaars, H Bravo, C S Menoni, J J Rocca, “The Ablation of Solid Targets Using a Capillary Discharge Laser”, Springer Proc. Phys. 241, International Conference on X-Ray Lasers 2018, 11, (2020).
- (III). J A Lolley, S A Wilson, G J Tallents, “Modelling extreme ultra-violet ablation interactions”, Proc. SPIE 11035, Optics Damage and Materials Processing by EUV/X-ray Radiation VII, 110350R, (2019).
- (IV). G J Tallents, S A Wilson, J Lolley, V Aslanyan, A West, A K Rossall, E Solis-Meza, E Wagenaars, C S Menoni, J J Rocca, ”Extreme ultraviolet laser ablation of solid targets,” Proc. SPIE 11111, X-Ray Lasers and Coherent X-Ray Sources: Development and Applications XIII, 1111106, (2019).

# Chapter 1

## Introduction

The Extreme Ultra-Violet (EUV) regime of the electromagnetic spectrum covers wavelengths from approximately 5 nm to 50 nm, corresponding to photon energies of 25 eV to 250 eV [2]. Generating high intensity focussed radiation at these wavelengths is not trivial, and many methods require a large scale source (i.e. a national facility) producing high output power. In addition, due to the large photon energy enabling direct photo-ionization, most materials are highly absorbing of light at these wavelengths which precludes the use of refractive optics and makes reflective optics difficult to design and manufacture. This high level of absorption extends to air, which has an attenuation length of  $\approx 20 \mu\text{m}$  for 46.9 nm light [3], so experiments have to be conducted under vacuum.

Laboratory scale EUV radiation sources have largely been low power sources, such as High Harmonic Generation (HHG) sources, and as such have been limited to imaging and diagnostic applications. Over the last 20 years, tabletop Capillary Discharge Lasers (CDLs) have been developed [4, 5, 6, 7] that are capable of producing pulses of EUV radiation with high enough pulse energies to conduct experiments such as ablation studies. In this thesis, we investigate EUV ablation of solid targets using a CDL source emitting up to 50  $\mu\text{J}$  pulses of radiation at a 46.9 nm wavelength. Using multilayer optics, on-target fluences of up to 500  $\text{J cm}^{-2}$  can be achieved, which is sufficient for ablation of solid targets.

Ablation of a solid can occur when a source of directed power is sufficient to cause a phase change to liquid, gas, or plasma. For example, electron beam lithography is used to ablate small features on solid substrates [8]. We consider for this thesis laser ablation of solid targets where the focussed laser intensity is sufficiently intense ( $\geq 10^{10} \text{ W cm}^{-2}$ ) to produce expanding plasma material. The physical processes im-

portant in laser ablation can be divided into three categories: (i) radiation processes such as the absorption mechanisms by which laser energy is deposited into the plasma; (ii) hydrodynamic processes that govern the fluid motion of the plasma; and (iii) thermodynamic processes such as the energy transport between areas of the plasma and between the plasma components. In this thesis we focus primarily on the first group of processes, the radiation processes, and in particular on the absorption mechanisms that deposit laser energy into the plasma.

The absorption mechanisms that occur in an EUV ablation interaction are different to those that occur in an optical wavelength ablation interaction. In optical ablation the critical density of the laser, the density at which the laser frequency and plasma frequency are equal, divides the plasma into an under-dense region and an over-dense region; the latter is opaque to the incoming radiation. This division limits laser penetration and enables the absorption of laser energy through collective processes such as resonance absorption. The critical density is inversely proportional to the laser wavelength, so as the wavelength decreases the critical density increases. In the case of EUV radiation, the critical density increases to above solid density and collective processes no longer play a significant role in the absorption. The decreased wavelength does, however, increase the photon energy above the photo-ionization threshold, activating this absorption process.

The change in the contributing absorption mechanisms will have an impact on the plasma conditions created during the ablation process. The contribution from photo-ionization and the lack of resonance absorption will likely result in a comparatively cool plasma, and this reduced plasma temperature will reduce hydrodynamic expansion, yielding a more dense plasma. This plasma state is referred to as Warm Dense Matter (WDM). WDM conditions differ significantly from those predicted by models for optical wavelength ablation, which would suggest that models for the ablation process at optical wavelengths cannot be easily translated across to EUV wavelengths.

Laser ablation is an important interaction for fusion energy as it acts as the mechanism for compressing the fuel in Inertial Confinement Fusion (ICF). The two main schemes of ICF are direct drive and indirect drive. In direct drive ICF, optical wavelength lasers are focussed directly onto the fuel pellet, ablating the target and sending shockwaves into it to compress and ignite the fuel. In indirect drive, optical wavelength lasers are used to ablate the interior of a gold cylinder (known as a hohlraum) that contains the fuel pellet, generating X-rays that heat and compress the fuel pellet, also

via ablation.

EUV ablation offers possible insights into both schemes of ICF. Firstly, the conditions produced in EUV ablation are a useful intermediate between the conditions in optical wavelength ablation (as used in direct drive ICF) and X-ray ablation (as used in indirect drive ICF). Secondly, the radiation produced by the hohlraum is broad spectrum, so understanding EUV/soft X-ray wavelength ablation and how these wavelengths may contribute to the overall heating of the fuel pellet is important in optimizing the shockwave and therefore the compression achieved during the interaction.

## 1.1 The premise of the Thesis

Although the work presented here is primarily theoretical, it was developed with an experimental mindset. The aim is to produce a simple, useful tool for predicting key features of ablation profiles generated on solid targets using EUV radiation – the most relevant of which is the depth of the ablated feature. To this end, a series of treatments have been presented that aim to relate the incident fluence with the depth of the ablation feature. This tool could be used by those interested in nano-machining, for example, to tailor their incident fluence to consistently generate a given depth of ablation feature.

A series of models are developed and their predictions are compared to ablation depths measured on metal targets collected in an ablation study using a CDL source emitting 46.9 nm light in 1.2 ns pulses with on-target fluences of  $50 \text{ J cm}^{-2}$  to  $500 \text{ J cm}^{-2}$ . Hydrodynamic simulations, conducted using MULTI-IFE [9], are also used to predict ablation depths and are compared to the experimental ablation depths in turn.

The modelling developed within the thesis is predicated on some key assumptions. Firstly, as the timescale of the laser pulses is long (nanoseconds) it is assumed that the initial energy deposition causing the phase transition from solid metal to dense plasma occurs in a negligibly short time frame. This allows the interaction to be treated as a solely laser-plasma interaction. This is a departure from the work previously conducted at short wavelengths, which is predominantly for short (femtosecond) pulses where this assumption cannot be made. A consequence of this assumption is that hydrodynamic motion becomes less important, especially when the attenuation length of the plasma is long, such as in aluminium.

Secondly, as is typical of ablation on the nanosecond timescale, it is assumed that the equilibration of thermal energy between the electrons and ions also occurs on a

comparably short timescale. This means the problem can be treated as a single temperature problem as the electrons and ions will equilibrate, provided the time resolution is on the order of 10 ps.

Finally, that the progression of the ablation front is radiation dominated. In ablation on long timescales the energy transport is typically dominated by thermal transport, largely due to the separation between the under-dense region of the plasma (where the laser energy deposition occurs) and the ablation front. For short wavelengths, the entire plasma is under-dense as the critical density is above solid density and the penetration of laser photons is not limited to the plume – the interaction is dominated by absorption at high densities.

These three assumptions reduce an otherwise very complicated mixed-phase problem to an interaction involving a single-temperature plasma. This introduces some inaccuracies at early times when the plasma is densest and coolest as the formulations used here are most accurate in classical plasmas. The classical equations have been adjusted to accommodate changes that occur in the low-temperature high-density regime but these are not without limitations. We show here however that, provided the optical absorption properties of the target atoms and ions is taken into consideration, a largely classical or semi-classical approach can be used to give acceptable approximations of EUV ablation depths.

## 1.2 Thesis structure

The thesis structure can be summarised as follows:

**Chapter 2** introduces the field of EUV research and briefly discusses sources of EUV radiation and their applications. This chapter also details the mechanics of ablation and the absorption processes that contribute to EUV ablation.

**Chapter 3** presents the details of an experimental ablation study conducted using a CDL emitting 46.9 nm radiation with a pulse duration of 1.2 ns and on-target fluences of  $50 \text{ J cm}^{-2}$  to  $500 \text{ J cm}^{-2}$ , incident on aluminium, gold, copper, and PMMA targets. Details of the experimental equipment, methodology, and data analysis are presented alongside two simple ablation depth models for the metal targets – an adaptation of Gamaly’s [10] femtosecond pulse optical ablation model and a ‘bleaching wave’ model.

**Chapter 4** constructs a zero-dimensional transmission model using classical photo-

ionization and inverse bremsstrahlung absorption coefficients and a Saha-Boltzmann ionization model to predict the plasma conditions on the metal targets indicated by the bleaching wave ablation depth model. Various corrections to the transmission model are considered to improve its accuracy at high plasma densities. The corrections investigated are the high-density limit of the Saha-Boltzmann model, ionization potential lowering, more accurate Gaunt factors, and degeneracy-corrected absorption coefficients. The predicted absorption coefficients are compared with those predicted by a selection of other works for a different EUV wavelength incident on an aluminium target. Finally, the electron densities, absorption coefficients, and transmission fractions are re-calculated using the existing ionization tool FLYCHK for comparison.

**Chapter 5** builds on the modelling started in Chapter 4 by expanding the transmission calculations to include time-dependent effects. A novel rate-equation based ionization model is briefly presented that includes photo-ionization in the population balance. A single cell transmission model with temporal resolution is developed to account for the temporal intensity variation and calculations are performed using both the Saha-Boltzmann and FLYCHK ionization models. These transmission calculations do not provide enough evidence to support the bleaching wave model, so it is replaced by expanding the time-resolved single cell model into a one-dimensional constant density ablation depth model neglecting energy transport. The ablation depth predictions of the constant density model using both the Saha-Boltzmann and FLYCHK ionization models are compared to the experimentally measured ablation depths.

**Chapter 6** uses the one-dimensional radiation-hydrodynamics code MULTI-IFE to simulate ablation interactions between 46.9 nm radiation and aluminium and gold targets. Different absorption and thermal transport models are investigated via the use of two electron-ion collision frequency models. The ablation depths predicted by the MULTI-IFE simulations are then compared to the experimentally measured ablation depths. The energy deposition is analysed and compared to that of the modelling performed in Chapter 5.

**Chapter 7** summarises the findings of the thesis and presents our conclusions. The direction of research following on from this work is also indicated.

## Chapter 2

# EUV radiation sources and laser-plasma interactions

This chapter reviews EUV radiation production and laser-plasma interactions. Methods of EUV photon production and the physical principles behind them are briefly discussed, as are the applications of such devices. The operation of a capillary discharge laser (CDL) is treated in some detail as we have used a CDL operating at 46.9 nm for our solid target ablation measurements. The application most relevant to this work, laser ablation, is also discussed in more detail with the mechanics of the process and contributing mechanisms being outlined. Derivations for the absorption coefficients and Saha-Boltzmann ionization model are provided in order to contextualise degeneracy corrections applied in Chapter 4.

### 2.1 EUV radiation sources

EUV radiation poses a challenge in generating lasing largely due to the efficiency of photon production at high energies. The efficiency of photon production drops rapidly as the photon energy increases due to the need to have a high energy density medium to produce high photon energies. The efficiency of coherent short wavelength sources typically scales with photon energy  $E_p$  as  $E_p^{-x}$ , where  $x$  varies from 4 to 9 depending on the radiation generation process [11]. Below are some successful methods of producing photons at these wavelengths.

### 2.1.1 Laser-Produced Plasma sources

EUV radiation is produced when a high power laser is incident on a target; the plasma generated by the laser is hot and dense enough to emit EUV radiation. The wavelength of the emitted radiation can be selected by choosing the target material. These incoherent sources are useful for experiments where longitudinal spatial coherence is not required and the spectral bandwidth can be broad – see EUV lithography discussed in section 2.3.2.

Incident radiation from a high power laser can also be used to produce a plasma on-target that is hot and dense enough for electron-ion collisions to pump a population inversion. This can be performed in two geometries, the first being longitudinally along the axis of the pump laser. Circularly polarized photons incident on a gas target can produce free electrons that are hot enough to pump a population inversion by collisional excitation. Saturated lasing in this geometry has been demonstrated in palladium-like xenon and nickel-like krypton at wavelengths of 41.8 nm and 32.8 nm respectively [12, 13].

The second pumping geometry uses a line focus and a pre-pulse to produce a column of plasma that can then be pumped with a laser, emitting EUV radiation perpendicular to the pump beam (i.e. along the axis of the plasma column). This was first demonstrated using the NOVA laser at the Lawrence Livermore National Laboratory [14]. The disadvantage to this method is the short gain duration. The gain duration can be increased by using a diffraction grating to tilt the pulse front of the pump beam [15], allowing the excitation from the pump beam to keep pace with the EUV beam as it is amplified along the column, enhancing the effect of the pumping.

### 2.1.2 Synchrotrons and Free Electron Lasers

Accelerating charged particles emit radiation (this is derived in section 2.4.2). Synchrotron radiation refers to the radiation emitted when a charged particle is accelerated by a magnetic field. In modern synchrotrons and Free Electron Lasers (FELs), this acceleration is performed by a device known as an undulator. Undulators use alternating dipolar magnetic fields to force transverse oscillations of a beam of relativistic electrons. The electrons emit broadband synchrotron radiation, however certain resonant frequencies are phase matched with the electron beam at the end of each undulator period. These constructively interfere over many periods (out-of-phase photons destructively interfere, removing them from the output). Only the fundamental and odd

harmonics ( $n = 1, 3, 5, \dots$ ) of the radiation are emitted on-axis (in a helical device only the fundamental is on-axis) and contribute to the output – see figure 2.1.

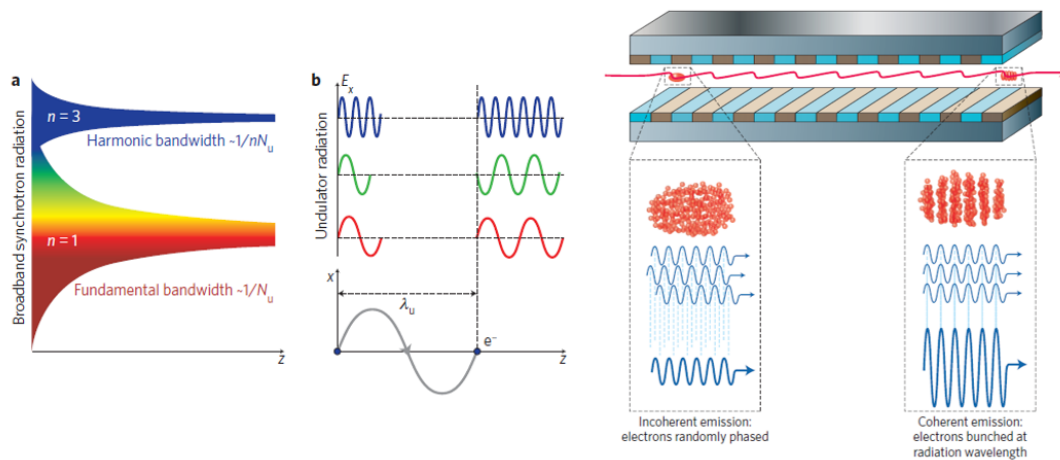


Figure 2.1: Left: only radiation in phase with the undulator frequency will constructively interfere. Right: Electrons in a FEL pass through the undulator and are steadily shifted into bunches by the potential wells [16].

Synchrotrons combine undulators with bending and focussing magnetic fields to produce radiation from electrons in a system known as a storage ring. The purpose of this structure is to maintain a consistent output spectrum at multiple points around its circumference, where experimental beamlines can be placed. Synchrotron radiation has high brightness, is highly collimated, and has a precise temporal structure. These properties combined with the continuous spectrum of the output make the radiation useful in a wide range of experiments, which can either be conducted with ‘white’ radiation or with a single wavelength by way of a monochromator. Injection of high energy particles into the storage ring is performed by a linear accelerator, sometimes used in conjunction with a so-called ‘booster’ synchrotron, which produces electrons with energies of several GeV for manipulation by the undulator(s).

In a spontaneous source of undulator radiation the output is incoherent due to a lack of correlation in the electron phases. FELs produce significantly higher gain by correlating all the electron phases, achieved by periodic bunching of the electrons at the resonant wavelength – see figure 2.1. Bunching occurs due to an exchange of energy between the electrons and resonant radiation field over many undulation periods. Electrons that are half a radiation period apart experience opposing energy exchange rates, and so half the electrons lose energy and half gain it. In this way, a series of potential wells are formed. The electrons ‘surf’ down the potential wells

causing further loss of their kinetic energy to the radiation field and subsequent growth in the radiation field. The electron bunching and field growth drive each other in an exponentially unstable loop, resulting in high gain [16]. This results in a high intensity beam with good coherence and a short pulse duration, making them ideal for a wide range of experiments.

Both synchrotrons and FELs operating at X-ray wavelengths (referred to as X-FELs) offer high energy photons in intense pulses. X-FELs have been used to conduct ablation experiments similar to those seen in these thesis, but largely with femtosecond pulse durations and higher intensities ( $\approx 10^{15} \text{ W cm}^{-2}$ ). The main limitation of these sources is their large scale, which means a small number of facilities exist with high demands on experimental time.

### 2.1.3 High Harmonic Generation

High harmonic generation (HHG) is a method for producing short duration, low power pulses of EUV radiation. The process of HHG can be described semi-classically in three steps. First, the applied electric field of a seed laser pulse warps the atomic potential well, allowing an electron to tunnel out. The laser field then accelerates the electron non-linearly away from and back towards the atom. Finally, the electron recombines with its atom, releasing the energy gained in acceleration as a photon. The photon energy is always an integer multiple of the input energy, i.e. a harmonic of the seed laser.

In 1987, it was discovered that for strong laser fields where  $I = 10^{13} \text{ W cm}^{-2}$  to  $10^{15} \text{ W cm}^{-2}$  (specifically where the laser electric field approaches the electric field binding electrons in the atom), the conversion efficiency reaches a constant value (known as the plateau region) that extends up to high harmonic numbers before dropping off at a very high order (the cut-off region) [17]. As a result, any harmonic in the plateau region can be produced with the same efficiency. The properties of the output beam are congruous with those of the input beam, meaning short pulses of coherent X-rays can be produced.

HHG sources share many advantages with X-FELs; good coherence, short (femtosecond) pulse duration, high repetition rate, and tunability. Their prevalence can largely be put down to their compactness (laboratory scale); the drawback being their low output power. The efficiency of producing harmonic radiation from gas targets is typically  $\approx 10^{-6}$  and short pulse ( $< 100 \text{ fs}$ ) lasers are needed so as not to significantly

ionize the plasma. Short pulse lasers are typically restricted to energies less than 1 J, meaning that harmonic output is less than 1  $\mu$ J.

## 2.2 Capillary Discharge Lasers

The EUV radiation source used in this work is a Capillary Discharge Laser (CDL). CDLs share some of the advantages of both X-FELs and HHG sources; they are coherent sources of radiation with a reasonably high pulse energy produced by a device of table-top size. They have longer pulse durations ( $\approx 1$  ns) than X-FELs and HHG sources as this pulse duration is determined by hydrodynamic processes occurring during the electrical discharge. Their main disadvantage is that the wavelength of the laser output is fixed by the gain medium. The conditions within the capillary also have to be very specific to support population inversion.

Population inversion in CDLs is achieved by fast electrical discharge through a capillary of gain medium. The discharge causes a wall-influenced z-pinch that generates the conditions necessary to create a population inversion pumped by electron-ion collisions. This method is applicable to neon like ions as their high ionization energy means their population is stable within the plasma and excitation without ionization can be achieved. The element chosen for the CDL system in this work is argon. Lasing occurs between the  $3s^1P_1$  and  $3p^1S_0$  lines of the neon-like argon ion, emitting light at 46.9 nm. An example Grotrian diagram for neon-like argon is shown in figure 2.2.

Amplification of neon-like ions by collisional electron excitation has also been shown in neon-like chlorine using a capillary discharge [18]. Neon-like elements from sulphur to silver have been seen to lase at wavelengths from 8.2 nm to 92.4 nm, with pumping by optical laser radiation [19]. The neon-like argon device is the most thoroughly characterised element employed in CDLs.

The systems that make up the neon-like argon CDL can be broken down by their position in the firing sequence, and this is the order in which we will consider them. The first stage of the firing sequence is the RF pre-ionization. A small coil, positioned around the front end of the capillary (into which the argon gas is fed), carries pulsed RF current at 60 MHz and generates an inductively coupled argon plasma in the capillary. A matching network is used to couple as much power into the plasma as possible; this must be tuned to the pressure in the capillary, the electrical conductivity of the oil surrounding the capillary, and other physical idiosyncrasies of the system.

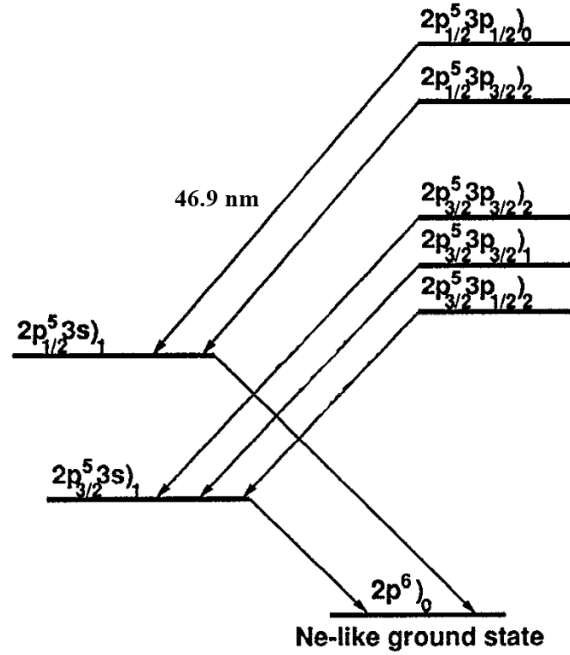


Figure 2.2: Example Grotrian diagram for neon-like argon showing the possible lasing transitions [20]. The lasing transition exploited by the CDL source is labelled with the photon wavelength.

The second stage in the firing system is a DC pre-ionization pulse. This pulse generates a higher population of neon-like argon ions in the plasma to maximise gain. The high ionisation energy of the neon-like ion results in a high abundance in both the RF plasma and in this second stage plasma. The pulse is transferred into the plasma by electrodes at either end of the capillary, as are the remaining pulse components of the firing sequence.

The third stage is the trigger pulse. This is generated by a device called a thyatron; a gas-filled tube containing an anode, a cathode, and one or more biased grids – see figure 2.3. Under resting conditions, a potential difference is applied across the anode and cathode, with a negative potential across the trigger grid preventing any current discharge from the cathode. When the potential on the trigger grid is reduced, electrons flow from the cathode, ionizing gas atoms by collisional ionization and producing electrons in an avalanche effect. The overall effect is an arc discharge between the cathode and the anode with a very short rise time. The thyatron acts as the trigger for the high voltage, high current pumping pulses in the argon filled capillary.

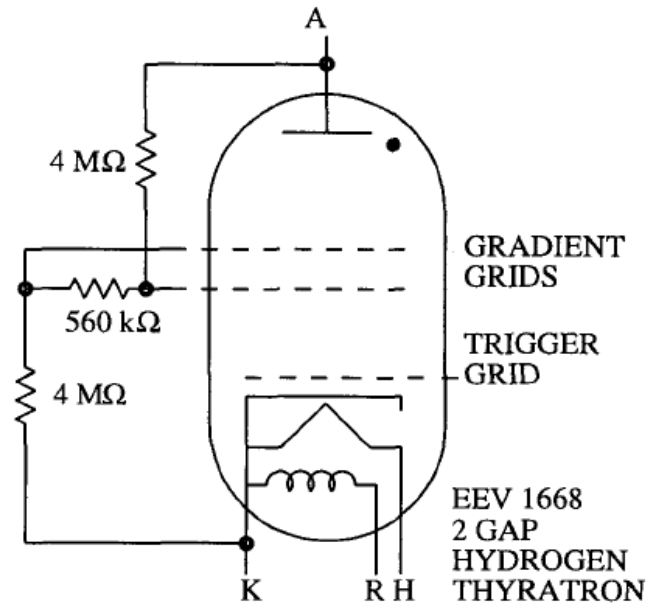


Figure 2.3: Diagram of an example high voltage 2-gap hydrogen thyatron trigger such as may be found in the capillary discharge laser [21].

The final stage in the firing sequence is the high voltage pulse. Electrical charge is stored in a capacitor bank and is transferred to the plasma after electrical pulse compression that increases the voltage and decreases the duration of the electrical pulse. The compression works by successive electrical pulse reflections in transmission lines, with each reflection doubling the pulse voltage and halving the electrical pulse duration. The pre-compression pulse has a voltage of 42 kV and a duration of  $\approx 80$  ns.

The resulting electrical pulse causes a large rapidly varying current in the capillary, which in turn generates a magnetic field. The current and magnetic field interact to generate a radially inward  $\vec{j} \times \vec{B}$  force that causes a rapid z-pinch of the plasma column along its length. The resulting plasma column, at full compression, has a very high abundance of Ne-like Ar ions, has high axial uniformity, is suitably dense for a large number of electron-ion collisions to occur, and is optically thin to the depopulation transitions of the ground state. This combination of strong pumping of the upper state by collisional electron excitation (and some recombination from the F-like ion) and strong radiative decay of the lower level to the ground state generates a suitable population inversion for lasing.

General characteristics of this laser are shown in table 2.1, along with the appropriate sources for the data. These are the parameters of the device used for the ablation depth study described in Chapter 3.

| Laser Parameter                                | Value  | Ref. |
|--|--|------|
| Pulse energy                                   | $(50 \pm 5) \mu\text{J}$                                   | [22] |
| Pulse time                                     | $(1.2 \pm 0.1) \text{ ns}$                                 | [22] |
| Divergence                                     | $\approx 1 \text{ mrad (inner) - } 3 \text{ mrad (outer)}$ | [23] |
| Relative linewidth ( $\Delta\lambda/\lambda$ ) | $(3.5 \pm 0.5) \times 10^{-5}$                             | [24] |

Table 2.1: Most important characteristics of the laser system, taken from various characterisation experiments of the prototypes.

A point of note is the spatial beam profile. During the z pinch, a high density plasma is produced in which the electron collision rate is high enough to pump the upper lasing level and produce a population inversion. The relaxation of this plasma generates a radial exponential decay in the electron density. This creates a corresponding increase in the refractive index radially outwards. As a result, any photon that is generated off the longitudinal axis is refracted away from the axis, generating an annular spatial beam profile.

## 2.3 Applications of EUV radiation sources

Applications of EUV radiation sources are largely those which traditionally use optical wavelength lasers but benefit from the reduction in wavelength as the challenges associated with using EUV radiation must be worthwhile. These applications are largely in two main areas; imaging and nanofabrication. According to the Rayleigh criterion the diffraction limited spot size  $d$  is proportional to the wavelength  $\lambda$ ; so the size of the smallest features that can be produced or imaged is improved by reducing the wavelength. Many techniques in both imaging and nanofabrication have been demonstrated with EUV radiation sources; a selection are detailed briefly below.

### 2.3.1 Imaging

To date, EUV radiation sources have been used in the demonstration of techniques such as transmission microscopy, reflection microscopy, diffraction microscopy, holography, and plasma interferometry. The simplest of these techniques is transmission microscopy. Transmission microscopes take incident radiation, pass it over the target, and collect any remaining radiation at a detector beyond the target. The use of EUV radiation in this technique has been demonstrated [25, 26] improving the resolution of the technique

from  $\approx 200$  nm (for optical wavelengths) to 50 nm [26]. The high absorption of EUV wavelengths by target materials make this an intrusive technique unsuitable for delicate targets such biological samples.

Reflection microscopy is a similar technique to transmission microscopy, however in reflection microscopy the sample is rotated so that the radiation is incident at  $45^\circ$ , reflecting off the target surface and onto the detector. Again, this technique has been demonstrated using 46.9 nm EUV radiation [26, 27], yielding a resolution of better than 250 nm [27]. This compares poorly to the 50 nm to 150 nm resolution for EUV transmission microscopy [25, 26] but is a less intrusive technique. The disadvantage of reflection microscopy is the challenge of producing suitably reflective optics.

The most common method for analysing the three-dimensional structure of crystalline materials is x-ray crystallography. For non-crystalline materials an alternative method called diffraction microscopy, or lens-less imaging, is used. In diffraction microscopy the sample is illuminated with a coherent light source, producing a detailed scatter pattern which is then sampled by a computer algorithm in order to reconstruct an image of the sample. EUV diffraction microscopy has been demonstrated with a CDL source operating at a 46.9 nm wavelength [28] with a resolution of 71 nm.

Holography is an imaging technique that captures both phase and amplitude information about the light field at the detector, allowing for the use of phase contrast and therefore the measurement of transparent objects. Holography in the EUV regime has been demonstrated [29, 30] using an in-line beam splitting method, imaging features as small as 150 nm [30].

Some imaging techniques can make use of both the shorter wavelength and the increased critical plasma density in the EUV regime. Plasma interferometry with EUV lasers can probe higher density plasmas than the same technique using optical lasers. Electron density maps of an LPP have been produced using a CDL source operating at a 46.9 nm wavelength [31], measuring densities up to  $9 \times 10^{20} \text{ cm}^{-3}$  ( $\approx 90\%$  of the critical density) – an area beyond the scope of optical interferometry.

### 2.3.2 Nanofabrication

Nanofabrication is an area of great interest to industry, in particular in the manufacturing of computer chips and other high-detail electrical components. The mechanics of nanofabrication depend on the desired outcome and many techniques can be employed. The most common processes are lithography and ablation.

### *EUV Lithography*

Lithography is a process used to etch patterns into the surfaces of bulk materials. This is achieved by applying a photoresist (a light-sensitive material) to the surface and using a light source to illuminate the sample followed by chemical etching of the exposed sample. This process is useful because it only requires enough light for the etching process, this need not be of high intensity or coherent.

EUV lithography has been demonstrated using a CDL source at a 46.9 nm wavelength using several patterning techniques [32, 33]. However, the most developed form of EUV lithography is employed in the production of computer chips [34]. In the devices designed by ASML, for example, 13.5 nm light is shone through a mask that encodes the desired pattern into the light source. The light is then focussed down onto a silicon wafer target and the pattern is chemically etched into the surface [35]. The source of the EUV light at 13.5 nm is obtained by laser irradiation of tin droplets at kilohertz rates, with collection of the EUV light obtained using large aperture multi-layer mirrors.

### *Ablation*

Ablation uses sufficiently high intensities of radiation to convert the surface of a solid material into an expanding plasma. This produces an ablation crater in the surface of the material. Manipulation of the focussing allows for the ablation of complex features into the surface [36]. As EUV ablation features are the focus of this thesis the mechanics of the ablation process are considered in greater detail below.

The plume produced in EUV ablation can also be employed in material characterisation techniques, such as Time-Of-Flight (TOF) mass spectrometry [37]. The advantage of using an EUV radiation source is the very small volume of material that can be ablated for use in the mass spectrometer (due to the small focussed spot size).

## **2.4 Laser ablation**

### **2.4.1 Properties of Laser-Produced Plasmas**

The term ‘plasma’ was coined by Irving Langmuir in 1928 when describing an ionized gas [38]. In actuality the definition of a plasma is more nuanced than a simple ionized gas. Chen defines a plasma as “a quasi-neutral gas of charged and neutral particles which exhibits collective behaviour” [39]. The term “quasi-neutral” refers to the overall

charge of the entire plasma, which is approximately zero, i.e.

$$n_e \approx Z_i n_i \quad (2.1)$$

where  $n_e$  is the electron density,  $Z_i$  is the average ionization, and  $n_i$  is the ion density. Quasi-neutrality is made possible by the high mobility of the free electrons, which essentially form an electron ‘cloud’ that shields each ion from the electrical potentials of surrounding ions. The length at which breakdown of this quasi-neutrality occurs is called the Debye length  $\lambda_D$  and is given by

$$\lambda_D^2 = \frac{\epsilon_0 k_B T_e}{n_e e^2} \quad (2.2)$$

where  $\epsilon_0$  is the permittivity of free space,  $k_B$  is the Boltzmann constant,  $T_e$  is the electron temperature, and  $e$  is the charge of an electron (in a plasma where the ion mobility is negligible).

At lengths beyond the Debye Length  $\lambda_D$ , collective effects occur due to the electric potentials of the charge particles. The most common form of these are plasma oscillations or waves that are excited by perturbations to the free electrons, such as incident photons. The angular frequency of these oscillations in the free electrons is dominated by the plasma frequency  $\omega_p$ , given by

$$\omega_p^2 = \frac{n_e e^2}{m_e \epsilon_0} \quad (2.3)$$

where  $m_e$  is the mass of the electron.

Characteristic frequencies determine the manner in which electromagnetic waves propagating through the plasma interact with that plasma. The dispersion relation for an electromagnetic wave with frequency  $\omega$  propagating through a plasma is given by

$$\omega^2 = \omega_p^2 + c^2 k^2 \quad (2.4)$$

where  $k$  is the wave vector  $2\pi/\lambda$  ( $\lambda$  is the laser wavelength) and  $c$  is the speed of light. When  $\omega_p < \omega$ ,  $k$  is real and the wave can propagate. When  $\omega_p > \omega$ ,  $k$  is imaginary and the wave is reflected and absorbed. In the case of a plasma with an electron density gradient, there will exist a boundary where  $\omega_p = \omega$  at which the incident radiation will be reflected. This density is known as the critical density  $n_{\text{crit}}$ , and is given by

$$n_{\text{crit}} = \frac{m_e \epsilon_0}{e^2} \omega^2 = \frac{m_e \epsilon_0}{e^2} \left( \frac{2\pi c}{\lambda} \right)^2. \quad (2.5)$$

The region where  $\omega_p < \omega$  is referred to as the underdense region and where  $\omega_p > \omega$  this is referred to as the overdense region. The majority of the absorption of radiation must occur in the underdense region, the exception being resonance absorption (described in section 2.4.2).

*Local thermodynamic equilibrium*

LPPs are characterised by high electron densities and temperatures, especially in the case of short pulse interactions where the laser pulse duration is much less than the equilibration time between the electrons and ions. When the electron density is sufficiently high, the processes occurring in the plasma are dominated by collisions and the plasma ionization is said to be in Local Thermodynamic Equilibrium (LTE). A minimum electron density was derived by McWhirter [40], based on the ratio of collisional and radiative decay rates, at which collisional processes dominate and LTE is valid. The McWhirter criterion for two quantum states separated by the energy gap  $\Delta E$  is given by

$$n_e > 1.7 \times 10^{14} \sqrt{T_e} (\Delta E)^3 \quad (2.6)$$

where  $\Delta E$  and the electron temperature  $T_e$  are measured in electron volts and  $n_e$  is measured in  $\text{cm}^{-3}$ . LPPs typically reach electron densities greatly exceeding the McWhirter criterion, and therefore LTE is valid.

The ionization model used for plasmas in LTE is the Saha-Boltzmann model [41], which calculates the ratio between the densities of each ionization stage in the plasma by balancing the collisional processes acting upon it. This balance is discussed in greater detail in section 5.1. The derivation of this ratio is brief and presented below.

Consider two ions with charges  $Z_i$  and  $Z_{i+1}$ , and densities  $n_{Z_i}$  and  $n_{Z_{i+1}}$  respectively. We want to find the ratio between the populations of these two states. We start by considering the ionization process from  $Z_i$  to  $Z_{i+1}$ . The Boltzmann ratio between two ionization states in a given ion, is

$$\frac{n_{Z_{i+1}}}{n_{Z_i}} = \frac{g_{Z_{i+1}}}{g_{Z_i}} \exp\left(-\frac{\Delta E}{k_B T}\right) \quad (2.7)$$

where  $g_{Z_{i+1}}$  and  $g_{Z_i}$  are the degeneracies of the two ionization states,  $T$  is the plasma temperature, and  $\Delta E$  is the energy gap between the two states – i.e. the ionization energy  $E_{\text{ion}}$  of the ion. However, when the ion  $Z_i$  is ionized to the  $Z_{i+1}$  state, an electron is simultaneously liberated with speed  $v$ . For the liberated electron, the Boltzmann ratio becomes

$$\frac{f_v(v)dv}{n_Z} = \frac{g_{Z_{i+1}}g(v)dv/n_{Z_{i+1}}}{g_Z} \exp\left(-\frac{E_{\text{ion}} + (1/2)m_e v^2}{k_B T}\right) \quad (2.8)$$

where  $f_v(v)dv$  is the density of electrons with speeds between  $v$  and  $v + dv$ ,  $g_{Z_{i+1}}$  and  $g_Z$  are the degeneracies of the two states, and  $g(v)dv$  is the density of free electron quantum states between  $v$  and  $v + dv$ . The  $g(v)dv/n_{Z_{i+1}}$  term gives the number of

free electron quantum states in the volume of one  $Z_{i+1}$  ion.  $f_v(v)dv$  and  $g(v)dv$  are well-known results of the Maxwell-Boltzmann distribution, and are given by

$$f_v(v)dv = n_e \left( \frac{m_e}{2\pi k_B T} \right)^{3/2} 4\pi v^2 \exp\left(-\frac{m_e v^2}{2k_B T}\right) dv. \quad (2.9)$$

and

$$g(v)dv = 8\pi v^2 \left( \frac{m_e}{h} \right)^3 dv \quad (2.10)$$

respectively, where  $h$  is the Planck constant. Combining equations 2.8, 2.9, and 2.10, we arrive at the familiar form of the Saha-Boltzmann ratio between the densities of two ion species with ionizations  $Z_i$  and  $Z_{i+1}$  respectively, given by

$$\frac{n_{Z_{i+1}}}{n_{Z_i}} = \frac{g_{Z_{i+1}}}{g_{Z_i}} \frac{2}{n_e} \left( \frac{m_e}{h} \right)^3 \left( \frac{2\pi k_B T}{m_e} \right)^{3/2} \exp\left(-\frac{E_{\text{ion}}}{k_B T}\right). \quad (2.11)$$

Using this ratio, one can construct a full set of ion populations for a given plasma.

### *Warm Dense Matter*

In the case of EUV laser radiation, lower plasma temperatures are anticipated due to a change in the balance of contributing absorption mechanisms. Whilst the plasma temperature is expected to be reduced, the density is not, leading to the generation of a state known as Warm Dense Matter (WDM). A phase diagram for aluminium, illustrating the approximate parameter space for WDM, is shown in figure 2.4.

The parameter spaces for ICF and the solar chromosphere are indicated on figure 2.4. Whilst neither circumstance would occur in an aluminium plasma (ICF conditions would be seen in a deuterium-tritium plasma and solar conditions occur in plasmas containing a mixture of hydrogen and helium), they are useful indicators of WDM's position as an intermediate state. The conditions anticipated in EUV ablation are also shown, sitting within the WDM zone.

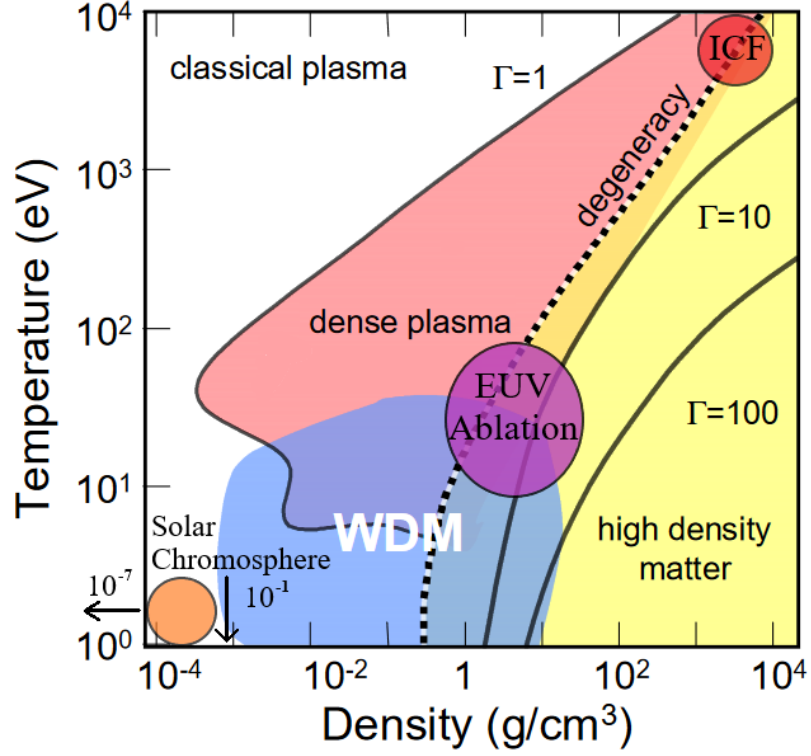


Figure 2.4: Phase diagram for aluminium showing the parameter space covered by Warm Dense Matter (WDM). Contours of constant coupling parameter and the boundary to the right of which degeneracy effects become significant are also shown [42]. The parameter spaces of ICF [43], EUV ablation (predicted), and the solar chromosphere [44] are shown to illustrate WDM's position as an intermediate parameter regime.

An important parameter in defining WDM is shown in figure 2.4, denoted by  $\Gamma$  and known as the coupling parameter. The coupling parameter  $\Gamma$  is a ratio between the inter-atomic potential energy and the thermal energy. This is given by

$$\Gamma = \frac{Z_i^2 e^2}{r_0 k_B T} \quad (2.12)$$

where  $r_0$  is the inter-particle spacing, given by

$$r_0 = \left( \frac{3Z_i}{4\pi n_e} \right)^{\frac{1}{3}}. \quad (2.13)$$

For  $\Gamma \gg 1$ , as in the case of WDM, the division between high-density plasma and condensed matter begins to blur, complicating the physics. Also of note is that WDM spans the line denoting the parameter space where degeneracy effects become significant (to the right of the dotted line). The significance of degeneracy effects on both ionization balance and absorption coefficients is explored in Chapter 4.

## 2.4.2 The mechanics of ablation

### *Initial absorption*

In laser-solid interactions, the electric field of the laser  $E$  scales with the intensity  $I$  as  $I = (c\epsilon_0/2)E^2$  for  $I$  measured in  $\text{W m}^{-2}$  and  $E$  in  $\text{V m}^{-1}$ . This means that even modest intensities are capable of producing very high electric fields. As a result, the electric field is usually sufficient to produce free electrons and ions at the surface after just a few oscillations (a few femtoseconds). The released electrons are accelerated further by the laser electric field as they oscillate across the vacuum-solid boundary, and when a sufficient number of electrons are released they expand to form a plasma with an exponential density gradient normal to the target surface. Once the plasma has formed, energy deposition is via the absorption of photons by free electrons.

### *Absorption mechanisms*

Optical wavelength ablation is dominated by two main absorption processes; inverse bremsstrahlung absorption and resonance absorption. Inverse bremsstrahlung absorption occurs when a photon is absorbed by an electron in the field of an ion. This is the dominant absorption coefficient in the under-dense region of the plasma. Absorption in this region follows the Beer-Lambert law [45], given by

$$T = \exp(-Kx), \quad (2.14)$$

where  $T$  is the transmission fraction,  $K$  is the plasma absorption coefficient (in the case of optical wavelength ablation this is equal to the inverse bremsstrahlung absorption coefficient) and  $x$  is the distance over which the photons are absorbed.

As mentioned above, the boundary between the under-dense and over-dense regions is known as the critical density  $n_{\text{crit}}$  (see equation 2.5). The laser light cannot penetrate beyond this into the target, and is instead reflected out of the plasma. However, if the polarization of the light is in the plane of the electron density gradient a process known as resonance absorption can occur. No absorption occurs in the over-dense region.

In cases where the photon energy is above the ionization energy, as is the case for EUV radiation, photo-ionization can also occur. Classical absorption coefficients for both inverse bremsstrahlung and photo-ionization are derived below to provide context for the corrections and adjustments made in Chapter 4.

*A note on Resonance Absorption*

Resonance absorption is a process that affects p-polarised electromagnetic waves entering a laser-produced plasma. The electromagnetic wave is reflected where the density is equal to  $n_{\text{crit}} \cos^2 \theta$ , where  $\theta$  is the angle of incidence, and at this point is split into a reflected component and an evanescent component. The evanescent wave tunnels to the critical density, where it excites an electron plasma wave, depositing its energy. Energy deposition only occurs when the polarization has a component parallel to the electron density gradient, as the oscillation of electrons across the plasma gradient generates an electron plasma wave. This process is responsible for a significant proportion of the laser absorption in optical wavelength ablation and generates a characteristic superthermal tail to the electron distribution.

In the EUV regime the wavelength is reduced, increasing the critical density. Even at the relatively long 46.9 nm wavelengths generated by a neon-like argon CDL, the critical density is increased to above the solid density of the target material. As a consequence, it is possible to neglect the resonance absorption process from models for EUV ablation.

*Radiation emission by accelerating charged particles*

To generate a classical formulation for inverse bremsstrahlung absorption one must first consider the radiation emitted by an accelerating charge. The treatment below, developed by Purcell [46], starts by taking a test particle of charge  $q$  initially moving at velocity  $v_0 \ll c$  at a time  $t = 0$ , viewed from the reference frame in which it is stationary (i.e. also travelling at  $v_0$ ). In this reference frame, the field lines propagate radially outwards from the test particle across all space. The test particle is decelerated uniformly over a time period  $\delta t$  to a complete stop. At a time  $T \gg \delta t$  after this has occurred, the test particle has been displaced by a distance  $v_0 T$ . As this change in the field lines can only propagate at  $c$ , we now have a non-uniform field line geometry with three distinct zones. Zone 1 lies within the radius  $R = cT$ , where the field lines have adjusted to the new position of the particle. Zone 3 lies outside the radius  $c(T + \delta t)$  where the field lines are still in their initial geometry (i.e. when  $t = 0$ ). Zone 2, the annulus with width  $c\delta t$  with inner radius  $R$ , now contains a ‘kink’ where the field line must maintain continuity by joining Zones 1 & 3; in this zone the field lines have a transverse component. The three-zone geometry discussed is shown in figure 2.5.

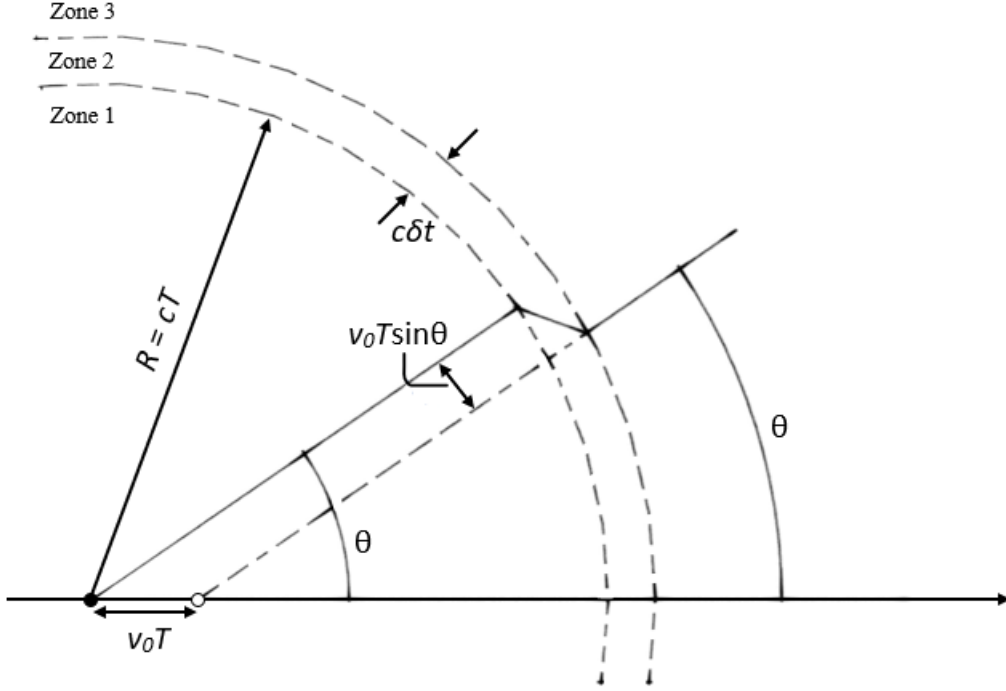


Figure 2.5: An illustration of a decelerated electron in the reference frame moving with velocity  $v_0$ . In Zone 1 the field lines have moved to correspond with the new electron position. In Zone 3 they are still positioned relative to the original electron position. Subsequently, in Zone 2 we have the field lines that must exist in order to connect Zones 1 & 3.

The transverse component of the field in Zone 2 is calculated by simple geometry. Taking an arbitrary field line at angle  $\theta$ , it is straightforward to determine that the transverse and radial components of the field at the kink will be proportional to their respective geometric lengths, such that  $E_t \propto v_0 T \sin \theta$  and  $E_r \propto c \delta t$ . The ratio of the transverse field to the radial field is therefore

$$\frac{E_t}{E_r} = \frac{v_0 T \sin \theta}{c \delta t} = \frac{R \sin \theta}{c^2} \frac{dv}{dt} \quad (2.15)$$

where  $dv/dt$  is the acceleration as  $\delta v = v_0$  and  $\delta v/\delta t = dv/dt$ . The radial field is given by Coulomb's law, so the transverse field  $E_t$  is given by

$$E_t = \left( \frac{R \sin \theta}{c^2} \right) \left( \frac{dv}{dt} \right) \left( \frac{q}{4\pi\epsilon_0 R^2} \right) = \frac{q}{4\pi\epsilon_0 c^2 R} \left( \frac{dv}{dt} \right) \sin \theta \quad (2.16)$$

In most cases, including the case of bremsstrahlung emission, the acceleration in a given direction is not uniform, rather it oscillates, oscillating the transverse electric field with it. The electric field oscillations can be described using sine waves, sinusoidally oscillating electric fields generate magnetic fields due to Ampere's law, and sinusoidal

oscillations of electric and magnetic fields are simply electromagnetic radiation. Hence, an accelerating charged particle emits electromagnetic radiation.

In order to calculate the irradiated power, we start by evaluating the Poynting vector around the test charge

$$|\vec{\mathbf{S}}| = \frac{1}{\mu_0} |\vec{\mathbf{E}} \times \vec{\mathbf{B}}| = \frac{1}{\mu_0} |\vec{\mathbf{E}}||\vec{\mathbf{B}}|\sin(90^\circ) = \frac{EB}{\mu_0}. \quad (2.17)$$

Using the relation  $E/B = c$  for an electromagnetic wave, we can write the Poynting vector with respect to just the electric field  $E$ , for which we have a relation given by equation 2.16;

$$|\vec{\mathbf{S}}| = \epsilon_0 c E^2 = \frac{q^2}{16\pi^2 \epsilon_0 c^3 R^2} \left( \frac{dv}{dt} \right)^2 \sin^2 \theta. \quad (2.18)$$

Finally, the expression is integrated over all angles in order to retrieve the total radiated power  $P$ , like so

$$\begin{aligned} P &= \int |\vec{\mathbf{S}}| R^2 d\Omega \\ &= \frac{q^2}{16\pi^2 \epsilon_0 c^3} \left( \frac{dv}{dt} \right)^2 \int_0^{2\pi} \int_0^\pi \frac{1}{R^2} \sin^2 \theta R^2 \sin \theta d\theta d\phi \\ &= \frac{q^2}{16\pi^2 \epsilon_0 c^3} \left( \frac{dv}{dt} \right)^2 \int_0^\pi \sin^3 \theta d\theta \int_0^{2\pi} d\phi = \frac{q^2}{16\pi^2 \epsilon_0 c^3} \left( \frac{dv}{dt} \right)^2 \left[ \frac{4}{3} \right] [2\pi] \\ &= \frac{q^2}{6\pi \epsilon_0 c^3} \left( \frac{dv}{dt} \right)^2. \end{aligned} \quad (2.19)$$

Equation 2.19 is known as the Larmor formula [47], named for its originator Joseph Larmor.

### *Inverse bremsstrahlung absorption*

To develop a formula for inverse bremsstrahlung absorption, we first consider its inverse process bremsstrahlung emission. The treatment below follows that of Tallents [48] which combines those of Purcell [46] (above) and Hutchinson [49] to generate a classical expression for bremsstrahlung emission.

In the bremsstrahlung emission interaction, an electron is accelerated in the field of a  $+Z_i e$  charged ion. The acceleration is dependent on the distance of closest approach  $p$  of the electron to the ion, also known as the ‘impact factor’ in the case of small angle collisions (the closest distance between electron and ion as the electron passes undeviated through the ion field). Calculated using the basic relations  $F = ma$  and  $|F| = q|E|$ , and Coulomb’s law, the acceleration of the particle is given by

$$\frac{dv}{dt} = \frac{Z_i e^2}{4\pi \epsilon_0 m_e p^2}. \quad (2.20)$$

The power radiated by the electron is then given by substituting this result into equation 2.19 to obtain

$$P = \frac{e^2}{6\pi\epsilon_0 c^3} \left( \frac{Z_i e^2}{4\pi\epsilon_0 m_e p^2} \right)^2 = \frac{2}{3} \left( \frac{e^2}{4\pi\epsilon_0 c} \right)^3 \frac{Z_i^2}{m_e^2 p^4}. \quad (2.21)$$

The acceleration due to the ion field acts on the electron for a finite period, defining the duration of the bremsstrahlung pulse, and in the case of small angle collisions this is given by

$$t_p = \frac{2p}{v} = \frac{1}{\omega}, \quad (2.22)$$

with the latter relation arising from Fourier analysis ( $\omega = 1/t_p$  is the dominant frequency of the bremsstrahlung pulse). As these are small angle collisions, a single electron will likely undergo many collisions in a given time period  $t$ , provided  $t \gg t_p$  and the electron energy loss per collision is small. The number of collisions per unit time for an electron with impact parameter between  $p$  and  $p + dp$  is given by  $n_{Z_i} v 2\pi p dp$  (where  $n_{Z_i}$  is the density of  $Z_i$  ions), and the energy emitted per collision (per bremsstrahlung pulse) is  $P t_p$ . From equation 2.22 we can deduce that  $dp = -(v/2\omega^2)d\omega$  and the power radiated by a single electron in the frequency range  $\omega$  to  $\omega + d\omega$  is therefore

$$\begin{aligned} \frac{dE(\omega)}{dt} d\omega &= P t_p n_{Z_i} v 2\pi p dp = \frac{2}{3} \left( \frac{e^2}{4\pi\epsilon_0 c} \right)^3 \frac{Z_i^2 4\omega^4}{m_e^2 v^4} \frac{1}{\omega} n_{Z_i} v 2\pi \frac{v}{2\omega} \frac{v}{2\omega^2} d\omega \\ &= \frac{16\pi}{3} \left( \frac{e^2}{4\pi\epsilon_0 c} \right)^3 \frac{Z_i^2 n_{Z_i}}{m_e^2 v}. \end{aligned} \quad (2.23)$$

Calculating the power radiated in frequencies between  $\omega$  and  $\omega + d\omega$  by all the electrons in a given plasma requires an integration of equation 2.23 with respect to velocity. Any electrons with kinetic energy lower than the photon energy  $\hbar\omega$  are incapable of emitting at frequency  $\omega$ , so the integration becomes

$$\varepsilon_{ff}(\omega) = \int_{\sqrt{2\hbar\omega/m_e}}^{\infty} \frac{dE(\omega)}{dt} f_v(v) dv$$

where  $f_v(v)dv$  is the number of electrons per unit volume with velocities between  $v$  and  $v + dv$  as found from the Maxwellian distribution

Substituting equation 2.9 into the integral above yields the total power emitted between frequencies  $\omega$  and  $\omega + d\omega$  per unit time and volume, which can be written with respect to the integral  $I_{ff}$  like so

$$\varepsilon_{ff}(\omega)d\omega = \frac{64\sqrt{\pi}}{3} \left( \frac{e^2}{4\pi\epsilon_0 c} \right)^3 \frac{Z_i^2 n_{Z_i} n_e}{m_e^2} \left( \frac{m_e}{2k_B T} \right)^{1/2} I_{ff} d\omega. \quad (2.24)$$

$I_{ff}$  is a standard integral of the form

$$I_{ff} = \int_a^{\infty} b v \exp(-bv^2) dv = \frac{1}{2b} \exp(-a^2 b)$$

where  $a = \sqrt{2\hbar\omega/m_e}$  and  $b = m_e/(2k_B T)$ . Finally, the total power emitted as bremsstrahlung radiation by a plasma can be evaluated to give

$$\varepsilon_{ff}(\omega)d\omega = \frac{32\sqrt{\pi}}{3} \left( \frac{e^2}{4\pi\epsilon_0 c} \right)^3 \frac{Z_i^2}{m_e^2} n_{Z_i} n_e \left( \frac{m_e}{2k_B T} \right)^{1/2} \exp\left(-\frac{\hbar\omega}{k_B T}\right) \frac{\langle G_{ff} \rangle}{\sqrt{3}} d\omega. \quad (2.25)$$

The factor  $\langle G_{ff} \rangle / \sqrt{3}$  has been introduced at this stage to correct the numerical multiplier. The factor  $\langle G_{ff} \rangle$  is the frequency-averaged Gaunt factor [50] and is evaluated by considering the electron-ion collision quantum mechanically. Several approximations for the Gaunt factor have been developed [49], but under most conditions  $\langle G_{ff} \rangle \approx 1$ . The factor  $1/\sqrt{3}$  arises from a precise classical treatment of the radiation emission; this was first done by Kramers [51]. The value  $\langle G_{ff} \rangle = 1$  so that when the multiplier is exactly  $1/\sqrt{3}$  the absorption coefficient for inverse bremsstrahlung referred to as the Kramers value.

In the inverse bremsstrahlung process, an electron in the field of an ion absorbs energy from an incident electromagnetic wave. For a system in equilibrium the absorption and emission processes must also be in equilibrium, so the rates of the two processes can be said to be in detailed balance. This being the case, we can relate the bremsstrahlung emission coefficient  $\varepsilon_{ff}$  to the inverse bremsstrahlung absorption coefficient  $K_{ff}$  by

$$K_{ff} \langle I_P(\omega) \rangle d\omega = \varepsilon_{ff}(\omega) d\omega$$

where  $\langle I_P(\omega) \rangle d\omega$  is the Planck black-body radiation intensity between frequency  $\omega$  and  $\omega + d\omega$ , given by the well known Planck black-body equation

$$\langle I_P(\omega) \rangle d\omega = \frac{\hbar\omega^3}{\pi^2 c^2} \frac{1}{\exp\left(\frac{\hbar\omega}{k_B T}\right) - 1} d\omega. \quad (2.26)$$

A straightforward combination of equations 2.25 and 2.26 gives the final result

$$K_{ff} = \frac{32\sqrt{\pi}}{3} \left( \frac{e^2}{4\pi\epsilon_0 c} \right)^3 \frac{Z_i^2}{m_e^2} n_{Z_i} n_e \left( \frac{m_e}{2k_B T} \right)^{1/2} \frac{\pi^2 c^2}{\hbar\omega^3} \left[ 1 - \exp\left(-\frac{\hbar\omega}{k_B T}\right) \right] \frac{\langle G_{ff} \rangle}{\sqrt{3}}. \quad (2.27)$$

So the absorption of radiation varies as  $n_{Z_i} n_e \omega^{-3} T^{-3/2}$  when  $\hbar\omega \ll k_B T$ , decreasing with shortening wavelength and with increasing temperature. At 46.9 nm wavelengths, a factor of ten shorter than the usual 300 nm to 500 nm wavelengths seen in optical ablation experiments, the rate of inverse bremsstrahlung is  $\approx 1000$  times lower and may not dominate the ablation process as it does in optical wavelength ablation. The quantum mechanical Gaunt factor  $\langle G_{ff} \rangle$  is discussed further in section 4.2.2.

*Photo-ionization*

The emission counterpart for photo-ionization is radiative recombination. In this process, an electron is captured by an ion, radiating the kinetic energy of the electron and the energy difference between the final quantum state and ionization energies of the ion. Again, we follow a treatment by Tallents [48] that uses a classical viewpoint to produce a formulation for the radiative recombination emission coefficient.

To treat radiative recombination in the same manner that we treated bremsstrahlung emission, we assume that equation 2.25 applies, and we make two changes. The first change is to the emitted photon energy; we adjust this to include the extra ionization energy released during the recombination process. The second change is to use an approximation for the range of electron kinetic energies capable of contributing to the recombination reaction. So, the range of free electrons  $dv$  with velocities (and therefore energies) capable of contributing to the recombination process of an ion is given by

$$dv = \frac{1}{m_e v} dE_\gamma \quad (2.28)$$

where  $dE_\gamma$  is the energy range of the emitted photons. We now assume that the quantum states into which the electron can recombine are those of a hydrogen-like ion with charge  $Z_i$ , and that the recombined ion will be hydrogen-like in a quantum state  $n$ . We can write that the ionization energy  $E_{\text{ion}}$  is given by

$$E_{\text{ion}} = R_d \frac{Z_i^2}{n^2} \quad (2.29)$$

where  $n$  is the principal quantum number of the state into which recombination has occurred, and  $R_d$  is the Rydberg energy of 13.6 eV. The range of photons  $dE_\gamma$  emitted by the recombination interaction is therefore given by

$$\begin{aligned} dE_\gamma &\approx R_d Z_i^2 \left[ \frac{1}{(n - \frac{1}{2})^2} - \frac{1}{(n + \frac{1}{2})^2} \right] \\ &= R_d Z_i^2 \frac{2n}{(n^2 - \frac{1}{4})^2} \\ &\simeq \frac{2R_d Z_i^2}{n^3}. \end{aligned} \quad (2.30)$$

Equation 2.30 is an approximation, but for large  $n$  it is a reasonable one as the quantum levels are close together in energy. We now take equation 2.23 as a guide, and determine that the total power radiated by the electron when it recombines is given by the expression for the power radiated by bremsstrahlung, multiplied by the Maxwellian

distribution for the number of electrons at a high enough velocity (equation 2.9). This relation

$$\varepsilon_{fb}(\omega) = \frac{dE\left(\omega - \frac{E_{\text{ion}}}{\hbar}\right)}{dt} f_v(v) dv$$

combines equations 2.23, 2.28, and 2.30 to give the expression

$$\varepsilon_{fb}(\omega) = \frac{32\sqrt{\pi}}{3} \left(\frac{e^2}{4\pi\epsilon_0 c}\right)^3 \frac{Z_i^2}{m_e^2} n_{Z_{i+1}} n_e \left(\frac{m_e}{2k_B T}\right)^{\frac{1}{2}} \left[ \frac{2R_d Z_i^2}{n^3} \frac{e^{\left(\frac{E_{\text{ion}}}{k_B T}\right)}}{k_B T} \langle G_{fb} \rangle \right] \frac{e^{\left(-\frac{\hbar\omega}{k_B T}\right)}}{\sqrt{3}} \quad (2.31)$$

where  $\langle G_{fb} \rangle$  is the Gaunt factor for free-bound emission, introduced in the same manner as we did for free-free emission. The above equation for  $\varepsilon_{fb}(\omega)$  is simply our equation for  $\varepsilon_{ff}(\omega)$  multiplied by the terms in square brackets.

As we did for inverse bremsstrahlung absorption, we can use detailed balance to find the photo-ionization coefficient  $K_{bf}$  from the radiative recombination emission coefficient  $\varepsilon_{fb}$ . So, we have the relation

$$K_{bf} \langle I_P(\omega) \rangle = \varepsilon_{fb}(\omega)$$

as before. This leads to the photo-ionization coefficient  $K_{bf}$

$$K_{bf} = \frac{32\sqrt{\pi}}{3} \left(\frac{e^2}{4\pi\epsilon_0 c}\right)^3 \frac{Z_i^2}{m_e^2} n_{Z_{i+1}} n_e \left(\frac{m_e}{2k_B T}\right)^{\frac{1}{2}} \frac{\pi^2 c^2}{\hbar\omega^3} \left(1 - e^{-\frac{\hbar\omega}{k_B T}}\right) C_{bf} \quad (2.32)$$

where the  $C_{bf}$  term is given by

$$C_{bf} = \left[ \frac{2R_d Z_i^2}{n^3} \frac{e^{\frac{E_{\text{ion}}}{k_B T}}}{k_B T} \right] \frac{\langle G_{bf} \rangle}{\sqrt{3}}.$$

It is important to note that our expression for  $K_{bf}$  so far is in terms of the density of the  $Z_{i+1}$  state due to our starting with the radiative recombination interaction. The photo-ionization absorption coefficient is much more useful in terms of the  $Z_i$  state, and so we use the relation  $n_{Z_{i+1}} = n_{Z_i} n_{Z_{i+1}} / n_{Z_i}$  and the Saha-Boltzmann equation (equation 2.11) for  $n_{Z_{i+1}} / n_{Z_i}$  to find the  $K_{bf}$  in terms of  $n_{Z_i}$  like so

$$K_{bf} = \frac{128\pi^2}{3} \frac{g_{Z_{i+1}}}{g_{Z_i}} \left(\frac{e^2}{4\pi\epsilon_0 c h}\right)^3 n_{Z_i} \frac{\pi^2 c^2}{\hbar\omega^3} \left(1 - e^{-\frac{\hbar\omega}{k_B T}}\right) \left[ \frac{2R_d Z_i^4}{n^3} \right] \frac{\langle G_{bf} \rangle}{\sqrt{3}}. \quad (2.33)$$

The  $\exp(\hbar\omega/k_B T)$  term accounts for stimulated emission reducing the amount of photo-ionization. Although not immediately obvious from equation 2.33, this only applies to those ionization stages with ionization energy  $E_{\text{ion}}$  below the photon energy  $\hbar\omega$ .

If we neglect stimulated emission, as occurs for high photon energies when  $\hbar\omega \gg k_B T$ , we can find an expression for the temperature-independent cross-section  $\sigma_{bf}$  by

evaluating the relation  $\sigma_{bf} = K_{bf}/n_{Z_i}$  such that

$$\begin{aligned}\sigma_{bf} &= \frac{128\pi^2}{3} \frac{g_{Z_{i+1}}}{g_{Z_i}} \left( \frac{e^2}{4\pi\epsilon_0 ch} \right)^3 n_{Z_i} \frac{\pi^2 c^2}{\hbar\omega^3} \left[ \frac{2R_d Z_i^4}{n^3} \right] \frac{\langle G_{bf} \rangle}{\sqrt{3}} \\ &= \frac{16}{3\pi} \alpha^3 \frac{\pi^2 c^2}{\hbar\omega^3} \left[ \frac{R_d Z_i^4}{n^5} \right] \frac{\langle G_{bf} \rangle}{\sqrt{3}}\end{aligned}\quad (2.34)$$

where  $\alpha$  is the fine structure constant given by

$$\alpha = \frac{e^2}{4\pi\epsilon_0 \hbar c} \approx \frac{1}{137}.$$

We have also been able to simplify equation 2.34 even further by assuming the absorbing ions are hydrogen-like, which allows us to use the relation  $g_{Z_{i+1}}/g_{Z_i} = 1/2n^2$  to replace the  $g_{Z_{i+1}}/g_{Z_i}$  term. We now have a temperature independent cross section that scales as  $Z_i^4 n^{-5} \omega^{-3}$  as is correct for hydrogen-like ions. The quantum mechanical Gaunt factor  $\langle G_{bf} \rangle$  is discussed in more detail in section 4.2.2.

### *Electronic structure and absorption*

In the previous two sections, the mechanisms of photoabsorption and inverse bremsstrahlung absorption have been discussed. These are photon interactions with bound and free electrons respectively, so it is pertinent to discuss the state of the electrons here.

In the metallic targets explored in this thesis the metal ions form a closely packed, uniform structure. The outermost electrons become delocalised and form the conduction band of quasi-free electrons, which bond the positive ions together via the Coulomb force. The nature of the conduction band means it can be treated physically in one of two ways.

The first is to effectively treat the conduction band electrons as free electrons part of a solid density plasma – similar to the Drude-Sommerfeld model [52]. This allows us to treat all the absorption as governed by inverse bremsstrahlung absorption and is commonly used in hydrodynamic codes to avoid the computational complexity generated by a phase transition. This is an approximation as the electrons do not in fact have the same kinetic freedom as true free electrons, and are often treated using an effective mass to compensate.

The second method is to treat the conduction band electrons as bound to each individual atom. This is consistent with our modelling as once the solid metal has been converted to plasma most of these conduction band electrons will occupy discrete atomic quantum states. In this case, one must now include absorption due to photoionization to accurately model all of the absorption.

It should largely be a matter of nomenclature whether conduction band electrons are treated as free or bound. If conduction electrons are treated as free electrons, light absorption can be calculated using expressions similar to inverse bremsstrahlung, while if conduction band electrons are treated as being bound, light absorption can be evaluated using expressions for bound-free photo-ionization. Provided the chosen treatment is self-consistent, the deposition of energy should also remain consistent i.e. there should be little difference between the two. Prevailing opinion is to use the first method, treating the conduction band electrons as free, and use inverse bremsstrahlung absorption as the absorption method [53, 54]. Given that we expect photo-ionization to dominate the absorption, it is assumed in the modelling presented below that the conduction band electrons largely occupy discrete atomic quantum states as they are released from the solid and converted to plasma.

Part of the reason for making this choice is the validity of the inverse bremsstrahlung absorption mechanism in the extreme conditions likely to be seen in EUV ablation interactions. Inverse bremsstrahlung absorption is most applicable to hot, lower density plasmas, such as those seen in the ablation plume. In the hydrodynamic codes used to model optical wavelength ablation, this parameter range can feasibly be stretched to include initial conditions because they are short-lived due to the higher electron heating increasing electron temperatures and driving more rapid expansion. In short wavelength ablation, the heated volume is larger due to the long attenuation lengths and less of the energy is deposited into the free electrons as thermal energy due to the contribution of photo-ionization. This results in a cooler, more dense plasma, where an inverse bremsstrahlung absorption coefficient may be a less accurate representation of the absorption. In the parameter space at early times during the EUV laser pulse, we anticipate the photo-ionization absorption will dominate the laser energy absorption, and inaccuracies in the much less significant inverse bremsstrahlung absorption coefficient will not affect the overall absorption. At later times in the EUV laser pulse the target is hotter, more highly ionised, and has dropped in density from solid, so the inverse bremsstrahlung absorption expressions become reasonably accurate.

### *Hydrodynamics*

The hydrodynamics of an ablation plasma, as with any fluid, centre around three continuity equations; the Navier-Stokes equation (detailing conservation of momentum), the continuity equation for mass, and the continuity equation for energy [55]. The

continuity equation for mass density  $\rho$  is given by [43]

$$\frac{\partial}{\partial t}\rho + \nabla \cdot (\rho \mathbf{v}) = 0. \quad (2.35)$$

where  $\mathbf{v}$  is the velocity. The Navier-Stokes equation is given by [43]

$$\left( \frac{\partial}{\partial t} \mathbf{v} + \mathbf{v} \cdot \nabla \mathbf{v} \right) = -\frac{1}{\rho} \nabla p \quad (2.36)$$

where  $p$  is the plasma pressure, given by

$$p = n_i(k_B T_i + Z_i k_B T_e) \quad (2.37)$$

where  $T_e$  and  $T_i$  are the temperatures of the electrons and ions respectively. Finally, the continuity equation for the specific energy  $U$  is given by [43]

$$\left( \frac{\partial}{\partial t} + \mathbf{v} \cdot \nabla \right) U + p \left( \frac{\partial}{\partial t} + \mathbf{v} \cdot \nabla \right) \frac{1}{\rho} = -\frac{1}{\rho} \nabla \cdot \mathbf{q} + \frac{1}{\rho} P \quad (2.38)$$

where  $\mathbf{q}$  is the thermal flux, and  $P$  accounts for external energy sources such as laser energy deposition.

Solving these equations is beyond the scope of this thesis. However, from equations 2.36, 2.35, and 2.38 it is clear that the process is dependent on the temperature and thermal transport between both regions of the plasma and the two different species. Fortunately, there exist freely available codes which do solve these equations as part of their simulations, including MULTI-IFE [9] which is used to perform simulations of EUV ablation experiments in Chapter 6.

### *Thermal transport*

Thermal transport in plasmas is dominated by the motion of free electrons, as these are the more mobile species. The majority of the thermal energy is carried away by the electrons, however some transfer between electrons and ions does occur. The thermal transport between electrons and ions is usually calculated by Spitzer's classical expression for the thermal conductivity  $\kappa$  of a hot, ideal plasma [56], given by

$$\kappa = \frac{\kappa_0 n_e k_B^2 T_e}{m_e \nu_{ei}} \quad (2.39)$$

where  $\kappa_0$  is a dimensionless correction factor [56] and  $\nu_{ei}$  is the electron-ion collision frequency. This equation scales non-linearly with temperature due to additional temperature scaling in the collision frequency.

In most cases, this classical form of the thermal conductivity over-predicts the thermal flux. This is managed in simulations by a constant  $f$  known as a flux limiter,

which is usually set to an empirically determined fraction of the free-streaming limit for thermal conductivity. The free-streaming limit is given by the limit where electrons move their energy  $n_e k_B T$  at the electron thermal velocity. We have

$$Q_{fs} = n_e k_B T_e v_{th} \quad (2.40)$$

where  $Q_{fs}$  is the free-streaming thermal flux and  $v_{th}$  is the thermal velocity of the electrons. The fraction  $f$  of the free-streaming flux used is typically somewhere between 0.03 and 0.08 [57].

In plasmas, thermal transport is complicated because it is non-local and is therefore dependent on the profile of temperature and density. In WDM, thermal transport is further complicated as the line between this phase and the condensed matter (solid) phase is blurred. Vibrational absorption of energy via phonons and the impact of this process on thermal conductivity has been investigated in white dwarf and neutron stars [58] and the similarity of these conditions to high-density plasmas produced by lasers has been noted, to the extent that these processes have been included in one of the possible electron-ion collision frequency expressions used by MULTI-IFE [59].

### 2.4.3 EUV Ablation

The transition to EUV wavelength radiation is anticipated to have several effects on the ablation process. Firstly, it is expected that the increase in photon energy will result in photo-ionization contributing to, if not dominating, the absorption of laser radiation. Secondly, the increase in critical density to above the solid density will result in no contribution from resonance absorption and so a high temperature tail in the electron temperature distribution will not be present. Thirdly, the general balance of absorption mechanisms will result in lower electron temperatures and a plasma in the WDM region of the phase diagram. The latter being due to the larger volume in which energy is absorbed and increased plasma density around the ablation front, both because of the generally increased attenuation lengths.

The attenuation length of materials for light at EUV wavelengths varies greatly; for example aluminium has an attenuation length of  $10^2$  nm for 46.9 nm radiation, whereas gold has an attenuation length of just 7 nm. This implies that the energy deposition in EUV ablation of an aluminium target will happen over a much greater volume than in EUV ablation of a gold target due to deeper penetration of the radiation into the target. This contributes to the usefulness of the EUV regime as an intermediate between direct and indirect drive ICF; long attenuation lengths mean greater penetration by

the radiation, as seen in indirect drive, whereas short attenuation lengths will see much less penetration into the target, as seen in direct drive. However, both scenarios will produce the high density of plasma generated during either ICF scheme.

In the following chapters, we test these predictions by performing an experimental ablation study using EUV radiation at 46.9 nm from a CDL source. The results of this experimental study are then compared against a series of models that aim to predict the depth of the ablation feature produced on target.

## Chapter 3

# EUV solid target ablation

In this chapter, an experiment is discussed that uses focussed CDL radiation to ablate solid metal and polymer targets. An on-axis experimental geometry using a multi-layer mirror as a focussing optic is employed, back reflecting the CDL output at 46.9 nm onto small planar targets. This focussing geometry allows most of the annular laser output profile to be focussed. The in-line geometry also reduces focussing aberrations. This experimental arrangement was used to produce ablation craters on target which were subsequently analysed post-shot using an atomic force microscope (AFM). Later chapters in this thesis model and simulate the ablation process in order to obtain models and simulations of the ablation depth.

This experiment was conducted with Sarah Wilson and in collaboration with Colorado State University (CSU) using a neon-like argon CDL source and vacuum system. Two-dimensional measurements of ablation crater profiles extracted using an AFM are presented. The depth and diameter of target ablation craters are interpreted from the two-dimensional maps to yield ablation depth measurements as a function of laser flux for a variety of target materials.

### 3.1 Experimental dimensions and components

#### 3.1.1 Experimental layout geometry

The ablation experiments conducted required the arrangement of four key components; the light source (a CDL), the detector (as detailed in section 3.1.4), the focussing optic (a spherical mirror), and the target (mounted on a holder). All of these components must be under vacuum for the laser light to propagate as the attenuation length for 46.9 nm radiation in air at atmospheric pressure is  $\approx 20 \mu\text{m}$  [3]. The target shape and

holder should be usable for multiple data shots to reduce pumping up and down the vacuum system as much as possible.

The CDL and mirror were placed such that the mirror was approximately 1.5 m from the output pinhole of the CDL, aligned with the axis of the CDL. Laser pulse energies were measured using an in-line detector, also aligned with the axis of the capillary laser. The target was mounted on an ‘H’ shaped sample holder set back approximately 50 mm from the mirror on the same axis (i.e. roughly 1.45 m from the laser). The targets were mounted onto the crossbar of the sample holder, allowing for long targets (1 cm to 2 cm) with a height of approximately 2 mm. Mounting the sample holder on a motorised stage allowed for fine manipulation in both the laser-mirror axis and the axis perpendicular to this and for multiple shots to be taken on one target. Figure 3.1 shows a schematic of this setup.

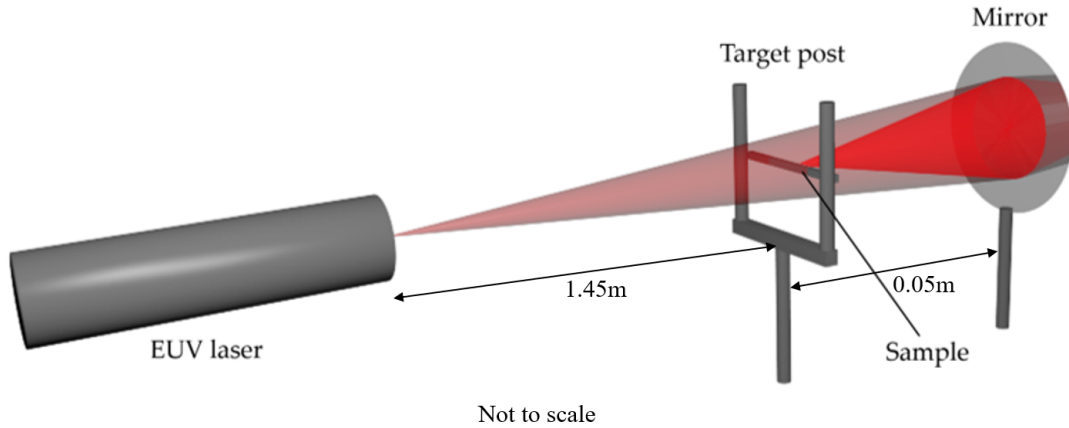


Figure 3.1: A schematic of the experimental setup illustrating the on-axis geometry for the mirror and sample holder.

The target and focussing arrangement block some laser flux from reaching the focussing mirror. However, as the laser beam intensity has an annular profile, the fraction of the beam blocked by the target before focussing is small. An approximate loss percentage can be calculated using the laser divergence data from Benware *et al.* [23]. Taking the divergences of the outer and inner limits of the annular laser profile, 3 mrad and 1 mrad respectively, one can use trigonometry to find the beam area blocked by the sample holder. The percentage of the beam area blocked by the sample holder is given simply by the ratio  $A_{\text{blocked}}/A_{\text{beam}}$ . The beam area  $A_{\text{beam}}$  is

$$A_{\text{beam}} \approx \pi \left[ (d \tan \theta_{\text{outer}})^2 - (d \tan \theta_{\text{inner}})^2 \right] = 5.28 \times 10^{-5} \text{m}^2 \quad (3.1)$$

where  $d$  is the laser-target distance and  $\theta_{\text{outer}}$  and  $\theta_{\text{inner}}$  are the divergences of the outer

and inner limits of the annular profile respectively. The blocked area  $A_{\text{blocked}}$  consists of two rectangles where the sample holder intersects with the capillary laser profile. These areas are given by

$$A_{\text{rectangle}} \approx hd (\tan \theta_{\text{outer}} - \tan \theta_{\text{inner}}) = 6.00 \times 10^{-6} \text{m}^2 \quad (3.2)$$

where  $h$  is the height of the sample holder crossbeam. The fraction  $F_{\text{blocked}}$  of the beam area blocked by the sample holder is therefore

$$F_{\text{blocked}} \approx \frac{2 [hd (\tan \theta_{\text{outer}} - \tan \theta_{\text{inner}})]}{\pi [(d \tan \theta_{\text{outer}})^2 - (d \tan \theta_{\text{inner}})^2]} = \frac{1.20 \times 10^{-5} \text{m}^2}{5.28 \times 10^{-5} \text{m}^2} = 0.22 \quad (3.3)$$

To enable off-axis focussing in order to avoid partially blocking the beam with the same design of sample holder (and therefore sample shape), the sample would need to be moved approximately the length of the crossbar (50 mm) off-axis to maintain normal incidence on target. This corresponds to an angle of incidence at the mirror of approximately  $60^\circ$ . Such off-axis focussing introduces severe spherical aberrations, as well as astigmatism and coma to the laser focus.

The flux reduction due to blocking by the sample holder in the on-axis case simplifies on-target spot calculations and allows for a convenient target and sample holder design. The reduction in on-target flux due to beam blocking by the sample holder is accounted for in flux calculations made during the analysis.

### 3.1.2 EUV laser light source

The light source used was a CDL as detailed in section 2.2. The laser is capable of pulse energies in the  $10 \mu\text{J}$  to  $26 \mu\text{J}$  range, as seen during calibration. Laser pulse energies used for the ablation study ranged from  $10 \mu\text{J}$  to  $16 \mu\text{J}$ . The temporal profile was approximately Gaussian with a pulse duration of  $1.2 \text{ns}$  [1]. Laser pulse energies and temporal profiles were measured using a gold foil photo-detector – see section 3.1.4.

Peak pulse energies and minimum energy variation were seen operating at a  $3 \text{Hz}$  repetition rate, so a shutter system was used to acquire single-shot data. This consisted of a shutter blade mounted on a rotary solenoid such that the blade is lifted when current is applied. The shutter was triggered by an electrical pulse from the laser's control box, used to control the trigger pulses, and a microcontroller held the shutter open for a pre-determined time (number of pulses), allowing the shots onto the target.

### 3.1.3 Optics and focussing

EUV optics are challenging due to the low reflectivity of materials in this spectral range. The principal reflective optic used was a spherical multilayer mirror [60, 61]. Multilayer mirrors consist of alternating layers of two materials deposited onto a substrate. The boundaries between the materials cause discontinuities in the refractive index, which cause partial reflections of incident radiation. The thicknesses of the materials are chosen carefully so that the partial reflections at each interface constructively interfere to produce an amplified reflection. A diagram of this process is shown in figure 3.2.

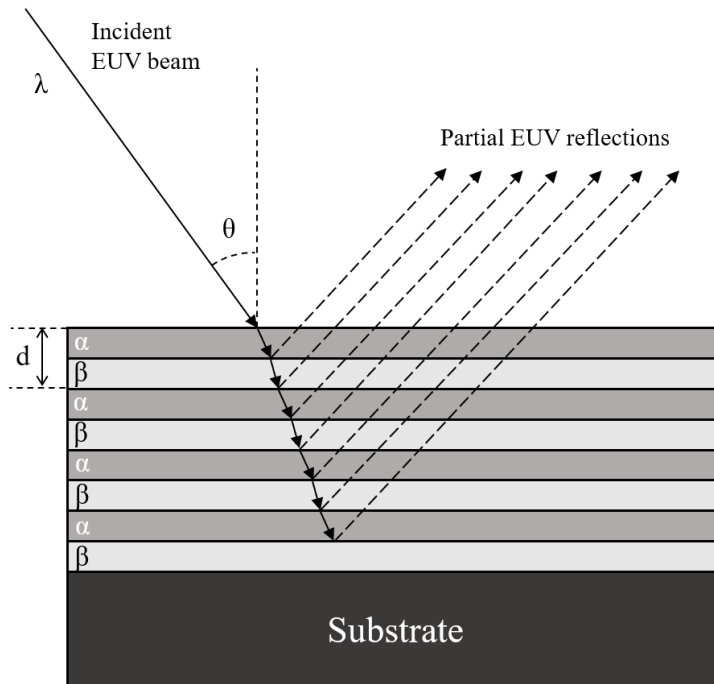


Figure 3.2: A cartoon illustrating the structure of a multilayer mirror and the partial reflections that occur at the material interfaces.

The materials of the layers in a multilayer mirror are chosen such that one material is a strong absorber to the chosen wavelength, and one is a weak absorber. At 46.9 nm wavelengths the two materials used are scandium and silicon, with attenuation lengths of 39 nm and 230 nm respectively [3]. The necessary thicknesses of the materials can be deduced from the Bragg condition

$$2l \cos \theta \simeq n\lambda, \quad n = 1, 2, \dots \quad (3.4)$$

where  $\theta$  is the angle of incidence (measured from the surface normal) and  $l$  is the period of the multilayer structure. The Bragg condition indicates that for radiation at normal

incidence the layers should be  $\approx \lambda/4$  thick, which in the case of 46.9 nm photons is  $\approx 10$  nm. The ratio of the thicknesses of the two materials is also important. Figure 3.3 shows the reflectivity of a range of multilayer mirrors with different bilayer periods (the combined thickness of one scandium and one silicon layer) and Sc:Si thickness ratios, calculated using the IMD software package [62]. These calculations do not include the effects of surface roughness, layer boundary roughness, or deviations in layer thickness. The Sc:Si multilayer mirror used in the ablation study had a reported reflectivity  $R$  of 0.4 (40%) at normal incidence.

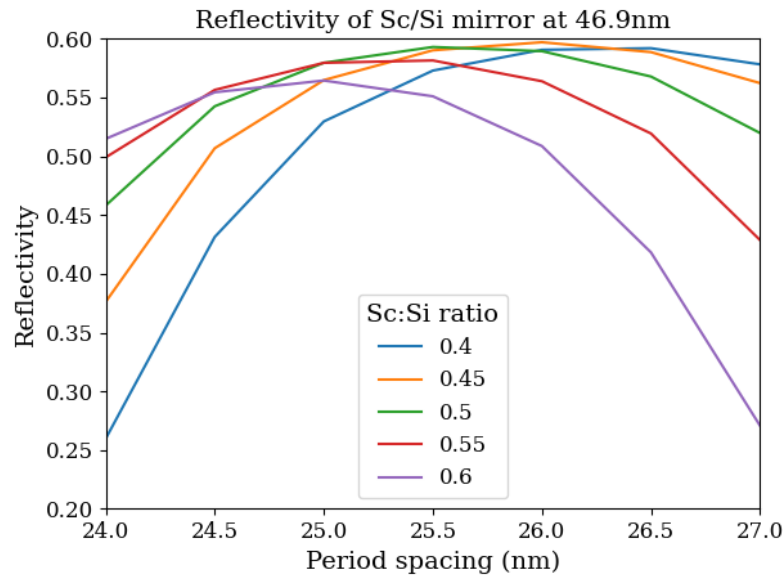


Figure 3.3: Reflectivity as a function of Sc:Si multilayer mirror bilayer spacing, with a range of thickness ratios between the two materials.

An unprotected gold mirror was also used in the ablation study. A sufficiently flat gold surface has a reflectivity of 0.08 (8%) at normal incidence for 46.9 nm photons. The gold mirror was included to extend the fluence range of the ablation study below  $10 \text{ J cm}^{-2}$ . Both multilayer and single element mirrors are significantly affected by the angle of incidence of the incoming radiation; but with different effects. The reflectivity of a single element mirror increases with deviation from normal incidence up to a maximum at grazing incidence, whereas the multilayer mirror reflectivity has a peak at normal incidence, drops to very low values at  $45^\circ$ , and then increases again up to grazing incidence. This is because at grazing incidence the reflectivity of the Sc:Si multilayer mirror becomes effectively the reflectivity of the outermost scandium layer. The reflectivity of both mirrors as a function of incident angle is shown in figure 3.4. In the ablation study, the laser radiation was incident normal to the mirror in order

to maximise both the highest fluence values and the difference between the fluences of the two mirrors.

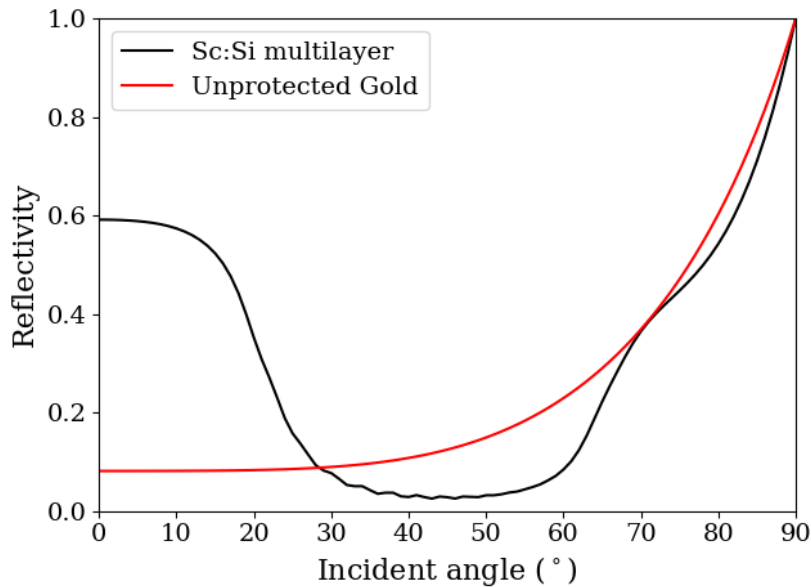


Figure 3.4: Reflectivity calculations for a Sc:Si multilayer mirror reflecting 46.9 nm light made using the IMD software package [62].

The Sc:Si multilayer and the unprotected gold mirror used in the ablation study were both spherical mirrors with focal lengths of 50 mm. The method chosen to establish the focal spot size on-target stipulates that the beam be Gaussian. Given the annular beam profile of the capillary laser, it must be assessed whether this is an accurate approximation at the focal spot. Focussing in the far field for a circularly symmetric beam incident on a lens can be deduced using the following expression for the focussed electric field  $E$ , given an electric field variation  $\varepsilon_A$  at the focussing lens. For Fraunhofer diffraction through an arbitrary 2D lens we have the surface integral [63]

$$E = \frac{1}{R} \exp(i[\omega t - kR]) \iint_{\text{Lens}} \varepsilon_A \exp\left(\frac{ik(Yy + Zz)}{R}\right) dS \quad (3.5)$$

where  $R$  is the distance from the lens,  $k$  is the wavenumber,  $\omega$  is the angular frequency, and  $(y, z)$  and  $(Y, Z)$  are the co-ordinates on the object and image surfaces respectively – see figure 3.5.

$\varepsilon_A$  is referred to as the source strength per unit area at the focussing lens. For a circular beam at the focussing lens we can write equation 3.5 in terms of polar coordinates such that  $z = \rho \cos \phi$ ,  $y = \rho \sin \phi$ ,  $Z = q \cos \Phi$ , and  $Y = q \sin \Phi$ , like so;

$$E = \frac{1}{R} \exp(i[\omega t - kR]) \int_{\rho=0}^a \int_{\phi=0}^{2\pi} \varepsilon_A \exp\left(\frac{ik\rho q}{R} \cos(\phi - \Phi)\right) \rho d\rho d\phi \quad (3.6)$$

where  $a$  is the radius of the beam at the focussing lens.

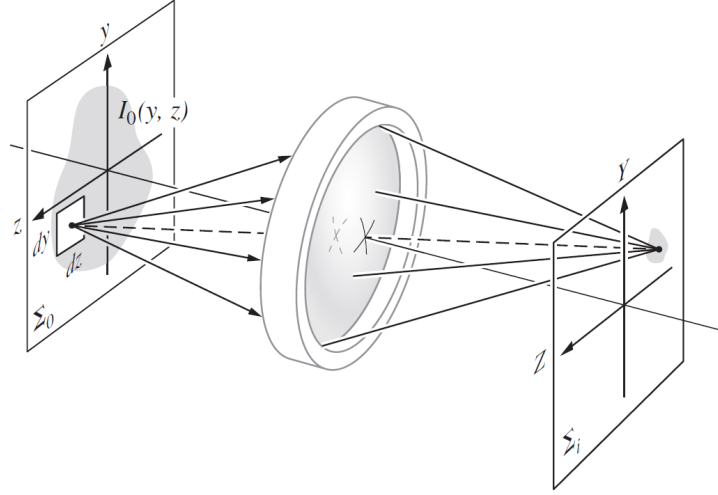


Figure 3.5: Diagram of the circular lens problem definition [63].

The solution to equation 3.6 must be independent of  $\Phi$  to maintain axial symmetry, so we shall consider the simple  $\Phi = 0$  case. The integral over  $\phi$  with  $\Phi = 0$ , given by

$$\int_0^{2\pi} \exp\left(i\frac{kq}{R}\rho \cos\phi\right) d\phi, \quad (3.7)$$

is in the form of a Bessel function of the first kind (and of zeroth order). The general form of these Bessel functions is

$$J_m(u) = \frac{i^{-m}}{2\pi} \int_0^{2\pi} \exp(i[m\nu + u\cos\nu]) d\nu. \quad (3.8)$$

To convert from a circular beam at the lens to an annular one, all we need do is alter the lower limit of  $\rho$  from 0 to  $\rho_0$ . So, our equation for an annular beam incident on a circular focussing lens with constant electric field between  $\rho_0$  and  $a$  (and zero field elsewhere) becomes

$$E = \frac{\varepsilon A}{R} \exp(i[\omega t - kR]) 2\pi \int_{\rho_0}^a J_0\left(\frac{kq}{R}\rho\right) \rho d\rho. \quad (3.9)$$

Now we must make use of two key properties of integrals and of the Bessel function. The first is known as the recurrence relationship, and it states that the  $m$ th and  $(m - 1)$ th order Bessel functions of the first kind are related by the expression

$$\frac{d}{du} u^m J_m(u) = u^m J_{m-1}(u). \quad (3.10)$$

The second is a property of integrals in general, and is known as the Newton-Leibniz axiom. It states that if a real-valued function  $F(x)$  is the antiderivative of a real-valued

function  $f(x)$ , then the definite integral in the interval  $[a, b]$  is given by

$$\int_a^b f(x)dx = F(b) - F(a). \quad (3.11)$$

If we temporarily substitute in the parameter  $w = k\rho q/R$ , we find  $d\rho = (R/kq)dw$ , and we can now apply these two expressions to equation 3.9 to and re-substitute for  $w$  to get a solution for the electric field

$$E = \frac{\varepsilon_A}{R} \exp(i[\omega t - kR]) 2\pi \left(\frac{R}{kq}\right)^2 \left[ \frac{kaq}{R} J_1\left(\frac{kaq}{R}\right) - \frac{k\rho_0q}{R} J_1\left(\frac{k\rho_0q}{R}\right) \right]. \quad (3.12)$$

Further simplification can be made using a second substitution  $u = kq/R$ ;

$$E = \frac{\varepsilon_A}{R} \exp(i[\omega t - kR]) 2\pi \left[ \frac{aJ_1(au)}{u} - \frac{\rho_0 J_1(\rho_0 u)}{u} \right]. \quad (3.13)$$

The intensity can now be found from the electric field using  $I = \frac{1}{2}E^*E$ ;

$$I = \frac{2\pi^2\varepsilon_A^2}{R^2} \left[ \frac{aJ_1(au)}{u} - \frac{\rho_0 J_1(\rho_0 u)}{u} \right]^2. \quad (3.14)$$

All that remains is to find the value of  $I$  at the limit  $q = 0$ . Both  $J_1 \rightarrow 0$  and  $u \rightarrow 0$  as  $q \rightarrow 0$ , resulting in  $I(0) = 0/0$ , so we need to invoke l'Hôpital's rule in order to find the value at  $q = 0$ . l'Hôpital's rule specifies that the limit of the ratio of two functions  $f(x)$  and  $g(x)$  will be equal to the limit of the ratio of their derivatives;

$$\lim_{x \rightarrow 0} \frac{f(x)}{g(x)} = \lim_{x \rightarrow 0} \frac{f'(x)}{g'(x)}. \quad (3.15)$$

The derivative of  $J_1(u)$  is given by

$$\frac{d}{du} J_1(u) = \frac{1}{2} [J_0(u) - J_2(u)] \quad (3.16)$$

so the value of  $I$  at  $q = 0$  will be

$$I(0) = \frac{\pi^2\varepsilon_A^2}{R^2} (a - \rho_0)^2 = \frac{\pi\varepsilon_A^2(A - 2\pi a\rho_0)}{R^2}. \quad (3.17)$$

where  $A$  is the area of the annulus at the aperture.

This non-zero value for  $I(0)$  demonstrates that the annular profile seen at the mirror will not be carried forward onto the focus. Using the `special` package from the SciPy library [64], the intensity function has been plotted as a fraction of the peak intensity  $I(0) \equiv I_0$  and as a function of radial position on-target for the focussing conditions of the ablation experiments in figure 3.6. Also shown in figure 3.6 is a Gaussian function fitted to the intensity curve. This shows that treating the beam as Gaussian on-target is a valid approximation, as the intensity of the secondary diffraction lobe is less than

5% of the main peak. This approximation is therefore limited to peak beam intensities less than 20 times the ablation threshold. In the ablation results for this thesis, there is an approximate peak fluence range up to an order-of-magnitude above the threshold fluence, so the secondary lobe fluence is not expected to cause target ablation.

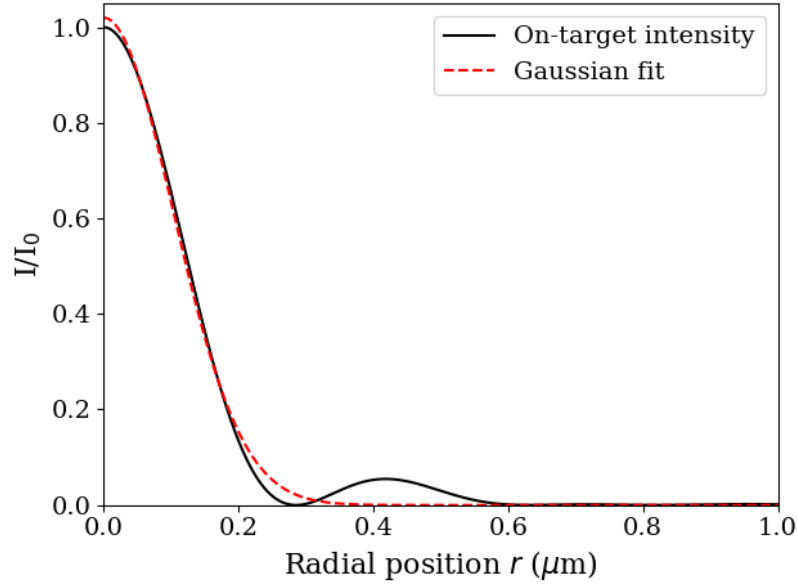


Figure 3.6: On-target intensity curve as a percentage of peak intensity plotted as a function of on-target radial position for a lens with a focal length of 50 mm focussing an annular beam of constant intensity between on-lens radii of 1.5 mm and 4.5 mm. The red curve is a Gaussian function fitted to the Bessel function curve and is a suitable approximation for the beam shape.

### 3.1.4 Detectors and pulse energy measurements

Measurements of the capillary laser pulse energy were made using two detectors; a normal incidence photodetector and an in-line photodetector. The normal incidence photodetector measures the incident radiation via the conversion of photons to electrons by the photo-electric effect. This conversion occurs on the surface of a gold-coated cathode biased to  $-1.8$  kV. Liberated electrons are then accelerated towards a grounded mesh, producing a measurable current between the biased mesh and the gold-coated cathode. Softer wavelengths, such as visible light, are unable to contribute to the electron production due to their low photon energy.

Figure 3.7(a) shows a diagram of the internals of the normal incidence photodetector. The voltage of the gold-coated anode is proportional to the total energy of the

incident photons, i.e. the laser pulse energy, which can be found using the relation

$$E_{\text{pulse}} = \frac{E_{\gamma} A}{q H Z_{\text{imp}}} \int_{-\infty}^{\infty} V dt \quad (3.18)$$

where  $E_{\gamma}$  is the photon energy (26.4 eV),  $A$  is the built-in signal attenuation at the detector's control unit,  $q$  is the quantum efficiency of the gold anode,  $H$  is the transmission fraction of the biased mesh, and  $Z_{\text{imp}}$  is the impedance of the detector. The quantum efficiency of gold for photons at 46.9 nm wavelengths is 0.054. The detector used had an impedance  $Z_{\text{imp}}$  of  $50 \Omega$ , the transmission fraction of the biased mesh  $H$  was 7%, and the detector control box attenuated the signal by a factor of 10. The voltage peak corresponding to a capillary laser pulse is approximately Gaussian [1], so the integral becomes  $V_{\text{peak}} \sqrt{2\pi} \sigma(t)$  where  $\sigma(t)$  is the temporal standard deviation of the laser pulse.

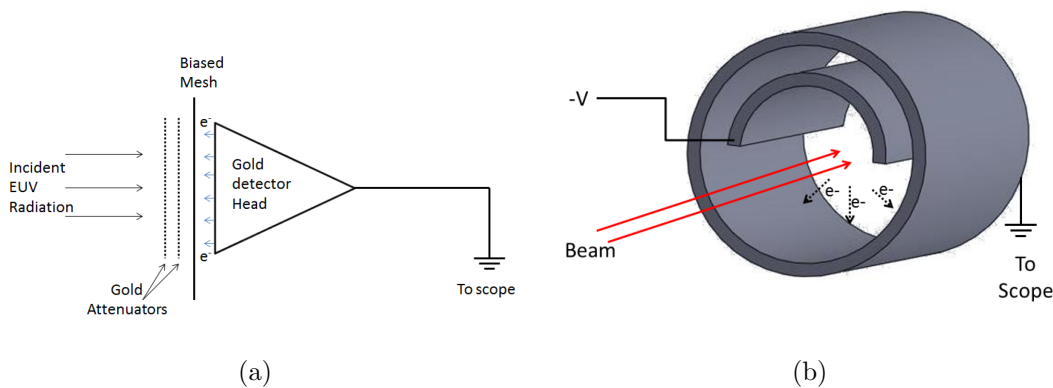


Figure 3.7: Diagrams of (a) the normal incidence photodetector and (b) the in-line photodetector [1].

The on-axis geometry of the ablation study prevents the normal incidence photodetector from taking laser pulse energy measurements during the ablation campaign. Laser pulse energy measurements were instead made by an in-line photodetector with a cylindrical design that allows the laser beam to pass through it. The in-line photodetector was then calibrated against the normal incidence photodetector to convert measured in-line photodetector voltages into laser pulse energies. The in-line photodetector collects electrons that are liberated by the laser beam photo-ionizing ambient argon gas particles in the vacuum system. The ambient argon leaks into the vacuum system through the pinhole at the exit of the laser's capillary tube. The electrons liberated from the argon gas particles are repelled by a biased semi-circular electrode, which forces the electrons onto a grounded outer electrode and generates a current. A

diagram of the in-line photodetector is shown in figure 3.7(b). The drawback of the in-line photodetector is its high dependence on the ambient argon pressure, which not only fluctuates naturally but must also be actively adjusted to produce the highest energy laser pulses. This is why it is calibrated against the more consistent normal incidence photodetector when determining laser pulse energies.

### 3.1.5 Vacuum system

EUV photons have an attenuation length of  $\approx 20 \mu\text{m}$  in air at this wavelength [3], so the experiment was conducted under vacuum. The vacuum system consisted of two six-way crosses attached to the laser front end, with a set of bellows connecting this to the target chamber. Vacuum was achieved using a standard arrangement of roughing pump and backed turbomolecular pump. A background pressure of a few mTorr was adequate in the main vacuum system, with the pressure rising once the laser system was operating due to argon leakage from the capillary housing through the laser output pinhole.

### 3.1.6 Target dimensions and materials

The target materials ablated using the focussed CDL were aluminium, copper, and gold. Aluminium was chosen for its long attenuation length  $l_a$  at 46.9 nm wavelengths and low density, whilst gold and copper were chosen for their short attenuation lengths and high densities as a contrast – see table 3.1. Aluminium and copper targets were polished for the cleanest ablation features. Gold samples had poorer surface qualities but ablation features were still distinguishable.

| $l_a$ (nm) | Aluminium | Copper | Gold |
|------------|-----------|--------|------|
| IMD        | 229       | 7      | 9    |
| CXRO       | 419       | 7      | 11   |

Table 3.1: Attenuation lengths in nm of 46.9 nm radiation for our target materials using the IMD software package [62] and the CXRO database [3].

The opacity of solid materials at this wavelength is a property that has not been measured experimentally; the values given above are theoretically determined. This remains an open issue, hence the two differing sets of values presented above.

## 3.2 Methodology

### 3.2.1 Detector calibration

The on-axis geometry chosen for the experiment means that the laser pulse energy cannot be measured using a normal incidence photodetector during ablation shots. This is the purpose of the in-line detector; non-intrusive beam energy measurements. The drawback of this detector is its variability with the ambient argon pressure in the vacuum system. Voltage readings from the in-line detector are converted to laser pulse energies by calibrating it against the normal-incidence photodetector.

The capillary discharge laser was calibrated by attaching it to a short vacuum system, with both the in-line photodetector and normal incidence photodetector mounted on the beamline; the former halfway along the system and the latter at the end with the beam directly incident upon it. A number of shots were then fired onto the photodetector and voltage readings were taken from both detectors. Results are plotted against each other in figure 3.8.

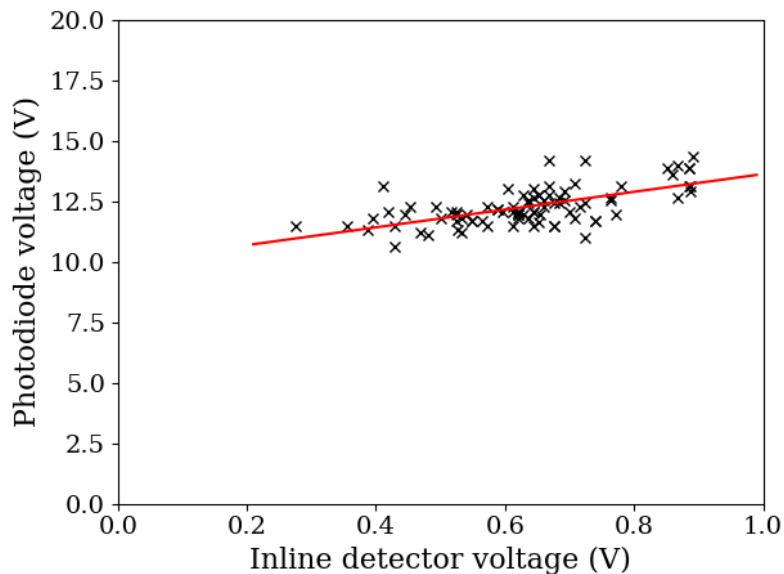


Figure 3.8: Normal-incidence photodetector voltage plotted as a function of in-line photodetector voltage, shown for a large number of different capillary laser shots.

Clearly, both detectors should read zero voltage when no beam is present. However, the behaviour of the in-line detector in the low fluence (and therefore low voltage) range is unknown. For this reason, the calibration curve, shown in red, is fitted only over the limited range shown (i.e. the range of the calibration data points). In the event

of further investigations, this range would need to be extended by the collection of additional calibration data points in the range of any additional shot energies.

The wide distribution of in-line photodetector voltages for a comparatively small range of normal-incidence photodetector voltages can be attributed to fluctuations in the background argon pressure, determined by the flow of argon from the capillary housing through the pinhole. However, the low spread of voltages at the normal-incidence photodetector gives us confidence that there is a low spread of pulse energies during ablation runs. Subsequently, the shot data should be well grouped according to the reflectivity of the mirror used.

### 3.2.2 Capillary laser alignment

The alignment of the capillary laser beam onto the mirror with focussing on the target is complicated by the non-visible nature of the EUV laser output and changes in focussing between vacuum and air conditions due to small movements of the vacuum vessels. To focus the laser beam onto the target, the EUV beam was imaged at two points along the beamline and a visible laser was aligned through these images – see figure 3.9.

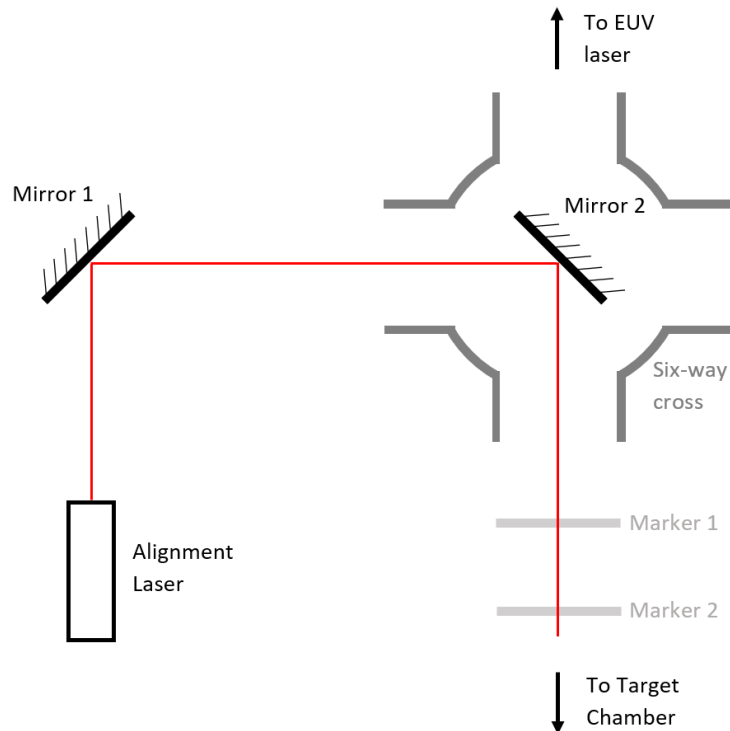


Figure 3.9: A schematic of the mirror layout required to align the EUV laser using an optical substitute.

The imaging is done by placing glass slides, spin-coated with PMMA, in the path

of the beam and firing a few hundred shots onto each of them. Even unfocussed, the energy in the beam is sufficient to ablate the PMMA coating. The slide can then be treated with a solution of 4-methyl-2-pentanone to accentuate the spot, although in the correct light it is typically visible to the naked eye already. The spots can then be marked up to find their approximate centres.

Once the glass slides have been marked, they can be re-installed in the beamline. Using the spot markings, a visible wavelength laser, in this case a He:Ne laser, can be directed from outside the vacuum system along the beamline and into the target chamber using a system of mirrors with fixed positions, as shown in figure 3.9.

When the alignment laser has been lined up with the centres of both markings we can assume it is in the same axis as the EUV laser to within a good tolerance. The visible laser can then be used inside the target chamber to choose the location of the motorised stages (to give maximum useful range) and the angle of the mirror (to focus onto the target).

### 3.2.3 Empirical ablation study

The process for collecting ablation data was the same for each target material. Parameter scans were conducted by moving the target simultaneously in both  $x$  (perpendicular to beam axis) and  $y$  (along beam axis) axes such that each point along the target corresponded to a different mirror-target distance. An initial scan was performed with 0.1 mm increments in  $y$  values and 10 shots at each point. Targets were then checked using an optical microscope for signs of ablation so that a higher precision scan could be conducted around the focal point. This process was then repeated with 0.01 mm increments and checked again, with a final scan being conducted at 0.001 mm increments to establish the focal point to a 10  $\mu\text{m}$  accuracy. Once these initial scans are done, the focal point can be reliably found without needing to repeat all the above steps, provided care is taken when removing and re-installing the sample holder. The process is repeated for a change in mirror.

The error in the laser energy measurement for each ablation measurement on the different targets is estimated at a minimum of  $\pm 10\%$  due to shot-to-shot variability. In addition, the absolute laser energy on target has a systematic error of  $\approx \pm 5\%$  due to the error in the multilayer mirror calibration.

The targets were ablated at a range of  $y$  positions, with out-of-focus spots being distinguishable by their unusual ‘hamburger’ shape. Figure 3.10 shows an image of

two shots, one in focus and one out of focus, to illustrate the difference in shape with focussing. This occurs when the target is suitably far from the focal plane that the parts of the beam that pass over the sample and the parts that pass under the sample do not overlap. A range of shot numbers was also tested, from 1 to 50, but only the single-shot ablation results have been analysed here.

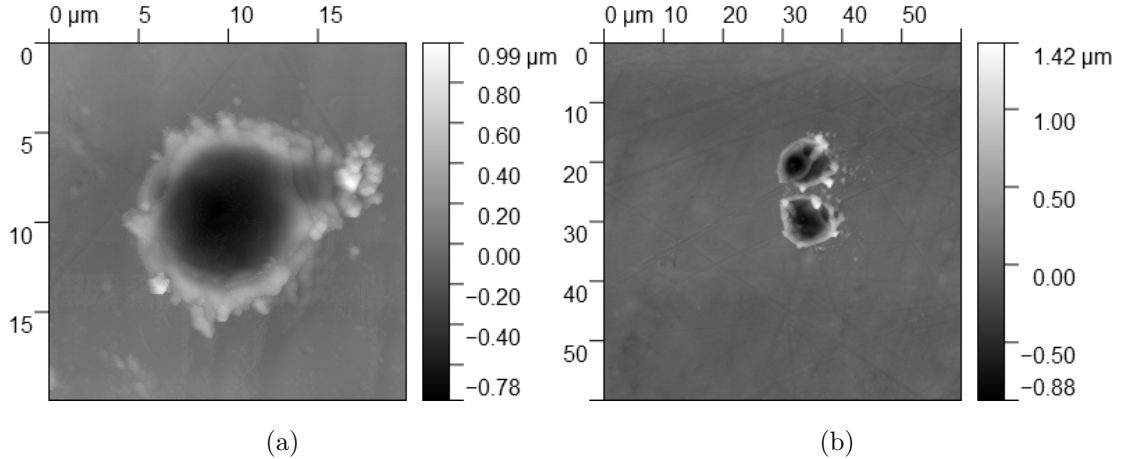


Figure 3.10: Example images of (a) an in-focus ablation shot and (b) an out-of-focus ablation shot demonstrating the ‘hamburger’ shape, both on gold targets.

### 3.2.4 Analysis of targets

Once the ablation results had been collected, the surface topography was measured with an atomic force microscope (AFM) manufactured by Bruker (Bioscope Resolve model). The principles of AFM imaging [65] are as follows. A cantilevered tip is brought close to the surface of the target so that forces between tip and sample generate a measurable deflection of the cantilever. In principle, the interaction between the surface and tip is the Van der Waals force, an attraction or repulsion arising from quantum fluctuations in the electron clouds surrounding atomic nuclei. In practice other stronger forces contribute, such as electrostatic forces generated by the ambient air or capillary forces occurring when natural humidity creates a liquid film on the surface that the tip then dips into. Regardless of the force mechanism acting upon it, the cantilever retains a linear relationship between force and tip displacement, allowing for measurements of these deflections which can be related to changes in topography.

Maintaining a constant relationship to the target surface is key to mapping topography accurately. The relation between force and cantilever displacement is a simple

linear relationship as denoted by Hooke's law

$$F = k\Delta z \quad (3.19)$$

where  $k$  is the cantilever spring constant and  $\Delta z$  is the tip displacement. In most real cases however, the force  $F$  is dependent on the  $z$  position of the tip, and so this must be expressed more generally as

$$\begin{aligned} F &= F_0 + \frac{\delta F}{\delta z} \Delta z = k\Delta z \\ F_0 &= \left( k - \frac{\delta F}{\delta z} \right) \Delta z. \end{aligned} \quad (3.20)$$

In the general case, the resonant frequency  $\omega_r$  of the cantilever is given by

$$\omega_r = \sqrt{\frac{1}{m} \left( k - \frac{\delta F}{\delta z} \right)}. \quad (3.21)$$

This provides a method for controlling the tip to sample spacing. The cantilever is mounted on a piezoelectric motion device and can be moved across the surface in a way that maintains a constant resonant frequency. In this region the gradient of the force must necessarily be constant, and so too, therefore, must the tip spacing. The cantilever can either be held steady or "tapped" up and down to build up a complete topography. The images in this thesis were taken in tapping mode.

The method used by the Bruker AFM for measuring the position of the cantilever tip is beam deflection. The upper surface of the cantilever is mirrored and a laser is reflected off this surface onto a position-sensitive photodetector. Proprietary software then converts the changes in laser position at the detector to surface positions and compiles a two-dimensional map. These data files can be used to produce a simple image of the surface (an example is shown in figure 3.11) or can be analysed to find more detailed topographical information, in this case to extract details of ablation features.

### 3.2.5 Two-dimensional profile extraction and analysis

The AFM images detailed above were taken to enable comparison between ablation features and incident beam properties and to measure the depth of laser ablation. Measuring the on-target laser fluence is not possible directly as the on-axis geometry makes imaging the focal spot impossible. The closest possible approximation is to use the in-line detector to measure the pulse energy and a fitting method developed by J Liu *et al.* [66] to determine the beam area from AFM images of the ablation features.

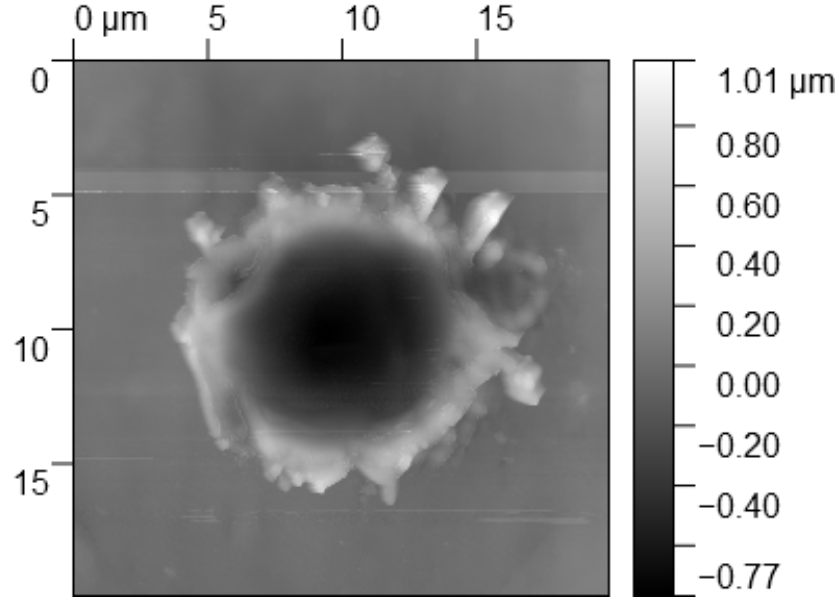


Figure 3.11: An AFM image of a Sc:Si multilayer mirror focussed shot on a gold target.

Each ablation depth can then be extracted from the corresponding AFM image, and a fluence against ablation depth graph can be plotted.

To measure the ablation depth from the AFM image, the topographical data was converted into a series of one-dimensional depth profiles. This was done in the program Gwyddion [67], which was used to extract depth data along an arbitrary line on the target. Four such ‘lineouts’ passing through the crater centre were chosen approximately  $45^\circ$  apart to capture any ellipticity in the ablation feature. These were then analysed individually and the peak ablation depth associated with the shot was taken as the average of these four one-dimensional scans.

The analysis for each ablation profile was undertaken as follows. Firstly, it was assumed that the beam has a Gaussian profile on-target, a valid approximation as discussed in section 3.1.3, given by

$$I = I_0 \exp\left(-2\frac{r^2}{w^2}\right) \quad (3.22)$$

where  $I_0$  is the maximum intensity and  $w$  is a measure of the beam radius. This value  $w$  can then be used to find the effective beam area  $A_{\text{eff}}$  by using

$$A_{\text{eff}} = \pi w_{\text{eff}}^2 \quad (3.23)$$

where  $w_{\text{eff}}$  is the effective beam radius, given by  $w/\sqrt{2}$ . The maximum on-target fluence  $F_0$  at the centre of the laser focus is then given by

$$F_0 = \frac{E_{\text{pulse}}}{\pi w_{\text{eff}}^2} \quad (3.24)$$

where  $E_{\text{pulse}}$  is the laser pulse energy. This definition for the effective beam area is taken from the American National Standard Z136.1-2007 for Safe Use of Lasers, and can be found from the initial Gaussian profile by a double integration of equation 3.22

$$\begin{aligned} E_{\text{pulse}} &= \int_0^{t_p} I_0(t) dt \int_0^\infty \exp\left(-2\frac{r^2}{w^2}\right) 2\pi r dr \\ &= \int_0^\infty F_0 \exp\left(-2\frac{r^2}{w^2}\right) 2\pi r dr. \end{aligned}$$

Using the substitution  $u = r^2$  and its differential  $dr = du/2r$ , the integration becomes

$$\begin{aligned} E_{\text{pulse}} &= F_0 \pi \int_0^\infty \exp\left(-\frac{2u}{w^2}\right) du \\ &= F_0 \pi \left[ -\frac{w^2}{2} \exp\left(\frac{-2u}{w^2}\right) \right]_0^\infty \\ &= \frac{F_0 \pi w^2}{2} = F_0 \pi w_{\text{eff}}^2, \end{aligned}$$

retrieving the result shown in equation 3.24.

The next step in the analysis, having assumed a Gaussian beam shape at the target, is to use the depth data to make an estimate of the parameters of this Gaussian. This was done by fitting a Gaussian of the form in equation 3.22 to the depth against position datasets produced in these lineouts. A curve fitting algorithm from the SciPy [64] Python package was used. The algorithm performs non-linear least squares analysis to generate a set of variables  $\mathbf{C} = \{C_1, C_2, \dots, C_n\}$  such that the function  $y = f(x, \mathbf{C})$  best fits a dataset of  $m$  points  $(x_1, y_1), (x_2, y_2), \dots, (x_m, y_m)$  – provided  $m \geq n$ . A “Trust Region Reflective” algorithm is used, which re-formulates the problem as a boundary-constrained minimization problem in the manner described by Branch, Coleman, and Li [68]. The fitting algorithm also provides variance data for the parameters in order to calculate associated errors. An example of a measured ablation depth cross-section, along with a fitted Gaussian, is shown in figure 3.12.

Data points above a surface height of zero are common due to large-scale surface contours and sample warping (see, for example, the slope seen at the right hand side of figure 3.12). Also present in figure 3.12 are examples of peaks around the crater edge caused by re-solidification of melted material. Surface peaks to the side of the ablation crater can affect the fitting algorithm, so the data is cropped to the shaded area enabling a close approximation of the peak position to be provided to the algorithm. Considering only a reduced range prevents the algorithm from erroneously fitting melt peaks or failing to find a solution.

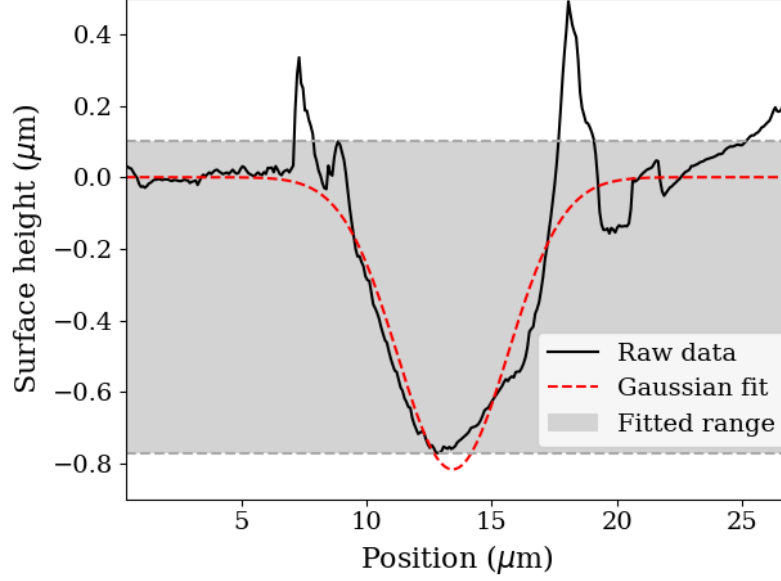


Figure 3.12: A linear profile extracted from a Sc:Si mirror shot on a gold target. The shaded area is the range the data is clipped to to ensure accurate fitting.

After fitting a Gaussian to the depth data, the effective width  $w_{\text{eff}}$  and maximum ablated depth  $d_{\text{abl}}$  were measured. The values from the four lineouts were then averaged to give an averaged value of  $w_{\text{eff}}$  and  $d_{\text{abl}}$  for the shot. Errors in these measurements were then calculated by taking the larger of the standard error in the mean  $\bar{x}$ , given by

$$\Delta\bar{x} = \frac{\sigma}{\sqrt{n}}, \quad (3.25)$$

and the combination of the individual errors, given by

$$\Delta\bar{x} = \frac{1}{4} \sqrt{(\Delta x_1)^2 + (\Delta x_2)^2 + (\Delta x_3)^2 + (\Delta x_4)^2}. \quad (3.26)$$

In order to calculate values for the incident fluence, the Liu method [66] was first employed to establish the focal spot size on-target. This method has previously been applied to experiments at similar wavelengths [69, 70, 71]. The Liu method assumes a Gaussian beam shape and absorption behaviour solely governed by the Beer-Lambert law. These two assumptions allow us to cast the crater area  $S$  as a linear function of  $\ln(E_{\text{pulse}})$ ;

$$S = A + B \ln(E_{\text{pulse}}). \quad (3.27)$$

Provided a range of pulse energies are investigated, we can now use a plot of crater area as a function of  $\ln(E_{\text{pulse}})$  to estimate the focussed beam area  $S_{\text{foc}}$  from the gradient  $B$  i.e.

$$S_{\text{foc}} = B. \quad (3.28)$$

We can also find a value for the threshold fluence  $F_{th}$  from the fitting parameters  $A$  and  $B$

$$F_{th} = \frac{1}{S_{\text{foc}}} \exp\left(-\frac{A}{B}\right), \quad (3.29)$$

enabling a comparison of  $F_{th}$  against literature values. The validity criterion for the model is that the Rayleigh length  $z_R$  is much greater than the attenuation length  $l_a$ . The Rayleigh length is given by

$$z_R = \frac{\pi\omega_0^2}{\lambda} \quad (3.30)$$

where  $\omega_0$  is the beam radius as measured at the focal point (i.e. the minimum beam radius), also known as the beam waist. For radiation at 46.9 nm and a beam waist of 1  $\mu\text{m}$  the Rayleigh length is 67  $\mu\text{m}$ . This is three orders of magnitude larger than the attenuation lengths for gold and copper, and two larger than the attenuation length for aluminium.

Figures 3.13, 3.14, and 3.15 show crater area as a function of the natural logarithm of the pulse energy for ablation shots on aluminium, gold, and copper respectively. A linear fit, or Liu plot, was plotted against the above data for each material, yielding an estimation of the focussed spot size. The ablation features on aluminium and gold predict spot sizes of 1.78  $\mu\text{m}$  and 1.80  $\mu\text{m}$  respectively. The prediction of the copper ablation features is 1.42  $\mu\text{m}$ , differing from the other materials notably. There is however a larger spread in the crater areas seen for a given pulse energy in the copper ablation features, and a fit predicting a spot size of 1.79  $\mu\text{m}$  still passes through all the data points except the smallest crater generated by the Sc:Si mirror and the largest crater generated by the gold mirror (both of which could be considered weak outliers). An average focal spot diameter of 1.79  $\mu\text{m}$  was used in calculations.

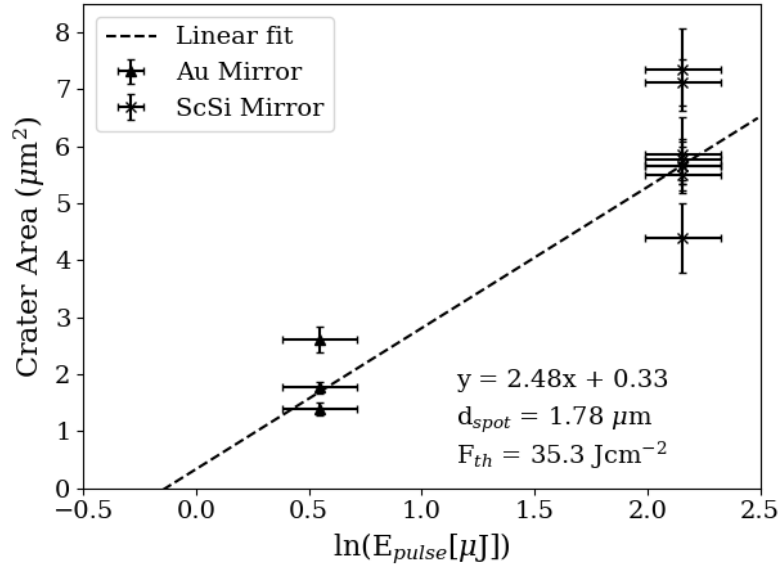


Figure 3.13: The ablation crater area, measured at the target surface, as a function of the natural logarithm of the pulse energy for aluminium. Also shown is a linear fit, or so-called Liu plot, of the data and the physical parameters that can be drawn from it.

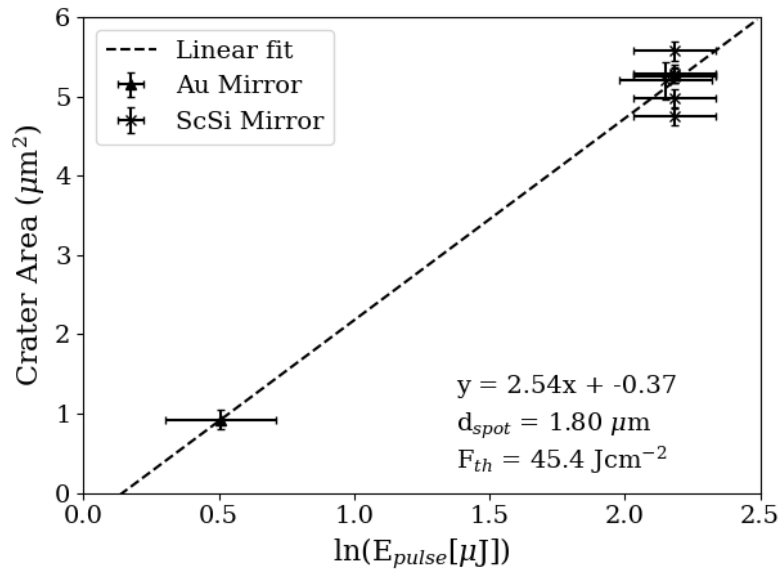


Figure 3.14: The ablation crater area, measured at the target surface, as a function of the natural logarithm of the pulse energy for gold. Also shown is a linear fit, or so-called Liu plot, of the data and the physical parameters that can be drawn from it.

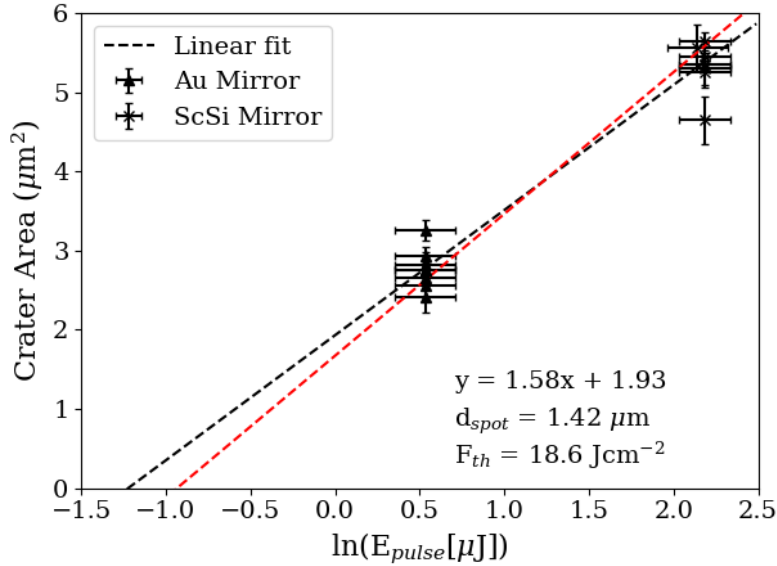


Figure 3.15: The ablation crater area, measured at the target surface, as a function of the natural logarithm of the pulse energy for copper. Also shown is a linear fit, or so-called Liu plot, of the data and the physical parameters that can be drawn from it.

Previous work by Wilson [1] on ablation of solid targets with this CDL source has included a ray-tracing study of the expected focussed beam size. Figure 3.16 shows plots of the focal spot size as a function of the radius of curvature of the reflective optic according to Abbe’s criterion (i.e. the diffraction limited spot size) and ray-tracing calculations performed using two dimensional ray-tracing software. In the case of the latter, the value plotted is the diameter of the circle of least confusion. For the focal length of our spherical mirrors, we have a radius of curvature of 100 mm which corresponds to a predicted focal spot size, dominated by the circle of least confusion, of 2.00  $\mu$ m. This value is within 10% of those predicted by the Liu plots, suggesting the Liu plots are a good approximation of the spot size.

Some ablation features, particularly on the aluminium targets, are elliptically-shaped. The Liu analysis assumes the beam to be Gaussian in two dimensions, generating circular ablation craters, so the elliptical ablation features have to be accounted for by large error bars in the crater area so as to avoid skewing the fit. By comparison, the gold target results show good symmetry (and therefore low fluence errors) throughout. Figure 3.17 shows example AFM images of different levels of symmetry in ablation features on aluminium and gold targets.

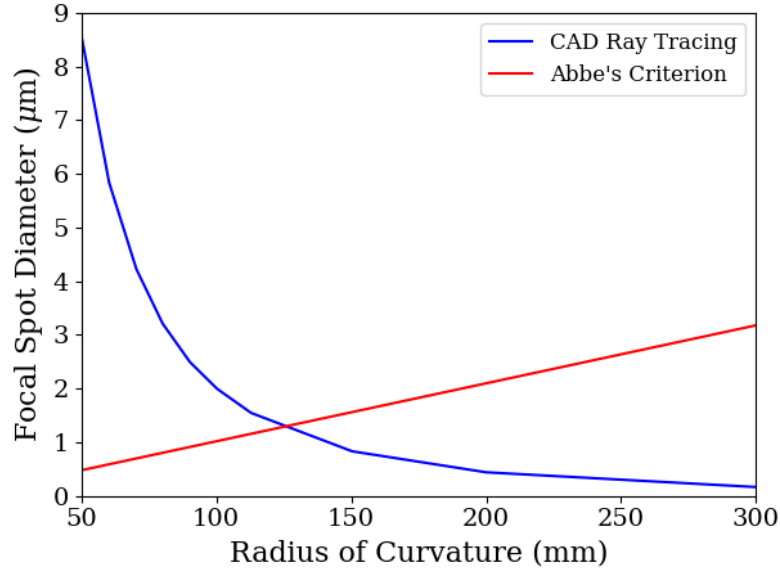


Figure 3.16: Focal spot size as predicted by Abbe's criterion and a two-dimensional ray tracing code as a function of radius of curvature of a spherical optic for 46.9 nm radiation.

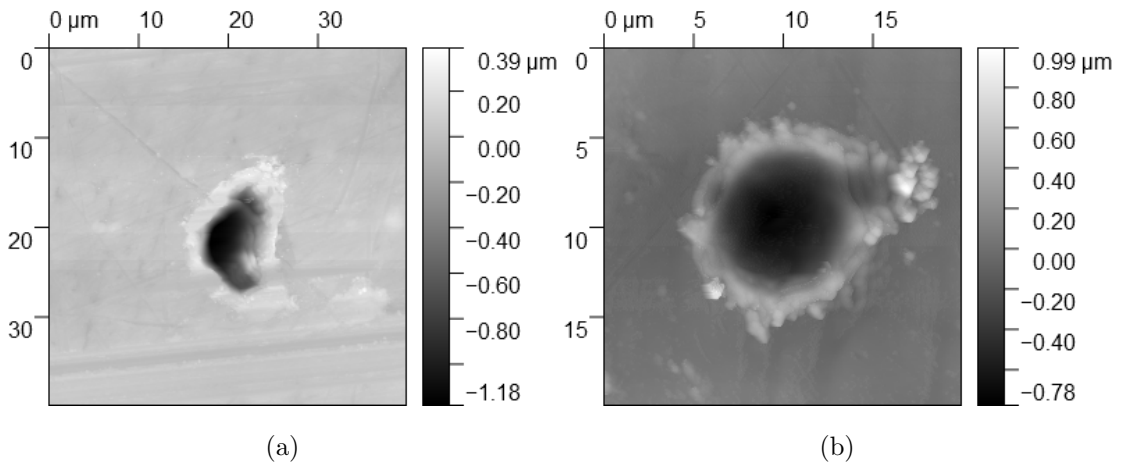


Figure 3.17: (a) A highly asymmetric ablation feature on aluminium compared to (b) a highly symmetric ablation feature on gold.

Experimentally measured ablation depths for targets of aluminium, gold, and copper are shown in figures 3.18, 3.19, and 3.20 respectively. It is apparent that consistent ablation depths are found for gold and copper targets. However, for aluminium targets (figure 3.18) with a long attenuation depth for the laser wavelength, the Lui analysis assuming a threshold local flux at each focal radius for ablation to occur may have reduced accuracy. Lateral transport (discussed in Section 6.1) can be expected to be more important for a long attenuation length.

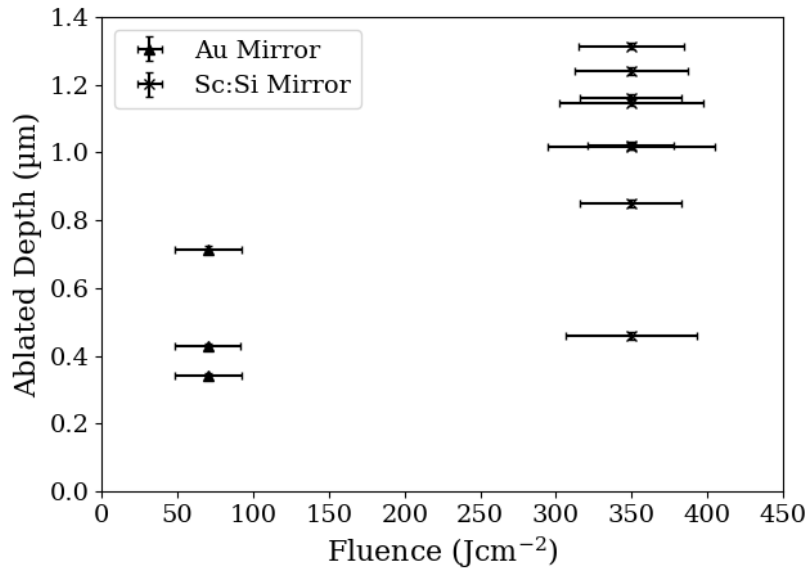


Figure 3.18: The ablation depth as a function of the laser fluence on target for aluminium.

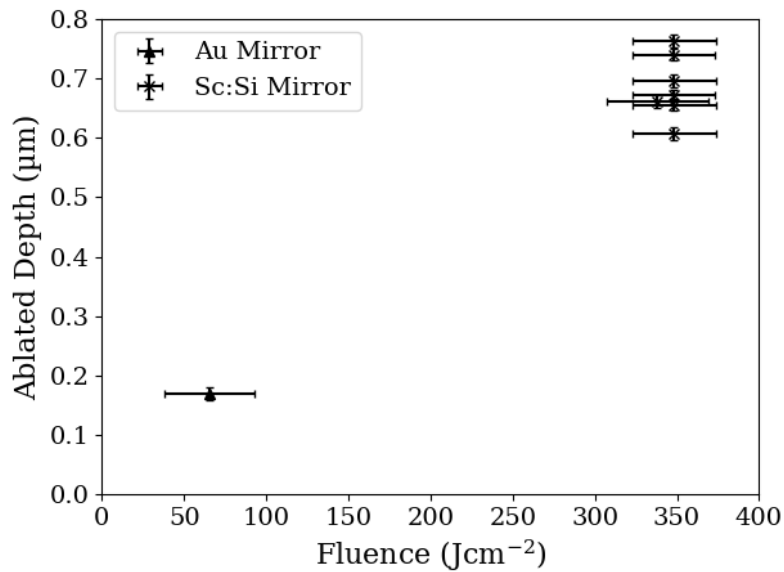


Figure 3.19: The ablation depth as a function of the laser fluence on target for gold.

The ablation depth results are localised to two narrow ranges of fluence corresponding to results obtained for the Sc:Si multilayer and gold mirrors. This is because there is little to no variation in the pulse energies between shots. This is one of the advantages of this laser; the shot-to-shot variation in pulse energy over short timescales is small, whereas the drift in energy over long timescales is more significant. The dataset for each mirror was largely collected in the same ablation run, in as little as a few hundred



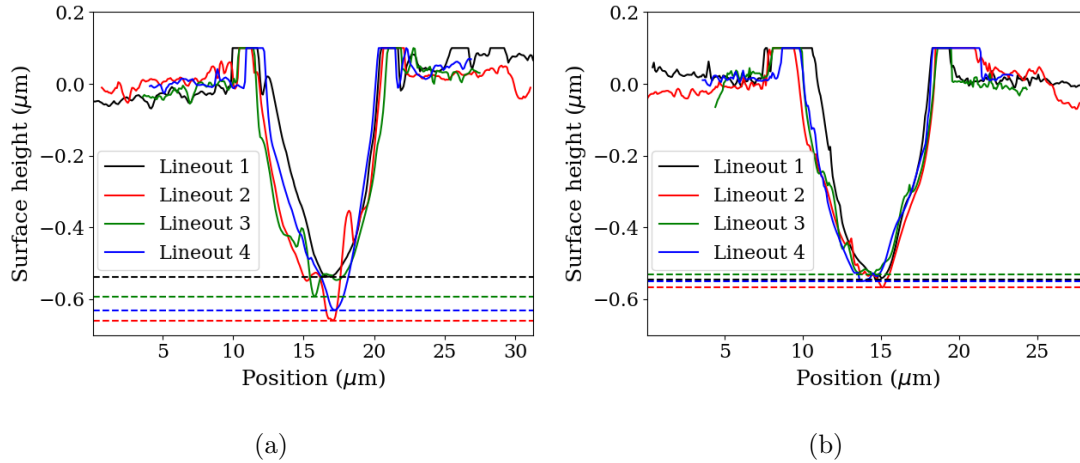


Figure 3.21: (a) An example of high ablation depth variance occurring in copper, compared to (b) a typical ablation depth variation (also copper). The maximum ablation depth is marked for each profile with a dotted horizontal line.

There are some conclusions that can be drawn at this stage. Aluminium, the material with the longest attenuation length, shows the deepest ablation depths, with gold and copper, which have short attenuation lengths, showing much lower ablated depths (roughly half the depth of aluminium). The gold mirror produced fluences in the region of  $5 \text{ J cm}^{-2}$  to  $10 \text{ J cm}^{-2}$  and these were sufficient to ablate all the targets. If there is an ablation threshold at this wavelength, it can be assumed that this threshold is  $\leq 5 \text{ J cm}^{-2}$  for aluminium and copper. Further low fluence data is needed to assert this for gold, however it can be assumed this threshold is  $\leq 12 \text{ J cm}^{-2}$ .

### 3.2.6 Lateral transport

When modelling fluid dynamics the dimensionality of the chosen model can impact the outcome of the simulation. In the case of laser ablation, transport of energy away from the peak intensity (i.e. laterally) can reduce the peak ablation depth achieved, reducing the accuracy of a one-dimensional treatment of ablation propagation into the target. The magnitude of this lateral thermal transport is dependent on the geometry of the plasma volume. The impact of lateral transport can be observed by comparing the shape of the ablation depth profile to the spatial beam profile. In cases where lateral energy transport is high, significant “squaring off” of the Gaussian shape of the crater will be seen – i.e. a spatial profile closer to a top-hat function.

The quantity of lateral transport depends on the geometry of the plasma volume [72]. Plasma volumes with a low aspect ratio, where the beam width  $w$  is much larger

than the depth of laser penetration  $l_a$ , will have the shallowest radial temperature gradients and will therefore see the least lateral transport. Short attenuation length materials, where the laser can only penetrate a few nanometres into the target, will not demonstrate significant lateral transport for this reason. Long attenuation length materials, such as aluminium, are more likely to show signs of lateral transport. However, the width of features seen on aluminium targets is larger than the depth penetrated for all shots, so it is less likely that significant lateral transport will occur.

Verification of the assertion that lateral transport does not significantly affect the ablation depth profiles in the short attenuation length materials can be found by examining example ablation depth profiles. Figure 3.22 shows an ablation depth profile for a shot on a gold target with the highest measured aspect ratio. The ablation crater profile is fitted closely by a Gaussian profile. The ablation profiles on copper targets are fitted similarly well by Gaussian profiles.

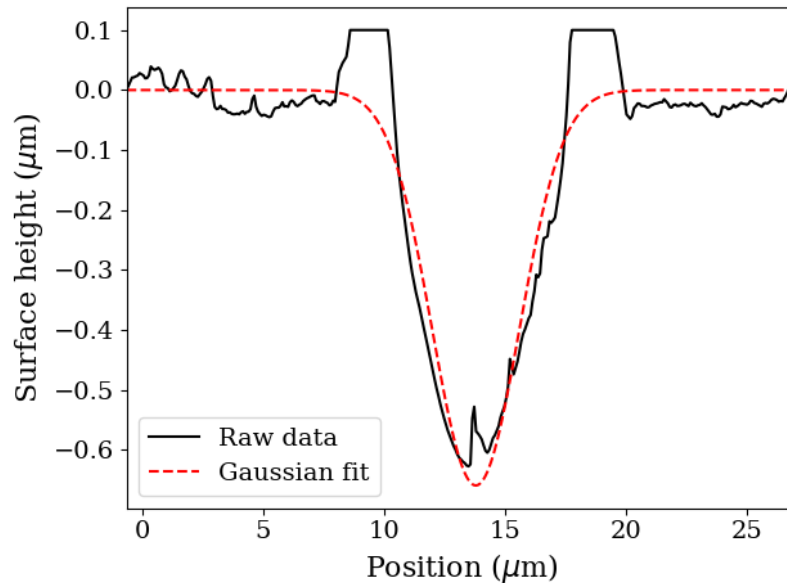


Figure 3.22: The ablation crater profile with the highest aspect ratio on the gold targets (black). Also shown is the corresponding fitted Gaussian profile (red).

Figure 3.23 shows an ablation crater profile for a shot on an aluminium target with the highest measured aspect ratio. The ablation crater profile deviates from Gaussian more than for the gold target, which may be indicative of increased lateral transport. However, this is the worst of the profiles and general fitting of Gaussian profiles is closer. Unfortunately this means there is a possibility of inaccuracies due to neglecting lateral transport in later simulations.

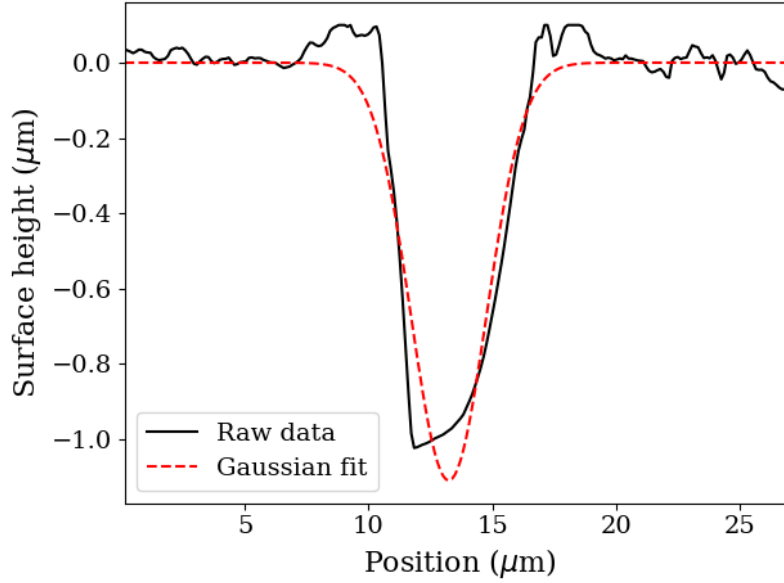


Figure 3.23: The ablation crater profile with the highest aspect ratio on the aluminium targets (black). Also shown is the corresponding fitted Gaussian profile (red).

### 3.3 Simple modelling of target ablation

The parameter range in which these experiments were conducted is unique to capillary laser ablation experiments. Other lasers do not have the same combination of photon energy ( $10^1$  eV) and pulse duration (ns). Developing a simple relation between the incident fluence and subsequent ablated depth therefore represents an interesting challenge.

Simple models of extreme ultra-violet laser ablation have been presented previously [1]. We discuss these models here. A model developed for short pulse optical laser ablation of targets [10] is first discussed, and then a model of ablation developed for X-FEL ablation is examined [73]. We show in this thesis in later chapters that both of the simplified models do not fully explain EUV laser ablation in the regime of the experiments undertaken with 1.2 ns duration pulses and pulse energies in the 10  $\mu$ J to 16  $\mu$ J range focussed to diameters from  $\approx 3 \mu$ m to 9  $\mu$ m.

### 3.3.1 The Gamaly model

A model used to understand the ablation of femtosecond duration optical laser pulses developed by Gamaly *et al* [10] has been adapted to treat ablation of EUV laser pulses [1]. The increase in critical density to above solid density would suggest that the majority of the interaction will occur with the highest density accessible material, i.e. the solid or near-solid density material. This is a similar situation to that seen in femtosecond pulse interactions. The volume accessible to the interaction in this case is limited by the attenuation length of the material. The longer timescale of our nanosecond pulses allows for the contribution of radiative and hydrodynamic processes to the energy distribution. This will be most acute when the energy gradients are steepest, i.e. the attenuation length is short. As a result, it is anticipated this model will compare best to long attenuation length materials such as aluminium – see table 3.2 for attenuation lengths.

The Gamaly model assumes that the laser electric field  $E$  penetrates into the target with an exponential dependence

$$E(x) = E(0) \exp\left(-\frac{x}{l_s}\right) \quad (3.31)$$

where  $l_s$  is the field penetration or ‘skin’ depth, as per the well known skin effect [74]. In this scenario the skin depth  $l_s$  is given by

$$l_s = \frac{c}{\omega n}$$

where  $n$  is the imaginary part of the refractive index  $\mathbf{n}$  and  $\omega$  is the laser frequency. The thermal conduction timescales are longer than the pulse duration, so the electron temperatures can be assumed to follow the same exponential shape as the electric field. The result is that for ablation fluence close to threshold a relation between the ablated depth  $d_{\text{abl}}$  and incident fluence  $F$  is found such that

$$d_{\text{abl}} = \frac{l_s}{2} \ln\left(\frac{F}{F_{\text{th}}}\right) \quad (3.32)$$

where  $l_s$  is the skin depth and  $F_{\text{th}}$  is the ablation threshold fluence.

Although this model was not developed with longer pulses in mind, the environment it describes within the target is somewhat similar to those anticipated in our specific situation. If we assume that photo-ionization dominates the absorption process, the ablation plasma will be significantly cooler and hydrodynamic expansion is reduced during the laser pulse as it is reduced for femtosecond optical laser ablation. Under these

conditions, a similar scenario, where the electron temperature follows an exponential decay into the target, may occur, this time limited by the attenuation length  $l_a$ . This gives us the relation

$$d_{\text{abl}} = l_a \ln \left( \frac{F}{F_{\text{th}}} \right). \quad (3.33)$$

Note that the definitions of  $l_a$  and  $l_s$  allow us to drop the factor of 1/2 used by Gamaly [10]. Due to the presence of photo-ionization, the threshold fluence can be calculated simply by

$$F_{\text{th}} = l_a H_{\text{abl}} = l_a (H_f + H_v) \quad (3.34)$$

where  $H_{\text{abl}}$  is the latent heat of ablation,  $H_f$  is the latent heat of fusion, and  $H_v$  is the latent heat of vaporization. These are material properties, and are tabulated for the three target metals in table 3.2.

| Target    | $l_a$ (nm) | $H_f$ (J cm <sup>-3</sup> ) | $H_v$ (J cm <sup>-3</sup> ) | $H_{\text{abl}}$ (J cm <sup>-3</sup> ) | $F_{\text{th}}$ (J cm <sup>-2</sup> ) |
|-----------|------------|-----------------------------|-----------------------------|--|---------------------------------------|
| Aluminium | 229 [62]   | $1.07 \times 10^3$ [75]     | $2.84 \times 10^4$ [76]     | $2.95 \times 10^4$                     | 0.67                                  |
| Gold      | 7 [62]     | $1.23 \times 10^3$ [76]     | $3.34 \times 10^4$ [77]     | $3.46 \times 10^4$                     | 0.02                                  |
| Copper    | 9 [62]     | $1.86 \times 10^3$ [76]     | $4.23 \times 10^4$ [76]     | $4.42 \times 10^4$                     | 0.04                                  |

Table 3.2: Relevant material properties for the target metals.

In reality, equilibration between electrons and ions and hydrodynamic expansion will occur during the 1.2 ns pulse time of the CDL. As a result, for materials with a short attenuation length where the density and temperature gradients are steeper, the assumptions of the Gamaly model are no longer applicable. This is confirmed when we compare the Gamaly model to the experimental results in figures 3.24, 3.25, and 3.26, where the Gamaly model fits the EUV ablation depths for aluminium to a first approximation because aluminium has a long attenuation length to 46.9 nm EUV light.

This adaptation of the Gamaly model fits the lower fluence values for aluminium well, but does not fit the higher fluence values as closely. At the higher fluences it is likely the plasma is gaining enough heat to deviate from the exponential electron temperature gradient. As expected, the short attenuation lengths of gold and copper result in poor agreement between the observed ablation depths and the Gamaly model. A different modelling approach is needed for these materials.

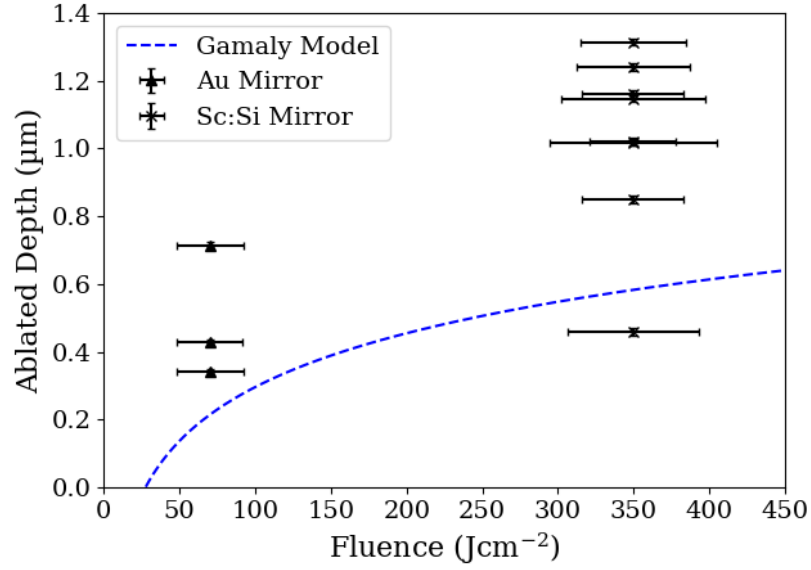


Figure 3.24: Ablation depth as a function of fluence incident on an aluminium target as experimentally measured and as calculated using the Gamaly model [10] with the parameters from table 3.2.

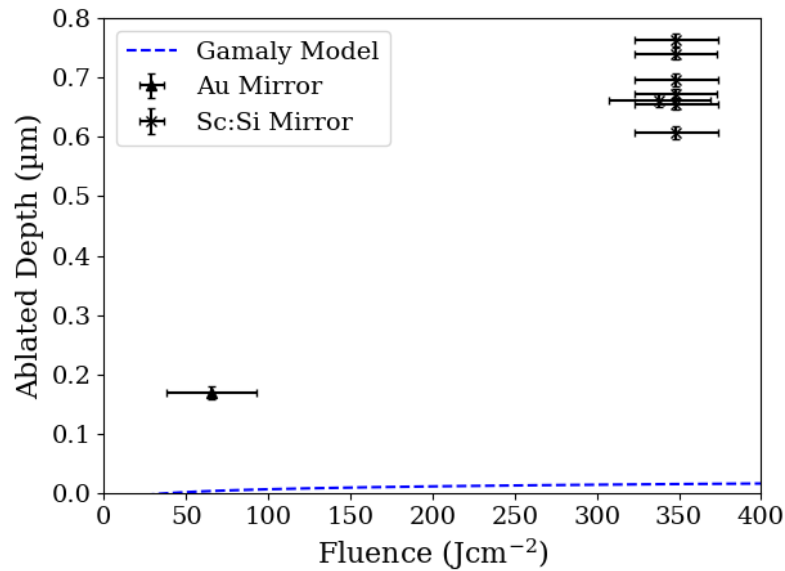


Figure 3.25: Ablation depth as a function of fluence incident on a gold target as experimentally measured and as calculated using the Gamaly model [10] with the parameters from table 3.2.

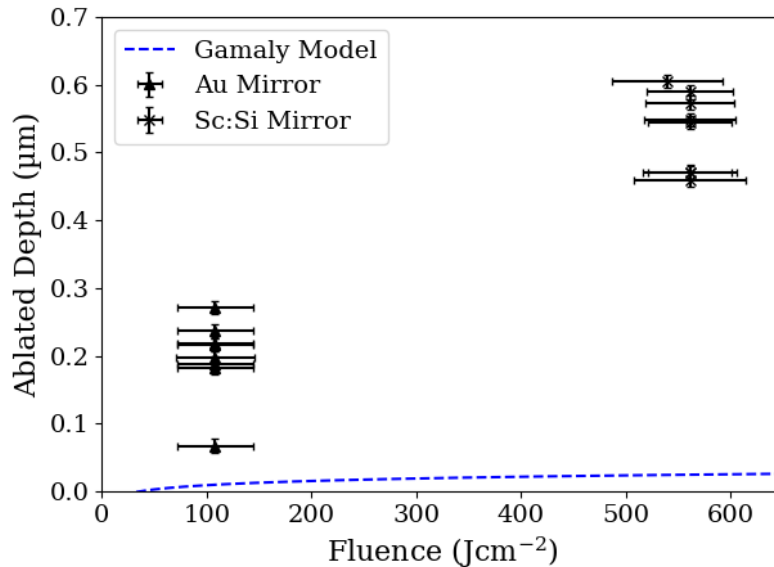


Figure 3.26: Ablation depth as a function of fluence incident on a copper target as experimentally measured and as calculated using the Gamaly model [10] with the parameters from table 3.2.

### 3.3.2 The bleaching wave model

The bleaching wave model is a proposed mechanism for the propagation of deposited laser energy into a plasma during the ablation interaction. It provides a physical explanation for a linear correlation between the incident fluence and the depth of the ablated feature in the target. This model has previously been proposed as a model for XFEL ablation by Tallents *et al* [73] and is inspired by similar propagation of Marshak waves [78, 79, 80] and ionization waves [81, 82].

For short attenuation length materials, the incident radiation penetrates and heats only a thin layer of material. Temperature and density gradients in this thin layer are steep, aiding in the rapid propagation of energy away from the ablation front. This causes heating and expansion of the generated plasma material. As the rate of inverse bremsstrahlung absorption follows temperature and density as  $n_{Z_i} n_e T^{-3/2}$ , this combination of expansion and heating will decrease absorption to the point the plasma becomes transparent to the incident radiation. Given the long pulse duration, 1.2 ns, the temporal evolution of this process is likely to progress as a heating and subsequent bleaching of a series of thin layers of the target of thickness approximately equal to the attenuation length. This could also be considered as a wave of bleached material propagating into the target.

Describing the model mathematically, we first define an energy density  $H_{\text{bl}}$  as the energy required to bleach a unit volume of plasma, i.e. to reduce the absorption to below a given percentage of the initial (cold) absorption such that it becomes negligible in comparison to the absorption of neighbouring volumes. For one dimensional ablation propagation, we simply equate the energy required to bleach a thin layer  $\Delta x$  with the radiation intensity  $I$  arriving in the short time taken to bleach  $\Delta t$ :

$$I\Delta t = H_{\text{bl}}\Delta x. \quad (3.35)$$

This means that the velocity  $v_{\text{bl}}$  of the ‘bleaching’ wave propagating into the target is given by a straightforward re-arrangement

$$v_{\text{bl}} = \frac{\Delta x}{\Delta t} = \frac{I}{H_{\text{bl}}}, \quad (3.36)$$

from which a temporal integration yields a relation between fluence and ablation depth, given by

$$d_{\text{abl}} = \int v_{\text{bl}} dt = \frac{1}{H_{\text{bl}}} \int I dt = \frac{F}{H_{\text{bl}}}. \quad (3.37)$$

This model notably predicts a linear relationship between ablated depth and fluence, and does not predict an ablation threshold.

The key element of this model is the bleaching energy density. Whilst *ab initio* calculations of a theoretical bleaching energy densities can be attempted, and some of these are presented in Chapter 4, the exact ‘bleached’ conditions are variable depending on the material and initial absorption conditions. We have opted instead to adopt an approach where the bleaching energy density is determined empirically by fitting the measured ablation depths with a linear plot and extracting the gradient – see figures 3.27, 3.28, and 3.29. These empirically determined values for bleaching energy density are  $H_{\text{bl}} = 2.08 \times 10^5 \text{ J cm}^{-3}$ ,  $3.89 \times 10^5 \text{ J cm}^{-3}$ , and  $4.78 \times 10^5 \text{ J cm}^{-3}$  for aluminium, gold, and copper respectively.

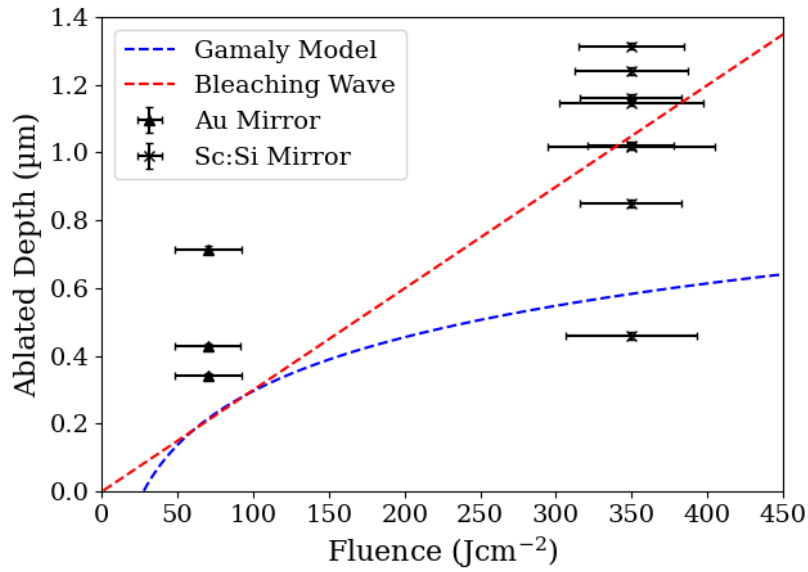


Figure 3.27: Ablation depth as a function of fluence incident on a aluminium target as experimentally measured and as calculated using the Gamaly [10] and bleaching wave [73] models with parameters from table 3.2.

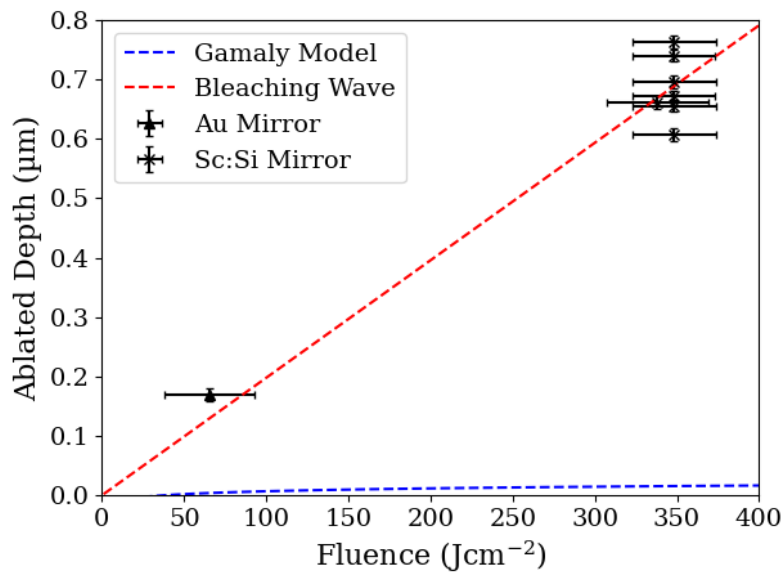


Figure 3.28: Ablation depth as a function of fluence incident on a gold target as experimentally measured and as calculated using the Gamaly [10] and bleaching wave [73] models with parameters from table 3.2.

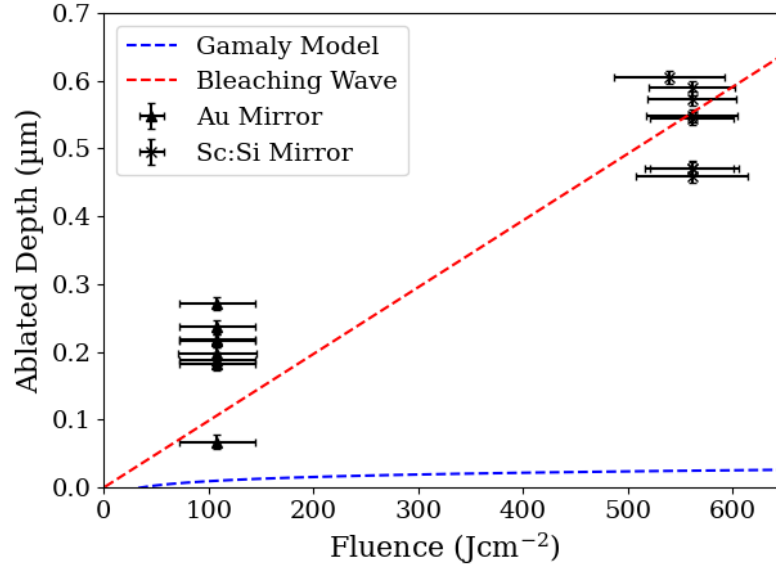


Figure 3.29: Ablation depth as a function of fluence incident on a copper target as experimentally measured and as calculated using the Gamaly [10] and bleaching wave [73] models with parameters from table 3.2.

For the short attenuation length materials the bleaching wave model fits more closely than the Gamaly model, however the plasma conditions it predicts need to be investigated properly. Also, the fit of any function to data that is largely grouped into two points requires further intermediate data points to ensure its accuracy.

### 3.4 Summary and conclusions

In this chapter we have outlined an ablation experiment where aluminium, copper, and gold targets were ablated using a capillary discharge laser emitting radiation at 46.9 nm with a pulse time of 1.2 ns. The pulses were focussed using two spherical mirrors – a scandium-silicon multilayer, and an unprotected gold mirror – with focal lengths of 50 mm to give a range of on-target fluences. The ablation depths were collected by extracting one-dimensional surface profiles and fitting Gaussian curves to post-shot ablation depth profiles measured using an AFM. The focal spot size was determined from the crater areas using the Liu method [66] and was found to be 1.79  $\mu\text{m}$ . This was compared to ray-tracing calculations performed by Wilson [1] that predicted a focal spot size of 2.00  $\mu\text{m}$  for a mirror of the same radius of curvature.

The ablation depths were plotted as a function of the laser fluence, and were found to be grouped in two clusters due to the small variation in pulse energy across multiple

shots. The fluence vs. ablation depth data was then compared against two models; an adapted form of the Gamaly fs-pulse model, and a ‘bleaching wave’ model. The Gamaly model was chosen for its accurate use in femtosecond pulse interactions. Analogies in energy deposition can be drawn between these short pulse interactions and the nanosecond CDL interactions due to the increase in critical density at EUV wavelengths; the absorption is consequently in solid or near-solid density material as a consequence and so the ablation volume is limited by the attenuation length. Ablation depths predicted by this model compared reasonably to the ablation depths for the aluminium targets, with a long attenuation length, but did not compare well to the gold and copper ablation depths, with short attenuation lengths.

The bleaching wave model, by comparison, is a mechanism that aims to account for the small volume over which energy is deposited and the steep temperature gradients that form as a consequence. The mechanism suggests that over the nanosecond timescale the energy deposited in the small volume at the ablation front is sufficient to heat it and drive significant expansion, to the point that absorption is negligible compared to the volume’s initial absorption and the absorption of neighbouring volumes, and the volume is said to be bleached. Over the pulse duration this effect would occur multiple times, creating a wave of bleached material propagating into the target. The bleaching wave model manifests as a linear relationship, which in place of *ab initio* calculations was fitted to the data and the gradient of which yielded a bleaching energy density for each material.

From the comparison of these various results we can draw several conclusions. Firstly, the use of multiple mirrors has generated a range of on-target fluences but the low shot-to-shot variation has meant these are clustered around two points. This means that subsequent models will be easier to fit as they effectively pass through two points. This is a key limitation of any comparison drawn between model and experiment. Secondly, neither of the two relatively simple models predicts the measured ablation depths accurately. The Gamaly model only compares well with long attenuation length materials, and the bleaching wave model needs further investigation to assess the empirical bleaching energy densities and their relation to actual plasma conditions. This was somewhat anticipated by previous analysis of these results [1].

The bleaching wave model compares favourably with the experimental data largely because it was fitted to that experimental data. Proper assessment of its usefulness as an ablation depth prediction tool can only be achieved by analysing the inferred plasma

conditions when the plasma energy content is equal to the empirical bleaching energy densities. In the following chapter, ionization models will be employed to extract key plasma conditions at the predicted bleaching energy density and these can then be cross-referenced against absorption coefficient calculations.

## Chapter 4

# A study of the assumptions behind the bleaching wave model

Ablation depths created by focussed EUV laser light were experimentally measured in Chapter 3 and two simple models of ablation depth as a function of fluence were compared to the experimental ablation depths. The first, the Gamaly model [10], assumes energy deposition in the plasma over the attenuation length of radiation in the solid and so only fits experimental ablation depth data well for aluminium targets which have a long attenuation length (see section 3.3.2). The second, the bleaching wave model, is characterised by the energy density at which the absorption of a small volume of plasma is reduced to a negligible amount in relation to neighbouring volumes. These bleaching energy densities have been empirically derived in Chapter 3 and the exact plasma conditions they correspond to are investigated in this chapter.

This chapter considers the absorption mechanisms in plasma material generated by EUV ablation in greater detail so that the empirically determined bleaching energy densities can be used to identify a well-defined bleached plasma state. Classical forms of the inverse bremsstrahlung (free-free) and photo-ionization (bound-free) absorption coefficients are presented in the form given by Hutchinson [49] using Kramers solution for the Gaunt factor [50, 51]. The critical density for the incident photons is greater than the solid density, so the transmission of any thickness of target plasma material can be determined by considering these two absorption processes alone. As free-free absorption of monochromatic light is dependent on  $n_e^2 Z_i^3$  and bound-free absorption is dependent on  $n_e Z_i^5$  (where  $Z_i$  is the average ion charge), the ionization conditions of the plasma are key to correctly modelling the photon-plasma interactions.

Starting with the Saha-Boltzmann ionization model [41], levels of complexity are

gradually included to account for inaccuracies that arise due to the warm dense plasma conditions generated in laser-plasma interactions at short wavelengths. The Saha-Boltzmann model is implemented in its low- and high-density limits [48], and the effects of ionization potential lowering [83] are considered in each case. Quantum mechanical effects are considered by the use of different Gaunt factors [84]. Degeneracy effects are considered by invoking the high-density limit of the Saha-Boltzmann model, and by applying a direct correction to the absorption coefficients.

## 4.1 Transmission calculations

The bleaching wave model presented in section 3.3.2 yields an empirically determined bleaching energy density for each of the metal targets shown in Chapter 3. In order to contextualise these empirical bleaching energy densities, we must calculate the transmission of a thin layer of target material with internal energy density equal to the bleaching energy density. The calculations start by implementing ionization models to relate plasma energy content to temperature, electron density, and ion populations. The ionization models can then be combined with absorption coefficients to calculate the transmission of an arbitrary thin layer of plasma.

It is possible to make simple temperature-dependent transmission calculations using the light absorption models for photo-ionization and inverse bremsstrahlung and the ionization model discussed in section 4.1.1. Our treatment neglects hydrodynamic expansion. In the EUV wavelength limit there are several factors that allow us to neglect hydrodynamic expansion for an approximate treatment. The reduction in inverse bremsstrahlung absorption due to the higher frequency of radiation compared to optical laser light will result in lower levels of electron heating. The lack of resonance absorption removes the superthermal tail from the electron distribution, further decreasing electron heating. The photo-ionization process at 46.9 nm wavelengths also releases little energy in the form of kinetic energy due to the closeness of the photon energy and ionization energies.

The consequence of the above effects combined is greatly reduced electron temperatures which mean considerably slower expansion speeds. For example, for an electron temperature of 10 eV in aluminium the ion sound speed  $c_s$ , given by

$$c_s = \sqrt{\frac{\gamma Z_i k_B T_e}{m_i}} \quad (4.1)$$

where  $\gamma$  is the adiabatic index, determining the rate of plasma expansion is  $7.7 \times$

$10^3 \text{ m s}^{-1}$ , compared to typically  $10^5 \text{ m s}^{-1}$  for much hotter optical laser-plasmas. Perhaps more importantly, EUV light heats a large depth of solid target with the absorption process occurring near solid density, so the behaviour of expanding plasma material has little effect on ablation depths. For optical laser interactions, absorption occurs at densities at or below the critical density (typically with densities  $10^2$  to  $10^3$  below solid density) and it is much more important to correctly model the plasma expansion.

This treatment assumes that the laser radiation penetration dominates the ablation propagation and that the phase transition from solid to plasma occurs on a negligibly short timescale. The implication of this is that most of the laser pulse energy absorption by the target can be expected to occur in material in a near-solid density gaseous state rather than in the solid state. This has two repercussions; first, that the electrons in the solid conduction band can be treated as occupying discrete quantum states; and second, that the energy content of the material can be calculated using a plasma energy content model, rather than the Fermi-Dirac model – see section 4.1.3.

As the ablation is on the order of microns during the laser pulse, the slower expansion speeds mean that the bulk of the plasma could be considered approximately stationary. Extending this to the whole of the plasma is therefore not as questionable as it would be for optical wavelength ablation. The long pulse time allows the electrons and ions to thermalize, reducing the problem to a single-temperature problem. For example, assuming an electron temperature of 10 eV, solid state density, and an ionization of 1, we can calculate an electron-ion collision frequency for aluminium of  $8.6 \times 10^{-15} \text{ s}^{-1}$ , corresponding to an equilibration time of  $\approx 0.1 \text{ fs}$ .

With the conditions of the calculations now set out, and the expressions required collected above, all that remains is to develop algorithms to allow computer calculation of the transmission across a range of plasma temperatures. The ionization model algorithm is considered first.

#### 4.1.1 Ion population algorithms

As discussed in section 4.1.1, there is a minimum electron density requirement for plasmas to be in LTE, given by the McWhirter criterion. The McWhirter criterion for two quantum states separated by the energy gap  $\Delta E$  is given by equation 2.6. The McWhirter criterion for the minimum electron density for LTE in the transition between the  $\text{Al}^{1+}$  and  $\text{Al}^{2+}$  states at 100 eV is  $n_e = 3.60 \times 10^{18} \text{ cm}^{-3}$ . This is orders of magnitude below the expected electron densities at the highest temperature we

anticipate. Based on this criterion, the Saha-Boltzmann model of ionization has been employed, as derived in section .

The Saha-Boltzmann equation (equation 2.11) gives a population ratio between two arbitrary states with charges  $Z_i$  and  $Z_{i+1}$ . The challenge when applying this to calculations assuming a constant material density is that the ratio  $n_{Z_{i+1}}/n_{Z_i}$  affects the electron density  $n_e$  but is also dependent upon it. This was managed by applying an iterative algorithm. The final result of these calculations is a series of ion population distributions, varying with plasma temperature.

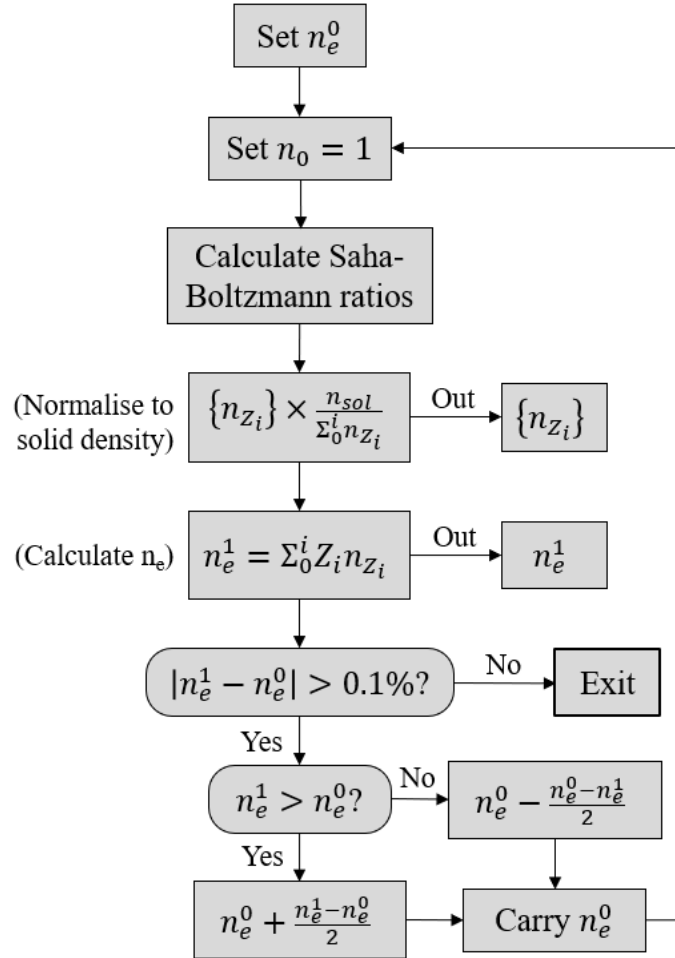


Figure 4.1: A flowchart of the computer algorithm used to calculate the ion populations predicted by the Saha-Boltzmann ratio for a given electron temperature  $T_e$ .

A flowchart of the algorithm for calculating ion populations is shown in figure 4.1. The ion population algorithm starts by assigning a test electron density  $n_e^0$  and a starting density for the neutrals of  $n_0 = 1$ . From there, we use the Saha-Boltzmann ratio (equation 2.11) to generate a full set of populations with respect to  $n_0 = 1$  for the given electron temperature  $T_e$ . We then take the ratio of the solid atom density

$n_{\text{sol}}$  to the sum of the population densities  $\Sigma n_i$  and multiply by the result, giving a set of population densities adding up to  $n_{\text{sol}}$ . These are then used to calculate a predicted electron density  $n_e^1$  associated with the electron temperature  $T_e$  and test electron density  $n_e^0$ .

The algorithm now progresses using a method similar to the bisection method in order to have the test electron density (used to evaluate the Saha-Boltzmann ratios) consistent with the predicted electron density from the Saha-Boltzmann ratios. The absolute difference  $|dn_e|$  between the test electron density  $n_e^0$  and the predicted electron density  $n_e^1$  is calculated, and which of the two values is larger is also assessed. Then, half of the difference  $|dn_e|$  is either added to or subtracted from the test electron density  $n_e^0$ , depending on whether the initial guess was too high or too low, and this is carried forward to the next iteration where the calculation begins again. An exit condition is set which stops the algorithm once the test and predicted values are within a specified tolerance, in this case 0.01%. This method is not the fastest choice but is quite robust. As a precaution, a maximum number of iterations was set as an exit condition for those cases where the algorithm oscillates around the correct value instead of converging.

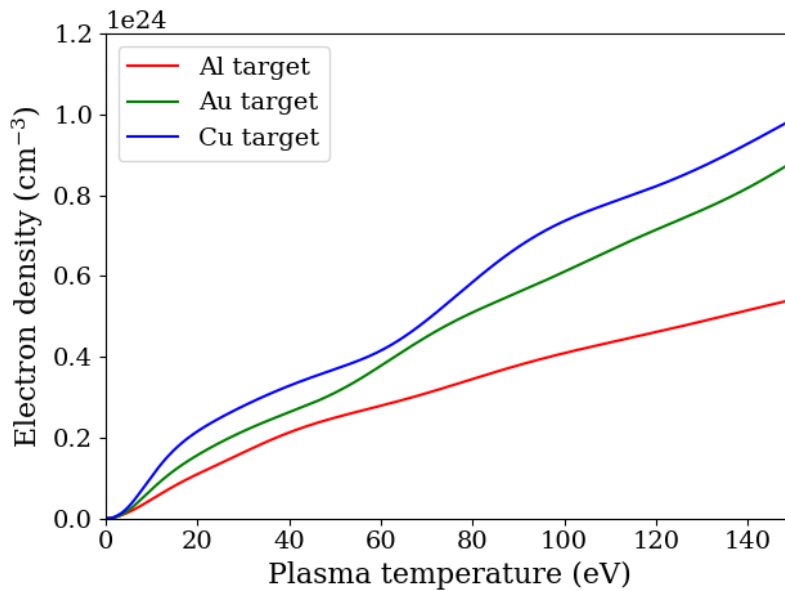


Figure 4.2: Free electron densities as a function of plasma temperature, as predicted by the Saha-Boltzmann ionization model for an aluminium, gold, and copper plasma at solid density.

Figure 4.2 shows the electron densities predicted by the Saha-Boltzmann ionization model as a function of temperature for aluminium, gold, and copper targets with solid material densities. The electron densities calculated in figure 4.2 (and elsewhere) do not include conduction band electrons added to the model as free electrons. At temperatures approaching 0 eV, quasi-free conduction band electrons could add between  $1 \times 10^{23} \text{ cm}^{-3}$  and  $4 \times 10^{23} \text{ cm}^{-3}$  to the assumed initial electron density, depending on the material.

### 4.1.2 Absorption coefficients

Once an ion population distribution was calculated by the algorithm above, the absorption coefficients were calculated. The inverse bremsstrahlung coefficient was calculated using equation 2.27 for each ionization stage and then these values were summed to give the total coefficient. The photo-ionization coefficient was calculated wherever possible using absorption cross-sections from the literature, however the uncommon photon energy emitted by the capillary laser (26.5 eV) means that these had to be either approximations or extrapolations. In the cases of aluminium and copper, the photo-ionization cross-sections of the neutral and 1+ ions at a photon energy of 25 eV have previously been calculated by Reilman and Manson [85] using a summation of Hartree-Slater central-field calculations [86] for each subshell; this was deemed a close enough approximation for our photon energy of 26.5 eV. In the case of gold, the neutral photo-ionization cross-section was extrapolated from calculations made by Ma *et al.* [87] using the Glauber-Lewenstein model [88]. No cross-section could be found for the gold 1+ ion, so equation 2.34 was used to calculate the absorption cross-section instead.

Figures 4.3, 4.4, and 4.5 show the free-free, bound-free, and total absorption coefficients, calculated as a function of plasma temperature, for aluminium, gold, and copper targets respectively. The main features we can take from these figures are as follows. Below a plasma temperature of  $\approx 10 \text{ eV}$  the dominant absorption mechanism is photo-ionization and above a plasma temperature of  $\approx 25 \text{ eV}$  the dominant mechanism is inverse bremsstrahlung absorption. This suggests that photo-ionization will dominate the early stages of laser-plasma interactions at EUV wavelengths, but inverse bremsstrahlung will dominate later once the plasma has been heated to  $\approx 25 \text{ eV}$ .

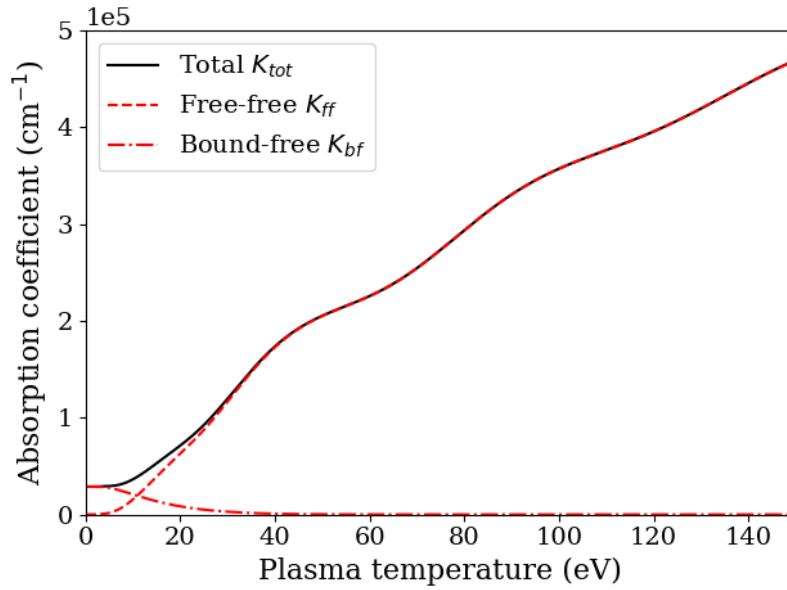


Figure 4.3: Absorption coefficient as a function of plasma temperature with Saha-Boltzmann ionization for an aluminium target at solid density. The dotted curves show the contribution to the total of the free-free and bound-free absorption coefficients.

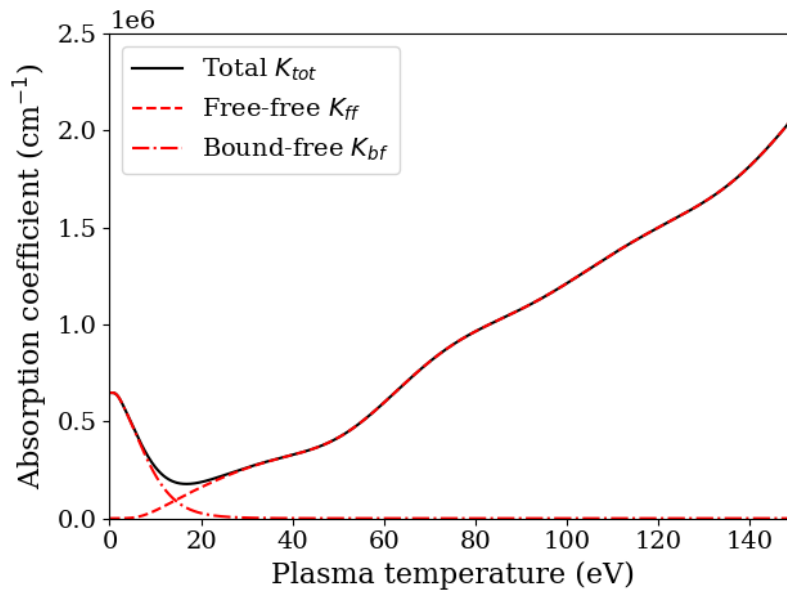


Figure 4.4: Absorption coefficient as a function of plasma temperature with Saha-Boltzmann ionization for a gold target at solid density. The dotted curves show the contribution to the total of the free-free and bound-free absorption coefficients.

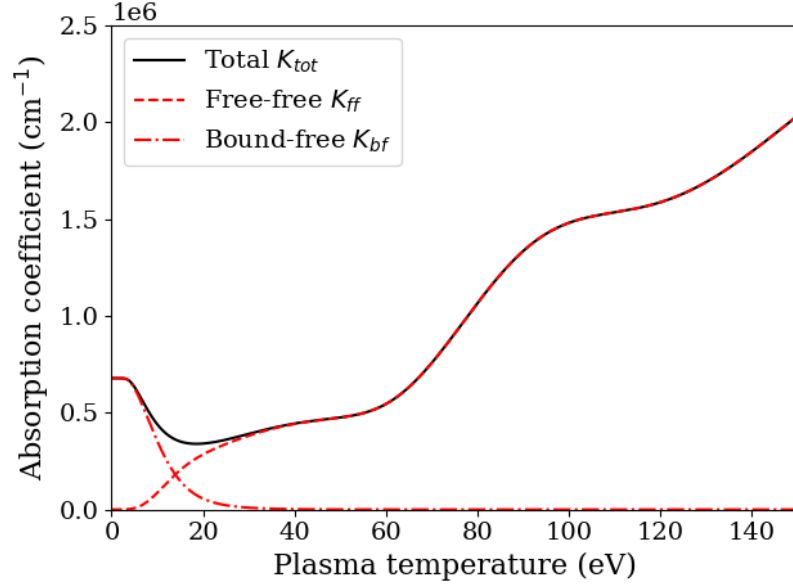


Figure 4.5: Absorption coefficient as a function of plasma temperature with Saha-Boltzmann ionization for a copper target at solid density. The dotted curves show the contribution to the total of the free-free and bound-free absorption coefficients.

### 4.1.3 Energy content

In order to compare to the bleaching wave model, the energy content of the plasma described by the ionization models must be calculated. It can be assumed that thermalization of the electrons and ions occurs (comparatively) instantaneously within their own populations. Given the long timescale, it can also be assumed that the high mobility of the electrons will allow them to thermalize with the ions as well, placing all the charged species at a single temperature. This means that the total energy can be calculated by adding the thermal energy of the electrons and ions together, and then adding the sum of the ionization energies

$$E_{\text{cont}} = \frac{3}{2}n_e k_B T + \sum_{i=0}^i n_i \left( \frac{3}{2}k_B T + E_{\text{ion}} \right). \quad (4.2)$$

This can then be compared against the bleaching energy density taken from the gradient of the fitted bleaching wave model to calculate the bleaching temperature of an arbitrary thin layer of target.

Figure 4.6 shows the energy content of aluminium, gold, and copper as a function of plasma temperature. The empirical bleaching energy densities determined in chapter 3 were  $H_{bl} = 2.08 \times 10^5 \text{ J cm}^{-3}$ ,  $3.89 \times 10^5 \text{ J cm}^{-3}$ , and  $4.78 \times 10^5 \text{ J cm}^{-3}$  for aluminium, gold, and copper respectively. These bleaching energy densities correspond

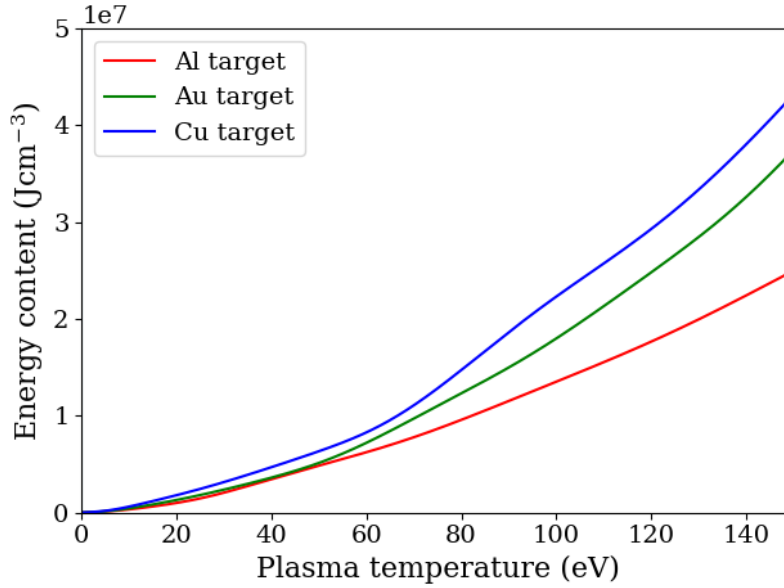


Figure 4.6: Plasma energy content (expressed as a density) as a function of plasma temperature with Saha-Boltzmann ionization for an aluminium, gold, and copper target at solid density.

to the energy content seen at bleaching temperatures of 7.7 eV, 9.5 eV, and 8.7 eV for aluminium, gold and copper respectively.

We can interpret these bleaching temperatures as being the plasma temperature (electrons and ions having equilibrated) at which the energy content of the plasma is equal to the bleaching energy density. This is therefore the temperature at which the absorption of the plasma has reduced such that it is negligible in comparison to the initial or solid absorption, and in the bleaching wave model to the absorption of neighbouring plasma volumes. This is a more convenient metric for the model as all of the plasma parameters calculated here are calculated as functions of temperature, not energy density.

The empirically determined bleaching temperatures are lower than might be anticipated, but fall well within the range at which photo-ionization is dominant. Using the results from figures 4.3, 4.4, and 4.5, we can calculate the transmission for a 10 nm slice of each material to assess the criterion for bleaching. The solid unheated target attenuation length  $l_a$  for gold and copper is approximately 10 nm, while the attenuation length for aluminium is 229 nm. For gold and copper, if the bleaching model applies, we should see a significant change in absorption over 10 nm.

The transmission is given by the Beer-Lambert law [45] (equation 2.14) which predicts a transmission  $T$  of 0.98, 0.78, and 0.65 for 10 nm slices of aluminium, gold,

and copper respectively at their respective predicted bleaching temperatures. Only aluminium shows very low levels of absorption at its bleaching temperature, with the absorbed fraction in gold and copper not dropping below 10% until the plasma has reached 13.8 eV and 16.7 eV respectively. In order to get a full picture, we should examine the transmission as a function of temperature.

The calculations made above of the absorption coefficients as a function of temperature can be converted using the Beer-Lambert law into calculations for the temperature-dependent transmission fraction. For the bleaching model to function as predicted, a well-defined increase in transmission should occur across a short temperature range, so that the arbitrary slice chosen, 10 nm, can be said to have transitioned from semi-opaque to ‘bleached’. Figure 4.7 shows transmission as a function of temperature for 10 nm slices of aluminium, gold, and copper. The plasma temperature range has been abbreviated to the sub-50 eV range as this is the region over which the transmission of the plasma slice changes most.

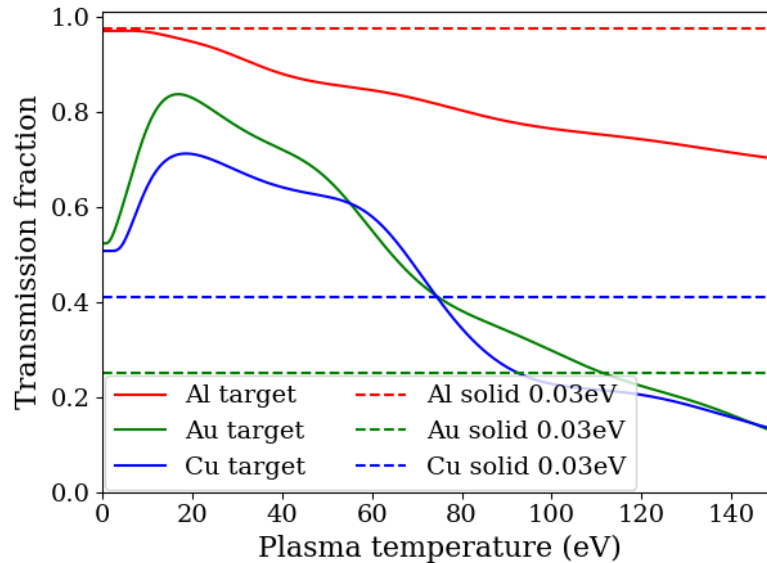


Figure 4.7: Transmission through a 10 nm slice as a function of plasma temperature with Saha-Boltzmann ionization for an aluminium, gold, and copper plasma at solid density. Also shown (dashed lines) are the transmissions of a 10 nm slice of unheated solid material for each element calculated using attenuation lengths from table 3.1.

Figure 4.7 does not show step-function increase in transmission as expected. The strong contribution to the transmission from free-free absorption means that there is a general decrease in transmission with temperature as the ionization and free-free absorption increase. In the sub-20 eV region of the gold and copper transmission curves

there is a transition from low transmission to significantly higher transmission, as predicted by the bleaching wave model, but no clear ‘bleached’ state is reached. The behaviour of the transmission for aluminium further supports the notion that the bleaching wave model does not apply to long attenuation length materials; the transmission of a 10 nm slice only decreases with plasma temperature.

The absolute values of the calculated transmission fractions shown in figure 4.7 agree with tabulated values [3] for solid room temperature materials at temperatures approaching zero for aluminium and copper and are approximately a factor of two lower for solid gold. The transmission calculations suggest absorption coefficient discrepancies for solid gold tabulations and the calculated values of approximately 70%, comparable to warm dense matter absorption coefficient variations determined by different authors (see, for example, figure 4.22). The good agreement for solid aluminium is possibly associated with a simpler band structure compared to solid gold, leading to more accurate extrapolation of the CXRO calculations [3] to our wavelength.

## 4.2 Model corrections

The transmission curves calculated in section 4.1 neglect some effects. The effects of high electron density on both the degree of ionization and the absorption coefficients will now be considered. The ion populations of high density plasmas can be affected by the electron degeneracy of the free quantum states and the effects of ionization potential lowering (IPL), also known as continuum lowering, need to be considered. Degeneracy can also affect the absorption coefficients. This is considered by investigating the accuracy of the Kramers value for the Gaunt factors and the use of Fermi-Dirac statistics in our formulation of the absorption coefficients (instead of Maxwellian statistics).

### 4.2.1 Ion population model corrections

The ion population model plays a key role in the transmission of a plasma as the absorption mechanisms scale with both electron density  $n_e$  and the ionization of the involved ions  $Z_i$  (as absorption coefficients for light vary as  $Z_i^2$  for free-free absorption and  $Z_i^4$  for photo-ionization). The degree of ionization of a plasma also affects the plasma energy content, and so changes the temperatures predicted by a given bleaching energy density. Considered below are two effects; conversion from Maxwellian to Fermi-Dirac statistics by using the high-density limit of the Saha-Boltzmann model, and the effect of ionization potential lowering.

*The high density Saha-Boltzmann model*

The Pauli exclusion principle prevents the occupancy of free-electron quantum states from exceeding their degeneracy limit, and when the electron density is sufficiently high this means the free electrons no longer abide by Maxwellian statistics. In the high-density case, the use of Fermi-Dirac statistics can provide a ratio similar to equation 2.11 that also accounts for the effects of the Pauli exclusion principle.

As with the low-density case, we begin by considering the ionization process of converting a  $Z_i$  ion to a  $Z_{i+1}$  ion. The ionization process releases an electron with energy  $E$  and a  $Z_{i+1}$  quantum state is filled. Fermi-Dirac statistics tells us that a state can only be occupied by one fermion, or it can be unoccupied. In thermodynamic equilibrium, the probability  $P(E)$  of a quantum state with energy  $E$  being occupied is given by the proportionality

$$P(E) \propto \exp\left(\frac{N(\mu - E)}{k_B T}\right) \quad (4.3)$$

where  $N$  is the number of particles occupying the state (either 0 or 1 in the case of fermions), and  $\mu$  is the chemical potential, which is defined as the energy required to add one more particle to the existing ensemble of particles. The average occupancy  $n(E)$  of a state can be determined by the ratio of the occupancy probability to the total probability (i.e.  $P_{occupied}/(P_{occupied} + P_{unoccupied})$ ), like so

$$n(E) = \frac{\exp((\mu - E)/k_B T)}{\exp((\mu - E)/k_B T) + 1} = \frac{1}{1 + \exp(-(\mu - E)/k_B T)}. \quad (4.4)$$

The equation for the average occupancy of a quantum state can then be applied to the  $Z_i$  ion state and the ionized electron to write a ratio in the same form as equation 2.8

$$\frac{f_{FD}(E)dE}{N_{Z_i}} = \frac{g_{Z_{i+1}}g(E)dE/N_{Z_{i+1}}}{g_{Z_i}} \frac{\exp[-(\mu + E_{ion})/k_B T] + 1}{\exp[-(\mu - E)/k_B T] + 1} P \quad (4.5)$$

where  $f_{FD}(E)dE$  is the density of electrons with energies from  $E$  to  $E + dE$ ,  $g(E)dE$  is the density of quantum states between  $E$  and  $E + dE$ , and  $P$  is the probability of the  $Z_{i+1}$  ion existing. The  $g(E)dE/N_{Z_{i+1}}$  term is the density of  $Z_{i+1}$  quantum states in the volume of a single  $Z_{i+1}$  ion. Note that the definition of ionization energy is negative with respect to the free electron energies, hence the opposing signs in the exponents of equation 4.5.

At this stage, it is useful to consider the chemical potential  $\mu$ . The physical definition of the chemical potential  $\mu$  is the energy required to add one more electron to the ensemble of electrons. Mathematically, we define this in terms of the total free electron

density  $n_e$ . The quantity  $n_e$  is evaluated by integrating the density of electrons between  $E$  and  $E + dE$ ,  $f_{\text{FD}}(E)dE$ , over all electrons. This integration takes the form

$$n_e = \int_0^{\infty} f_{\text{FD}}(E)dE = \frac{4}{\sqrt{\pi}} \left( \frac{2\pi m_e k_B T}{h^2} \right)^{3/2} I_{1/2}(\mu/k_B T) \quad (4.6)$$

where  $I_m(\eta)$  is the Fermi-Dirac integral of order  $m$ , given by

$$I_m(\eta) = \int_0^{\infty} \frac{x^m dx}{\exp(x - \eta) + 1}.$$

The use of  $\eta$  to represent  $\mu/k_B T$  is common, and  $\eta$  is consequently referred to as the reduced chemical potential.

Returning to equation 4.5, we integrate both sides to find a relation for all electrons, obtaining

$$\frac{n_e}{N_{Z_i}} = \frac{1}{N_{Z_{i+1}}} \frac{g_{Z_{i+1}}}{g_{Z_i}} \frac{4}{\sqrt{\pi}} \left( \frac{2\pi m_e k_B T}{h^2} \right)^{3/2} \left[ \exp\left(-\frac{\mu + E_{\text{ion}}}{k_B T}\right) + 1 \right] I_{1/2}(\eta) P \quad (4.7)$$

provided the probability  $P$  is independent of free-electron energy  $E$ . Using the definition of chemical potential in equation 4.6, equation 4.7 can be simplified to

$$\frac{N_{Z_{i+1}}}{N_{Z_i}} = \frac{g_{Z_{i+1}}}{g_{Z_i}} \left[ \exp\left(-\frac{\mu + E_{\text{ion}}}{k_B T}\right) + 1 \right] P. \quad (4.8)$$

All that remains is to determine the form of the probability  $P$  of a  $Z_{i+1}$  ion existing.

The existence of a  $Z_{i+1}$  ion depends on the number of occupied  $Z_i$  ion states. For example, if the  $Z_i$  states are all occupied then no electrons have been released from which we can infer that there are no  $Z_{i+1}$  ions. So, the probability for the  $Z_{i+1}$  state is simply

$$P(Z_{i+1}) = 1 - P(Z_i) = 1 - \frac{1}{\exp\left(-\frac{\mu + E_{\text{ion}}}{k_B T}\right) + 1}. \quad (4.9)$$

$P$  is also known as a ‘blocking factor’. Substituting this into equation 4.8 yields a Saha-Boltzmann ratio of populations for high density plasmas

$$\frac{N_{Z_{i+1}}}{N_{Z_i}} = \frac{g_{Z_{i+1}}}{g_{Z_i}} \exp\left(-\frac{E_{\text{ion}}}{k_B T}\right) \exp\left(-\frac{\mu}{k_B T}\right). \quad (4.10)$$

Using the high-density Saha-Boltzmann equation (equation 4.10) in the algorithm detailed in section 4.1.1 adds an additional layer of complexity as the relationship between the reduced chemical potential  $\eta = \mu/k_B T$  and the electron density  $n_e$  is also dependent on the electron temperature  $T_e$ . The solution to this was to calculate in advance an array of values  $I_{1/2}(\eta)$ , calculated numerically using the trapezium method, for a wide range of  $\eta$  values. Equation 4.6 was rearranged into the form

$$I_{1/2}(\eta) = \frac{\sqrt{\pi}}{4} n_e \left( \frac{h^2}{2\pi m_e k_B T} \right)^{3/2} \quad (4.11)$$

and calculated for the conditions predicted by the test electron density  $n_e^0$  and the electron temperature  $T_e$ . The calculated value for  $I_{1/2}(\eta)$  was then compared against the list of  $I_{1/2}(\eta)$  values pre-calculated from a range of arbitrary  $\eta$  values and the closest value of  $\eta$  was used in the high-density Saha-Boltzmann ratio calculations. This introduces a minimum absolute error of 0.1 to the reduced chemical potential  $\eta$  but is simple and quick.

Figure 4.8 shows the electron density as a function of temperature for the low- and high-density Saha-Boltzmann ionization model and for aluminium, gold, and copper targets. Even at solid ion density, there is very little difference between the low- and high-density Saha Boltzmann models in electron density prediction. The mean percentage differences between the low- and high-density models are 3%, 4%, and 6% for aluminium, gold, and copper respectively. Some differences may occur in the relative populations of the ions that contribute to the overall electron density, but the similarity is sufficiently close to use the low-density limit in further calculations.

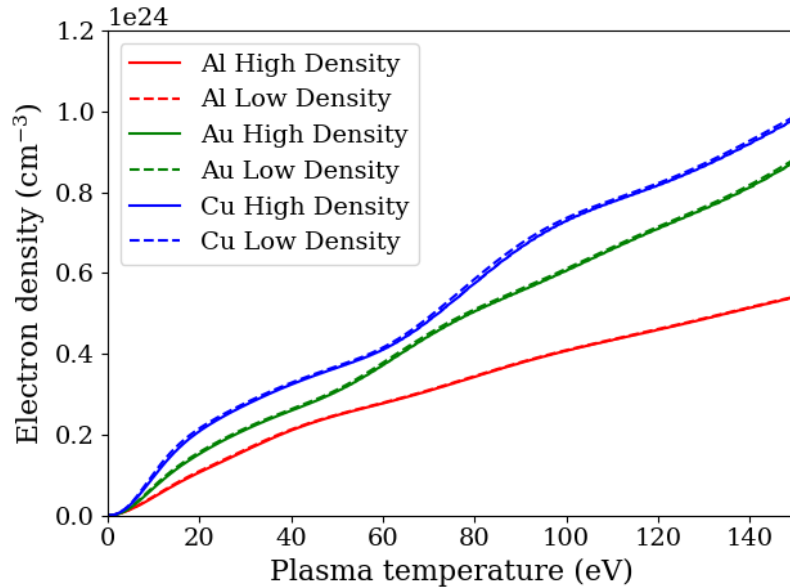


Figure 4.8: Electron density as a function of plasma temperature, as predicted by the high- and low-density forms of the Saha-Boltzmann ionization model, for an aluminium, gold, and copper target at solid density.

The reduction in electron density shown in figure 4.8 would result in reduced free-free absorption but increased bound-free absorption (due to the increased number of neutrals and 1+ ions), further smoothing the transition between the bleached and unbleached regions and shifting it to slightly higher temperatures.

*Ionization potential lowering*

Ionization potential lowering (IPL) is a bulk effect that occurs in all plasmas but is more pronounced in high density plasmas. The ionization potential of an ion in the plasma is perturbed by the free electrons, other ions, and to a small degree even neutral atoms. The combined effect of these perturbations is to lower the ionization potentials of the ion in question and therefore reduce the ionization energies of said ion. The most widely-used formulation of this effect is that of Stewart and Pyatt [83] which is, in essence, a form of the Thomas-Fermi ionization model extended to include neighbouring ions (and neglecting contributions from the neutrals).

An approximate result of the Stewart & Pyatt model can be expressed as a correction to the ionization energy, given by

$$\frac{\Delta E_{\text{ion}}}{E_{\text{ion}}} = \frac{a_0}{Z_i + 1} \left( \frac{2}{a_C} \right) \quad (4.12)$$

where  $a_0$  is the Bohr radius. The term  $a_C$  is distance given by the larger of the Debye length  $\lambda_D$ , given by

$$\lambda_D = \sqrt{\frac{\epsilon_0 k_B T}{n_e e^2}}, \quad (4.13)$$

and the ion sphere radius  $r_0$ , given by

$$\frac{4\pi}{3} r_0^3 = \frac{1}{n_i}. \quad (4.14)$$

The  $a_C$  term is chosen to satisfy the correspondence principle so that the principles of Debye shielding and quasi-neutrality are preserved.

Other formulations of this effect have been developed, perhaps the most notable being that of Ecker & Kröll [89]. More recent investigations have been made [90, 91, 92], but a general consensus has yet to be reached. The Stewart & Pyatt model has historically shown good agreement with laser-plasma experiments and this is why it was chosen for this work.

A notable effect of the IPL is that new photo-ionization transitions become available to the incident photons. The reduction in the ionization energy of the 2+ state below the photon energy of 26.5 eV means photo-ionization of this state can occur. Cross-sections for this transition do not exist in the literature, however we can calculate these using the equation for the photo-ionization cross-section (equation 2.34).

Figure 4.9 shows the electron densities predicted by the Saha-Boltzmann ionization model both with and without ionization potential lowering (IPL) for aluminium, gold, and copper targets. The impact on the predicted electron densities is much larger

here than it was for the high-density Saha-Boltzmann model. The mean percentage differences between the ionization models with and without IPL are 50%, 85%, and 81% for aluminium, gold, and copper respectively.

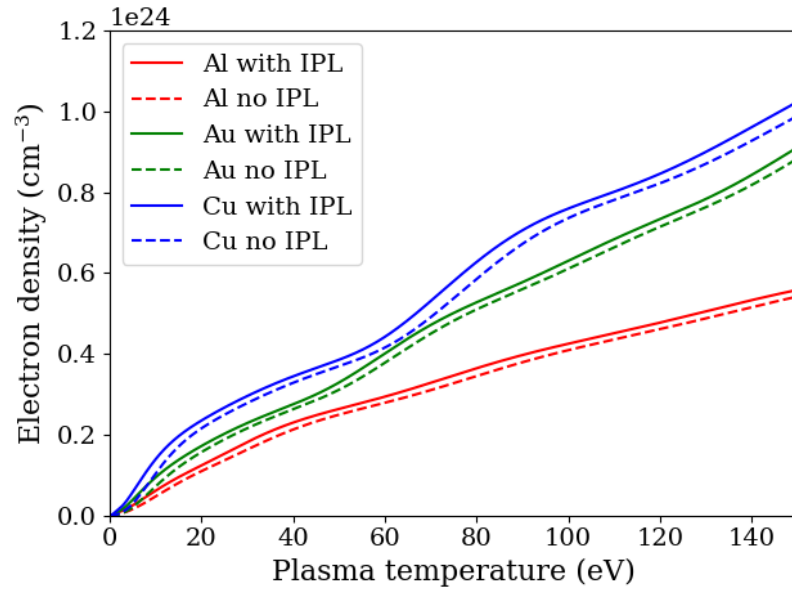


Figure 4.9: Free electron density as a function of plasma temperature, as predicted by the Saha-Boltzmann ionization model with and without ionization potential lowering (IPL), for an aluminium, gold, and copper target at solid density.

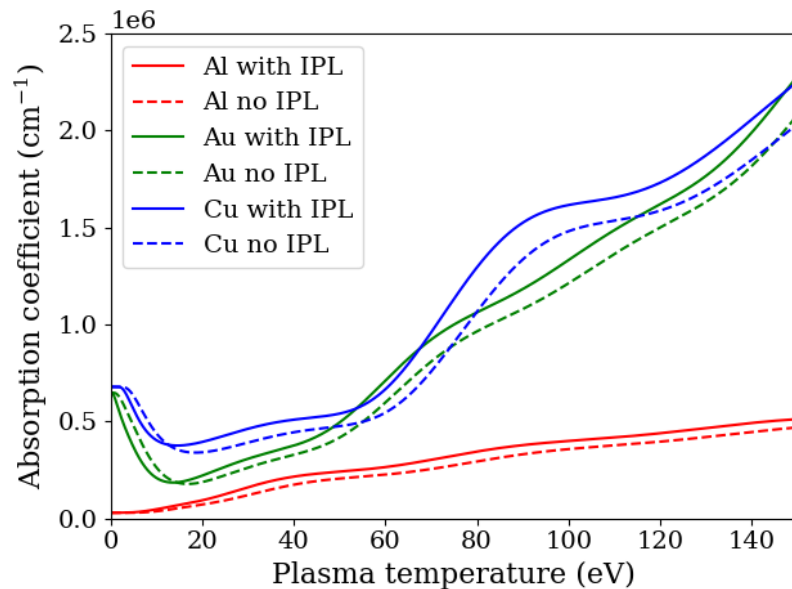


Figure 4.10: Total absorption coefficient as a function of plasma temperature, as predicted by the Saha-Boltzmann ionization model with and without ionization potential lowering (IPL), for an aluminium, gold, and copper target at solid density.

Having had such a significant impact on the electron density, calculations including IPL were also made for the absorption coefficients and energy content – see figures 4.10 and 4.11. It is interesting to note that the effect on the absorption coefficient for gold and copper is a reduction in the photo-ionization dominant region and an increase in the inverse-bremsstrahlung dominant region.

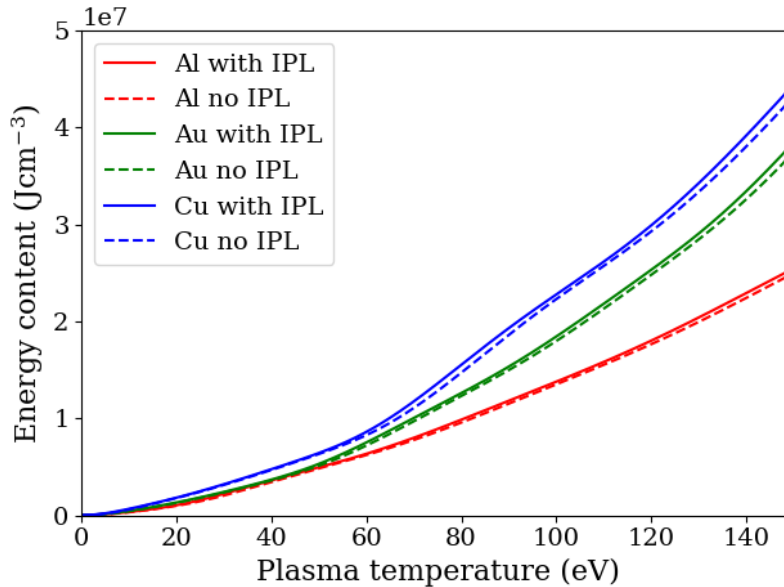


Figure 4.11: Plasma energy content as a function of plasma temperature, as predicted by the Saha-Boltzmann ionization model with and without ionization potential lowering (IPL), for an aluminium, gold, and copper target at solid density.

Once again, the energy content values were compared against the empirical bleaching energy density values of  $H_{bl} = 2.08 \times 10^5 \text{ J cm}^{-3}$ ,  $3.89 \times 10^5 \text{ J cm}^{-3}$ , and  $4.78 \times 10^5 \text{ J cm}^{-3}$ . Including the effects of continuum lowering, the bleaching temperatures reduce to 7.2 eV, 8.9 eV, and 8.1 eV for aluminium, gold, and copper respectively, with transmission fractions of 0.98, 0.84, and 0.72 for 10 nm slices of target.

Figure 4.12 shows the transmission fraction, with and without IPL, as a function of plasma temperature for aluminium, gold, and copper. The transition region between the low transmission region and high transmission region has shifted, but the overall shape of the curve has not changed. Again, we see no clear ‘bleached’ state being reached at higher temperatures.

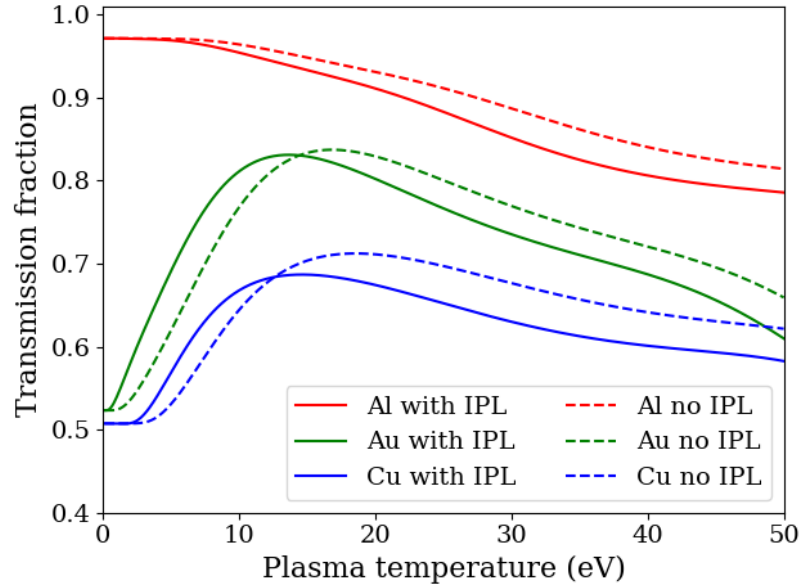


Figure 4.12: Transmission through a 10 nm slice as a function of plasma temperature, as predicted by the Saha-Boltzmann ionization model with and without ionization potential lowering (IPL), for an aluminium, gold, and copper target at solid density.

#### 4.2.2 Absorption coefficient corrections

Calculating the transmission of a given slice will also be affected by any adjustments that can be made to the absorption coefficient. We discuss below two significant ways in which the expressions for the absorption coefficients can be adjusted to account for high-density and further quantum-mechanical effects.

##### *Gaunt factors*

Equation 2.27 includes a quantity known as the Maxwell-averaged Gaunt factor  $\langle G_{ff} \rangle$  for free-free absorption. Until now, we have used the Kramers value for this parameter of  $\langle G_{ff} \rangle \approx 1$ . We can improve upon the accuracy of our free-free absorption coefficient values by using more accurate approximations of the Gaunt factor. This is also true of the bound-free absorption coefficient but only in the cases when we must calculate the photo-ionization cross-section rather than using a cross-section taken from the literature. This occurs only in the ionization of the 1+ gold ion and in the ionization of 2+ ions predicted by the ionization potential lowering model.

Karzas & Latter [84] have made non-relativistic calculations of the Maxwell-averaged Gaunt factor for free-free absorption  $\bar{g}_{ff}$  in the presence of hydrogen-like ions ( $\bar{g}_{ff} \equiv \langle G_{ff} \rangle$ , our notation has been changed here to match that of Karzas & Latter). These

are shown in figure 4.13 plotted as a function of the dimensionless quantity  $\gamma^2$ . The Gaunt factor  $\bar{g}_{ff}$  is in fact dependent on two dimensionless parameters,  $\gamma^2$  and  $u$ , which are given by

$$\gamma^2 = \frac{Z_i^2 R_y}{k_B T} \quad \text{and} \quad u = \frac{\hbar\omega}{k_B T}$$

respectively.

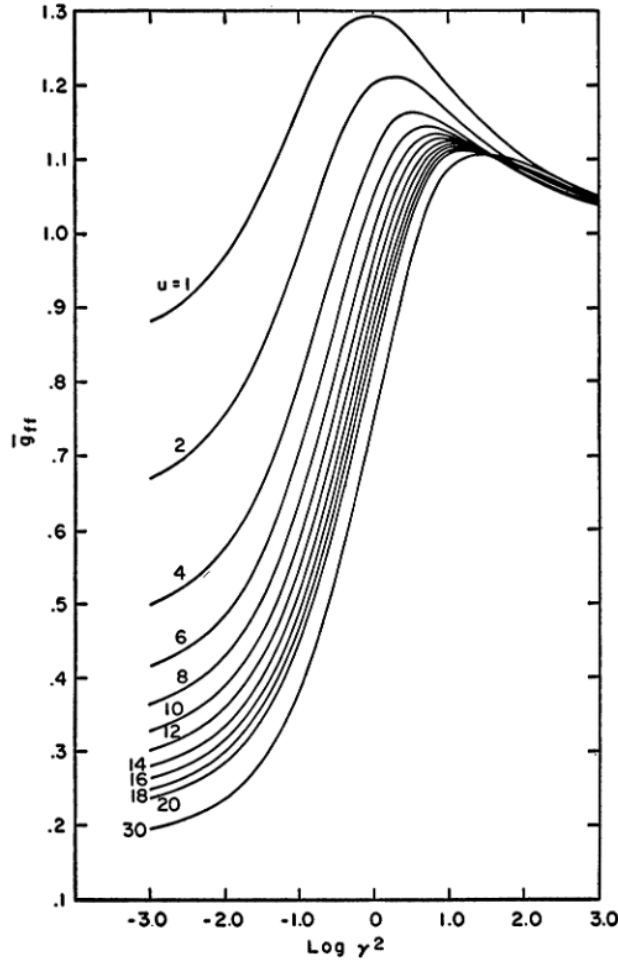


Figure 4.13: Maxwell-averaged free-free Gaunt factors as a function of the dimensionless parameter  $\gamma^2 = Z_i^2 R_y / k_B T$  for a range of values of  $u$  where  $u = \hbar\omega / k_B T$  [84].

Using the ion population algorithm detailed above, one can produce temperature-dependent calculations of  $\gamma^2$  and  $u$ , which can be used to estimate a temperature dependence for the Gaunt factor  $\bar{g}_{ff}$ . Using linear interpolation at selected values of plasma temperature, a curve has been produced for each of the three metals, using the Saha-Boltzmann ionization model both with and without IPL, that relates the Maxwell-averaged Gaunt factor  $\bar{g}_{ff}$  to the plasma temperature – see figure 4.14. The curves for gold and copper are so similar that at this resolution they are difficult to

distinguish in figure 4.14.

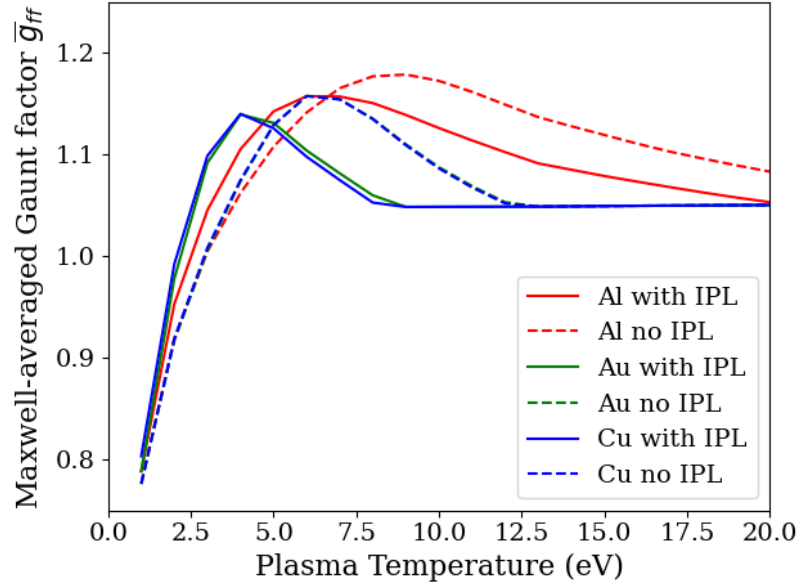


Figure 4.14: Maxwell-averaged free-free Gaunt factor  $\bar{g}_{ff}$  as a function of plasma temperature, for conditions predicted by the Saha-Boltzmann ionization model with and without ionization potential lowering (IPL), for an aluminium, gold, and copper, target at solid density.

We can see quite clearly from figure 4.14 that the Gaunt factor  $\bar{g}_{ff}$  tends to the Kramers value ( $\bar{g}_{ff} = 1$ ) for our wavelength and ionization conditions at temperatures above  $\approx 15$  eV. At temperatures lower than  $\approx 5$  eV we see deviation from  $\bar{g}_{ff} = 1$  of, at most, 15% to 20%. The impact of applying a correction of this magnitude to a region in which the free-free absorption is contributing very little to the total absorption coefficient would be negligible on our transmission calculations. It seems reasonable, therefore, to continue to treat the Kramers value as a suitable approximation.

Calculating the Maxwell-averaged bound-free Gaunt factor  $\bar{g}_{bf}$  (again,  $\bar{g}_{bf} \equiv \langle G_{bf} \rangle$ ) is more challenging, as the results are dependent on the structure of the ion nucleus, the principal and orbital quantum numbers  $n$  and  $l$ , the incident electron energy, and the photon energy. Rather than extend this work to include this large topic, we consider the level-averaged bound-free Gaunt factors  $G_{bf}$  as calculated by Karzas & Latter, shown in figure 4.15 as a function of incident electron energy for  $n = 1 - 15$ , and conclude that overall these corrections are small enough to be neglected ( $\leq 10\%$ ).

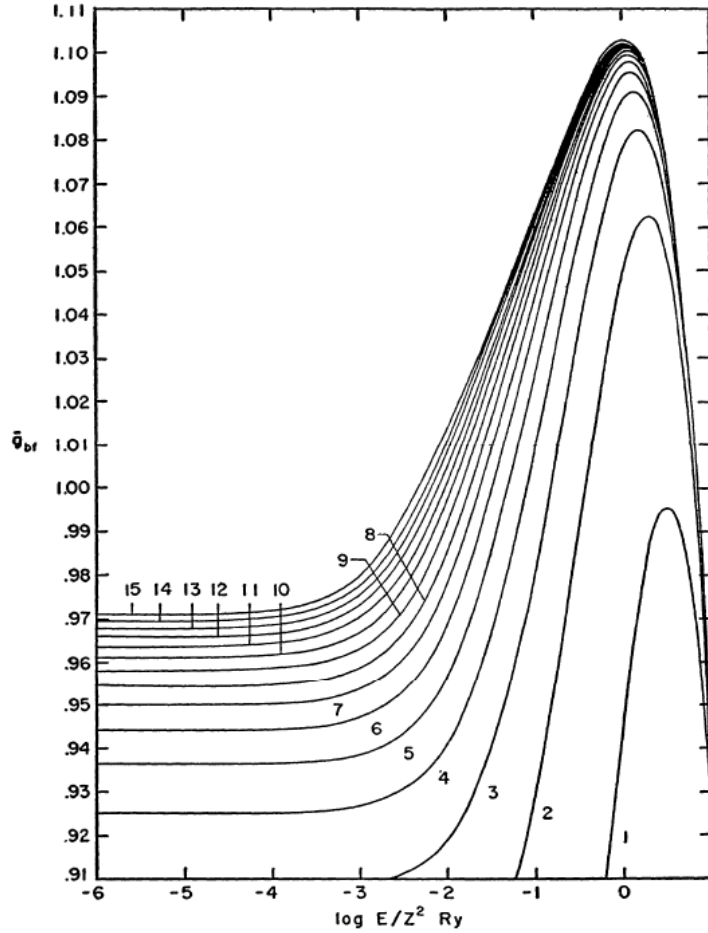


Figure 4.15: Level-averaged bound-free gaunt factors  $\bar{g}_{bf}$  as a function of  $E/Z^2 R_y$  where  $E$  is the incident electron energy.  $\bar{g}_{bf}$  is shown for a range of principle quantum number  $n$  values.

#### *Degeneracy corrections*

The equations formulated above for free-free and bound-free absorption, equations 2.27 and 2.33, are classical formulations valid for Maxwellian plasmas. We have seen above how the high density of laser-produced plasmas affects the Saha-Boltzmann ionization model, now we consider the effect it has on the absorption coefficients.

We begin with the free-free absorption coefficient. Equation 2.27 takes the power radiated by a single electron (equation 2.23) and integrates this over the Maxwellian velocity distribution to account for all the contributing electrons. If, however, the electron distribution is non-Maxwellian due to the high electron density, the Pauli exclusion principle will reduce the number of electrons contributing to the bremsstrahlung emission. In this case, we must use the Fermi-Dirac distribution to describe the electrons instead of the Maxwell-Boltzmann distribution. There are two possible approaches to

making this change; one can go back to equation 2.23, or one can apply a corrective factor to equation 2.27. The latter option is presented here.

The correction we must make to the bremsstrahlung emission coefficient will remove its Maxwellian integration and replace it with a Fermi-Dirac integration. The correction to the bremsstrahlung emission coefficient therefore takes the form

$$\varepsilon_{ff}^* = \varepsilon_{ff} \frac{\int_{\hbar\omega}^{\infty} E^{-1/2} f_{FD}(E) dE}{\int_{\hbar\omega}^{\infty} E^{-1/2} f_E(E) dE} P(E - \hbar\omega) \quad (4.15)$$

where  $P(E - \hbar\omega)$  is the blocking factor as given by equation 4.9. The Fermi-Dirac distribution of energies is given by

$$f_{FD}(E) dE = \frac{4}{\sqrt{\pi}} \left( \frac{2\pi m_e}{h^2} \right)^{3/2} E^{1/2} \frac{dE}{\exp\left(-\frac{\mu-E}{k_B T}\right) + 1}. \quad (4.16)$$

The Maxwell-Boltzmann distribution of energies is given by

$$f_E(E) dE = n_e \frac{2}{\sqrt{\pi}} \left( \frac{1}{k_B T} \right)^{3/2} E^{1/2} \exp\left(-\frac{E}{k_B T}\right) dE. \quad (4.17)$$

At this stage we introduce three dimensionless parameters to simplify this correction;  $x = E/k_B T$ ,  $\eta = \mu/k_B T$  (as before) and  $\beta = \hbar\omega/k_B T$ . This simplifies our correction to

$$\frac{\varepsilon_{ff}^*}{\varepsilon_{ff}} = \frac{2}{n_e} \left( \frac{2\pi m_e k_B T}{h^2} \right)^{\frac{3}{2}} e^{\beta} \int_{\beta}^{\infty} \frac{1}{1 + \exp(-\eta + x)} \left( 1 - \frac{1}{\exp(-\eta + x - \beta) + 1} \right) dx. \quad (4.18)$$

Equation 4.6 can now be substituted in for the electron density  $n_e$ , and we can apply the approximation  $I_{1/2}(\eta) \approx (\sqrt{\pi}/2) \exp(\eta)$  to yield a final correction

$$\frac{\varepsilon_{ff}^*}{\varepsilon_{ff}} = \frac{K_{ff}^*}{K_{ff}} = \exp(-\eta + \beta) \int_{\beta}^{\infty} \frac{1}{1 + \exp(-\eta + x)} \left( 1 - \frac{1}{\exp(-\eta + x - \beta) + 1} \right) dx. \quad (4.19)$$

As the free-free absorption coefficient correction requires a calculation of the chemical potential, the high-density limit of the Saha-Boltzmann ionization model has been used in our temperature-dependent calculations. Figure 4.16 shows the effect of the degeneracy correction on the free-free absorption coefficient as a function of plasma temperature for aluminium, gold, and copper. There is a mean percentage reduction in the free-free absorption coefficient of 7%, 10%, and 12% for aluminium, gold, and copper respectively. We can see from the percentage deviations that the degeneracy effects are limited at our electron densities, as we saw with the difference between the low- and high-density Saha-Boltzmann ionization models above.

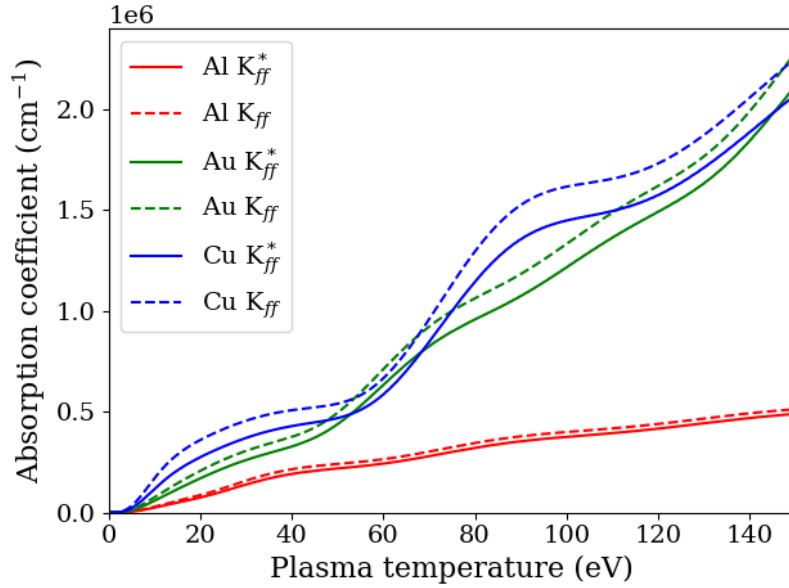


Figure 4.16: Free-free absorption coefficient as a function of plasma temperature, as predicted by absorption coefficients both with (solid lines) and without (dashed lines) our degeneracy correction, for an aluminium, gold, and copper target at solid density.

A degeneracy correction can also be applied to the photo-ionization cross section. Earlier, we used the blocking factor (equation 4.9) to calculate the probability of a  $Z_{i+1}$  state being occupied. A similar correction can be applied to the photo-ionization cross-section, as photo-ionization can only occur if there is a state free for the electron to be released into. The photo-ionization cross-section correction is given by  $P(\hbar\omega - E_{\text{ion}})$ , and has the form

$$\frac{\sigma_{bf}^*}{\sigma_{bf}} = 1 - \frac{1}{\exp(-\eta + \beta - x_{\text{ion}}) + 1} \quad (4.20)$$

where  $x_{\text{ion}} = E_{\text{ion}}/k_B T$  is the reduced ionization energy.

As with the free-free absorption coefficient, we have made temperature-dependent calculations of the bound-free absorption coefficient, shown in figure 4.17 as a function of plasma temperature for aluminium, gold, and copper. The degeneracy correction for the bound-free absorption process has little effect on the absorption coefficient. For aluminium the difference between the degenerate and non-degenerate curves is imperceptible.

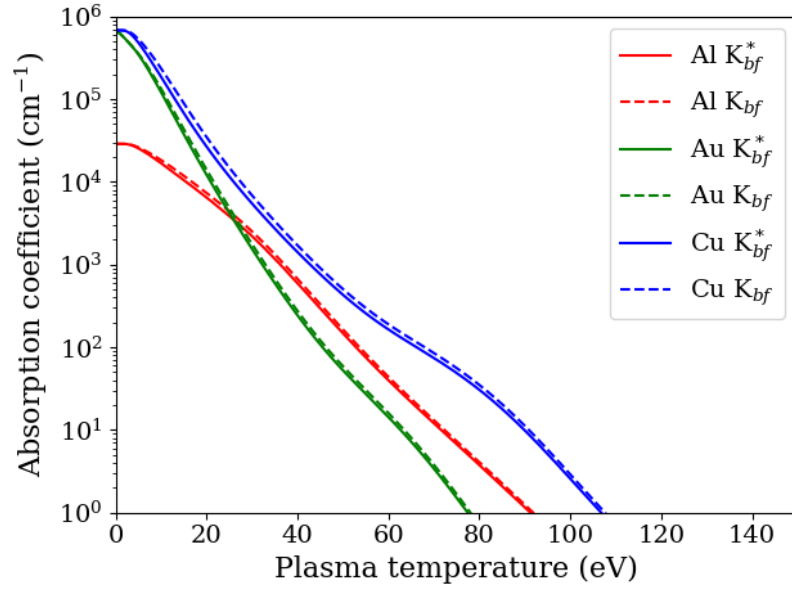


Figure 4.17: Bound-free absorption coefficient as a function of plasma temperature, as predicted by absorption coefficients both with (solid lines) and without (dashed lines) our degeneracy correction, for an aluminium, gold, and copper target at solid density.

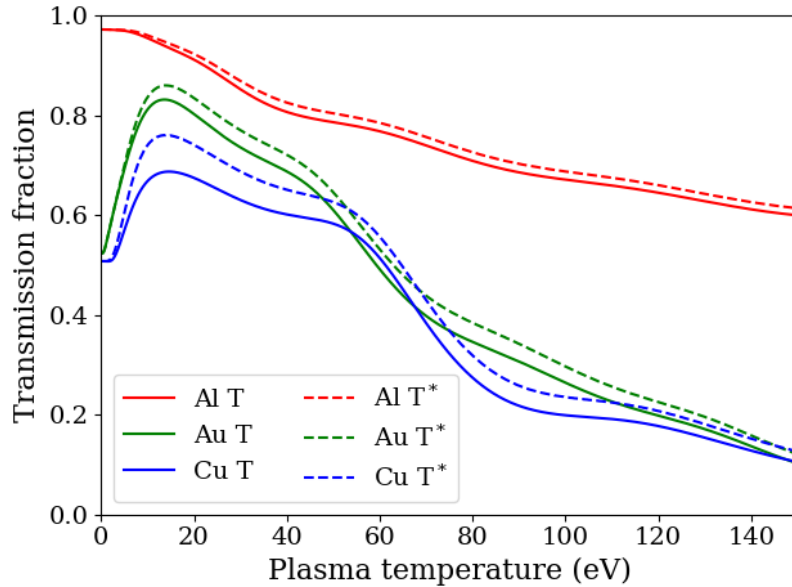


Figure 4.18: Transmission through a 10 nm slice as a function of plasma temperature, as predicted by absorption coefficients both with (solid lines) and without (dashed lines) our degeneracy correction, for an aluminium, gold, and copper target at solid density.

Figure 4.18 shows the transmission fraction of a 10 nm slice of plasma as a function of plasma temperature for aluminium, gold, and copper. Whilst a significant adjustment to the absorption coefficients is made, the impact on these calculations to the bleaching

wave model is not significant. The decrease in transmission at higher temperatures remains due to the increase in free-free absorption. The significance of degeneracy effects on the transmission of a 10 nm slice shows higher material dependence than seen for the previously investigated effects. The most dense material, copper, shows the highest reduction in transmission due to degeneracy effects, and likewise aluminium (the least dense material) shows the lowest reduction.

### 4.3 Benchmarking against an existing model

FLYCHK [93, 94] is an ionization and population distribution model designed as an extension of the K-shell spectroscopy code FLY [95]. The code solves the rate equations for collisional and radiative transfers between ionization levels and generates a population distribution accordingly. The FLYCHK development of FLY is a generalisation, extending its applicability to include; coronal, LTE, or collisional-radiative plasmas; steady state or time-dependent plasmas; collisionally-driven or radiatively-driven plasmas; Maxwellian or non-Maxwellian plasmas; optically thick or thin plasmas; and single species or mixed plasmas. Employing a schematic atomic structure, FLYCHK includes full ionization stages for ions up to  $Z = 93$ , covering all the target materials.

Using FLYCHK offers the chance to compare the simpler models investigated above with a fully benchmarked, established tool. It should be noted, however, that the regime in which FLYCHK is implemented here is not its most accurate. Fortunately, in the case of aluminium at least, somewhat similar pulse conditions ( $E_\gamma = 200 \text{ eV}$  &  $20 \mu\text{m}$  Al target but 200 fs pulse duration) have been investigated using FLYCHK and have been compared with other independent calculations to establish that the population distributions correctly reach equilibrium and the total energy deposition is accurate over short timescales [94].

FLYCHK was employed to calculate population distributions for a solid density plasma of each of the three target metals in steady-state LTE. This was repeated for a range of temperatures and these values were interpolated to give a temperature-dependent curve for the population of each level. The corresponding electron densities, shown in comparison with those predicted by the Saha-Boltzmann model with IPL, are plotted in figure 4.19 as a function of temperature.

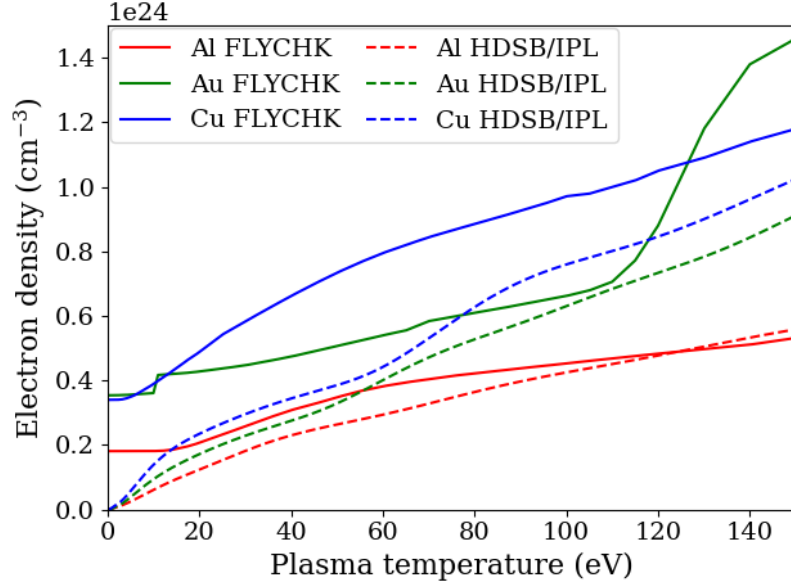


Figure 4.19: Free electron densities as a function of plasma temperature, as predicted by the FLYCHK ionization model (solid lines) and the High-Density Saha-Boltzmann model with Ionization Potential Lowering (HDSB/IPL - dashed lines) for an aluminium, gold, and copper plasma at solid density.

The most immediate difference between the two models is in the  $<10$  eV plasma. FLYCHK treats the ionic structure of the solid metal as a lightly ionized plasma i.e. the conduction band acts as a free electron cloud. As a result, the initial ionization is much higher than that of the Saha-Boltzmann model. The two models do tend towards each other in the  $>100$  eV regime however. This has an impact on the absorption coefficients. Figure 4.20 shows the absorption coefficients, calculated in the same manner as in section 4.1, as a function of plasma temperature for the three target materials as predicted by the high density Saha-Boltzmann with IPL and FLYCHK, both including degeneracy corrections.

The initial ionization state predicted by FLYCHK reduces the photo-ionization absorption to a negligible amount throughout the temperature range and the absorption is consequently dominated by inverse bremsstrahlung, as is the case during optical wavelength ablation. The overall absorption has also increased, as the rate of inverse bremsstrahlung goes as  $n_e n_{Z_i} T^{-1/2} [1 - \exp(-\hbar\omega/k_B T)]$  and FLYCHK predicts significantly higher electron densities at low temperatures.

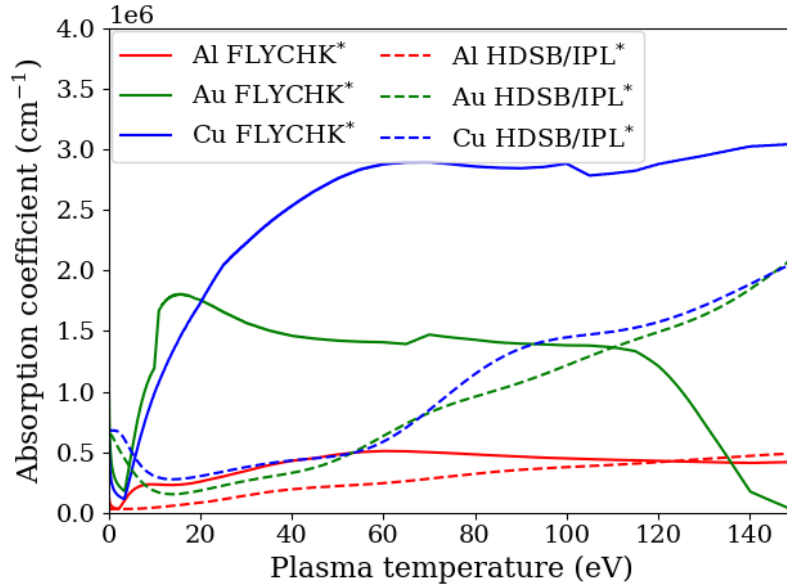


Figure 4.20: Total absorption coefficients as a function of plasma temperature, as predicted by the FLYCHK ionization model (solid lines) and the High-Density Saha-Boltzmann model with Ionization Potential Lowering (HDSB/IPL - dashed lines) for an aluminium, gold, and copper plasma at solid density.

The subsequent transmission fractions, as a function of plasma temperature, are shown in figure 4.21. The shape of these transmission vs temperature curves is now markedly different for all three metals. The copper plasma is almost completely opaque to the incident radiation throughout the temperature range. A sharp drop in absorption, consistent with bleaching behaviour, does occur in the sub 10 eV region for aluminium, but it is unlikely that a plasma slice would remain at such a low temperature during a nanosecond ablation interaction. Over the rest of the temperature range the aluminium remains at a low level of absorption but crucially not low enough to be considered bleached. The gold however appears to bleach properly at temperatures exceeding 120 eV, significantly higher than the temperature predicted by the fitted bleaching wave model. Interestingly, this would indicate that the bleaching wave model is not accurate for aluminium and copper, but is for gold. To assess this surprising outcome accurately, a temporally resolved calculation of the plasma conditions needs to be undertaken – this is considered in Chapter 5.

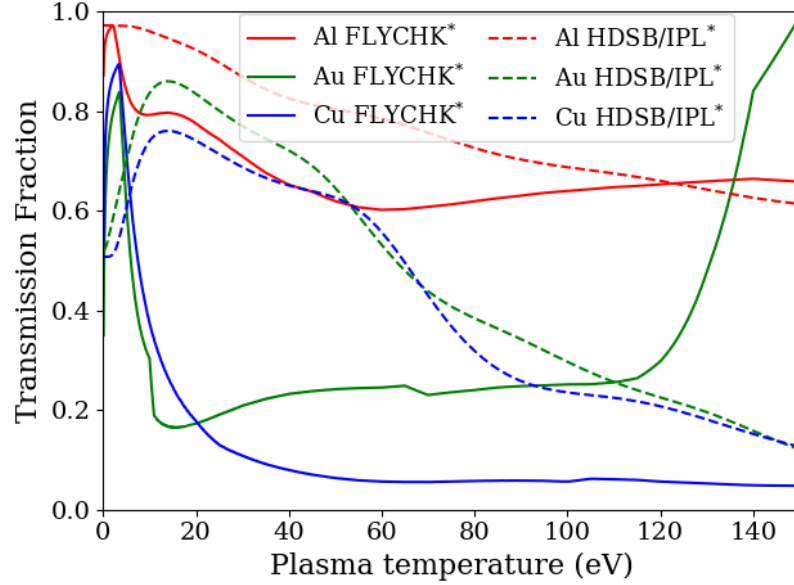


Figure 4.21: Transmission fractions through 10 nm slices of solid material as a function of plasma temperature, as predicted by the FLYCHK ionization model (solid lines) and the High-Density Saha-Boltzmann model with Ionization Potential Lowering (HDSB/IPL - dashed lines) for an aluminium, gold, and copper plasma at solid density.

If we compare the transmission fraction values predicted by FLYCHK and the Saha-Boltzmann model with the literature values for the transmission of a similar 10 nm slice of solid target at room temperature, we find that the models agree with varying accuracy dependent on material. The literature values for a 10 nm slice of aluminium, gold, and copper are 0.976, 0.249, and 0.411 respectively. The Saha-Boltzmann model predicts transmission fractions of 0.972, 0.523, and 0.507, and the FLYCHK model predicts transmission fractions of 0.872, 0.349, and 0.525. In the case of aluminium, the Saha-Boltzmann model is more accurate, in the case of gold FLYCHK is closer, and in the case of copper, they are comparably accurate.

#### 4.4 On the opacity of warm dense aluminium

The opacity of warm dense aluminium is a topic that has seen a significant body of research over recent years. Many current theoretical predictions of the absorption coefficient exist, using different approaches. We have compared our approach to those of Iglesias [53], Shaffer *et al.* [96], and Hollebon *et al.* [97] in figure 4.22.

The Iglesias approach is a semi-classical inverse-bremsstrahlung based model that uses the refractive index and electron-ion collision frequency to account for collective

effects, dispersion, and multiple collisions. The Shaffer approach uses the average atom model to calculate the electronic structure of an atom in the plasma, then calculates the optical conductivity using the Kubo-Greenwood approach, and finally uses the Kramers-Kronig dispersion relation to calculate the subsequent refractive index and opacity. The Hollebon approach uses full density functional theory (DFT) calculations to improve upon the accuracy of the Kubo-Greenwood approach and calculate the dielectric function accordingly. Each of these three approaches seeks to account for more physical effects, and so improve the accuracy of their opacity calculations.

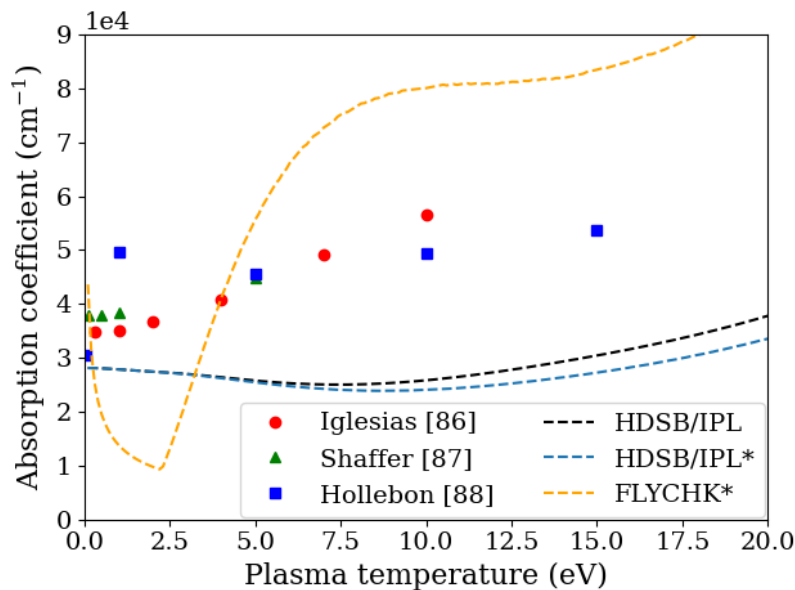


Figure 4.22: Total absorption coefficient of an aluminium plasma for 32 nm wavelength radiation as a function of plasma temperature calculated using the High Density Saha-Boltzmann ionization model with ionization potential lowering and classical absorption coefficients both with (blue line) and without (black line) degeneracy corrections. The degeneracy-corrected coefficient predicted by the FLYCHK ionization model is shown in orange. Also shown are absorption coefficient values from the models of Iglesias [53] (red points), Shaffer [96] (green points), and Hollebon [97] (blue points).

In figure 4.22 we can see how the three approaches compare and how they compare to our approach. We have used a test wavelength of 32 nm, following a similar comparison of studies by Vinko *et al.* [98], and have plotted the absorption coefficients predicted by the models as a function of plasma temperature. Interestingly, neither model compares that well with the other theoretical approaches to this issue. The simpler Saha-Boltzmann based model (in the high density limit, both the non-degeneracy corrected – no star – and degeneracy corrected – starred – coefficients are shown)

agrees most closely but underestimates the absorption coefficient, largely due to the low average ionization this model predicts and the dominance of photo-ionization absorption this implies. For this model, the degeneracy corrections have a limited effect. Conversely, for FLYCHK the non-degeneracy corrected absorption coefficient is greatly overestimated (an order of magnitude, hence being omitted from figure 4.22) due to the high initial average ionization predicted. The degeneracy corrected absorption coefficient is at least the right order of magnitude, however agreement is still largely poor. As this absorption is dominated by inverse bremsstrahlung absorption, it should most closely match the results predicted by Iglesias. However, significant discrepancies are present due to the collective, dispersion, and multi-collision effects that are included in the Iglesias model.

## 4.5 Summary and conclusions

In this chapter a series of investigations have been made to qualitatively evaluate the results of fitting a linear ‘bleaching wave’ model of ablation to experimental data. Using the Saha-Boltzmann ionization model and classical expressions for the free-free and bound-free absorption coefficients, transmission calculations were undertaken that aimed to link the predictions of the fitted model to a set of real plasma conditions. The bleaching wave model implies two zones in the temperature-dependent transmission curve, a bleached and an un-bleached region, separated by a steep gradient. The bleaching energy densities were linked to plasma energy content values, and transmission fractions were calculated at the implied temperatures. For gold and copper, the materials for which the bleaching wave model should be most valid, the transmission as a function of temperature did not closely follow the behaviour required for a strict implementation of the bleaching wave model; a step-function increase in transmission with temperature at some bleaching temperature.

Several accuracy improvements for the plasma ionization and absorption coefficient calculations were tested to see if EUV transmission variations with temperature closer to a step-function could occur. Moving to the high-density Saha-Boltzmann ionization model did not produce any significant changes in the predicted electron densities and ion populations. The inclusion of ionization potential lowering (IPL), as formulated by Stewart & Pyatt, produced significant changes in both the electron density and absorption coefficients. This is understandable as IPL reduces the energy required for higher levels of ionization and makes photo-ionization of higher charged ions possible.

The effect of these changes on the transmission fraction was a small shift in the transmission region to lower temperatures, and did not notably change the gradient of the transmission region.

Other corrections were made to the absorption coefficients. The use of the Kramers value for the Gaunt factor was tested for both free-free and bound-free absorption. The corrections for the bound free have been calculated by Karzas & Latter, and when level-averaged they have a maximum of  $\approx 10\%$ , so were not evaluated for our simulated plasma conditions. Maxwell-averaged Gaunt factors for free-free absorption have also been calculated by Karzas & Latter, and were interpolated to produce curves for predicted plasma conditions in aluminium, gold, and copper. The maximum deviation was found at low temperatures (when the free-free absorption contribution to overall absorption is at its lowest) and had a maximum of 20%, so the Kramers value was deemed a suitable approximation.

The final correction to the absorption coefficients was the inclusion of degeneracy effects in their formulation. Correction factors were applied to each that accounted for Fermi-Dirac statistics for the free electrons rather than Maxwellian. The effect on the free-free absorption was a  $\approx 10\%$  reduction for all three metals. These degeneracy corrections show a stronger material dependence than any other correction, with the highest transmission reduction occurring in the highest density material. The bound-free degeneracy correction is negligible for the temperatures at which this process is activated.

Once these results were collected, the predicted population distributions (and average ionizations) were compared with those predicted by an existing and trusted tool; FLYCHK. Agreement between the models was poor at low plasmas temperatures due to the treatment of the conduction band as a free electron cloud in FLYCHK. This change means that FLYCHK predicts that inverse bremsstrahlung dominates the absorption throughout the temperature range, contrary to the initial hypothesis that photo-ionization would play a significant role. Comparison of the absorption coefficients predicted by both FLYCHK and the high density Saha-Boltzmann model (with IPL) with other theoretical absorption calculations in aluminium plasmas showed inaccuracies due to the lack of bulk phenomena in our calculations, however the Saha-Boltzmann model compared most favourably.

Investigation of the Saha-Boltzmann ionization model has shown limited evidence to back the bleaching wave model. Possible ‘bleaching’ behaviour was seen over the 0 eV to

10 eV range in aluminium in the FLYCHK calculations but the plasma is likely to heat up above this range rapidly. Surprisingly, FLYCHK predicts that the gold plasma will fully bleach at temperatures exceeding 120 eV. The copper remained highly absorbing of the incident radiation throughout the tested temperature range.

Deficiencies in calculations using both the Saha-Boltzmann model, with corrections, and the FLYCHK tool have been exposed in comparison to other models that account for bulk effects. However, the changing to the use of such complex models is contrary to the spirit of our search for a simple tool relating the fluence and ablation depth. As a consequence, the two models compared in section 4.3 are carried forward into Chapter 5 and a new time-dependent model is developed.

## Chapter 5

# Time-resolved constant density models of EUV ablation

In Chapter 4 we described a series of investigations that produced temperature-dependent transmission curves for an arbitrary thin slice of target plasma. These investigations were undertaken to contextualise the bleaching wave model introduced in Chapter 3. Despite the consideration of many effects and corrections to the model, a clear step function increase of transmission at some threshold plasma temperature was not apparent. In this chapter we use the framework of the ion population and absorption algorithms developed for Chapter 4 in order to produce time-resolved calculations of plasma parameters.

The first half of this chapter extends the transmission calculations made in Chapter 4 to model the behaviour of a target cell irradiated with a time-dependent radiation pulse. By making these calculations for a unit volume cell, one can investigate the temporal evolution of the cell for a bleached state as predicted by the bleaching wave model. The second half of this chapter takes these time-resolved measurements and expands on them to include spatial resolution. The result is a one-dimensional model that neglects hydrodynamics and predicts radiation propagation into a target. From these calculations an ablation depth is extracted and compared to the experimental depths measured in Chapter 3. As the predicted ionizations varied between models in Chapter 4, the calculations in this chapter have been performed for both the Saha-Boltzmann based model (in the high density limit and including IPL and degeneracy corrections to the absorption coefficient) and FLYCHK.

## 5.1 Novel rate equation model

In Chapters 3 and 4 our modelling of plasma ionization and EUV transmission treated the plasma as being in equilibrium with a Saha-Boltzmann distribution of ionization. The (comparatively) long pulse duration of the capillary discharge laser means that equilibration is certainly possible, however laser-produced plasmas are a driven system and a more accurate alternative may be to consider the plasma as being in a steady-state, rather than true equilibrium. In order to formulate such a model, we must first consider the equilibrium described by the Saha-Boltzmann model.

When a plasma is considered to be in equilibrium, the populating and de-populating mechanisms that act upon the various ionization levels are in balance, so that the overall state of the plasma is unchanging. For plasmas in LTE these processes are dominated by collisional processes, and can cause either excitations or full ionizations. The McWhirter criterion for the minimum electron density for LTE in the transition between the  $\text{Al}^{1+}$  and  $\text{Al}^{2+}$  states at 100 eV is  $n_e = 3.60 \times 10^{18} \text{ cm}^{-3}$  – orders of magnitude below the expected electron densities. It is therefore valid to assume LTE for our EUV laser-produced plasmas and to treat the collisional processes as dominant in the development of a rate equation-based ionization model.

For an unperturbed plasma in LTE, there are two dominant processes that affect discrete ionizations; collisional ionization and three body recombination. To maintain equilibrium, the rates of these two processes (with rate coefficients  $K_{iC}$  and  $K_{Ci}$  for collisional ionization and three-body recombination respectively) must be balanced – see figure 5.1. However, as we have mentioned before, the photon energy at EUV

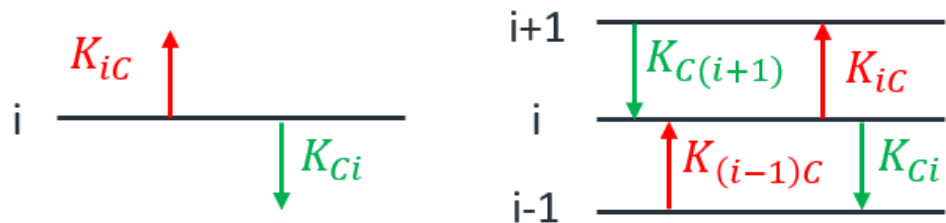


Figure 5.1: A cartoon of the populating and de-populating processes affecting a single ionization stage  $i$  and a plasma with three relevant ionization stages.

wavelengths is high enough to allow photo-ionization to occur. The photo-ionization process is a populating and de-populating process for some of the ionization levels, and

so it should be included in an ionic population calculation. Figure 5.2 shows a cartoon of the updated balance between these three processes.

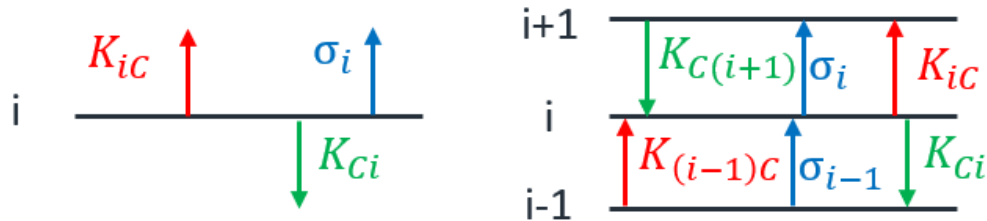


Figure 5.2: A cartoon of the populating and de-populating processes, including photo-ionization, affecting a single ionization stage  $i$  and a plasma with three relevant ionization stages.

From the balance between these three processes it is possible to construct a system of equations that describe the ion population distribution. In the low fluence limit, the model will tend to the Saha-Boltzmann ionization model, deviating once the photo-ionization is of a similar order of magnitude to the collisional processes. Implementation of this system of equations can be achieved using a similar method to the one used for the Saha-Boltzmann model in Chapter 4.

The behaviour of this model was briefly investigated and example curves are shown in figure 5.3 for an aluminium target. It was found that there is no deviation from the Saha-Boltzmann model at intensities  $\leq 1 \times 10^{12} \text{ W cm}^{-2}$ , so at the EUV laser intensities of our experiment ( $< 1 \times 10^{11} \text{ W cm}^{-2}$ ) it is not necessary to use the rate equation model for the ionization evaluation. As can be seen, the rate equation model only affects the ion population below 30 eV, even at intensities of  $1 \times 10^{15} \text{ W cm}^{-2}$  and above. In the future it may be of interest to conduct an investigation into the predictions of this model for the intensities seen in XFEL experiments.

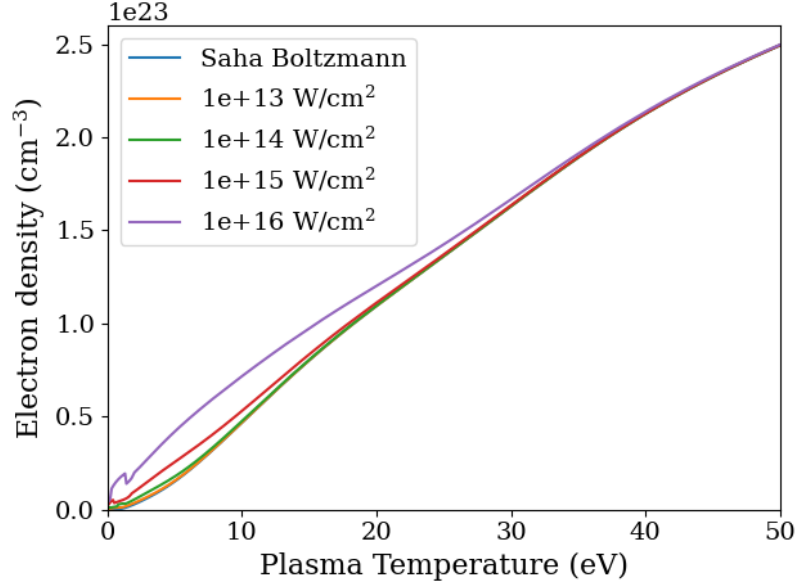


Figure 5.3: Electron density as a function of plasma temperature predicted by the Saha-Boltzmann and rate equation ionization models for a range of intensities of 46.9 nm radiation incident on a solid density aluminium target. The Saha-Boltzmann curve is obscured by higher intensity curves.

## 5.2 Temporal intensity variations

Time-dependent effects are largely unaccounted for in our consideration of the plasma conditions for the bleaching wave model. The most obvious of these is temporal variation in the radiation intensity. Thus far we have considered the radiation intensity as constant at the peak value. In reality this is not the case, and the majority of the laser pulse is at intensities below this peak value. Also, by making temporally-resolved calculations of the transmission one can observe if a unit cell transitions into a bleached state at any point during the interaction.

The model developed to carry out these calculations is a simple single target cell of unit volume which is irradiated by a time-dependent radiation pulse. The plasma temperature is evaluated at each time step by adding energy to the free electrons and ions (assuming the ion temperature is equal to the electron temperature) allowing for energy loss due to plasma ionization. The ionization balance is calculated assuming a Saha-Boltzmann distribution (other models are used later in this chapter) and the EUV laser energy is absorbed by the calculated rates of inverse bremsstrahlung and photo-ionization. The investigations in Chapter 4 have shown that only the effect of

ionization potential lowering is significant enough on the overall transmission of a slice of target material to include in the calculations. The effect of ionization potential lowering is therefore included in the time-resolved model.

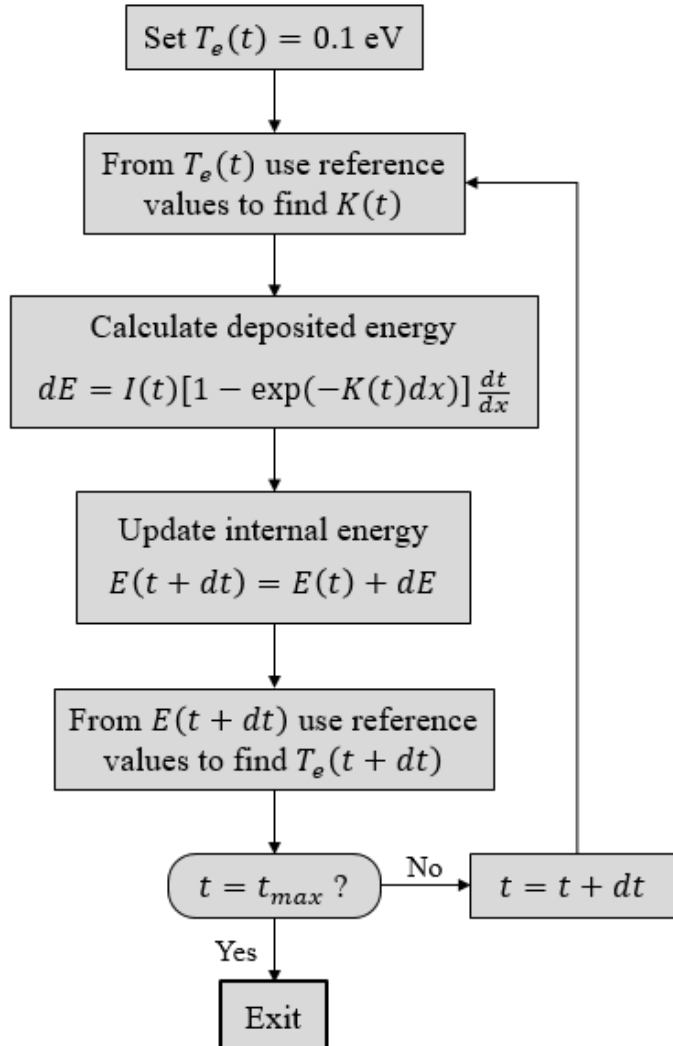


Figure 5.4: A flowchart of the computer algorithm used to calculate the time-resolved energy deposition (and consequent electron density, temperature, absorption coefficients and energy content) in a single target cell.

A flowchart of the algorithm for calculating the plasma conditions in a time-resolved system is shown in figure 5.4. The single-cell algorithm begins by calculating electron density, absorption coefficient, and energy content values over a wide range of temperatures in advance of the time-resolved measurements. The time-resolved measurements then define a single cell of unit area and thickness  $dx = 10 \text{ nm}$ , initially at temperature  $T = 0.1 \text{ eV}$ . The algorithm then takes the radiation intensity value for that time step and calculates the energy absorbed using the absorption coefficients for inverse

bremsstrahlung and photo-ionization (equations 2.27 and 2.33) and the Beer-Lambert law (equation 2.14). This absorbed energy is then added to the energy content value and compared to the array of pre-calculated energy densities. The nearest energy content value is chosen as the new cell energy and the temperature adjusted accordingly. The algorithm can then move on to the next time step.

The time-dependent intensity used in these simulations has a  $\sin^2 t$  pulse shape as this has defined zero values and is a common approximation for a Gaussian used in laser-plasma interaction simulation. The full expression used for the intensity was

$$I(t) = I_0 \sin^2 \left( \frac{\pi t}{t_{\text{pulse}}} \right). \quad (5.1)$$

The range of fluences investigated experimentally corresponds to peak intensities  $I_0$  in the  $1 \times 10^9 \text{ W cm}^{-2}$  to  $1 \times 10^{11} \text{ W cm}^{-2}$  range. The value used for the pulse duration  $t_{\text{pulse}}$  was 1.2 ns.

### 5.2.1 Saha-Boltzmann based ionization model

The first of the ionization models studied was the Saha-Boltzmann model. Calculations were conducted in the high density limit (to facilitate degeneracy correction calculations) and included corrections for ionization potential lowering and degeneracy corrections to the absorption coefficients. Figure 5.5 shows plasma temperature as a function of elapsed time for a range of peak intensities irradiating an aluminium target cell.

The plasma temperature curves as a function of time increase up to a maximum value at the end of the 1.2 ns pulse (as in figure 5.5) for all three metals. The maximum temperature achieved for each target metal is shown as a function of incident fluence in figure 5.6.

The relation between the maximum cell temperature and the incident fluence is approximately linear for all three materials. The similarity between the behaviour of gold and copper is once again apparent, with little difference in maximum temperature between the two materials at fluences above  $\approx 35 \text{ J cm}^{-2}$ .

Figures 5.7, 5.8, and 5.9 show the transmission of the cell as a function of time for aluminium, gold, and copper. These transmission curves confirm that there is no consistent bleached state for the cell even accounting for temporal variation in the intensity. Some increase in transmission is seen for gold and copper at lower irradiances ( $< 1 \times 10^{10} \text{ W cm}^{-2}$ ) however, which is consistent to some degree with the bleaching wave model. As expected, aluminium does not exhibit any bleaching behaviour.

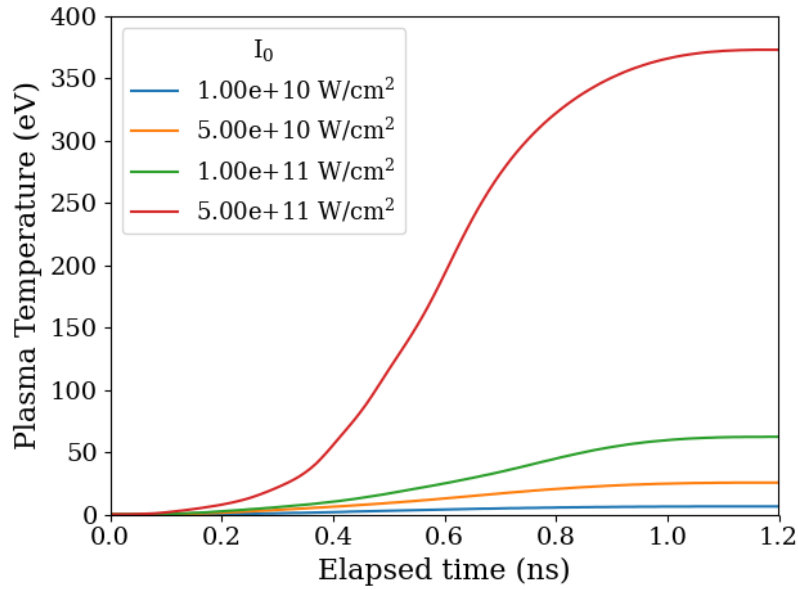


Figure 5.5: Plasma temperature as a function of time for a range of peak incident intensities  $I_0$  irradiating an aluminium target cell modelled using Saha-Boltzmann ionization. The EUV laser pulse has a  $\sin^2 t$  temporal shape with a pulse duration of 1.2 ns.

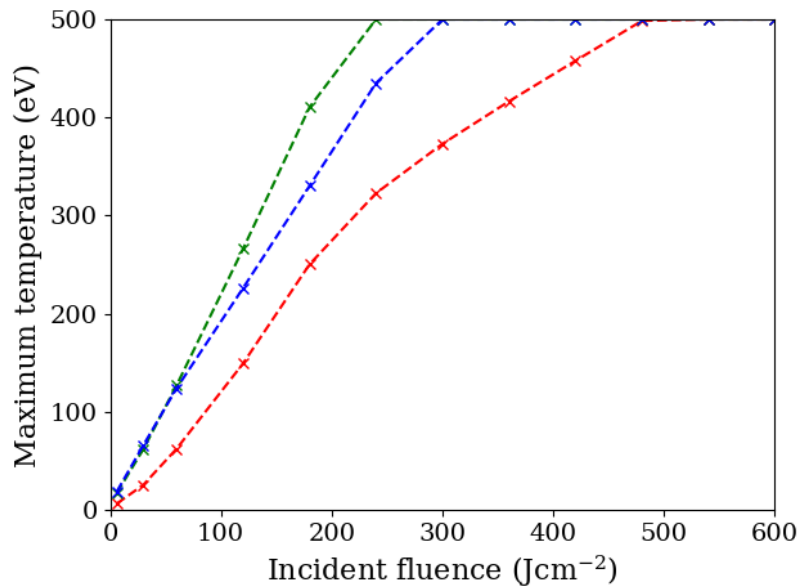


Figure 5.6: Maximum achieved plasma temperature as a function of peak incident fluence for aluminium, gold, and copper target cells at solid density as predicted by the Saha-Boltzmann ionization model.

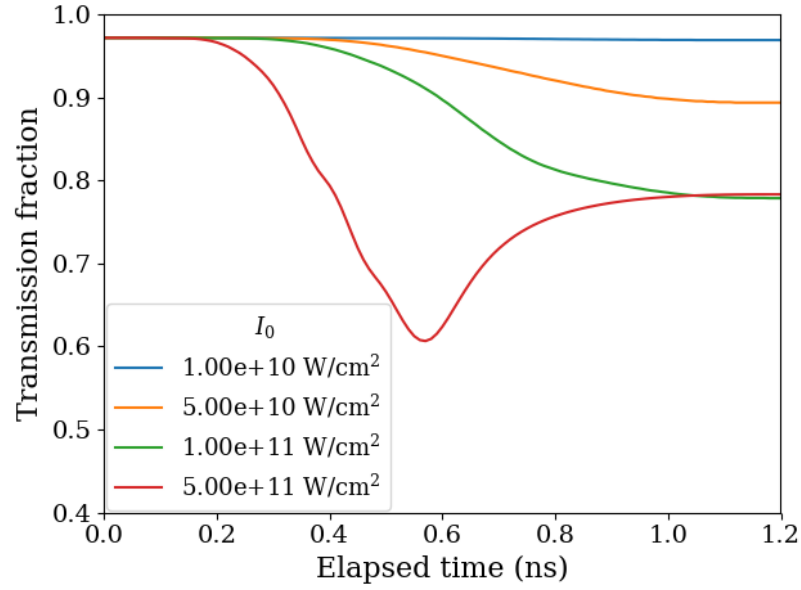


Figure 5.7: Transmission fraction as a function of time for a 10 nm thick aluminium target cell at solid density for EUV laser pulses with peak intensities as labelled.

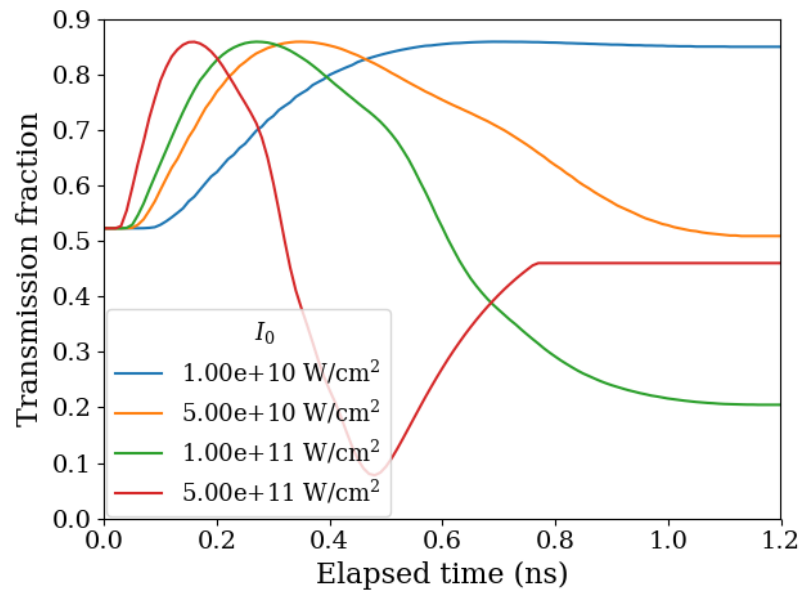


Figure 5.8: Transmission fraction as a function of time for a 10 nm thick gold target cell at solid density for EUV laser pulses with peak intensities as labelled.

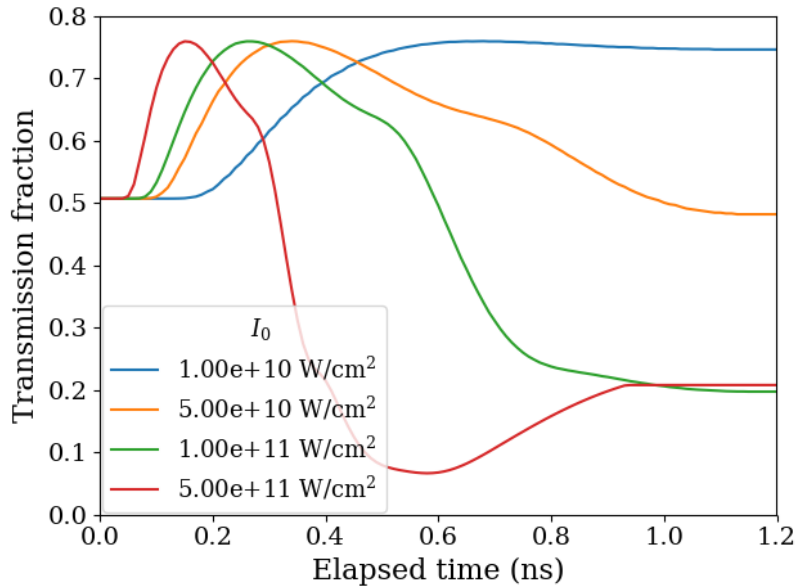


Figure 5.9: Transmission fraction as a function of time for a 10 nm thick copper target cell at solid density for EUV laser pulses with peak intensities as labelled.

The approximations made by this single cell algorithm should be noted at this point. The model takes no account of fluid motion, and the density of the target remains constant at solid density. There is no accounting for scattering in the absorption model as this is likely to be a small contribution due to the low reflectivity of the plasma at 46.9 nm wavelengths. No thermal transport is modelled either.

### 5.2.2 FLYCHK ionization model

As with the Saha-Boltzmann based model, calculations were conducted using the algorithm in figure 5.4 to produced temporally-resolved plasma temperature curves and subsequent transmission fraction curves for a range of peak incident intensities. Figure 5.10 shows the plasma temperature as a function of elapsed time for an aluminium plasma irradiated by a range of peak intensities modelled using the FLYCHK ionization model. As can be seen from the change in scale, the final plasma temperatures reached are higher than those predicted by the Saha-Boltzmann ionization model. This is true for all three metals at all irradiances, evidenced by the plots of maximum achieved plasma temperature as a function of incident fluence shown in figure 5.11.

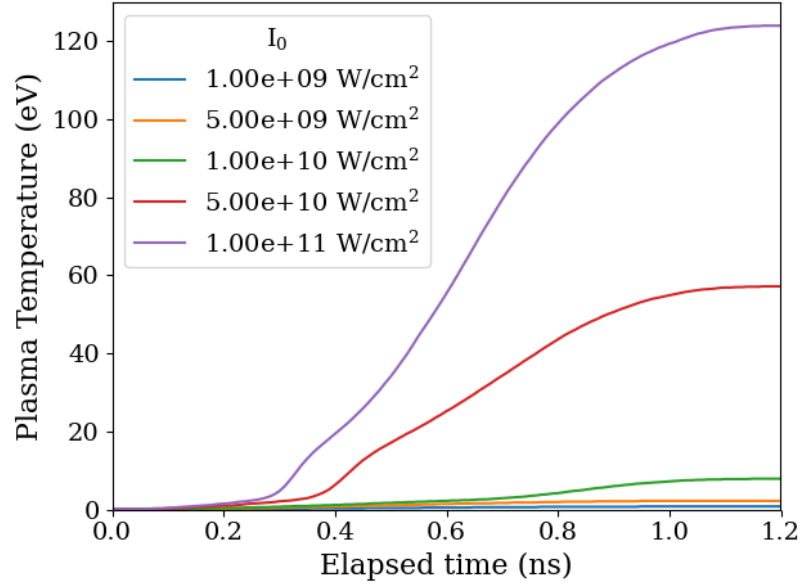


Figure 5.10: Plasma temperature as a function of elapsed time for a range of peak incident intensities  $I_0$  irradiating an aluminium target cell modelled using FLYCHK ionization. The EUV laser pulse has a  $\sin^2 t$  temporal shape with a pulse duration of 1.2 ns.

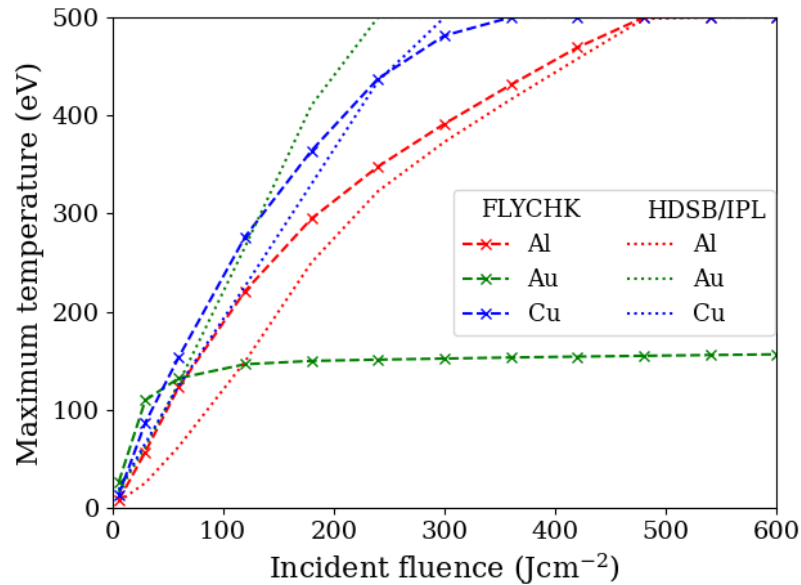


Figure 5.11: Maximum achieved plasma temperature as a function of peak incident fluence for aluminium, gold, and copper target cells at solid density as predicted by the FLYCHK ionization model (dashed lines) and by the previous calculations using a Saha-Boltzmann based model (HDSB/IPL - dotted lines).

The transmission curves predicted by the FLYCHK ionization model are shown in figures 5.12, 5.13, & 5.14.

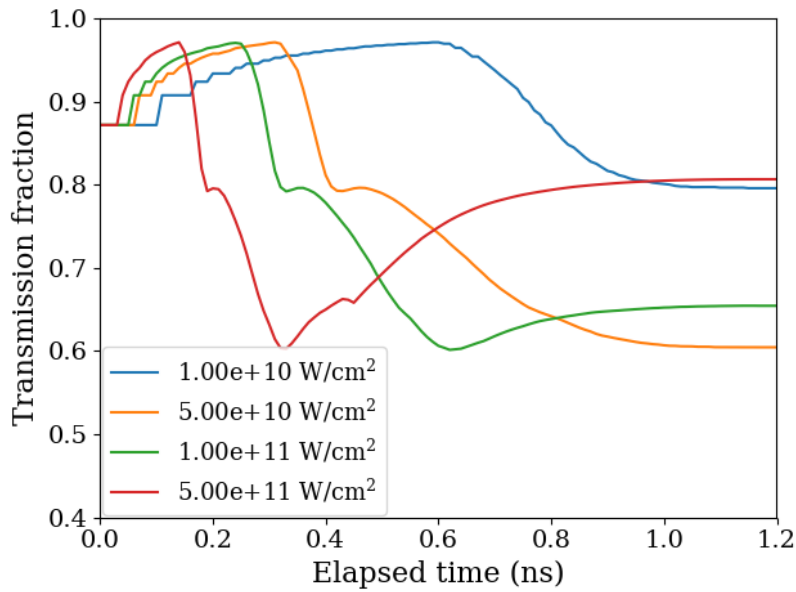


Figure 5.12: Transmission fraction as a function of time for a 10 nm thick aluminium target cell at solid density for EUV laser pulses with peak intensities as labelled and ionization calculated using the FLYCHK code.

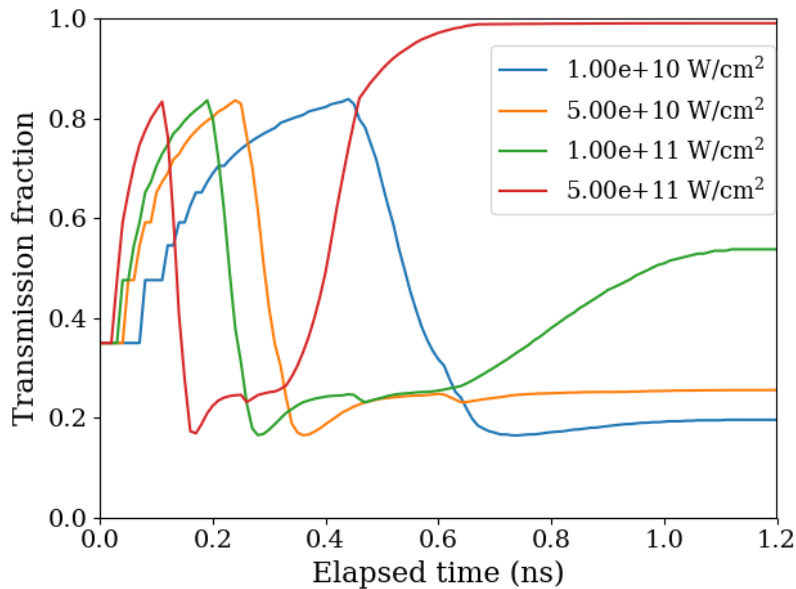


Figure 5.13: Transmission fraction as a function of time for a 10 nm thick gold target cell at solid density for EUV laser pulses with peak intensities as labelled and ionization calculated using the FLYCHK code.

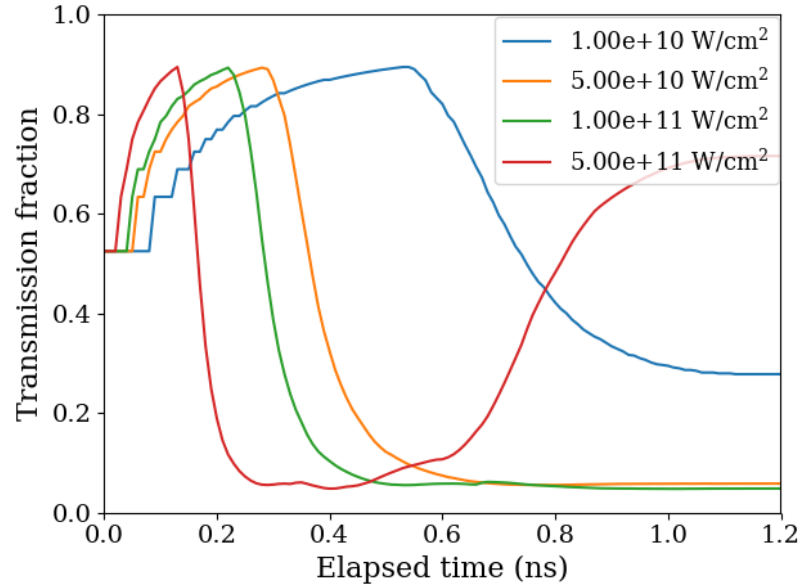


Figure 5.14: Transmission fraction as a function of time for a 10 nm thick copper target cell at solid density for EUV laser pulses with peak intensities as labelled and ionization calculated using the FLYCHK code.

The behaviour is largely similar to that predicted by the Saha-Boltzmann model but compressed in time. The extremes of the transmission values have also increased. In the gold and copper targets the combination of these two effects is to give a brief period where the transmission is increasing rapidly enough to mimic ‘bleaching’ behaviour. Unfortunately the transmission does not reach a high enough value to suggest true bleaching, nor is the lifetime of the bleached state long enough to support the idea that once bleached a slice will no longer contribute to the absorption. Interestingly, the increased absorption that FLYCHK predicts for cold aluminium results in aluminium exhibiting some weak ‘bleaching’ behaviour at early times.

The transmission curves for both ionization models do not support a bleaching wave model in all but the highest fluences on a gold target. However, the principle of radiation propagating gradually into the target through a series of slices need not be abandoned, we simply have to account for the energy deposited in each non-bleached slice of material. Such a model should be robust enough to predict accurate depths whether the slice is bleached or not.

### 5.3 Replacing the bleaching wave model

A simple replacement for the bleaching wave model can be developed from our transmission calculations by adding spatial resolution in the target normal axis. In doing this, the absorption of each thin slice of material will be accounted for throughout the ablation interaction, rather than being ignored once it is ‘bleached’ as per the bleaching wave model. This should capture the effect of the limited and brief periods of bleaching-like behaviour seen in the time-resolved calculations above.

All the approximations from the single-cell model detailed in section 5.2 are retained. The spatially-resolved model is hydrostatic, neglecting both fluid motion (density changes) and heat transfer between cells. The absorption is modelled as before. The model is essentially constructed by putting a sequence of single-cell models next to each other and adjusting the intensity accordingly between each cell.

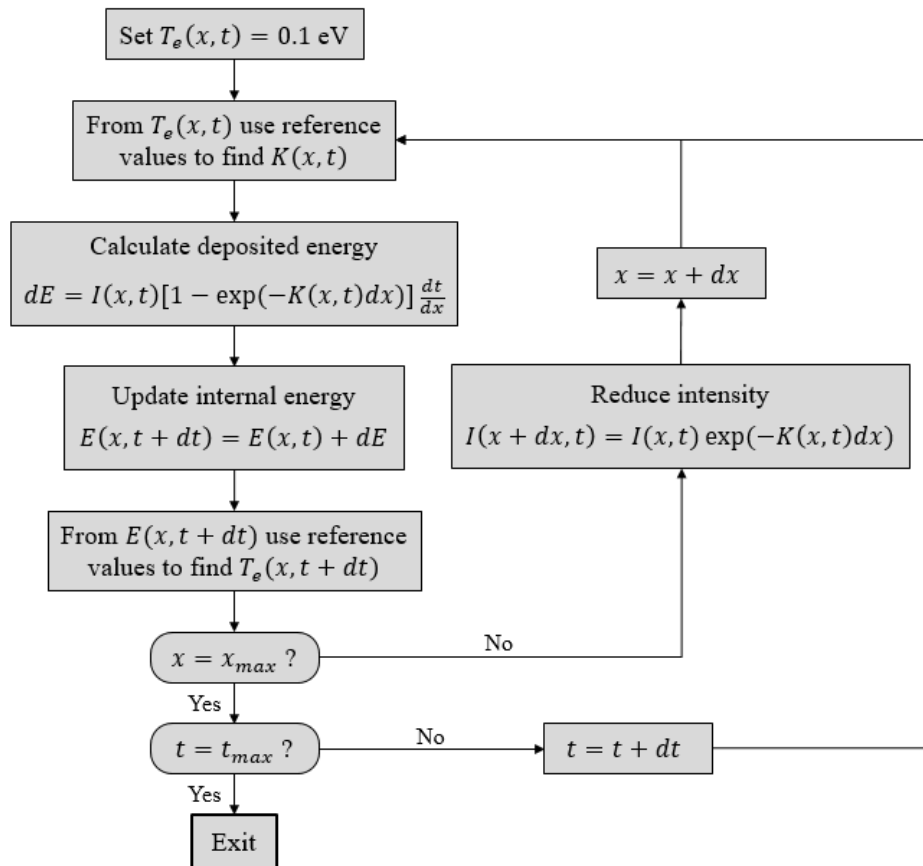


Figure 5.15: A flowchart of the computer algorithm used to calculate the time-resolved energy deposition (and consequent electron density, temperature, absorption coefficients and energy content) in a mesh of target cells.

A flowchart of the algorithm for calculating the plasma conditions in a time- and

space-resolved system is shown in figure 5.15. The algorithm for time-resolution remains as described in section 5.2. In each time step, the algorithm calculates the energy absorbed for a given cell as before. Once a given cell has been updated, the algorithm calculates the beam intensity that passes through the cell and onto the next. The algorithm then calculates the plasma conditions for the next cell. These calculations are made for all cells in the mesh.

The spatially-resolved algorithm produces values for plasma temperature, electron density, and energy content for each cell and each time step. Figure 5.16 shows plasma temperature as a function of cell position for a series of time snapshots in aluminium. The targets shown in these figures were irradiated with an intensity of  $5 \times 10^{10} \text{ W cm}^{-2}$ . The spatial profile of the temperatures is close to exponential, as might be expected given that the absorption is calculated using the Beer-Lambert law.

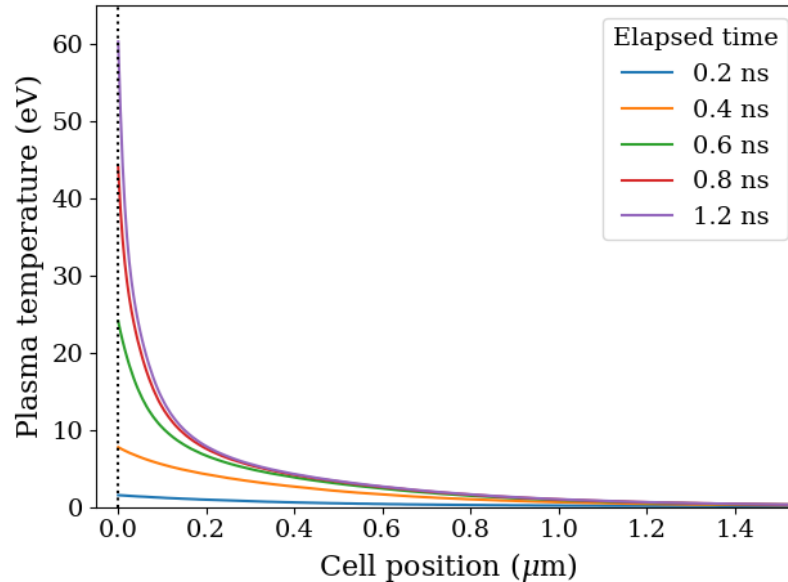


Figure 5.16: Plasma temperature as a function of cell position at a range of times for an aluminium target at solid density irradiated with a peak intensity of  $5 \times 10^{10} \text{ W cm}^{-2}$  of 46.9 nm wavelength radiation delivered in a 1.2 ns pulse.

In order to extract an ablation depth from this spatial profile of plasma conditions, a criterion must be chosen for which cells are considered ablated. This would usually be determined by a phase transition, but our model treats the target as a solid density gas (i.e. ignoring solid state properties) so this cannot be our criterion. Two possibilities seem sensible; a minimum temperature such as the boiling point (above which the material is likely to have become plasma), or a minimum electron density (above which plasma properties such as quasi-neutrality apply).

### 5.3.1 Saha-Boltzmann based ionization model

Initially, the calculations were made using the Saha-Boltzmann ionization model in the high density limit including Ionization Potential Lowering (IPL) and degeneracy corrections to the absorption coefficients. Figure 5.17 shows the ablation depths predicted by our hydrostatic algorithm with three different ablation criteria as a function of incident fluence on an aluminium target. The shape of these ablation depth vs fluence curves is close to logarithmic, supporting the Gamaly model (i.e. an exponential propagation of radiation into the target) shown in Chapter 3. The significance of the ablation criterion is clear, as the curves are separated by a large offset. As it is only the ablation criterion we are changing between the curves, the gradient remains the same. The closest fitting curve is the strictest of the three criteria (the criteria that applies to the fewest cells); that the electron density is higher than 10% of solid density.

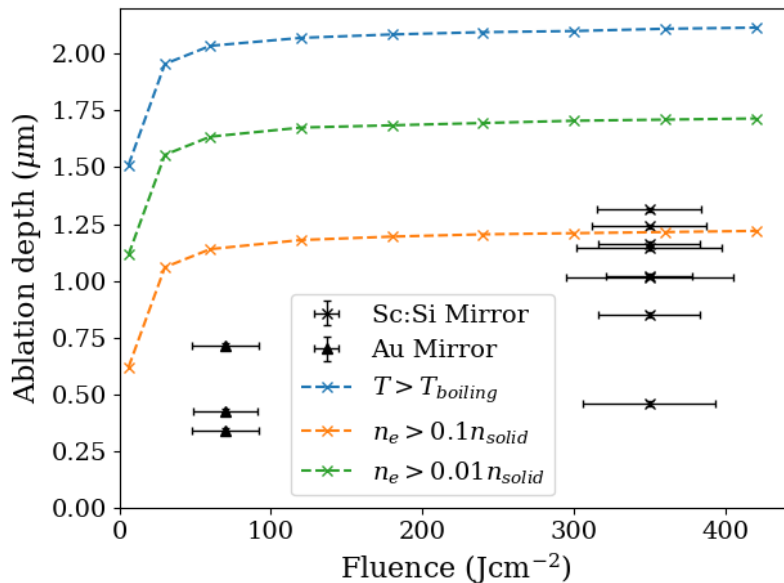


Figure 5.17: Ablation depths as a function of incident fluence as predicted by the spatially-resolved model with a range of ablation criteria for an aluminium target at solid density. Experimentally measured ablation depths (see Chapter 3) are also shown.

Figures 5.18 and 5.19 show the ablation depths predicted by our hydrostatic algorithm with three different ablation criteria as a function of incident fluence on gold and copper targets respectively. Again, the shape of these curves is close to logarithmic,

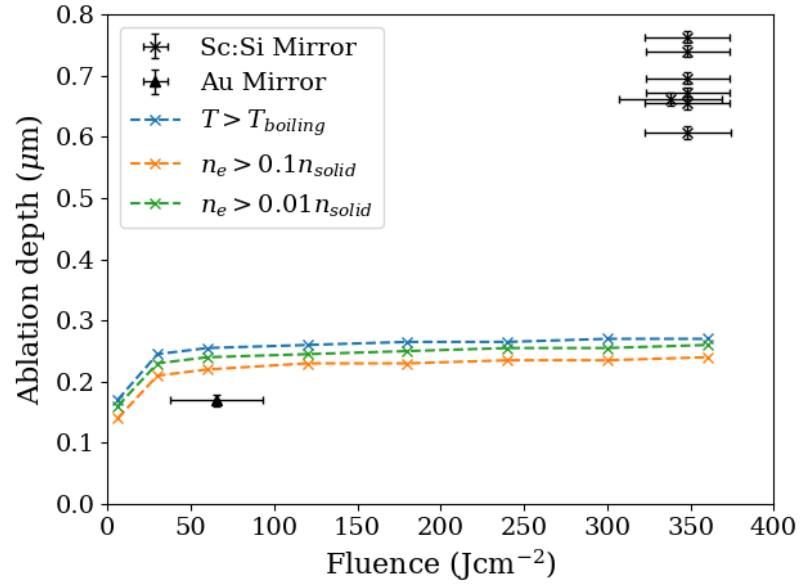


Figure 5.18: Ablation depths as a function of incident fluence as predicted by the spatially-resolved model with a range of ablation criteria for a gold target at solid density. Experimentally measured ablation depths (see Chapter 3) are also shown.

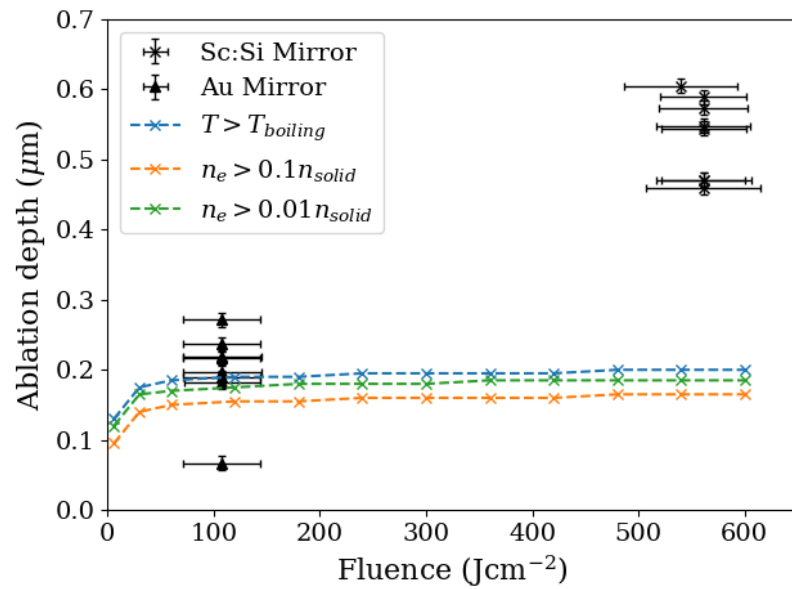


Figure 5.19: Ablation depths as a function of incident fluence as predicted by the spatially-resolved model with a range of ablation criteria for a copper target at solid density. Experimentally measured ablation depths (see Chapter 3) are also shown.

and has a similar saturation point to the results seen for the Gamaly model on gold and copper. The closest fitting curve is the least strict criterion; that the cell temperature be above the material's boiling point. This cannot be called a close fit however as the model predicts a maximum achievable ablated depth of  $\approx 0.1 \mu\text{m}$  to  $0.2 \mu\text{m}$  for both gold and copper whereas experimentally we recorded ablation depths of  $\approx 0.7 \mu\text{m}$  and  $0.5 \mu\text{m}$  respectively.

### 5.3.2 FLYCHK ionization model

The algorithm was also run using the FLYCHK ionization model. Figures 5.20, 5.21, & 5.22 show the ablation depths predicted by the hydrostatic algorithm as a function of incident fluence for aluminium, gold, and copper respectively. As the initial ionization predicted by FLYCHK is so high, the ablation criterion was selected to be temperature above the boiling point of the target. The results of the Saha-Boltzmann based model are also shown for comparison. In the case of aluminium these are the results using the  $n_e > 0.1n_{\text{sol}}$  ablation criterion, and in the case of gold and copper these are the  $T > T_{\text{boiling}}$  ablation criterion.

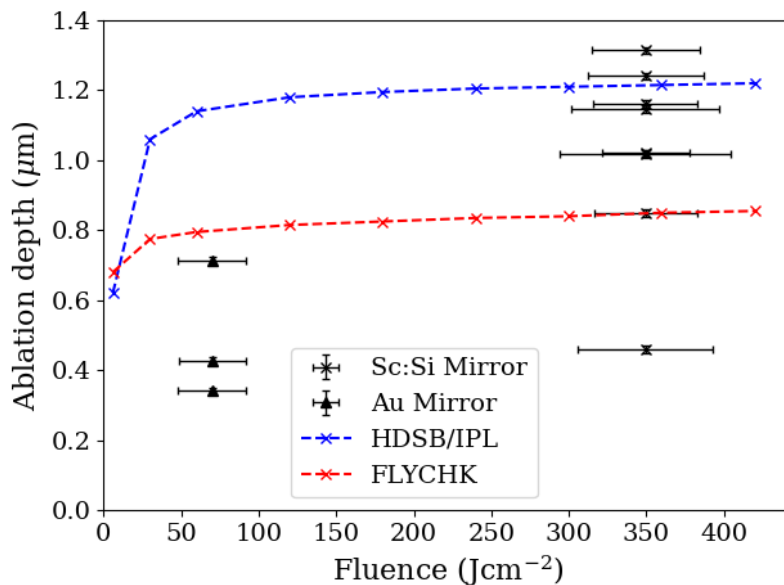


Figure 5.20: Ablation depths as a function of incident fluence as predicted by the spatially-resolved model with ionization calculated using FLYCHK (red curve) and the Saha-Boltzmann model (blue curve) for an aluminium target at solid density. Experimentally measured ablation depths (see Chapter 3) are also shown.

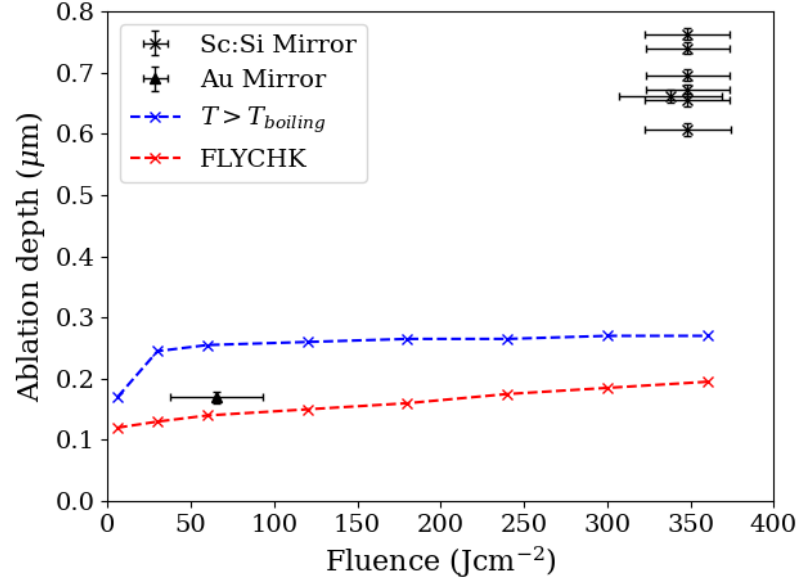


Figure 5.21: Ablation depths as a function of incident fluence as predicted by the spatially-resolved model with ionization calculated using FLYCHK (red curve) and the Saha-Boltzmann model (blue curve) for a gold target at solid density. Experimentally measured ablation depths (see Chapter 3) are also shown.

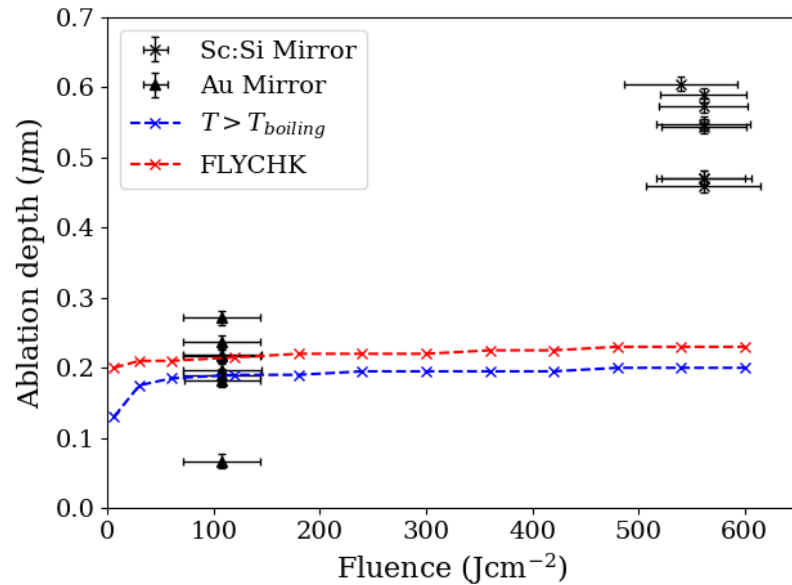


Figure 5.22: Ablation depths as a function of incident fluence as predicted by the spatially-resolved model with ionization calculated using FLYCHK (red curve) and the Saha-Boltzmann model (blue curve) for a copper target at solid density. Experimentally measured ablation depths (see Chapter 3) are also shown.

Interestingly, the difference between the absorption coefficients predicted by the two ionization models is not reflected in the final ablation profiles. As before, the algorithm predicts much lower ablation depths on the gold and copper than seen in experiment. The FLYCHK ionization model predicts generally lower ablation depths than the Saha-Boltzmann based model in the aluminium plasma, retaining the near-logarithmic shape.

## 5.4 Aluminium Oxide

It is necessary at this point to make a brief comment on the effect of aluminium oxide on the results of these simulations. Aluminium oxides very readily, so the targets irradiated in this experiment will have a thin layer of aluminium oxide on their surface, roughly 2 nm to 3 nm thick [99, 100, 101]. The transmission of aluminium oxide at 46.9 nm is significantly lower than that of pure aluminium [3], so it is important to verify that this does not significantly reduce the validity of the spatially resolved algorithm.

To simulate the effect of the aluminium oxide two layer thicknesses were tested, 2 nm and 3 nm, which were applied to the incident radiation as a simple multiplier on the radiation incident at the target surface (i.e. effectively acting as a perfect filter). This is a crude approximation, but given the lack of hydrodynamic motion in the algorithm it is an adequate one. It will however overestimate the reduction in the radiation reaching the pure aluminium as in reality the oxide layer would after time heat up and expand away from the surface, reducing any effect it had on the absorption.

Figure 5.23 shows the ablation depths predicted by the algorithm using both the Saha-Boltzmann based and FLYCHK ionization models for a range of incident fluences and both thicknesses of aluminum oxide layer, as well as the simulation results without aluminium oxide shown in figure 5.20. The effect of these aluminium oxide layers on the ablation depth is predicted to be very minimal, in the order of a few nanometers. As this is an over estimation of the impact of this layer on the final result, it is confirmation that neglecting this layer in our simulations is justified. This conclusion makes sense as the layer is only a few nanometers thick and on the scale of the ablation this is almost negligible, not to mention the rapid expansion the layer will undergo in experiment.

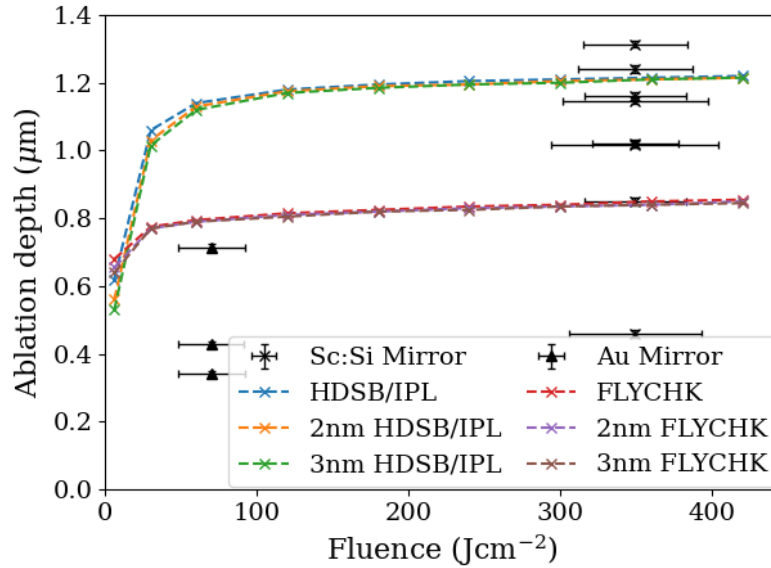


Figure 5.23: Ablation depths as a function of incident fluence as predicted by the spatially-resolved model with ionization calculated using FLYCHK (red, purple, & brown curves) and the Saha-Boltzmann model (blue, orange, & green curves) for an aluminium target at solid density. The three curves shown for each model are calculations simulating an aluminium oxide layer at the surface of 0 nm, 2 nm, and 3 nm thickness. Experimentally measured ablation depths (see Chapter 3) are also shown.

## 5.5 Summary and Conclusions

In this chapter we have taken the zero dimensional calculations made in Chapter 4 and extended them to a temporally-resolved version and a one-dimensional temporally-resolved version. The initial temporally-resolved model was intended to account for temporal variation in the incident radiation. This algorithm showed an approximately linear relationship between the maximum plasma temperature achieved and the peak incident fluence. Transmission calculations showed little support for the bleaching wave model at most irradiances, however the gold did show complete bleaching of the cell at high fluence. For aluminium and copper the transmission equilibrates below 80%, which is still a significant amount of absorption. These results would indicate that a bleaching wave model should be applicable for a gold target.

The spatially resolved algorithm was then used to predict the depth of ablation propagation into the three target metals using both ionization models. The shape of this propagation was approximately logarithmic, which is consistent with the absorption mechanism's basis in the Beer-Lambert law. Both ionization models predicted

significantly lower ablation depths in the high  $Z$  metals gold and copper. This is the result that was initially expected, given the similarity of this model to the Gamaly model, but was not suggested by the zero-dimensional model for gold. The maximum temperatures reached for gold peak at around 150 eV, which is consistent with the temperatures at which bleaching behaviour was observed in the earlier calculations. It appears however that there is still a limit to the penetration of radiation into the target. This is likely a result of the lack of hydrodynamic motion in the model.

The results for aluminium agreed more closely with experimentally observed ablation depths, but spread of the experimental data makes accurate assessment of this difficult. The algorithm does predict the sharpest part of the logarithmic curve to occur at much lower fluences than the experimental results would suggest. It also implies a limit, or saturation point, to the ablation depth which again is likely due to the lack of hydrodynamic motion. In an experimental interaction the plasma would expand out of the interaction region which would allow for greater penetration into the target, and higher fluences would speed up this process allowing for even greater depths to be achieved.

The comparison of the absorption coefficients in Chapter 4 was favourable for the Saha-Boltzmann based model, which indicates that a degeneracy-corrected absorption model dominated by inverse bremsstrahlung absorption should prove accurate, certainly in aluminium if not in gold and copper. The results shown here suggest that the lack of hydrodynamic motion is limiting the achievable ablation depth un-physically, which is most apparent in the high  $Z$  metals gold and copper. The ideal model would therefore combine these more accurate absorption coefficients with a model containing hydrodynamic motion. Chapter 6 looks at a possible one dimensional candidate and uses it to replicate some of the results shown here.

## Chapter 6

# Hydrodynamic simulations of EUV ablation

In Chapter 5 a constant density model of ablation was presented and compared to experimental ablation depths presented in Chapter 3. These simulations showed good agreement with the experimental ablation depths seen on aluminium targets, but not with those seen on gold and copper targets. Particularly for gold and copper, where EUV attenuation lengths are short ( $\approx 10$  nm), hydrodynamic expansion is likely to play an important role in allowing radiation to propagate into the target. For this reason, a hydrodynamics code was sought to model short wavelength ablation interactions. The detailed modelling of ionization and EUV laser absorption in earlier chapters shows that the standard models of ionization (e.g. the Saha-Boltzmann model) and laser absorption (by inverse bremsstrahlung) are suitably accurate and hence that standard laser-plasma hydrodynamic codes can be employed.

In this Chapter a series of simulations are undertaken using the one-dimensional radiation-hydrodynamics code MULTI-IFE. The code incorporates some sophisticated energy transport modelling involving electron-phonon energy conduction which is important in modelling laser ablation at moderate intensities ( $10^{10}$  W cm $^{-2}$  to  $10^{12}$  W cm $^{-2}$ ) in the EUV wavelength range. The hydrodynamics modelled by the code also account for the motion of ablated material. The plasma ionization is calculated using a modified form of the Thomas-Fermi model [102, 103], which is most accurate in systems with partially ionized ions of high atomic number material at high densities – as is the case in our EUV ablation interactions. For each combination of parameters a range of fluences are simulated and an ablation depth extracted from each in order to produce curves of ablation depth as a function of fluence. These curves are

compared against those collected experimentally to see if MULTI-IFE could be used as a suitable model for predicting the ablation depths seen in short wavelength ablation interactions.

The source code for MULTI-IFE is freely available [104] and is designed to be easily edited to suit the intended purpose. The ability to edit the source code is important. MULTI-IFE was originally designed for visible or infra-red laser plasma interactions with absorption by inverse bremsstrahlung, so in order to model EUV laser-plasma interactions the code must be adjusted to model EUV inverse bremsstrahlung more accurately.

## 6.1 MULTI-IFE

MULTI-IFE is a one-dimensional radiation-hydrodynamics code and is the culmination of a series of developments of the code MULTI [57, 105, 9]. The MULTI-IFE iteration of the code includes physics relevant to inertial fusion energy (or IFE – another name for ICF) such as thermonuclear burning and alpha particle transport. This is in addition to the calculation of two-temperature hydrodynamics, laser light absorption, heat conduction, and multi-group radiation transport included in MULTI and MULTI-fs.

The plasma is modelled as a two component fluid described by continuous variables in space and time. The fluid description is Lagrangian, meaning the independent variable is not the position  $x$ , but the mass variable  $\mu(x, t)$ , given by

$$\mu(x, t) = \int_{-\infty}^x \rho(x', t) dx'. \quad (6.1)$$

Cells therefore conserve mass and may not necessarily be of equal physical size.

In ICF plasmas, quasi-neutrality is preserved, meaning the densities of the electrons and ions,  $n_e$  and  $n_i$ , satisfy the relation  $n_e \simeq Z_i n_i$ . A consequence of this is that the species have roughly the same fluid velocity ( $v_e \simeq v_i$ ). This in turn results in a significant discrepancy between the species temperatures  $T_e$  and  $T_i$  due to the differences in electron and ion mass; hence the development and use of a two-temperature approach. As mentioned in section 4.1 however, the long timescales of CDL interactions make electron-ion equilibration likely, so these temperatures would be expected to be approximately equal at late times.

The equation of state is an important part of a plasma fluid model, as it relates important thermodynamic properties such as pressure and temperature and captures information about the state of the simulated matter. MULTI-IFE uses the Quotidian

Equation of State (QEOS) [102, 103], a general-purpose theoretical model designed to operate without an external database such as the SESAME look-up tables [106]. QEOS is a two-temperature model that generates smooth functions of pressure, energy, entropy, Helmholtz free energy, and their derivatives. The electron ionization equilibrium is calculated using the Thomas-Fermi model [107], adjusted using a semi-empirical bonding correction propose by Barnes [108]. The ion equation of state combines the Debye, Grüneisen, and liquid-scaling laws using a method developed by Cowan [109]. Significantly, QEOS can be used to differentiate between the ablated and non-ablated mass in our simulations.

Of the remaining physical details of the code, the laser deposition algorithm is the most important from our perspective and is detailed below. Details of the algorithms for hydrodynamics, heat transport, and radiation transport are given (in their most up-to-date form) in reference [9].

The principle drawback to using MULTI-IFE is the one-dimensional structure of the code. Laser ablation is a three-dimensional interaction, and treating it in just one dimension will lead to inaccuracies. However, as discussed in section , the aspect ratio of these interactions is low, meaning the lateral temperature gradients are shallow and significant lateral transport is unlikely. Of the materials investigated, the effect of lateral transport on the aluminium target ablation depths is likely to be much higher than on those of the gold target due to the longer attenuation length of aluminium to 46.9 nm radiation.

## 6.2 Laser deposition algorithm

Laser deposition in MULTI-IFE is treated in the quasi-static approximation meaning density and temperature profiles are used to calculate deposition and any photon time of flight retardation effects are ignored. The absorption is considered as solely due to inverse bremsstrahlung in the under-dense region and then as a dump at the critical density (simulating resonance absorption). When the laser wavelength is not of the order of the plasma scale length, as is the case for ICF plasmas, the code can calculate the deposition using the Wentzel-Kramers-Brillouin (WKB) approximation. With EUV laser ablation at 46.9 nm, the critical density ( $5.07 \times 10^{23} \text{ cm}^{-3}$ ) is above the electron densities produced by the laser, so the critical density dump does not occur.

The WKB approximation is a mathematical method for finding approximate solutions to linear differential equations [110]. It is named after physicists Gregor Wentzel,

Hendrik Anthony Kramers, and Léon Brillouin, who developed the method in 1926 [111, 112, 113]. The method applies to differential equations whose highest order derivative is multiplied by some small parameter  $\epsilon$ . The general form of the WKB approximation asserts that a differential equation of the form

$$\epsilon \frac{d^n y}{dx^n} + a(x) \frac{d^{n-1} y}{dx^{n-1}} + \dots + k(x) \frac{dy}{dx} + m(x)y = 0 \quad (6.2)$$

has a solution in the form of an asymptotic series expansion, given by

$$y(x) \sim \exp \left[ \frac{1}{\delta} \sum_{n=0}^{\infty} \delta^n S_n(x) \right], \quad (6.3)$$

provided we are in the limit where  $\delta \rightarrow 0$ . By substituting this solution into the original equation and cancelling out the exponential terms, it is possible to solve for any number of terms  $S_n(x)$ . In modelling of light propagation, the WKB approximation becomes equivalent to ray tracing following the refractive index  $n$ , allowing for a ‘swelling’ of the laser electric field  $E$  to  $E/n$ .

The application of the WKB approximation in MULTI-IFE is described as follows. The incident laser radiation can actually be considered to be two beams, an incident beam propagating in the positive  $x$  direction, and a reflected beam propagating in the negative  $x$  direction. Reflected beam components are generated wherever the refractive index changes, however these reflections are only significant close to the critical density. The intensities of these beams are given by

$$\begin{aligned} \frac{dI_+}{dx} &= KI_+ \\ \frac{dI_-}{dx} &= -KI_- \end{aligned} \quad (6.4)$$

where  $K$  is the absorption coefficient. Appendix B of [105] gives the full derivation of  $K$ , we shall simply quote this here, as

$$K \simeq \frac{\nu_{ei} \omega_e^2}{c \omega} \frac{1}{\sqrt{1 - \omega_e^2/\omega^2}} \quad (6.5)$$

where  $\nu_{ei}$  is the electron-ion collision frequency and  $\omega_e$  is the electron plasma frequency. The WKB approximation is then used to solve the expression

$$\frac{dI_{\pm}}{dx} \mp \frac{\nu_{ei} \omega_e^2}{c \omega} \frac{I_{\pm}}{\sqrt{1 - \omega_e^2/\omega^2}} = 0. \quad (6.6)$$

The discretization of this calculation is detailed further in [57, 105].

The formulation of the inverse bremsstrahlung absorption coefficient used by MULTI-IFE’s WKB algorithm places significance on the electron-ion collision frequency calculation and the model by which this is calculated. The two relevant models available to use in MULTI-IFE are discussed in section 6.3.

### 6.2.1 Adjustments

Expressions for the absorption coefficient of plasma material to light of frequency  $\nu$  vary with frequency  $\propto 1/\nu^3$  for x-rays and  $\propto 1/\nu^2$  for visible/infra-red radiation [48]. The difference arises because at visible and infra-red wavelengths, stimulated emission effects on the absorption can be neglected. If we wish to use MULTI-IFE for EUV laser simulations, we need to take account of stimulated emission as the low frequency (visible/infra-red) approximation for inverse bremsstrahlung is used in MULTI-IFE's laser absorption model.

In order to include stimulated emission into the absorption coefficient, a corrective factor was developed from equation 2.27. In the long wavelength limit, where  $\hbar\omega \ll k_B T$ , the stimulated emission term in equation 2.27 will tend to its exponent like so

$$1 - \exp\left(-\frac{\hbar\omega}{k_B T}\right) \rightarrow \frac{\hbar\omega}{k_B T}. \quad (6.7)$$

The correction factor  $C$  must remove this implicitly included factor and multiply by the full form.  $C$  is therefore given by

$$C = \frac{k_B T}{\hbar\omega} \left[ 1 - \exp\left(-\frac{\hbar\omega}{k_B T}\right) \right]. \quad (6.8)$$

The corrected and un-corrected forms of the absorption coefficients for 1.064  $\mu\text{m}$  and 46.9 nm light incident on an aluminium plasma with an electron density of  $1 \times 10^{20} \text{ cm}^{-3}$  (below the critical density for both wavelengths) are calculated as a function of temperature (using the Saha-Boltzmann model for the ionization populations) and shown in figures 6.1 and 6.2 respectively. Figure 6.1 shows good agreement between the corrected and un-corrected absorption coefficients at temperatures above 10 eV. In the lower temperature limit, the condition  $k_B T \gg \hbar\omega$  no longer applies. Under these conditions we would expect the corrected version to be more accurate. For optical wavelength ablation interactions this regime is rarely seen due to the higher typical electron temperatures, hence the use of the approximate form. Figure 6.2 shows almost no agreement between the corrected and un-corrected absorption coefficients, with the two curves differing in both magnitude and general shape. The adjustment to MULTI-IFE would therefore seem necessary for accurate ablation modelling.

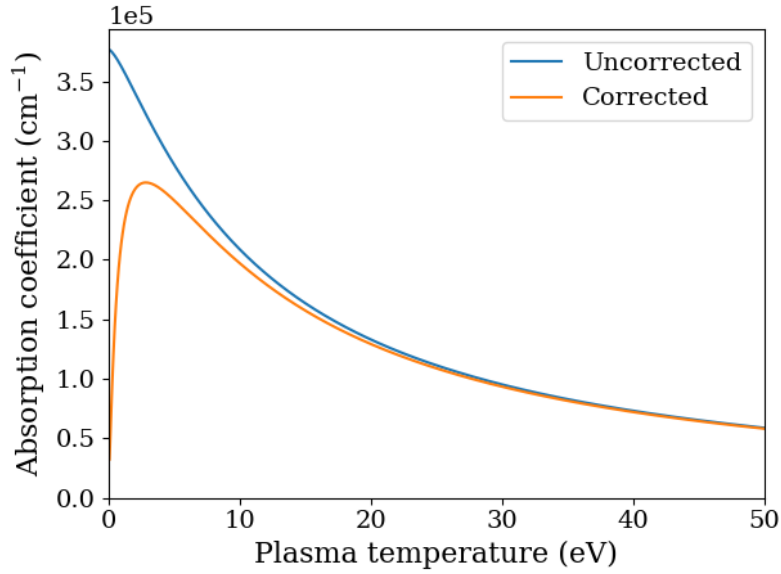


Figure 6.1: Corrected and un-corrected absorption coefficients as a function of plasma temperature for an aluminium plasma with electron density  $n_e = 1 \times 10^{20} \text{ cm}^{-3}$  and incident radiation at  $1.064 \mu\text{m}$ .

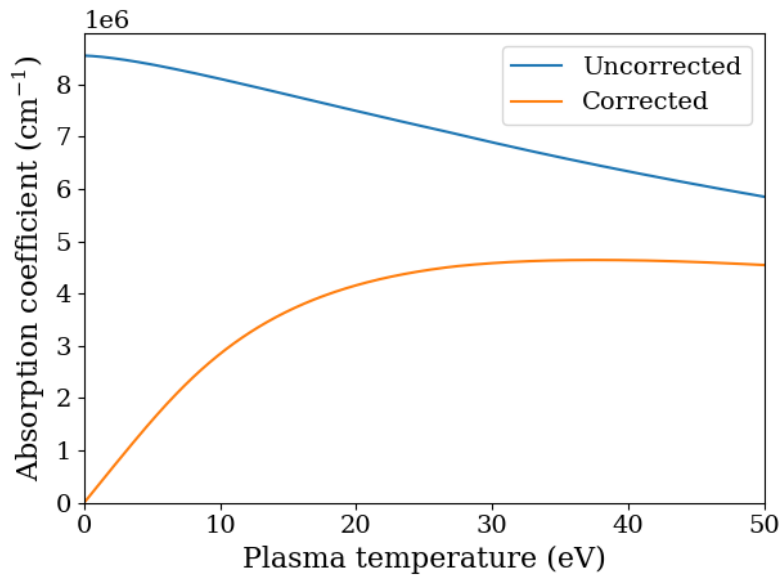


Figure 6.2: Corrected and un-corrected absorption coefficients as a function of plasma temperature for an aluminium plasma with electron density  $n_e = 1 \times 10^{20} \text{ cm}^{-3}$  and incident radiation at  $46.9 \text{ nm}$ .

A small number of changes needed to be made to MULTI-IFE in order to apply the correction factor  $C$  without any errors. A list of these changes is included in Appendix A. In making any changes to the source code, we must be careful to preserve the

existing functionality. This is easily assessable with a simple test; the affect of this change to the absorption coefficient will only become apparent at shorter wavelengths. We can therefore run the code both with and without the change at an arbitrary test intensity for optical and EUV wavelengths and observe the outcome – see section 6.5.1.

### 6.3 Electron collision frequency

As mentioned in section 6.2, the laser deposition module uses an absorption coefficient expression that is dependent on the electron-ion collision frequency. This parameter is the frequency of collisions between electrons and ions within the plasma and plays a key role in important processes in laser-plasma interactions such as laser absorption, electron-ion energy transfer, electronic heat conduction, and electrical conductivity to name but a few. MULTI-IFE has three possible calculation methods for calculating the electron-ion collision frequency, of which two were used in our investigations. The two models used were a classical model, treating the target as an ideal plasma even at  $t = 0$ , and an electron-phonon model, that aims to account for electron scattering by the electron-phonon interaction by an ad hoc interpolation scheme.

#### 6.3.1 Classical collision frequency

For high temperature, well ionized plasmas, a well established classical theory exists that gives an expression for the electron-ion collision frequency. For an ideal plasma, the electron-ion collision frequency  $\nu_{ei}$  is given by Spitzer’s formula [56]

$$\nu_{\text{Spitzer}} = \frac{4}{3} \sqrt{\frac{2\pi}{m_e}} \frac{\ln \Lambda e^4 Z_i n_e}{(k_B T_e)^{3/2}} \quad (6.9)$$

where  $T_e$  is the electron temperature and  $\ln \Lambda$  is the Coulomb logarithm. The plasma ionization  $Z_i$  is given by a modified Thomas-Fermi model [102, 103].  $\Lambda$  is given by the ratio  $b_{\text{max}}/b_{\text{min}}$  between the maximum  $b_{\text{max}}$  and minimum  $b_{\text{min}}$  impact parameter for collisions between electrons and ions. The maximum impact parameter  $b_{\text{max}}$  is usually given by the Debye length  $\lambda_D$  where

$$\lambda_D = \frac{v_{th}}{\omega_e} = \sqrt{\frac{k_B T_e}{m_e}} \sqrt{\frac{m_e}{\epsilon_0 n_e e^2}} \quad (6.10)$$

where  $v_{th}$  is the electron thermal velocity. The minimum impact parameter  $b_{\text{min}}$  is the larger of the classical distance of closest approach for an electron-ion collision  $d_{ei}$ , given by

$$d_{ei} = \frac{Ze^2}{2k_B T_e}, \quad (6.11)$$

and the de Broglie wavelength  $\lambda_{dB}$ , given by

$$\lambda_{dB} = \frac{h}{m_e v_{th}} = \frac{h}{2\sqrt{k_B T_e m_e}}. \quad (6.12)$$

In the case of laser absorption the maximum impact parameter  $b_{\max}$  is actually chosen to be

$$b_{\max} = \frac{v_{th}}{\max(\omega_e, \omega)} \quad (6.13)$$

in order to account for dynamical effects that occur when high frequency laser radiation is concerned, i.e. where  $\omega > \omega_e$ .

This expression for the electron-ion collision frequency is most applicable to hot, low density, high ionized plasmas. This is therefore clearly not ideal in the case of nanosecond pulse EUV laser-plasma interactions where WDM is likely to be generated. A more appropriate model for these plasma conditions is given by the electron-phonon collision frequency.

### 6.3.2 Electron-phonon collision frequency

The electron-phonon formulation of the electron-ion collision frequency aims to reconcile the two limits of cold solid material and hot ideal plasma. A unique theory covering the entire range does not exist, so the results for each limit are applied and then joined smoothly with an interpolation in the transition range. This model is detailed fully in reference [59]; the key points are quoted here.

In the hot ideal plasma limit, Spitzer's formula is used (equation 6.9). In the cold solid limit the electron-ion collision frequency is no longer dependent on electron temperature, rather it is dominated by phonon scattering and lattice vibrations. An electron-ion collision frequency for the degenerate matter of white dwarf and neutron stars is developed in reference [58] and is implemented in MULTI-IFE in its approximate form

$$\nu_{el-phonon} \approx 2k_s \frac{e^2 k_B T_i}{\hbar^2 v_F} \quad (6.14)$$

where  $T_i$  is the ion temperature and  $v_F$  is the Fermi velocity given by

$$v_F = \frac{\hbar}{m_e} (3\pi^2 n_e)^{1/3}. \quad (6.15)$$

The approximate form is accurate when  $v_F \ll c$  and the ion plasma frequency  $\omega_i$  fulfills the criterion  $\hbar\omega_i \ll k_B T_i$ . The constant  $k_s$  is used to adapt the electron-ion collision frequency to measured values of the cold metal. As this is an approximation, the value of  $k_s$  must be changed for each material property being calculated. Equation 6.14 has

the correct linear scaling for the electron-ion collision frequency as it rises with the lattice temperature of the solid  $T_i$ .

Interpolation between equations 6.9 and 6.14 is conducted by taking the harmonic mean of the two electron-ion collision frequencies like so

$$\nu_{ei}^{-1} = \nu_{\text{Spitzer}}^{-1} + \nu_{\text{el-phonon}}^{-1}. \quad (6.16)$$

The electron-ion collision frequency curve as a function of temperature generated by this interpolation for an aluminium target is shown in figure 6.3.

The limiting curve marked  $v_e/r_0$  is a plausible criterion that the electron mean free path  $\lambda_e$  cannot be less than the inter-atomic distance  $r_0$ , i.e.

$$\lambda_e > r_0 = \left( \frac{3}{4\pi n_i} \right)^{1/3}. \quad (6.17)$$

This is equivalent to the requirement that  $\nu < v_e/r_0$ , where  $v_e$  is the characteristic electron velocity given by

$$v_e = \sqrt{v_F^2 + \frac{k_B T_e}{m_e}}. \quad (6.18)$$

The value of electron-ion collision frequency calculated for cold, solid aluminium in figure 6.3 has been calculated from a measured reflectivity of  $R = 0.92$  for optical wavelength light incident on aluminium. The reflectivity of a material at normal incidence is given by

$$R = \left| \frac{\hat{n} - 1}{\hat{n} + 1} \right|^2 \quad (6.19)$$

where  $\hat{n}$  is the refractive index of the material, given by

$$\hat{n}^2 = 1 - \frac{\omega_e^2}{\omega(\omega - i\nu_{ei})}. \quad (6.20)$$

By combining and rearranging these two equations it is possible to calculate a value for the electron-ion collision frequency of cold solid aluminium;  $\nu_{ei} = 8.5 \times 10^{14} \text{ s}^{-1}$  assuming  $Z_i = 2.5$  for cold aluminium [**h:More**] giving  $n_e = 1.5 \times 10^{23} \text{ cm}^{-3}$ . This value is consistent with a constant in the expression for  $\nu_{\text{el-phonon}}$  (equation 6.14) of  $k_s = 9.4$ .

There are two further parameters, other than the inverse bremsstrahlung absorption coefficient, where the electron-ion collision frequency is required in MULTI-IFE's calculations. These are the thermal heat conductivity and the electron-ion coupling coefficient. The interpolated form of the electron-ion collision frequency is used for both, which means that the constant  $k_s$  in equation 6.14 must be changed to correspond to the correct cold solid value in each case.

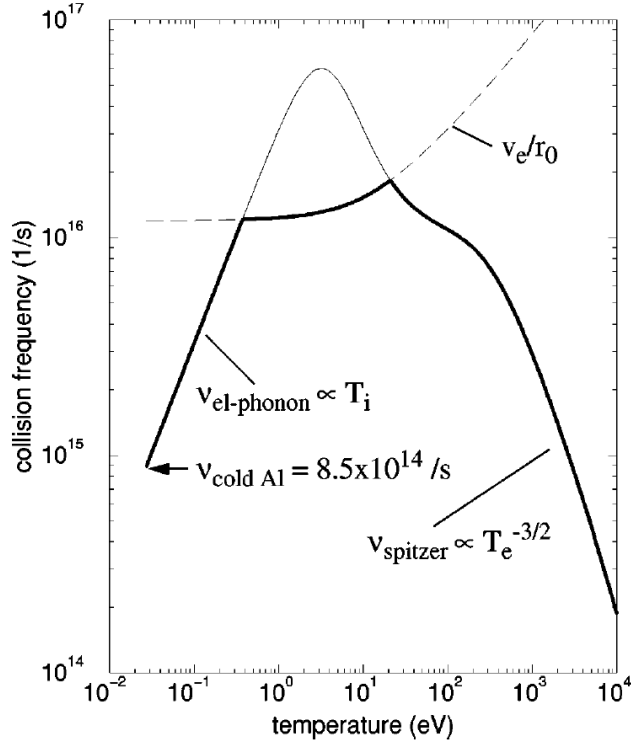


Figure 6.3: Electron-ion collision frequency values as a function of temperature as predicted by the electron-phonon and Spitzer (classical) collision frequency models. An interpolation between the electron-phonon and Spitzer model is shown as a solid curve [59].

The thermal heat conductivity  $\kappa$  is related to the electrical conductivity (and through this to the electron-ion collision frequency) by the Wiedemann-Franz law;  $\kappa \propto \sigma T$ . The Spitzer formula for  $\kappa$  in a hot ideal plasma is given by [56]

$$\kappa = \frac{\kappa_0 n_e k_B^2 T_e}{m_e \nu_{ei}} \quad (6.21)$$

where  $\kappa_0$  is a dimensionless correction factor [56] and  $\nu_{ei}$  uses the Spitzer value (equation 6.9). To extend this model to the warm dense matter and cold solid limit, the Spitzer value for the electron-ion collision frequency is replaced with the interpolated value (equation 6.16). For cold solid aluminium, this correspond to a constant in  $\nu_{el-phonon}$  of  $k_s = 2.3$ .

The electron-ion coupling coefficient  $\gamma$  for a hot ideal plasma is given by [56]

$$\gamma = \frac{1}{\tau_i} \frac{d\epsilon_i}{dT} = \frac{3m_e k_B \nu_{ei}}{m_i^2} \quad (6.22)$$

where  $d\epsilon_i/dT$  is the specific heat capacity of the ions (given by  $3k_B/2m_i$  in an ideal gas) and  $\tau_i$  is the characteristic heating time for the ions (given by  $\tau_i = m_i/2m_e \nu_{ei}$ ).

Again, to generalize across the entire temperature range the interpolated value of the electron-ion collision frequency is used (equation 6.16). The value of the characteristic heating time  $\tau_i$  for cold solid aluminium has not been reported, and so this value has been extrapolated in reference [59] from reported values for heavier metals. For cold solid aluminium,  $\tau_i = 10$  ps to 20 ps. Eidmann *et al.* [59] choose  $\tau_i = 20$  ps for their simulations, which corresponds to a constant in  $\nu_{\text{el-phonon}}$  of  $k_s = 13$ .

## 6.4 Methodology for simulations

As with all modelling discussed in Chapters 3, 4, and 5, MULTI-IFE will be used to generate predictions of ablation depth as a function of fluence that can be compared to experimental data. This is where a key limiting factor of MULTI-IFE arises – the use of externally generated equation of state (EOS) tables to reduce computation times. The package is provided with relevant files for aluminium and gold, but no such files for copper. Fortunately, the general ablation behaviour of gold and copper appears to be similar (as may be expected from their similar attenuation lengths) and so the omission of copper simulations does not detract from the usefulness of simulations with MULTI-IFE.

### 6.4.1 The electron-phonon model for gold

As we wish to use both the classical and electron-phonon models for the electron-ion collision frequency, it is necessary to calculate the values of the constant  $k_s$  (in equation 6.14) required for the calculation of the absorption coefficient, thermal heat conductivity, and electron-ion coupling coefficient for a gold target. Values of the constant  $k_s$  for aluminium given by Eidmann *et al.* [59] are summarised in table 6.1. A value for the electron-ion collision frequency for gold (corresponding to the absorption coefficient) is given in [114], so equation 6.14 can be used to find a value for the constant  $k_s$  of 1.04 for the absorption coefficient. The measured properties of gold needed to calculate  $k_s$  for the electron-ion coupling coefficient are given in [115], so equations 6.14 and 6.22 were used to find a range of values for the constant  $k_s$  of 7.4 – 51.7. This range is due to the range of measured characteristic ion heating times in gold.

The value of  $k_s$  required for the thermal heat conductivity  $\kappa$  calculation for gold was calculated by another route. The full equation (substituting in where appropriate)

| Target | K (fheat) | $\kappa$ (fei) | $\gamma$ (flaser) |
|--------|-----------|----------------|-------------------|
| Al     | 9.4       | 2.3            | 13 – 26           |
| Au     | 1.04      | 1.7            | 7.4 – 51.7        |

Table 6.1: Constant  $k_s$  values for aluminium and gold as required by the electron-phonon electron-ion collision frequency model, labelled with associated variables in the MULTI-IFE input file. Al values are from [59] and Au values are deduced in the text.  $K$  is the absorption coefficient (equation 6.5),  $\kappa$  is the thermal heat conductivity (equation 6.21) and  $\gamma$  is the electron-ion coupling coefficient (equation 6.22).

for the thermal heat conductivity using the electron-phonon model value for  $\nu_{ei}$  is

$$\kappa = \frac{\kappa_0 n_e k_B^2 T_e \hbar^3 (3\pi^2 n_e)^{1/3}}{2k_s m_e^2 e^2 k_B T_i}. \quad (6.23)$$

This means that the proportionality for  $\kappa$  can be reduced to  $\kappa \propto (\kappa_0 n_e^{4/3} T_e)/(k_s T_i)$ . Assuming  $T_e \simeq T_i \simeq 0.03eV$  and  $\kappa_0^{\text{Al}} \simeq \kappa_0^{\text{Au}}$  [56] means that to find  $k_s^{\text{Au}}$  one can use the expression

$$k_s^{\text{Au}} = \left( \frac{n_e^{\text{Au}}}{n_e^{\text{Al}}} \right)^{4/3} \frac{\kappa^{\text{Al}}}{\kappa^{\text{Au}}} k_s^{\text{Al}}, \quad (6.24)$$

which yields a value of  $k_s = 1.7$  for the electron-ion collision frequency in the thermal heat conductivity calculation. A summary of the values of  $k_s$  for aluminium and gold is shown in table 6.1.

#### 6.4.2 Controlling MULTI-IFE

MULTI-IFE simulation parameters are set in an input file which is read at the beginning of each simulation. The input file is divided into sections from which different aspects of the simulation can be controlled. The first section of the input file is the `&parameters` section. From here, different physical models can be selected, levels of functionality can be turned on or off, and program boundaries set. The parameters relevant to the simulations in this chapter are shown in table 6.2 with explanatory notes.

The next two sections are linked; these are the sections that define the material and the target mesh. The `&layer` section defines the mesh and the `&material` section imports the relevant material properties to accurately model the correct target material. The bulk of the `&material` section is devoted to importing parameters from the correct file, however the atomic and mass numbers are set in this section. The simulation parameters defined in the `&layer` section are detailed in table 6.3, again with explanatory notes.

| Input parameter                 | Input value | Notes   |
|---------------------------------|-------------|---|
| <code>igeo</code>               | 1           | This sets the simulation geometry to planar   |
| <code>nfuel</code>              | 0           | This sets the number of cells with DT fuel to zero so that no fusion is modelled  |
| <code>textit</code>             | 1.3 ns      | The total time model by the simulation  |
| <code>iright/ileft</code>       | 0 or 1      | These two parameters either do or do not limit the fluid motion of the model at the right and left boundaries respectively        |
| <code>iradio</code>             | 1           | Enables radiation modelling   |
| <code>ihydro</code>             | 1           | Enables hydrodynamics modelling   |
| <code>iheation</code>           | 1           | Enables ion heat conduction modelling   |
| <code>model</code>              | 0 or 1      | Selects the electron-ion collision frequency model: 0 = classical (Spitzer), 1 = electron-phonon                                  |
| <code>fheat, flaser, fei</code> | #           | Values for $k_s$ if model = electron-phonon; values in table 6.1  |
| <code>zmin</code>               | 0.1         | A minimum value for $Z_i$ must be set, 0.1 is chosen arbitrarily  |
| <code>flf</code>                | 1e6 or < 1  | The flux limiting factor (1e6 = unlimited)  |
| <code>dtmax, dtinit</code>      | 10 ps       | The maximum and initial time steps (a dynamic time step is used); setting <code>dtmax = dtinit</code> prevents loss of resolution |
| <code>dtaout</code>             | 100 ps      | The time interval between data outputs in the ascii output file   |

Table 6.2: List of relevant switches in the `&parameters` section of the input file with chosen or default values (in the correct units) and explanatory notes.

The final section of the input file is used to set the parameters of the incident laser pulse. This section is named after the algorithm used to calculate the laser deposition, in our case `&pulse_wkb` after the WKB algorithm. The simulation parameters defined in the `&pulse_wkb` section are detailed in table 6.4, again with explanatory notes.

| Input parameter       | Input value                    | Notes   |
|-----------------------|--------------------------------|---|
| <code>nc</code>       | #                              | The number of cells in the target   |
| <code>thick</code>    | $10^{-4}$ cm                   | The initial physical thickness of the target  |
| <code>r0</code>       | 2.7 or 19.3 g cm <sup>-3</sup> | The density of the target material  |
| <code>te0</code>      | 0.03 eV                        | Initial electron temperature (293 K)  |
| <code>ti0</code>      | 0.03 eV                        | Initial ion temperature (293 K)   |
| <code>zonpar</code>   | 0.975                          | The ‘gridding factor’   |
| <code>material</code> | ‘Al’ or ‘Au’                   | Calls the material defined in the <code>&amp;material</code> section; name must include quotation marks |

Table 6.3: List of relevant switches in the `&layer` section of the input file with chosen or default values (in the correct units) and explanatory notes.

| Input parameter     | Input value   | Notes  |
|---------------------|---|--|
| <code>inter</code>  | 1   | Determines direction of laser incidence (1 = from RHS)                   |
| <code>pimax</code>  | $10^{16}$ to $10^{18}$ erg s <sup>-1</sup> cm <sup>-2</sup> | Maximum laser intensity  |
| <code>pitime</code> | 1.2 ns  | Laser pulse duration   |
| <code>wl</code>     | $46.9 \times 10^{-7}$ cm                                    | Laser wavelength   |
| <code>itype</code>  | 1   | Sets the temporal pulse shape to $\sin^2 t$ (approximation for Gaussian) |
| <code>delta</code>  | 1   | Fraction of laser pulse absorbed at critical density                     |

Table 6.4: List of relevant switches in the `&pulse` section of the input file with chosen or default values (in the correct units) and explanatory notes.

### 6.4.3 Data output from MULTI-IFE

As MULTI-IFE carries out a simulation, it deposits values at requested intervals into an output file, `fort.11`, in the ascii format. A second file of values is also produced, `fort.10`, that can be interpreted by the graphic user interface that comes with the code. The former is preferred for our purposes as it is more easily manipulated using Python.

The output file contains a series of blocks of data, each labelled with the time step at which they were output. The blocks contain data points for each cell for each of

the chosen output values. The default output values are cell number ( $\#$ ), cell position (cm), fluid velocity ( $\text{cm s}^{-1}$ ), material density ( $\text{g cm}^{-3}$ ), electron temperature (eV), and deposited energy ( $\text{erg cm}^{-3}$ ). We have adjusted the code to allow output values for absorption coefficient ( $\text{cm}^{-1}$ ), and ion temperature (eV) as well.

Once a simulation has been complete, the `fort.11` file is opened and data plotted using a Python script combined with the Matplotlib figure plotting library. This code is used to assess ablation depths by inspection. Once a cursory inspection has been made, an accurate value for the ablation depth can be extracted from the MULTI-IFE simulations from the temperature using the equation of state.

## 6.5 Simulations of experimental ablation conditions

MULTI-IFE was used to model EUV laser-target interactions for fluences in the range seen in our ablation experiments. There are six independent parameters that can be varied in our simulations. The target material, and incident fluence have been key in earlier modelling investigations, and remain so here. Aspects of the MULTI-IFE code that add to these parameters are the two options for the electron-ion collision frequency model, a switch to limit fluid expansion at the rear of the target, and the adjustable thermal flux limiting factor. Before the main body of simulations can be conducted however, the adjustments made to the absorption mechanism – see section 6.2.1 – must be checked.

### 6.5.1 Testing the absorption coefficient correction

The adjustment made to the absorption coefficient in section 6.2.1, given by equation 6.8, effectively replaces the implicit approximation ignoring the effect of stimulated emission with a more accurate formula including stimulated emission (see equations 2.27 and 2.33). To test the absorption coefficient correction, MULTI-IFE was used to simulate the same intensity,  $1 \times 10^{11} \text{ W cm}^{-2}$ , of both  $1.064 \mu\text{m}$  and  $46.9 \text{ nm}$  wavelength light incident on an aluminium target; with and without the correction. For the time being the classical electron-ion collision frequency model was used. The absorption coefficient curves as a function of position at the end of the simulation ( $t = 1.3 \text{ ns}$ ) are shown in figure 6.4.

The curves shown in figure 6.4 suggest very similar absorption coefficients for both wavelengths with only a small deviation in value, mostly at lower temperatures. This does, however, ignore the method by which the code models resonance absorption (i.e. as a dump at the critical density). Figures 6.5 and 6.6 show the material density and electron temperature as a function of cell position for the same simulations ( $I = 1 \times 10^{11} \text{ W cm}^{-2}$ ,  $\lambda = 1.064 \mu\text{m}$  and  $46.9 \text{ nm}$ , aluminium target).

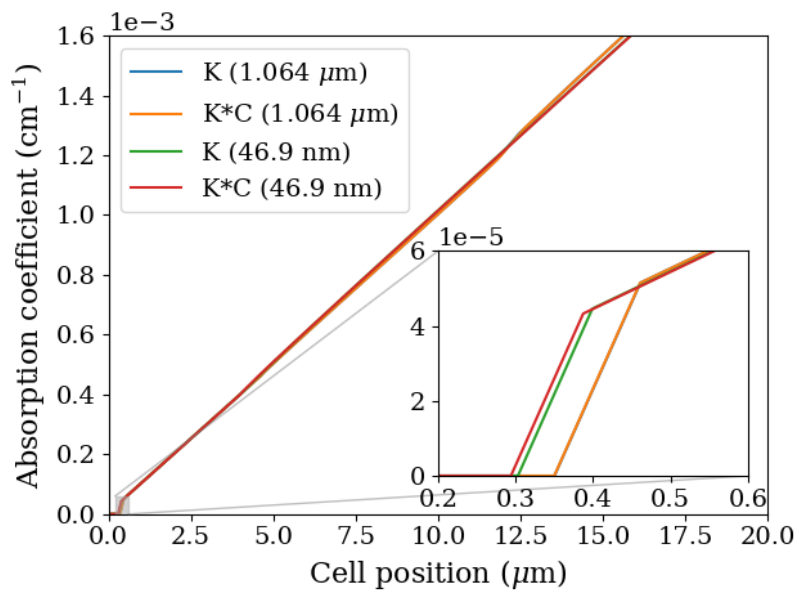


Figure 6.4: Absorption coefficient as function of cell position for a MULTI-IFE simulation of  $1 \times 10^{11} \text{ W cm}^{-2}$  of radiation incident on an aluminium target at time  $t = 1.2 \text{ ns}$ .  $K$  is the uncorrected absorption coefficient and  $K*C$  is the corrected form allowing for stimulated emission. The absorption coefficient for both  $1.064 \mu\text{m}$  and  $46.9 \text{ nm}$  wavelengths are shown.

These figures show the difference between the two scenarios much more clearly. Figure 6.5 shows the change in the density gradient that occurs in the under-dense region due to the extra heating from resonance absorption. This significantly lower density in the plume is reflected in figure 6.6 in the factor of 4 difference between the peak electron temperatures of the two wavelengths. The curves on both graphs also show how the effect of the correction for stimulated emission is larger for the shorter wavelength.

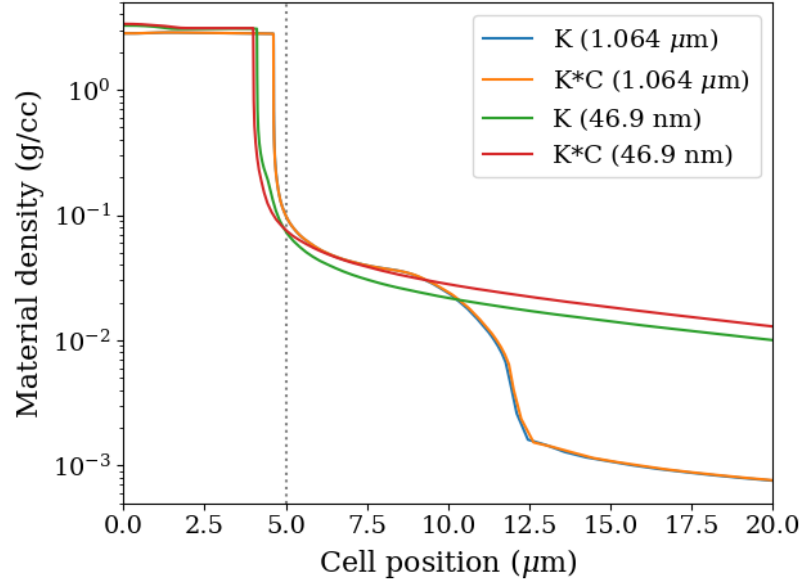


Figure 6.5: Material density as function of cell position for a MULTI-IFE simulation of  $1 \times 10^{11} \text{ W cm}^{-2}$  of radiation incident on an aluminium target at time  $t = 1.2 \text{ ns}$ . Curves for both corrected and uncorrected absorption at  $1.064 \mu\text{m}$  and  $46.9 \text{ nm}$  are shown.

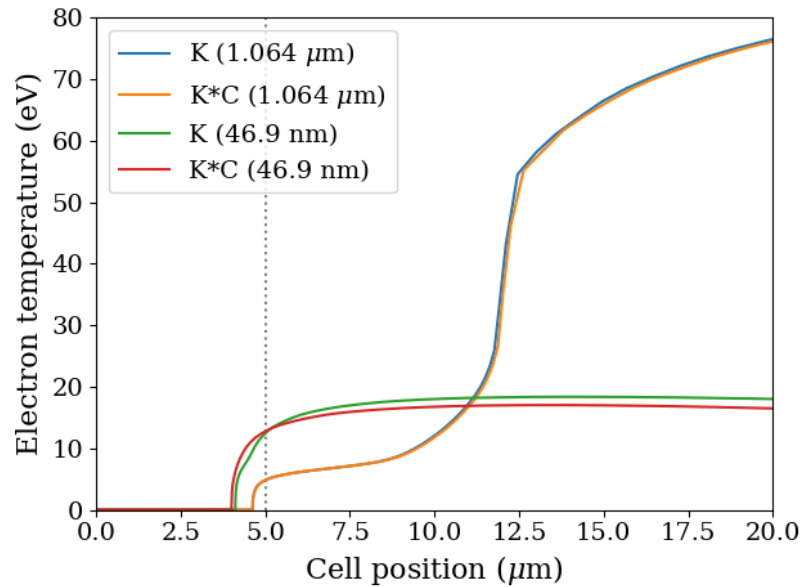


Figure 6.6: Electron temperature as function of cell position for a MULTI-IFE simulation of  $1 \times 10^{11} \text{ W cm}^{-2}$  of radiation incident on an aluminium target at time  $t = 1.2 \text{ ns}$ . Curves for both corrected and uncorrected absorption at  $1.064 \mu\text{m}$  and  $46.9 \text{ nm}$  are shown.

### 6.5.2 Initial testing of independent variables

Conducting simulations in MULTI-IFE introduces a number of additional independent variables to our problem. The large majority of these additional independent parameters are problem definition parameters. These affect the outcome of a simulation but are only present in the simulation and not in the physical system being represented. These will be investigated first, in the context of an aluminium target with an electron-phonon electron-ion collision frequency model. The parameters that fall into this category are the boundary at the backside of the target (fixed or unfixed), and the flux limiting factor. We must also consider the three values of  $k_s$  given in table 6.1 – there are a range of valid values of the constant  $k_s$  for calculating the electron-ion coupling coefficient of both materials. A parameter scan over the range of incident fluences was conducted for each parameter, with the same target material and electron-ion collision frequency model.

#### *The simulation backside boundary*

The first simulation parameter we will examine is the backside boundary. As mentioned earlier, the simulation treats the target as a block of solid density gas. This means that the target is more compressible than in reality, and will naturally expand without any energy input. The effect this has on the way the target behaves in a laser ablation interaction can be seen from figures 6.8 and 6.7. Figures 6.8 and 6.7 show material density as a function of cell position for an aluminium target, irradiated with a range of laser intensities. The electron-ion collision frequency model used is the electron-phonon model, with a value of  $k_s = 13$  for the `flaser` parameter.

In figure 6.8, the maximum density is very high, almost up to 40% above solid density due to material being compressed against the fixed rear of the target. More realistic maximum densities are seen in figure 6.7, but the rear of the target has expanded, which does not occur experimentally as the experimental targets are thicker (typically 100  $\mu\text{m}$ ) than those assumed for the simulations (5  $\mu\text{m}$ ). Assuming thinner targets in the simulations reduces simulation overheads in time and data storage.

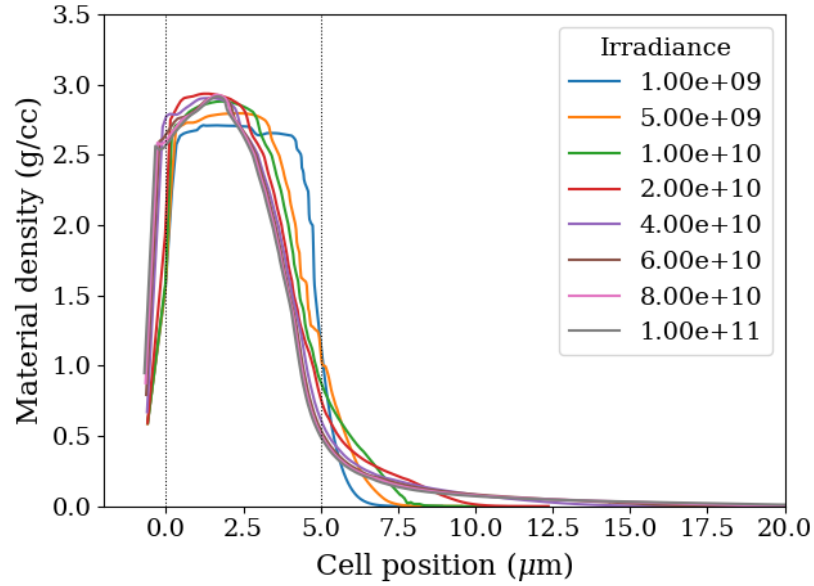


Figure 6.7: Material density as a function of cell position for a MULTI-IFE simulation of an aluminium target irradiated with a range of intensities in  $\text{W cm}^{-2}$  at 46.9 nm at time  $t = 1.2 \text{ ns}$ . The rear boundary of the target is allowed to expand. The thermal conduction includes electron-phonon conduction.

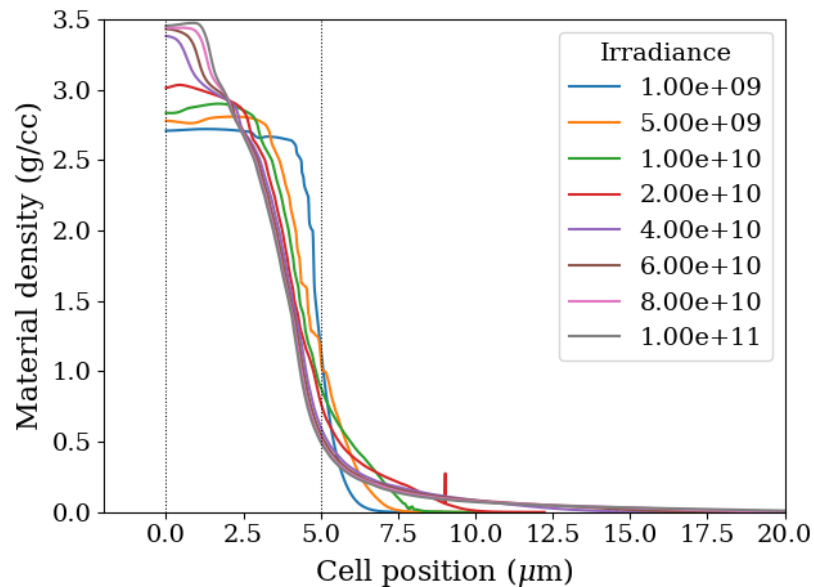


Figure 6.8: Material density as a function of cell position for a MULTI-IFE simulation of an aluminium target irradiated with a range of intensities in  $\text{W cm}^{-2}$  at 46.9 nm at time  $t = 1.2 \text{ ns}$ . The rear boundary of the target is fixed. The thermal conduction includes electron-phonon conduction.

Figure 6.9 shows the ablation depths predicted by the simulations shown in figures 6.8 and 6.7, using a criterion for ablated material of the density dropping below solid density ( $\rho < \rho_{\text{solid}}$ ). There is little difference between the ablation depths predicted using either a fixed or an unfixed boundary. Given the small difference between the models, the fixed boundary will be retained as it simplifies ablation depth extraction.

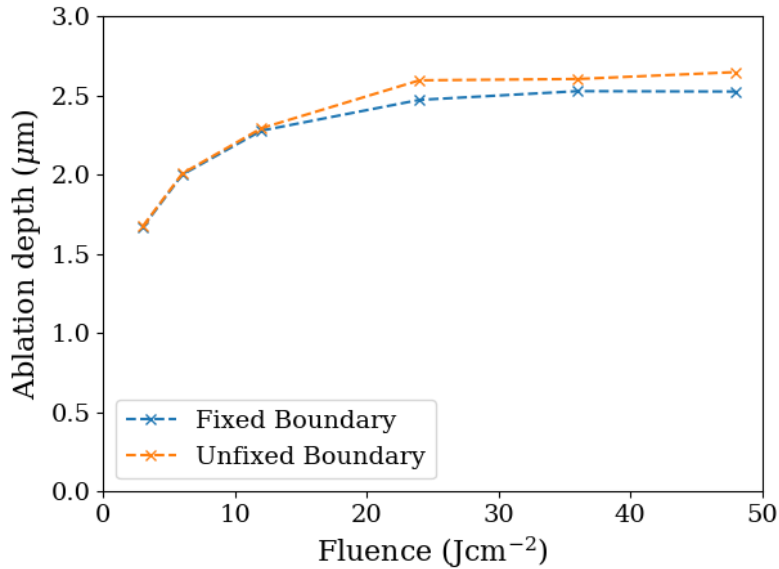


Figure 6.9: Ablation depths predicted by MULTI-IFE simulations of a range of fluences of 46.9 nm radiation incident on an aluminium target. Results for simulations with a fixed and unfixed (free) left boundary are shown.

### *The flux limiting factor*

Under some radiation conditions, the heat transport algorithm becomes invalid due to extreme temperature gradients. In these circumstances, an approximation is employed (see Section 4 of [9]) that sets a maximum value for the heat flux, limited to the physical maximum (the free-streaming limit – see section 2.4.2) multiplied by a flux limiting factor  $f$ . The value of  $f$  is set using the parameter `flf` in the input file. For our radiation conditions, EUV wavelengths at intensities of  $1 \times 10^9 \text{ W cm}^{-2}$  to  $1 \times 10^{11} \text{ W cm}^{-2}$ , the high critical density, lack of resonance absorption, and relatively low fluence mean extreme temperature gradients are unlikely. Nevertheless, we have investigated the effect of the flux limiter on the ablation depth as confirmation.

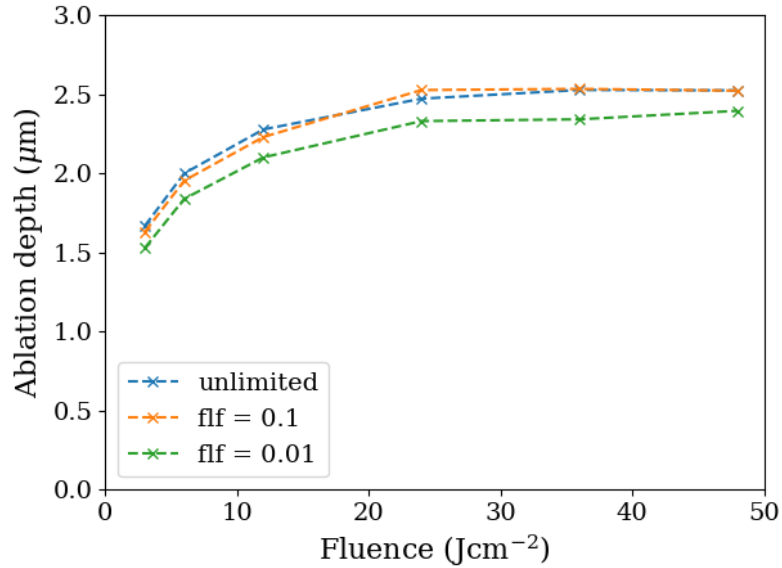


Figure 6.10: Ablation depths predicted by MULTI-IFE simulations of a range of fluences of 46.9 nm radiation incident on an aluminium target. Results for simulations without a flux limiting factor, and with a flux limiting factor of 0.1 and 0.01 are shown.

As with the left boundary investigation, the target is aluminium, the electron-ion collision frequency model is the electron-phonon model, and the criterion for ablated material is  $\rho < \rho_{\text{solid}}$ . Figure 6.10 shows the ablation depths as a function of fluence for simulations using flux limiting factors of  $f = 1 \times 10^6$  (unlimited), 0.1, and 0.01 and shows little effect from the flux limiting factors on the ablation depth. The factor of 100 reduction ( $f = 0.01$ ) has a larger impact as would be expected, but this is a smaller than typical value for the flux limiting factor. Overall, this is good evidence that the prediction of few extreme temperature gradients is correct, and a flux limiting factor is not required.

#### *The values for `flaser`*

The nature of the electron-phonon collision model is inherently empirical. The accuracy of the model depends on the accuracy of the measured properties that yield the  $k_s$  values shown in table 6.1. In the case of the electron-ion coupling constant  $\gamma$ , the values of  $k_s$  for aluminium are only approximate as they are interpolated from values for heavier elements (copper, silver, and gold). The values for gold are experimentally determined however the parameters of this experiment ultimately yield a range of values for  $\gamma$ . As a result, both materials have a range of possible suitable values for `flaser`. `flaser` is the parameter in the input deck into which you type the correct value of  $k_s$  (i.e. the

one for the electron-ion coupling constant  $\gamma$ ).

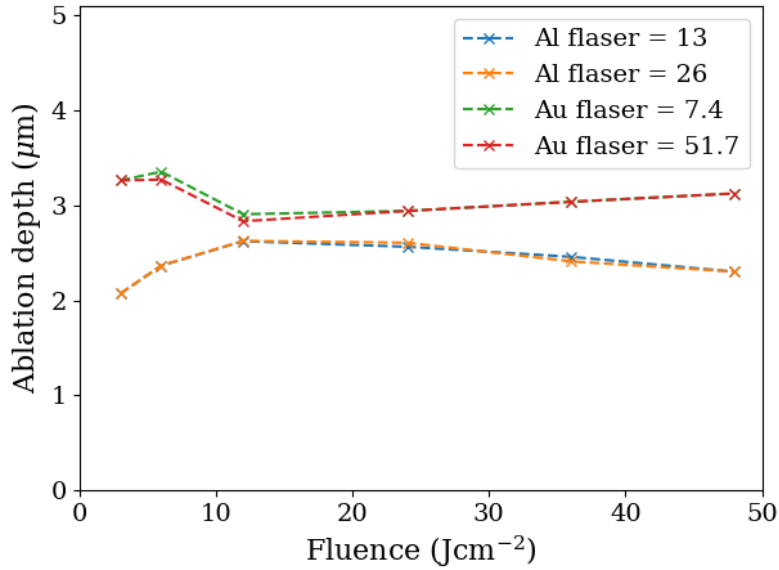


Figure 6.11: Ablation depths predicted by MULTI-IFE simulations of a range of fluences of 46.9 nm radiation incident on both aluminium and gold targets. Results for simulations with the maximum and minimum possible values of `flaser` are shown.

Figure 6.11 shows the ablation depth as a function of fluence for aluminium and gold targets with both maximum and minimum values of `flaser` (using the density-based ablation criterion). For both target materials, the impact of the change in `flaser` is very small. This is likely because the electron-ion coupling constant effects the heat transfer between the electrons and ions. On our nanosecond timescales, equilibration is not only possible but likely, and so a small change in the rate at which this occurs does not have a significant impact on the global ablation process. We shall follow Eidmann *et al.* [59] by using  $k_s = 13$  for aluminium, and  $k_s = 7.4$  for gold (i.e. the minimum  $k_s$  value for each material).

### 6.5.3 Comparing to experimental ablation depths

In order to compare the MULTI-IFE simulations to experimental results, a parameter scan over the range of incident fluences was conducted for each target material and each electron-ion collision frequency model. Extracting an ablation depth from such simulations requires that a criterion is chosen to determine which cells have been ablated. This is discussed below. The parameters discussed in 6.5.2 have been set as the following; left hand boundary fixed, flux limiter set to  $1 \times 10^6$  (unlimited), and `flaser`

set to the minimum values  $k_s = 13$  &  $7.4$  for aluminium and gold respectively.

The simulated ablation depth for each simulation was extracted from the equation of state by using the temperature and density of each cell to determine its phase. The empirical model developed by Cowan [109] that MULTI-IFE employs takes the Lindemann Melting Law [116] as its foundation for the solid-liquid phase transition, given by

$$T_m = \alpha \rho^{2/3} \Theta_D^2 \quad (6.25)$$

where  $T_m$  is the melting temperature,  $\Theta_D^2$  is the Debye temperature, and  $\alpha$  is a material specific constant independent of density or temperature. Cowan then uses the ratio between a reference density, given by  $\rho_{\text{ref}} = A/9Z^{0.3}(\text{gcm}^{-3})$  where  $A$  and  $Z$  are atomic mass and number respectively, and the solid density,  $\xi = \rho/\rho_{\text{ref}}$ , to determine whether the material is tightly or loosely bound. This gives the melting temperature  $T_m$  to be

$$k_B T_m = 0.32 \left[ \xi^{(2b+10/3)} / (1 + \xi)^4 \right] \text{ (eV)} \quad (6.26)$$

where  $b$  is a constant for any material given by  $b = 0.6Z^{1/9}$ . Cells with temperature above this density-dependent value are treated as being ablated and contribute to the ablation depth.

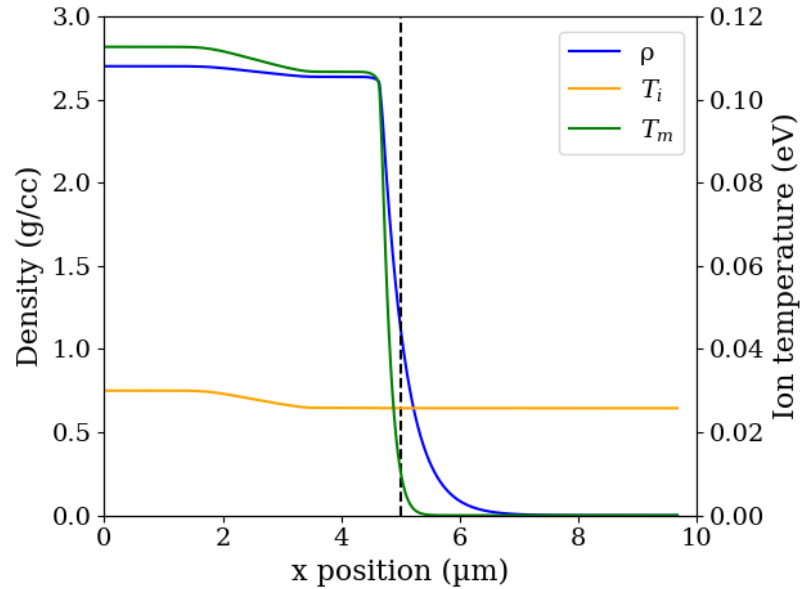


Figure 6.12: Density  $\rho$  and ion temperature  $T_i$  profiles predicted by MULTI-IFE after 1.2 ns simulations of an aluminium target with no incident radiation. Also shown is a profile of the melting temperature  $T_m$  for each cell.

MULTI-IFE treats the solid target essentially as a solid density fluid, so a degree of expansion can occur in the target without any incident radiation. Figure 6.12 shows

the density profile of an aluminium target as predicted by MULTI-IFE after 1.2 ns of simulation time with no incident radiation. The expansion of the target is fairly minor, but crucially the proportion of cells within the initial target with cell temperature above the melting temperature is small – roughly 0.2%, corresponding to an “ablation depth” of 0.12  $\mu\text{m}$ . For the gold target the entire initial target volume remains below the melting temperature, with the melting transition occurring in the expanded plume approximately 0.16  $\mu\text{m}$  from the target surface. As the effect of laser energy deposition on expansion is non-linear, this initial level of expansion cannot simply be removed as a consistent baseline. We have chosen to neglect the effect of this initial target expansion on the final ablation depths, however a more rigorous characterisation of its impact would improve the accuracy of subsequent work.

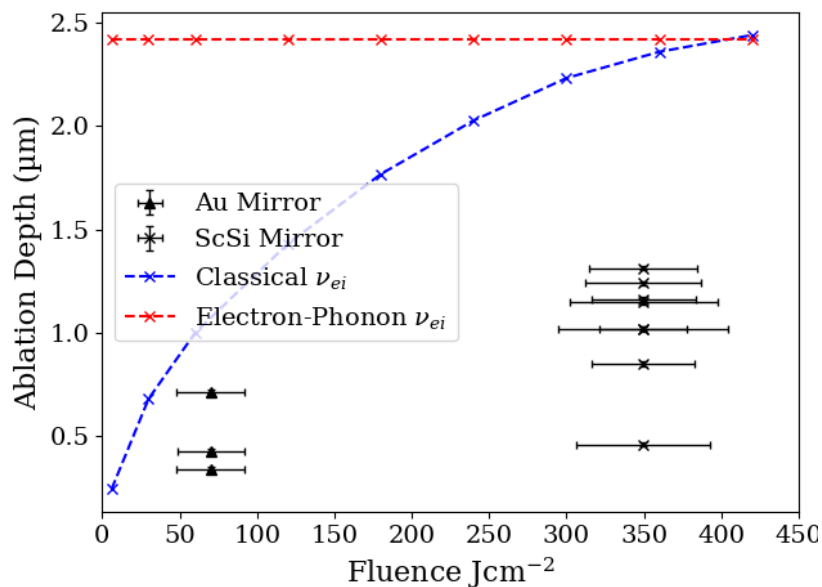


Figure 6.13: Ablation depths predicted by MULTI-IFE simulations of a range of fluences of 46.9 nm radiation incident on an aluminium target compared to results collected experimentally in Chapter 3. Results for simulations using both the classical and electron-phonon electron-ion collision frequency models are shown.

Figure 6.13 shows the ablation depths predicted by MULTI-IFE simulations using the classical and electron-phonon electron-ion collision frequency models for an aluminium target, compared against the experimental ablation depths. Surprisingly, the electron-phonon model predicts significantly higher ablation depths than those seen experimentally, and little variation in the ablation depth with fluence. The classical model predicts lower ablation depths, much closer to those seen in experiment, but still too large. The classical model also predicts much greater variation in ablation

depth with fluence, with a logarithmic form as predicted by the bleaching wave model. Crucially, neither model predicts ablation depths that correlate well with those seen experimentally.

Figure 6.14 shows the ablation depths predicted by the classical and electron-phonon electron-ion collision frequency models for a gold target, compared against the experimental ablation depths. Similarly to aluminium, the electron-phonon model predicts ablation depths that are much too high, shown here in figure 6.14 in an insert. However, the classical model predicts ablation depths that agree rather well with the experimental results. Clearly, the hydrodynamic expansion of the target limited the accuracy of earlier simulations and this has now been rectified.

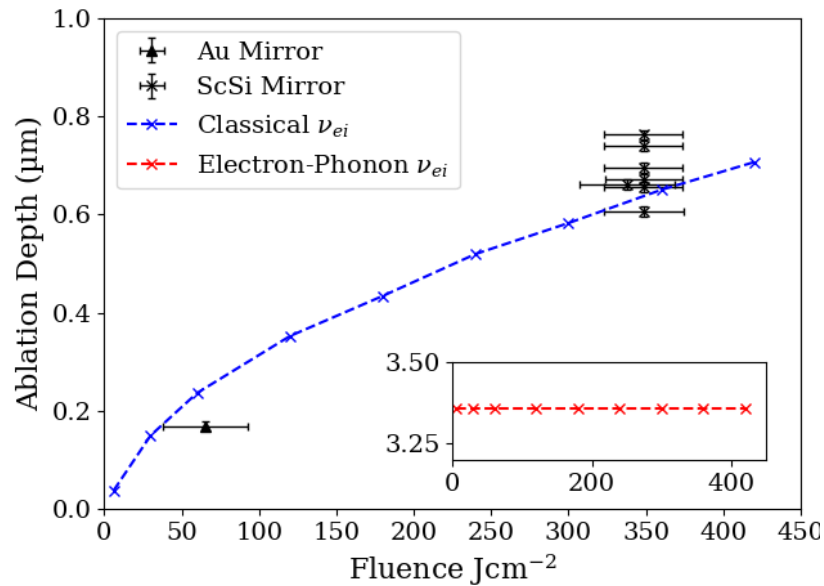


Figure 6.14: Ablation depths predicted by MULTI-IFE simulations of a range of fluences of 46.9 nm radiation incident on a gold target compared to results collected experimentally in Chapter 3. Results for simulations using both the classical and electron-phonon electron-ion collision frequency models are shown.

## 6.6 Energy Deposition

A key point of comparison between the hydrostatic and hydrodynamic simulation techniques is the position and density of energy deposited by the laser into the target. For the simulations to be comparable, the total energy deposited in the target must be approximately the same, and the energy densities should be of comparable orders of magnitude. The latter is considered first.

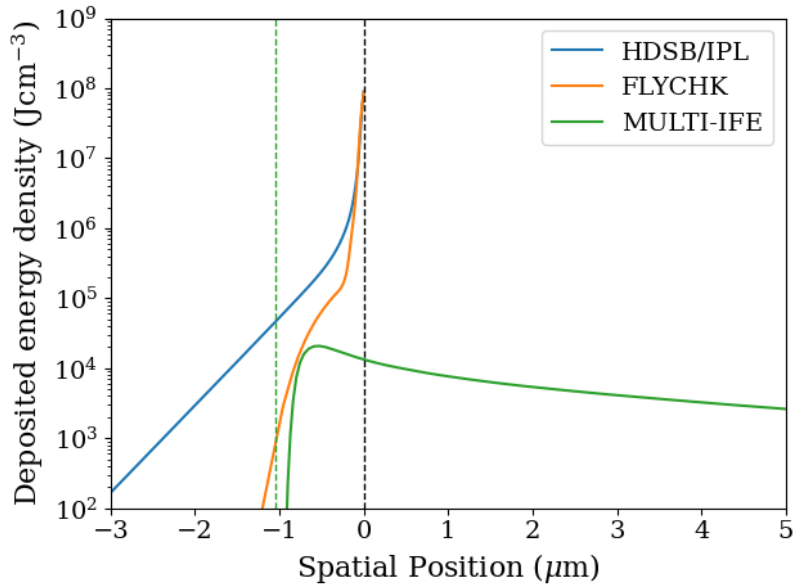


Figure 6.15: Deposited laser energy as a function of spatial position for the Saha Boltzmann (HDSB/IPL) and FLYCHK hydrostatic models and MULTI-IFE hydrodynamic model at time  $t = 0.637$  ns with  $1 \times 10^{12}$  W cm $^{-2}$  incident on an aluminium target. The broken green line shows the ablation depth predicted by the MULTI-IFE simulation.

Figure 6.15 shows deposited laser energy per unit volume as a function of spatial position for the HDSB/IPL and FLYCHK hydrostatic models, and the MULTI-IFE hydrodynamic model at time  $t = 0.637$  ns just after the peak of a  $1 \times 10^{12}$  W cm $^{-2}$  laser pulse incident on an aluminium target. The simulations have been aligned so that the front face of the targets are located at  $x = 0$ . The spatial range is truncated to only show the most relevant area around the target face. The broken green line shows the ablation depth predicted by MULTI-IFE at this time.

Figure 6.15 shows good agreement between the MULTI-IFE and FLYCHK simulations within the target close to the ablation front. As we approach the front of the target, this agreement weakens due to the much higher density of material in the hydrostatic target caused by a lack of expansion. As these deposited energy density values are cumulative, the energy deposited in the plume (i.e. in front of the target surface) can be attributed to the low level of direct absorption in the plume combined with earlier energy deposition into material that has subsequently expanded.

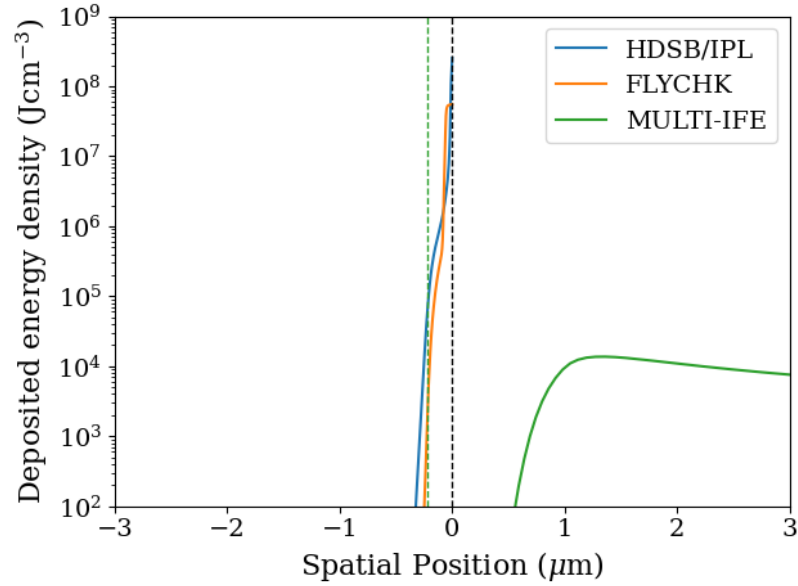


Figure 6.16: Deposited laser energy as a function of spatial position for the Saha Boltzmann (HDSB/IPL) and FLYCHK hydrostatic models and MULTI-IFE hydrodynamic model at time  $t = 0.637$  ns with  $1 \times 10^{12}$  W cm $^{-2}$  incident on a gold target. The broken green line shows the ablation depth predicted by the MULTI-IFE simulation.

Figure 6.16 shows deposited laser energy per unit volume as a function of spatial position for the HDSB/IPL and FLYCHK hydrostatic models, and the MULTI-IFE hydrodynamic model at time  $t = 0.637$  ns just after the peak of a  $1 \times 10^{12}$  W cm $^{-2}$  laser pulse incident on a gold target. Here, agreement is not good within the target, in fact the MULTI-IFE simulations predict no energy has been deposited into material still in the target at this time. Material originally within the ablation depth of the target has now expanded so that the energy absorbed in ablation is now found in the expanding plume of plasma. Again the broken green line shows the ablation front.

Given the lack of movement in the hydrostatic model, it is a more direct comparison to examine the total energy deposited into the mass liberated by the ablation interaction. This can be achieved by summing the deposited energies to give a total deposited energy and dividing this by the mass that was contained in the crater that is left after ablation. The mass is calculated using the density and ablation depth and assuming a spot size of  $1.8 \mu\text{m}$ , as we determined in Chapter 3, to convert the energy density into energy per gram.

Figures 6.17 and 6.18 show the deposited energy per gram of ablated material as predicted by both hydrostatic models, Saha-Boltzmann (HDSB/IPL) and FLYCHK, and MULTI-IFE for aluminium and gold targets respectively. The values are broadly similar across all three simulation methods, and between materials. This shows that the absorption mechanisms utilised in all simulations agree.

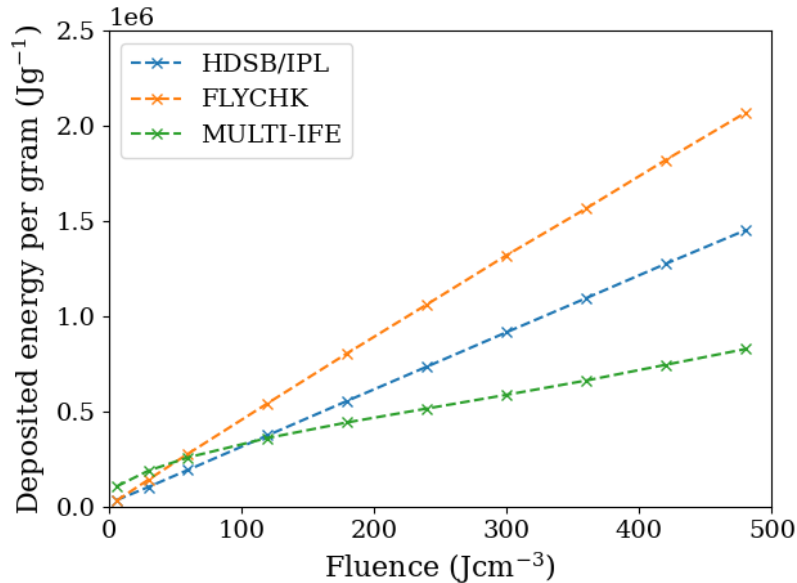


Figure 6.17: Total energy deposited per gram of ablated mass as predicted by the Saha-Boltzmann (HDSB/IPL) and FLYCHK hydrostatic models and the MULTI-IFE hydrodynamic model for an aluminium target.

Finally, the total energy deposited into the target has been calculated in order to ensure that the energy densities above for the different simulations are comparable. Again assuming a spot size of  $1.8\ \mu\text{m}$  and summing over all the volumes in which energy is deposited, we get the total deposited energies shown in figure 6.19. Both simulations deposit the same amount of laser energy for each material, as expected, and the laser energies deposited are approximately equal to those measured during the ablation experiment. There is only a slight difference in the total energy deposited between the simulation methods, possibly accounted for by MULTI-IFE's inclusion of reflected radiation and radiative losses.

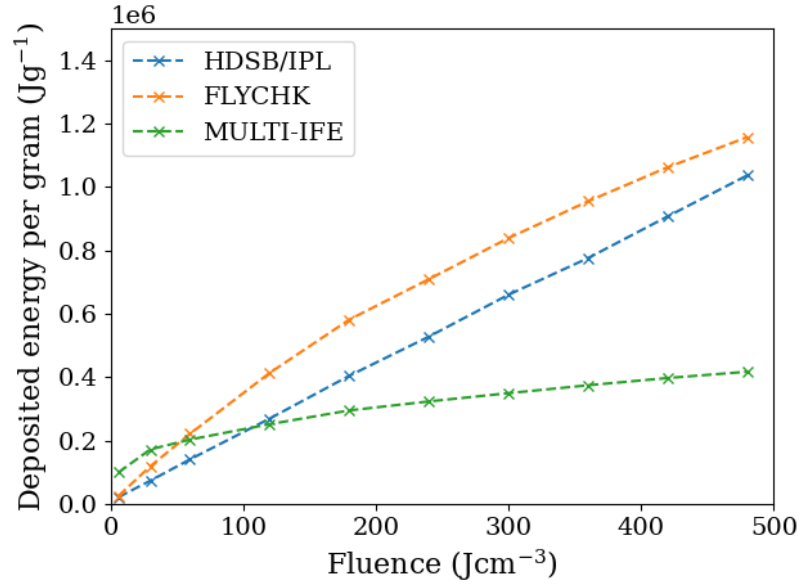


Figure 6.18: Total energy deposited per gram of ablated mass as predicted by the Saha-Boltzmann (HDSB/IPL) and FLYCHK hydrostatic models and the MULTI-IFE hydrodynamic model for a gold target.

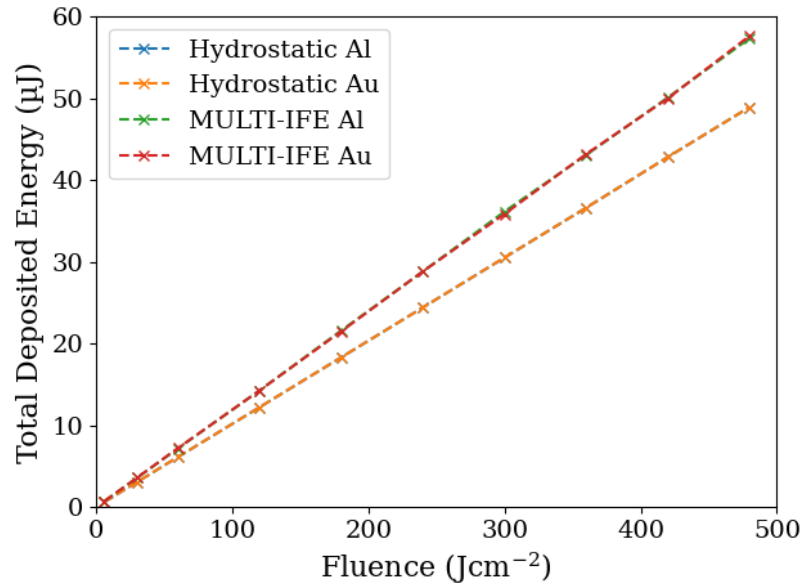


Figure 6.19: Total deposited laser energy as a function of fluence for the High Density Saha-Boltzmann simulations (with IPL), and for the MULTI-IFE simulations of both aluminium and gold targets.

## 6.7 Summary and Conclusions

In this chapter, the one-dimensional radiation-hydrodynamics code MULTI-IFE was briefly described and was used to conduct simulations with the intention of replicating the ablation depth behaviour as a function of fluence seen in experiment. The formula for bremsstrahlung absorption within the code was adjusted to accurately include the effects of stimulated emission. This was tested and was found to have a negligible impact on the outcome of the simulations. Internal parameters of the simulation such as a fixed boundary at the rear of the target, and a heat flux limiting factor were also tested and were found to have little impact on the outcome of the simulations too.

Simulations were performed over a range of fluences to compare the depth of ablation predicted by MULTI-IFE with those seen experimentally in Chapter 3. As the code uses an absorption coefficient model formulated around the electron-ion collision frequency (other processes are similarly dependent), the choice of electron-ion collision frequency model significantly affected the outcome of the simulations. The two models tested were a classical model using the Spitzer formula for the collision frequency and an electron-phonon model that uses empirical coefficients to account for lattice vibrations and phonon absorption. For both materials, the electron-phonon model predicted much greater ablation depths than those seen experimentally. The outcome for the Spitzer model was better, with simulated ablation depths matching those seen experimentally on the gold target well, but overestimating those seen on the aluminium target.

The energy densities of the MULTI-IFE simulations were compared to those of the High Density Saha-Boltzmann model from Chapter 5. It was found that the total energy deposited by the laser was consistent across materials for both models and only differed slightly between the two simulation methods. The deposited energy densities differed due to the plasma expansion in the MULTI-IFE simulations decreasing these values.

This leads us to several key conclusions. Firstly, the electron-phonon collision frequency model, which before conducting the simulations looked to be the more physically accurate model for our parameter space, does not accurately predict the ablation behaviour of metals at these wavelengths and intensities. The classical Spitzer model is more accurate for both metals, suggesting the plasma is closer to an ideal plasma and less like warm dense matter than previously envisaged. This is supported by the findings in Chapter 4, that the absorption mechanism is dominated by inverse

bremsstrahlung absorption and not photo-ionization, as the inverse bremsstrahlung interaction produces higher electron temperatures that facilitate more rapid expansion and lower plasma densities.

Secondly, for aluminium, i.e. long attenuation length metals, the fluid motion does not play a significant role in the final ablation depth. This is supported by the good agreement between the hydrostatic model and the experimental ablation depths. The poorer agreement with the hydrodynamic simulations can be attributed to an increase in lateral transport, not accounted for in the one-dimensional modelling, caused by the longer attenuation length and therefore higher aspect ratio. This may also support the initial assertion that, for aluminium at least, the ablation rates are dominated by laser absorption, as opposed to being driven by thermal conduction as with optical wavelength ablation.

Finally, the ablation of short attenuation length materials, such as gold, appears to be very similar to optical ablation of similar metals. This is supported by the accuracy of the ablation depths predicted by MULTI-IFE using the Spitzer electron-ion collision frequency model. This accuracy also supports the assertion that there is a low level of lateral transport in these short attenuation length materials.

# Chapter 7

## Conclusions

### 7.1 Summary of results

Chapter 3 detailed an experimental ablation study using a CDL radiation source lasing at 46.9 nm from neon-like argon ions with pulse energies of up to 50  $\mu\text{J}$  and a pulse duration of 1.2 ns. Aluminium, gold, and copper targets were ablated with fluences ranging from 50  $\text{J cm}^{-2}$  to 500  $\text{J cm}^{-2}$ . Ablation features on aluminium, gold, and copper had depths in the region of 1.2  $\mu\text{m}$ , 0.7  $\mu\text{m}$ , and 0.5  $\mu\text{m}$  respectively and crater radii between 2  $\mu\text{m}$  and 3.5  $\mu\text{m}$ .

Also in Chapter 3, a pair of simple models for relating fluence and ablation depth were presented. The first was based on the Gamaly model [10], predicting a logarithmic relation between ablation depth and fluence. This model predicted reasonable ablation depths for aluminium, which has a long attenuation length at 46.9 nm wavelengths, but greatly underestimated the ablation depths for gold and copper, which have short attenuation lengths. The second model, referred to as the bleaching wave model, predicts a linear progression of ablation into the target as each thin layer is bleached in turn. This model was empirically fitted to the ablation depths, predicting no ablation threshold and a bleaching temperature for each material (given by the gradient). We investigated these bleaching temperatures in Chapter 4.

Chapter 4 aimed to contextualise the predicted bleaching temperatures from Chapter 3 by modelling the plasma conditions at these temperatures. A Saha-Boltzmann model was used for the ionization balance and classical absorption coefficients were used to calculate the absorption by inverse bremsstrahlung and photo-ionization. These models were used to calculate the internal energy of the plasma and the transmission of radiation through a 10 nm slice of plasma using the Beer-Lambert law. The transmission behaviour as a function of temperature anticipated by the bleaching wave model is a step function, with lower transmission at low temperatures, a transition region, and then close to 100% transmission at higher temperatures. This behaviour was not seen clearly, although there was a temperature region in which transmission was significantly increased. Above  $\approx 20$  eV however, the increasing ionization and dominance of inverse bremsstrahlung absorption reduced the transmission significantly.

Having not seen the step function behaviour initially expected in the transmission curves as a function of temperature, the model was revisited to account for previously neglected effects that may improve this. The ionization model was considered first. A high density form of the Saha-Boltzmann model was trialled that uses Fermi-Dirac statistics rather than Maxwellian statistics. This was seen to have a very small impact on the electron densities predicted by the ionization model so for simplicity was not included in further modelling. An ionization potential lowering model, formulated by Stewart and Pyatt [83], was also trialled, and this was found to have a greater impact on the electron density (increases of up to 85% were seen), and so this correction was carried forward.

The next group of corrections were made to the absorption coefficient expressions. We began by investigating the quantum mechanical Gaunt factors for inverse bremsstrahlung and photo-ionization and how these compared to the Kramers value ( $\langle G_{ff,bf} \rangle = 1$ ) used up until this point. Both were found to be close to 1 for the plasma conditions predicted by the model, so the Kramers value was retained. Degeneracy corrections were also made to the absorption coefficients by replacing Maxwellian statistics in their original derivations with Fermi-Dirac statistics. This was found to have a material-dependent impact on the predicted transmission which was most significant for the more dense materials (i.e. highest impact on copper, lowest on aluminium).

None of the corrected models predicted the clear step function behaviour anticipated by the bleaching wave model. In light of this, the calculations were repeated using the existing ionization tool FLYCHK [93] for comparison. The FLYCHK ionization

model predicted considerably higher electron densities at low temperatures due to the treatment of conduction band electrons as quasi-free electrons. The result of this is that inverse bremsstrahlung absorption dominates throughout the temperature range, as opposed to above a certain temperature. The FLYCHK calculations showed signs of true bleaching behaviour in the gold target only, at temperatures above 120 eV.

The absorption coefficients predicted by both the Saha-Boltzmann and FLYCHK ionization models were compared against three models from the literature for 32 nm light incident on an aluminium target, following a recent comparison by Vinko *et al.* [98]. Of these three models, by Iglesias [53], Shaffer *et al.* [96], and Hollebon *et al.* [97], the Iglesias coefficients compared most favourably against the absorption coefficients predicted by the Saha-Boltzmann based model, despite its comparative simplicity. The FLYCHK model showed poor agreement with all of the other models, however it is known that FLYCHK's accuracy is limited in this temperature and density range.

This investigation therefore does not support the bleaching wave model, although more experimental data would be useful in confirming this.

Chapter 5, building on the lack of strong evidence supporting the bleaching wave model in Chapter 4, aimed to replace the bleaching wave model by adding in time-resolved effects. A brief comment on the effect of photo-ionization on the balance of populating and de-populating collisional processes was made first, with a scheme outlined by which the ion populations this would predict could be calculated. Initial calculations showed that the impact of photo-ionization on the collisional balance is minimal below  $1 \times 10^{13} \text{ W cm}^{-2}$ , and only significant at intensities of  $1 \times 10^{15} \text{ W cm}^{-2}$  or greater.

Chapter 5 also included the development of a simple hydrostatic transmission model with spatial resolution. This one-dimensional model was used to simulate ablation of aluminium, gold, and copper targets with 46.9 nm wavelength radiation in 1.2 ns duration pulses of varying fluences. Ablation depths were extracted using three criteria for considering a cell to have been ablated; a cell electron density above 1% solid density, a cell electron density above 10% solid density, and a cell temperature above the boiling point of the target material. The transmission model predicted ablation depths similar to those seen on aluminium when the  $n_e = 10\%$  of solid density criterion was used, and over-predicted these ablation depths for the other criteria. The transmission model greatly under-predicted the ablation depths on gold and copper targets with all three criteria.

Calculations were then repeated using the FLYCHK ionization model, and these ablation depths were found to be in better agreement with the experimental ablation depths for aluminium. The agreement was still poor in comparison to experimental ablation depths seen on gold and copper

The final point investigated in Chapter 5 was the effect of aluminium oxide on the predicted ablation depths, the consensus being that a layer of aluminium oxide around 2 nm to 3 nm thick [99] forms on the surface of any bulk aluminium. Using transmission values from the literature [3] the peak intensities were reduced to simulate an aluminium oxide filter of appropriate thickness. This is an overestimation of the impact of this layer and was found to have a very minimal effect on the predicted ablation depth.

The study in Chapter 4 showing that the EUV laser absorption is dominated by inverse bremsstrahlung, especially in the case when the conduction band electrons are treated as quasi-free, indicated that a fluid code modelling only inverse bremsstrahlung absorption is capable of accurately simulating EUV ablation. Chapters 4 and 5 also confirmed that the use of standard ionization models (i.e. the Saha-Boltzmann model) is also valid. In Chapter 6 the radiation-hydrodynamics code MULTI-IFE [9] was used to produce simulations of 1.2 ns pulses of 46.9 nm radiation incident on aluminium and gold targets at a range of fluences. The absorption coefficient for inverse bremsstrahlung was adjusted to correctly account for stimulated emission, although this was found to have limited impact on the absorption. Using an empirical fitting from the equation of state model QEOS [102], ablation depths were extracted and plotted as a function of fluence. The results of two electron-ion collision frequencies were explored; the classical formulation of Spitzer [56], and an electron-phonon model that takes account of bulk effects [59].

For the aluminium target, both the classical Spitzer electron-ion collision frequency and the electron-phonon collision frequency over-predicted the ablation depth, however the Spitzer model was the more accurate of the two. The Spitzer model also predicted a more physically accurate behaviour of ablation depth increasing with fluence. The relation between fluence and ablation depth had an approximately logarithmic shape, similar to that predicted by the Gamaly model. For the gold target, the Spitzer model gave good predictions of ablation depth, and the electron-phonon model once again predicted much greater ablation depths than seen experimentally.

## 7.2 Conclusions

The investigations presented in the thesis have led to a number of conclusions, particularly regarding the assumptions that have been made in the course of the investigation.

First, the contribution of photo-ionization to this interaction is not as significant as expected; the absorption is entirely inverse bremsstrahlung dominated at temperatures above 20 eV. This implies that the use of models containing only the inverse bremsstrahlung interaction, such as MULTI-IFE, is valid apart from at early times within the interaction when the electron temperatures are low and photo-ionization is important. If the conduction band electrons are treated as quasi-free, as in FLYCHK, photo-ionization does not occur due to the non-availability of ionizable species and inverse bremsstrahlung also dominates. This means that the absorption in EUV ablation is similar to optical wavelength ablation where inverse bremsstrahlung absorption dominates at all densities below critical.

Second, for materials with long EUV attenuation lengths (aluminium in this study), time-resolved simulations need not be made; the Gamaly model predicts ablation depths that are close to those measured experimentally at lower fluences. However, the hydrostatic model predicted ablation depths closer to those measured experimentally throughout the fluence range investigated. Both models predict an exponential decay of radiation into the target, leading to a logarithmic relation between ablation depth and incident fluence. The deposition of energy over a larger volume (due to the longer EUV attenuation length) produces shallower temperature and density gradients, meaning that fluid motion plays a less important role in the ablation propagation and can be ignored without sacrificing ablation depth accuracy. The over-prediction of ablation depths by the one-dimensional fluid code suggests lateral transport may be significant in ablation of these materials.

Third, our studies in Chapters 4 and 5 gave no strong evidence to support the bleaching wave model. Transmission behaviour as a function of temperature showed some increase at mid-low temperatures but above this, where we would expect to see high transmission, the absorption increased due to the dominance of inverse bremsstrahlung in the absorption. The only material that showed signs of bleaching was gold at temperatures above 120 eV as predicted by the FLYCHK model, but this did not translate into bleaching wave behaviour in the time-resolved simulations.

Finally, our study in Chapter 6 shows that the EUV ablation of short attenuation

length materials (gold and copper in this study) can be modelled with reasonable accuracy using existing fluid codes. This is supported by our findings in Chapters 4 and 5; that inverse bremsstrahlung dominates the absorption process and that ignoring the hydrodynamic motion underestimates the achieved ablation depth. The deposition of energy over a smaller volume (due to the shorter EUV attenuation length) produces sharper temperature and density gradients, meaning that fluid motion is significant and plays an important role in the ablation propagation. The low aspect ratio of the ablation volume in short EUV attenuation length materials results in lower levels of lateral transport, hence the one-dimensional fluid simulations can be expected to be accurate.

In order to accurately simulate EUV ablation interactions we can separate target materials into two groups by attenuation length. Those materials with long attenuation lengths, of the order of  $10^2$  nm, can be treated using a hydrostatic approach, similar to those used for short pulse interactions, like the Gamaly model or the model described in Chapter 5. Those materials with short attenuation lengths, of the order of 10 nm, can be accurately modelled using one-dimensional fluid codes.

### 7.3 Future work

The most obvious direction for future work is in the collection of further experimental results. The fluence ranges covered in Chapter 3 are as large as can be achieved with a CDL device of this type, but a greater variety data points within the range would make the assessment of the different models clearer. This could be achieved using any form of attenuation along the beamline, for example using varying thicknesses of aluminium foil or an argon gas cell with variable internal pressure.

Further comparison between optical and EUV wavelength ablation interactions would benefit from producing ablation features on similar targets at similar fluences. The comparison between ablation features with only the wavelength variable between them would be very efficient in determining which effects were dominant. In such an experiment a measure of the plasma temperature would be beneficial, either by electron collection, using a Faraday cup for example, or using a probing technique.

Finally, the rate equation model could be explored in greater detail for XFEL parameters. At present, these are largely investigated using inverse-bremsstrahlung absorption approaches and treating the conduction band electrons as quasi-free. We have shown that the alternative, treating the electrons as bound and including photo-

ionization absorption, can be as accurate, and the rate equation model may prove to be more accurate than a simpler treatment using the unaltered Saha-Boltzmann model.

# Appendix A

## Changes to MULTI-IFE source code

This appendix lists the line-by-line changes made to the MULTI-IFE source code, should there be a wish to replicate the adjustments made in this thesis.

The steps below assign absorption coefficient  $k$  to a variable so that it can be output and apply the correction to the absorption expression.

- Line 286 – `real*8, pointer :: k(:) => null()` (added)
- Line 1416 – `intent(in)` (changed to) `intent(inout)`
- Line 1460 – `intent(in)` (changed to) `intent(inout)`
- Line 1498 – `* &` (added)
- Line 1499 – `((bolz*t%te)/(hb*omega))*(1-exp(-(hb*omega)/(bolz*t%te)))`  
(added - new line required)
- Line 1500 – `t%k = a` (added)

The steps below allocate and deallocate memory to the new variable  $k$  and print it to the output file.

- Line 2423 – `allocate(t%k(n))` (added)
- Line 2424 – `13` (changed to) `14`
- Line 2445 – `t2%k = t1%k` (added)
- Line 2457 – `deallocate(t%k(n))` (added)

- Line 2458 – 13 (changed to) 14
- Line 3448 – `write(11, '(i4,1x,5e14.6)')`  
(changed to) `write(11, '(i4,1x,5e14.5e3)')`
- Line 3449 – (changed to) `t%te(i), e%d(i)*s%r(i), t%k(i), t%ti(i)`
- Line 3451 – `write(11, '(i4,1x,5e14.6)')`  
(changed to) `write(11, '(i4,1x,5e14.5e3)')`

Line numbers given are correct *including* any additions to lines above.

# References

- [1] S. A. Wilson, “A Study of Extreme Ultraviolet Capillary Discharge Lasers and the Ablation of Solid Targets,” PhD Thesis, 2018.
- [2] D Attwood, *Soft X-Rays and Extreme Ultraviolet Radiation: Principles and Applications*. Cambridge, UK: Cambridge University Press, 1999.
- [3] B. L. Henke, G. E. M, and D. J. C, “X-ray interactions: photoabsorption, scattering, transmission, and reflection at E+50-30000 eV, Z=1-92,” *Atomic Data and Nuclear Data Tables*, vol. 54, no. 2, p. 181, 1993.
- [4] J. J. Rocca, V Shlyaptsev, F. G. Tomasel, O. D. Cortázar, D Hartshorn, and J. L. A. Cilla, “Demonstration of a Discharge Pumped Table-Top Soft-X-Ray Laser,” *Physical Review Letters*, vol. 73, no. 16, p. 2192, 1994.
- [5] J. J. Rocca *et al.*, “Discharge-pumped soft-x-ray laser in neon-like argon,” *Physics of Plasmas*, vol. 2, no. 6, p. 2547, 1995.
- [6] J. J. Rocca, M. C. Marconi, J. L. A. Chilla, D. P. Clark, F. G. Tomasel, and V. N. Shlyaptsev, “Discharge-Driven 46.9 nm Amplifier with Gain-Length Approaching Saturation,” *IEEE Journal of Selected Topics in Quantum Electronics*, vol. 1, no. 3, p. 945, 1995.
- [7] J. J. Rocca, D. P. Clark, J. L. A. Chilla, and Shlyaptsev, “Energy Extraction and Achievement of the Saturation Limit in a Discharge-Pumped Table-Top Soft X-Ray Amplifier,” *Physical Review Letters*, vol. 77, no. 8, p. 1476, 1996.
- [8] Y Chen, “Nanofabrication by electron beam lithography and its applications: A review,” *Microelectronic Engineering*, vol. 135, p. 57, 2015.
- [9] R Ramis and J Meyer-ter Vehn, “MULTI-IFE - A one-dimensional computer code for Inertial Fusion Energy (IFE) target simulations,” *Computer Physics Communications*, vol. 203, p. 226, 2016.

- [10] E. G. Gamaly, A. V. Rode, B Luther-Davies, and V. T. Tikhonchuk, “Ablation of solids by femtosecond lasers: Ablation mechanism and ablation thresholds for metals and dielectrics,” *Physics of Plasmas*, vol. 9, no. 3, p. 949, 2002.
- [11] R. C. Elton, *X-Ray Lasers*. Cambridge, MA, USA: Academic Press, 1990.
- [12] B. E. Lemoff, C. P. J. Barty, and S. E. Harris, “Femtosecond-pulse-driven, electron-excited XUV lasers in eight-times-ionized noble gases,” *Optics Letters*, vol. 19, no. 8, p. 569, 1994.
- [13] S. M. Hooker and S. E. Harris, “Femtosecond-pulse-driven electron-excited extreme-ultraviolet lasers in Be-like ions,” *Optics Letters*, vol. 20, no. 19, p. 1994, 1995.
- [14] D. L. Matthews *et al.*, “Demonstration of a Soft X-Ray Amplifier,” *Physical Review Letters*, vol. 54, no. 2, p. 110, 1985.
- [15] J Collier, D Pepler, C Danson, J Warwaick, C Lewis, and D Neely, “The ‘travelling wave’ focus on VULCAN,” *CLF Annual Report*, p. 609, 1996.
- [16] B. W. J. McNeil and N. R. Thompson, “X-ray free-electron lasers,” *Nature Photonics*, vol. 4, p. 814, 2010.
- [17] P Salières and M Lewenstein, “Generation of ultrashort coherent xuv pulses by harmonic conversion of intense laser pulses in gases: Towards attosecond pulses,” *Measurement Science and Technology*, vol. 12, p. 1818, 2001.
- [18] J. J. Rocca *et al.*, “Capillary discharge tabletop soft x-ray lasers reach new wavelengths and applications,” *Comptes Rendus de l’Académie des Sciences, t. 1, Série IV*, p. 1065, 2000.
- [19] J Nilsen and J. H. Scofield, “Wavelengths of Neon-like  $3p \rightarrow 3s$  X-ray laser transitions,” *Physica Scripta*, vol. 49, p. 588, 1994.
- [20] B. J. MacGowan *et al.*, “Short wavelength x-ray laser research at the Lawrence Livermore National Laboratory,” *Physics of Fluids B: Plasma Physics*, vol. 4, p. 2326, 1992.
- [21] C Jensen and D Qunell, “A thyratron trigger with low jitter,” *Proceedings of the 1997 Particle Accelerator Conference*, vol. 1, p. 1281, 1997.
- [22] V Aslanyan *et al.*, “Ablation and transmission of thin solid targets irradiated by intense extreme ultraviolet laser radiation,” *APL Photonics*, vol. 1, p. 066 101, 2016.

- [23] B. R. Benware, C. D. Macchietto, C. H. Moreno, and J. J. Rocca, "Demonstration of a High Average Power Tabletop Soft X-Ray Laser," *Physical Review Letters*, vol. 81, no. 26, p. 5804, 1998.
- [24] L Urbanski *et al.*, "Spectral linewidth of Ne-like Ar capillary discharge soft x-ray laser and its dependence on amplification beyond gain saturation," *Physical Review A*, vol. 85, p. 033837, 2012.
- [25] G Vaschenko *et al.*, "Nanoimaging with a compact extreme ultraviolet laser," *Optics Letters*, vol. 30, p. 2095, 16 2005.
- [26] F Brizuela *et al.*, "Imaging at the nanoscale with practical tabletop EUV laser-based full-field microscopes," *IEEE Journal of Selected Topics in Quantum Electronics*, vol. 18, p. 434, 1 2012.
- [27] F Brizuela *et al.*, "Reflection mode imaging using a compact extreme ultraviolet laser," *Optics Express*, vol. 13, no. 11, p. 3983, 2005.
- [28] R. L. Sandberg *et al.*, "High numerical aperture tabletop soft x-ray diffraction microscopy with 70 nm resolution," *PNAS*, vol. 105, p. 24, 1 2008.
- [29] P. W. Wachulak *et al.*, "Sub 400 nm spatial resolution extreme ultraviolet holography with a tabletop laser," *Optics Express*, vol. 14, p. 9636, 21 2006.
- [30] J Nejdil *et al.*, "Image plane holographic microscopy with a table-top soft x-ray laser," *IEEE Photonics Journal*, vol. 7, no. 1, p. 6900108, 2015.
- [31] J. J. Rocca *et al.*, "Application of extremely compact capillary discharge soft x-ray lasers to dense plasma diagnostics," *Physics of Plasmas*, vol. 10, p. 2031, 2003.
- [32] M. G. Capeluto *et al.*, "Nanopatterning with Interferometric Lithography Using a Compact  $\lambda = 46.9$  nm Laser," *IEEE Transactions on Nanotechnology*, vol. 5, no. 1, p. 3, 2006.
- [33] L Urbanski, M. C. Marconi, A Isoyan, A Stein, C. S. Menoni, and J. J. Rocca, "Analysis of a scheme for de-magnified Talbot lithography," *Journal of Vacuum Science and Technology B*, vol. 29, no. 6, 06F504, 2011.
- [34] G. J. Tallents, E Wagenaars, and G Pert, "Lithography at EUV wavelengths," *Nature Photonics*, vol. 4, p. 809, 2010.
- [35] ASML, *Lithography principles*, <https://www.asml.com/en/technology/lithography-principles>, Accessed: August 2021.

- [36] H Bravo *et al.*, “Demonstration of Nanomachining with Focused Extreme Ultraviolet Laser Beams,” *IEEE Journal of Selected Topics in Quantum Electronics*, vol. 18, no. 1, p. 443, 2012.
- [37] T Green *et al.*, “Characterisation of extreme ultraviolet laser ablation mass spectroscopy for actinide trace analysis and nanoscale isotopic imaging,” *Journal of Analytical Atomic Spectrometry*, vol. 32, p. 1092, 2017.
- [38] I Langmuir, “Oscillations in Ionized Gases,” *Proceedings of the National Academy of Sciences*, vol. 14, no. 8, p. 627, 1928.
- [39] F. F. Chen, *Plasma Physics and Controlled Fusion*. New York, NY, USA: Plenum, 1984.
- [40] R. W. P. McWhirter, *Plasma Diagnostic Techniques*, R. H. Huddlestone and S. L. Leonard, Eds. New York, NY, USA: Academic Press, 1965.
- [41] M. N. Saha, “LIII. Ionization in the solar chromosphere,” *Philosophical Magazine*, vol. 40, no. 238, p. 472, 1920.
- [42] R. Schoenlein *et al.*, “Proposal to doe basic energy sciences: Ultrafast x-ray science facility at the advanced light source,” Sep. 2021. DOI: 10.2172/816276.
- [43] S Atzeni and J Meyer-ter Vehn, *The Physics of Inertial Fusion*. Oxford, UK: Oxford University Press, 2004.
- [44] NASA, *World book at nasa - sun*, [https://web.archive.org/web/20050217044235/http://www.nasa.gov/worldbook/sun\\_worldbook.html](https://web.archive.org/web/20050217044235/http://www.nasa.gov/worldbook/sun_worldbook.html), Accessed: August 2021.
- [45] A Beer, “Bestimmung der Absorption des rothen Lichts in farbigen Flüssigkeiten,” *Annalen def Physik und Chemie*, vol. 162, no. 5, p. 78, 1852.
- [46] E. M. Purcell, *Electricity and Magnetism*. New York, NY, USA: McGraw-Hill, 1984.
- [47] J Larmor, “LXIII. On the theory of the magnetic influence on spectra; and on the radiation from moving ions,” *Philosophical Magazine*, vol. 44, no. 271, p. 503, 1897.
- [48] G. J. Tallents, *An Introduction to the Atomic and Radiation Physics of Plasmas*. Cambridge, UK: Cambridge University Press, 2018.
- [49] I. H. Hutchinson, *Principles of plasma diagnostics*. Cambridge, UK: Cambridge University Press, 2002.

- [50] J. A. Gaunt, “Continuous Absorption,” *Philosophical Transactions of the Royal Society of London. Series A, Containing Papers of a Mathematical or Physical Character*, vol. 229, p. 163, 1930.
- [51] H. A. Kramers, “On the theory of X-ray absorption and of the continuous X-ray spectrum,” *The London, Edinburgh, and Dublin Philosophical Magazine and Journal of Science*, vol. 46, no. 275, p. 836, 1923.
- [52] A Sommerfeld, “Zur Elektronentheorie der Metalle auf Grund der Fermischen Statistik,” *Zeitschrift für Physik*, vol. 47, p. 1, 1928.
- [53] C. A. Iglesias, “XUV absorption by solid-density aluminium,” *High Energy Density Physics*, vol. 6, p. 311, 2010.
- [54] M. Z. Mo, Z Chen, S Fourmaux, A Saraf, S Kerr, *et al.*, “Measurements of Ionization States in Warm Dense Aluminium with Betatron Radiation,” *Physical Review E*, vol. 95, p. 053 208, 5 2017.
- [55] S. I. Braginskii, “Transport processes in a plasma,” in (Reviews of Plasma Physics), *Reviews of Plasma Physics*. New York, NY, USA: Consultants Bureau, 1965, vol. 1.
- [56] L Spitzer, *Physics of Fully Ionized Gases*. New York, NY, USA: John Wiley & Sons, 1962.
- [57] R Ramis, R Schmalz, and J Meyer-ter Vehn, “MULTI - A computer code for one-dimensional multigroup radiation hydrodynamics,” *Computer Physics Communications*, vol. 49, p. 475, 1988.
- [58] D. G. Yakovlev and V. A. Urpin, “Thermal and electrical conductivity in white dwarfs and neutron stars,” *Soviet Astronomy*, vol. 24, no. 3, p. 303, 1980.
- [59] K Eidmann, J Meyer-ter Vehn, T Schlegel, and S Hüller, “Hydrodynamic simulation of subpicosecond laser interaction with solid-density matter,” *Physical Review E*, vol. 62, no. 1, 2000.
- [60] T Sekikawa, A Kosuge, T Kanai, and S Watanabe, “Nonlinear optics in the extreme ultraviolet,” *Nature*, vol. 432, p. 605, 2004.
- [61] Y. P. Pershin, E. N. Zubarev, V. V. Kondratenko, V. A. Sevryukova, and S. V. Kurbatova, “Reactive diffusion in Sc/Si multilayer X-ray mirrors with CrB<sub>2</sub> barrier layers,” *Applied Physics A: Materials Science and Processing*, vol. 103, p. 1021, 2011.

- [62] D. L. Windt, “IMD - Software for modeling the optical properties of multilayer films,” *Computers in Physics*, vol. 12, no. 4, p. 360, 1998.
- [63] E Hecht, *Optics*. Harlow, UK: Pearson Education Limited, 2017.
- [64] P Virtanen, R Gommers, T. E. Oliphant, M Haberland, T Reddy, *et al.*, “SciPy 1.0: Fundamental Algorithms for Scientific Computing in Python,” *Nature Methods*, vol. 17, p. 261, 2020.
- [65] C. F. Quate, “The AFM as a tool for surface imaging,” *Surface Science*, vol. 299-300, p. 980, 1994.
- [66] J. M. Liu, “Simple technique for measurements of pulsed Gaussian-beam spot sizes,” *Optics Letters*, vol. 7, no. 5, pp. 196–198, 1982.
- [67] D Nečas and P Klapetek, “Gwyddion: an open-source software for SPM data analysis,” *Central European Journal of Physics*, vol. 10, no. 1, p. 181, 2012.
- [68] M. A. Branch, T. F. Coleman, and Y Li, “A Subspace, Interior, and Conjugate Gradient Method for Large-Scale Bound-Constrained Minimization Problems,” *SIAM Journal on Scientific Computing*, vol. 21, no. 1, p. 1, 1999.
- [69] J Chalupský, L Juha, J Kuba, J Cihelka, V Hájková, *et al.*, “Characteristics of focused soft X-ray free-electron laser beam determined by ablation of organic molecular solids,” *Optics Express*, vol. 15, no. 10, pp. 6036–6043, 2007.
- [70] J Chalupský, P Boháček, V Hájková, S. P. Hau-Riege, P. A. Heimann, *et al.*, “Comparing difference approaches to characterization of focused X-ray,” *Nuclear Instruments and Methods in Physics Research A*, vol. 631, pp. 130–133, 2011.
- [71] J Chalupský, P Boháček, T Burian, V Hájková, S. P. Hau-Riege, *et al.*, “Imprinting a Focused X-Ray Laser Beam to Measure Its Full Spatial Characteristics,” *Physical Review Applied*, vol. 4, p. 014004, 2015.
- [72] Y Al-Hadithi, G. J. Tallents, J Zhang, M. H. Key, P. A. Norreys, and R Kodama, “Energy transport in plasmas produced by a high brightness krypton fluoride laser focused to a line,” *Physics of Plasmas*, vol. 1, p. 1279, 1994.
- [73] G. J. Tallents, D. S. Whittaker, L. A. Wilson, and E. Wagenaars, “Heating of high energy density plasmas using EUV and x-ray lasers,” in *X-ray Lasers and Coherent X-ray Sources: Development and Applications IX*, J. Dunn and A. Klisnick, Eds., International Society for Optics and Photonics, vol. 8140, SPIE, 2011, p. 105.

- [74] W Rozmus and V. T. Tikhonchuk, “Skin effect and interaction of short pulse laser pulses with dense plasmas,” *Physical Review A*, vol. 42, no. 12, p. 7401, 1992.
- [75] D. R. Lide, Ed., *CRC Handbook of Chemistry and Physics, 84th Edition*. Boca Raton, FL, USA: CRC Press, 2003.
- [76] J. A. Dean, Ed., *Lange’s Handbook of Chemistry, 15th Edition*. New York, NY, USA: McGraw-Hill, 1999.
- [77] Y Zhang, J. R. G. Evans, and S Zhang, “Corrected Values for Boiling Points and Enthalpies of Vaporization of Elements in Handbooks,” *Journal of Chemical Engineering Data*, vol. 56, no. 2, p. 328, 2011.
- [78] R. E. Marshak, “Effect of Radiation on Shock Wave Behaviour,” *The Physics of Fluids*, vol. 1, p. 24, 1958.
- [79] T. K. Lane and R. G. McClarren, “New self-similar radiation-hydrodynamics solutions in the high-energy density, equilibrium diffusion limit,” *New Journal of Physics*, vol. 15, p. 095 013, 2013.
- [80] A. P. Cohen, G Malamud, and S. I. Heizler, “Key to understanding supersonic radiative Marshak waves using simple models and advanced simulations,” *Physical Review Research*, vol. 2, p. 023 007, 2020.
- [81] M. J. Edwards, A. J. MacKinnon, J Zweiback, K Shigemori, D Ryutov, *et al.*, “Investigation of Ultrafast Laser-Driven Radiative Blast Waves,” *Physical Review Letters*, vol. 87, no. 8, p. 085 004, 2001.
- [82] S Bouquet, C Stéhlé, M Koenig, J. P. Chièze, A Benuzzi-Mounaix, *et al.*, “Observation of Laser Driven Supercritical Radiative Shock Precursors,” *Physical Review Letters*, vol. 92, no. 22, p. 225 001, 2004.
- [83] J. C. Stewart and K. D. Pyatt, “Lowering of ionization potentials in plasmas,” *Astrophysical Journal*, vol. 144, p. 1203, 1966.
- [84] W. J. Karzas and R Latter, “Electron radiative transitions in a Coulomb field,” *Astrophysical Journal Supplement*, vol. 6, p. 167, 1961.
- [85] R. F. Reilman and S. T. Manson, “Photoabsorption cross sections for positive ions with  $Z \leq 30$ ,” *The Astrophysical Journal Supplement Series*, vol. 40, p. 815, 1879.

- [86] F Herman and S Skillman, *Atomic Structure Calculations*. Englewood Cliffs, NJ, USA: Prentice-Hall, 1963.
- [87] X.-G. Ma, W. M-S, W. D-H, and Q. Z-J, “Theoretical Studies on Expressions of Condensed-Phase Photoionization Cross Section,” *Communications in Theoretical Physics*, vol. 46, p. 727, 2006.
- [88] R. J. Glauber and M Lewenstein, “Quantum optics of dielectric media,” *Physical Review A*, vol. 43, p. 467, 1991.
- [89] W Ecker and G Kröll, “Lowering of the ionization potential for a plasma in thermodynamic equilibrium,” *Physics of Fluids*, vol. 6, no. 1, p. 62, 1963.
- [90] S. M. Vinko, O Ciricosta, and J. S. Wark, “Density functional theory calculations of continuum lowering in strongly coupled plasmas,” *Nature Communications*, vol. 5, p. 3533, 2014.
- [91] T. R. Preston *et al.*, “The effects of ionization potential depression on the spectra emitted by hot dense aluminium plasma,” *High Energy Density Physics*, vol. 9, p. 258, 2013.
- [92] B. J. B. Crowley, “Continuum lowering - A new perspective,” *High Energy Density Physics*, vol. 13, p. 84, 2014.
- [93] H. K. Chung, M. H. Chen, W. L. Morgan, Y Ralchenko, R. W. Lee, *et al.*, “FLYCHK: Generalized population kinetics and spectral model for rapid spectroscopic analysis for all elements,” *High Energy Density Physics*, vol. 1, p. 3, 1 2005.
- [94] H. K. Chung, W. L. Morgan, and R. W. Lee, “FLYCHK: an extension to the K-shell spectroscopy kinetics model FLY,” *Journal of Quantitative Spectroscopy and Radiative Transfer*, vol. 81, p. 107, 2003.
- [95] R. W. Lee and J. T. Larsen, “A time-dependent model for plasma spectroscopy of k-shell emitters,” *Journal of Quantitative Spectroscopy and Radiative Transfer*, vol. 56, p. 535, 1996.
- [96] N. R. Shaffer, N. G. Ferris, J Colgan, D. P. Kilcrease, and C. E. Starett, “Free-free opacity in dense plasmas with an average atom model,” *High Energy Density Physics*, vol. 23, p. 31, 2017.
- [97] P Hollebon *et al.*, “Ab initio simulations and measurements of the free-free opacity in aluminium,” *Physical Review E*, vol. 100, p. 043 207, 2019.

- [98] S. M. Vinko *et al.*, “Time-resolved XUV Opacity Measurements of Warm Dense Matter,” *Physical Review Letters*, vol. 124, p. 225 002, 2020.
- [99] P Dumas, J Dubarry-Barbe, D Rivière, Y Levy, and J Corset, “Growth of thin alumina film on aluminium at room temperature: A kinetic and spectroscopic study by surface plasmon excitation,” *Journal de Physique Colloques*, vol. 44, p. 205, 1983.
- [100] M. J. Bartolomé, J. F. del Río, E Escudero, S Feliu Jr., V López, *et al.*, “Behaviour of different bare and anodised aluminium alloys in the atmosphere,” *Surface & Coatings Technology*, vol. 202, p. 2783, 2008.
- [101] J Gorobez, B Maack, and N Nilus, “Growth of Self-Passivating Oxide Layers on Aluminum – Pressure and Temperature Dependence,” *Physica Status Solidi B*, vol. 258, p. 2 000 559, 2021.
- [102] R. M. More, K. H. Warren, D. A. Young, and G. B. Zimmerman, “A new quotidian equation of state (QEOS) for hot dense matter,” *The Physics of Fluids*, vol. 31, p. 3059, 1988.
- [103] A. J. Kemp and J Meyer-ter Vehn, “An equation of state code for hot dense matter, based on the QEOS description,” *Nuclear Instruments and Methods in Physics Research A*, vol. 415, no. 3, p. 674, 1998.
- [104] R Ramis and J Meyer-ter Vehn, *MULTI-IFE—A one-dimensional computer code for Inertial Fusion Energy (IFE) target simulations*, 2016. [Online]. Available: <https://data.mendeley.com/datasets/cnrvy8czt7/1>.
- [105] R Ramis, K Eidmann, J Meyer-ter Vehn, and S Hüller, “MULTI-fs - A computer code for laser-plasma interaction in the femtosecond regime,” *Computer Physics Communications*, vol. 183, p. 637, 2012.
- [106] T. Group, “SESAME Report on the Los Alamos Equation of State Library, Report No. LALP-83-4,” Los Alamos National Laboratory, Los Alamos, USA, 1983.
- [107] R. P. Feynman, N Metropolis, and E Teller, “Equations of State of Elements Based on the Generalized Fermi-Thomas Theory,” *Physical Review*, vol. 75, p. 1561, 1949.
- [108] J. F. Barnes, “Statistical Atom Theory and the Equation of State of Solids,” *Physical Review*, vol. 153, p. 269, 1967.

- [109] R. M. More, K. H. Warren, D. A. Young, and G. B. Zimmerman, “A new quotidian equation of state (QEOS) for hot dense matter,” *Physics of Fluids*, vol. 31, p. 3059, 10 1988.
- [110] C. M. Bender and S. A. Orszag, *Advanced Mathematical Methods for Scientists and Engineers*. New York, NY, USA: McGraw-Hill, 1978.
- [111] G Wentzel, “Eine Verallgemeinerung der Quantenbedingungen für die Zwecke der Wellenmechanik,” *Zeitschrift für Physik*, vol. 38, no. 6-7, p. 518, 1926.
- [112] H. A. Kramers, “Wellenmechanik und halbzahlige Quantisierung,” *Zeitschrift für Physik*, vol. 39, no. 10-11, p. 828, 1926.
- [113] L Brillouin, “La mécanique ondulatoire de Schrödinger: une méthode générale de resolution par approximations successives,” *Comptes Rendus de l’Académie des Sciences*, vol. 183, p. 24, 1926.
- [114] C Fourment *et al.*, “Experimental determination of temperature-dependent electron-electron collision frequency in isochorically heated warm dense gold,” *Physical Review B*, vol. 89, 161110(R), 2014.
- [115] R. W. Schoenlein, W. Z. Lin, J. G. Fujimoto, and G. L. Eesley, “Femtosecond Studies of Nonequilibrium Electronic Processes in Metals,” *Physical Review Letters*, vol. 58, no. 16, p. 1680, 1987.
- [116] R. M. More, *Handbook of Plasma Physics*, M Rosenbluth, R Sagdeev, A Rubenchik, and S Witkowski, Eds. Amsterdam, Netherlands: Elsevier, 1991, vol. 3.